

## Abstract

# A new microwave resonator readout scheme for superconducting qubits

Michael B. Metcalfe

2008

Quantum computation is a relatively new field of research, which uses the properties of quantum mechanical systems for information processing. While most proposals for constructing such a quantum computer involve using microscopic degrees of freedom such as those of trapped ions or nuclear spins, this thesis concentrates on using the collective electromagnetic response of a macroscopic electrical circuit to construct the fundamental building block of a quantum computer - a qubit. These macroscopic systems are inherently more difficult to protect from decoherence compared to the microscopic qubit systems because of strong environmental coupling through, for example, the measurement leads. However, superconducting quantum circuits should be easier to scale to large multi qubit systems since they involve simple electrical elements, such as inductors and capacitors for coupling qubits. Furthermore, they can be produced using the highly developed fabrication techniques of integrated circuits.

One of the outstanding issues in superconducting qubit circuits is to read out the qubit state without introducing excessive noise. Such a readout scheme requires speed, sensitivity and should minimally disturb the qubit state. To meet these requirements we have developed a new type of dispersive bifurcating amplifier, called the cavity bifurcation amplifier (CBA), which consists of a Josephson

junction imbedded in a microwave on-chip resonator. The optimum resonator design is based on a simple coplanar waveguide (CPW), imposing a pre-determined frequency and whose other RF characteristics like the quality factor are easily controlled and optimized.

The CBA is sensitive to the susceptibility of the superconducting qubit with respect to an external control parameter (e.g., flux) and hence during both qubit manipulation and readout sequences, the qubit can be biased on a so-called “sweet spot”, where it is immune to first order fluctuations in this parameter. This readout has no on-chip dissipation, minimizing the back-action on the qubit states. Furthermore, due to the CBA’s megahertz repetition rate and large signal to noise ratio, we can measure drifts in qubit parameters in real time and either compensate for these drifts as they are detected, or simply study them to discover their source.

In addition, the CPW resonator architecture of the CBA is easily multiplexed on-chip, enabling the simultaneous readout of several qubits at different frequencies; opening the door to scalable quantum computing.

# A new microwave resonator readout scheme for superconducting qubits

A Dissertation

Presented to the Faculty of the Graduate School

of

Yale University

in Candidacy for the Degree of

Doctor of Philosophy

by

Michael B. Metcalfe

Dissertation Director: Professor Michel H. Devoret

May, 2008

Copyright ©2008 by Michael Brian Metcalfe

All rights reserved.

# Contents

<b>1</b>	<b>Introduction</b>	<b>1</b>
1.1	Quantum computing . . . . .	1
1.1.1	History and background . . . . .	1
1.1.2	Implementations of qubit systems . . . . .	6
1.2	Superconducting quantum circuits . . . . .	13
1.2.1	Non-linear superconducting devices: Josephson junction . . . . .	15
1.2.2	Superconducting qubit types . . . . .	17
1.3	Main fabrication technique used in this work . . . . .	21
1.3.1	Dolan bridge shadow mask evaporation technique . . . . .	21
1.3.2	Limitations . . . . .	26
1.3.3	Multilayer techniques . . . . .	27
1.4	Cooper pair box . . . . .	29
1.4.1	Split Cooper pair box energy levels . . . . .	29
1.4.2	Initial measurements . . . . .	30
1.4.3	Improved readout Schemes . . . . .	32
1.5	Dispersive readout . . . . .	35
1.5.1	Cavity bifurcation amplifier . . . . .	35
1.6	Quantronium with bifurcating readout . . . . .	38
1.7	Conclusion . . . . .	45

1.8	Dissertation overview . . . . .	46
<b>2</b>	<b>Principle and implementation of bifurcation readout</b>	<b>47</b>
2.1	Dynamics of a non-linear oscillator . . . . .	49
2.1.1	Physics of a Duffing oscillator . . . . .	49
2.1.2	Readout principle . . . . .	52
2.2	Implementations . . . . .	54
2.2.1	Josephson bifurcation amplifier . . . . .	55
2.2.2	Cavity bifurcation amplifier . . . . .	58
2.3	JBA lumped element fabrication . . . . .	64
2.3.1	Cu ground plane fabrication . . . . .	65
2.3.2	Capacitor and junction fabrication . . . . .	65
2.4	CBA fabrication . . . . .	67
2.4.1	Resonator lift-off process . . . . .	67
2.4.2	Resonator etching process . . . . .	69
2.4.3	Finished CBA resonator and junction fabrication . . . . .	72
2.4.4	Comparison of JBA and CBA implementations . . . . .	74
2.5	CBA - Experimental demonstration of bistability . . . . .	75
2.5.1	Experimental setup . . . . .	76
2.5.2	Phase diagram . . . . .	80
2.5.3	Universal Duffing oscillator behavior . . . . .	87
2.5.4	Hysteresis . . . . .	88
2.5.5	Parameter extraction . . . . .	90
2.6	Time domain measurements . . . . .	93
2.6.1	Theoretical escape rate . . . . .	94

2.6.2	Experimental demonstration of switching between metastable states . . . . .	96
2.6.3	Escape rate measurement methods . . . . .	98
2.6.4	Experimentally measured escape rates . . . . .	101
2.6.5	S-curves and predicted contrast . . . . .	105
2.7	Conclusions . . . . .	112
<b>3</b>	<b>The Quantronium qubit with CBA readout</b>	<b>114</b>
3.1	Superconducting qubit: split Cooper pair box (SCPB) . . . . .	115
3.1.1	Hamiltonian of SCPB . . . . .	116
3.1.2	Energy levels . . . . .	118
3.2	SCPB readout scheme . . . . .	121
3.2.1	Charge readout . . . . .	121
3.2.2	Current measurement . . . . .	122
3.2.3	SCPB with CBA readout . . . . .	122
3.2.4	Fabrication of SCPB in a CBA resonator . . . . .	125
3.2.5	Experimental setup . . . . .	127
3.3	Qubit characterization . . . . .	132
3.3.1	Gate modulations . . . . .	133
3.3.2	Spectroscopy of qubit energy levels . . . . .	136
3.4	Qubit manipulation . . . . .	139
3.4.1	Rabi oscillations and relaxation time . . . . .	143
3.4.2	Readout discrimination of qubit states . . . . .	144
3.5	Decoherence . . . . .	146
3.5.1	Highly averaged Ramsey fringe experiment . . . . .	146
3.5.2	Decoherence noise source . . . . .	147

3.6	Tomography . . . . .	150
3.7	Conclusion . . . . .	152
<b>4</b>	<b>Future directions</b>	<b>154</b>
4.1	Multiplexed CBA readout . . . . .	154
4.1.1	Design of a sample with five multiplexed resonators . . . . .	155
4.1.2	Measurement setup . . . . .	156
4.1.3	Phase Diagram . . . . .	158
4.2	Multiplexed Qubits . . . . .	162
4.2.1	Design of 2 multiplexed qubits . . . . .	163
4.2.2	Fabrication of two coupled qubits with multiplexed readouts	165
4.2.3	Preliminary measurements on 2 multiplexed qubits . . . . .	166
4.3	Reduced noise geometry - the “in-line Transmon” . . . . .	171
4.3.1	Charge noise reduction . . . . .	171
4.3.2	Flux noise reduction . . . . .	173
4.4	Alternative CBA geometry - coupled stripline . . . . .	173
4.5	Other applications of CBA . . . . .	175
4.5.1	Readout for other superconducting qubits . . . . .	175
4.5.2	Cooper pair counting . . . . .	177
4.5.3	Coupling with molecular systems . . . . .	179
<b>5</b>	<b>Conclusions of thesis</b>	<b>181</b>
<b>A</b>	<b>Alternative fabrication methods and supplemental procedures</b>	<b>183</b>
A.1	Limitations of traditional Dolan bridge technique - Quantronium with JBA readout case study . . . . .	183
A.1.1	Geometry limitations . . . . .	183

A.1.2 Undercut . . . . .	184
A.2 Multi-layer Al junctions . . . . .	186
A.3 Aluminium oxide capacitors . . . . .	188
A.4 Sapphire substrate . . . . .	188
A.5 Quasiparticle traps and gap engineering . . . . .	190
<b>B Dissipative RF filters</b>	<b>192</b>
<b>C Simulation procedure</b>	<b>196</b>
C.1 Equations of motion . . . . .	196
C.2 Runge Kutta algorithm . . . . .	198
C.3 Noise generation . . . . .	199
C.4 Schematic simulation procedure . . . . .	200
<b>D Table of variables, acronyms and fundamental constants</b>	<b>202</b>

# List of Figures

1.1	Illustration of 7-qubit NMR molecule . . . . .	7
1.2	Ion trap quantum computing technology . . . . .	9
1.3	Theoretical proposal and initial experimental implementation for 2-DEG quantum dot qubits . . . . .	11
1.4	Cartoon, schematic and SEM picture of a Josephson junction . . .	16
1.5	The three main types of superconducting qubit along with their potential energy landscapes . . . . .	18
1.6	Cartoons of resist spinning and SEM writing . . . . .	23
1.7	Cartoon of e-beam evaporation and lift-off steps . . . . .	24
1.8	Optical image of resist mask for a Josephson junction and an SEM of the final evaporated junction . . . . .	25
1.9	Images of different fabrication steps for multilayer qubit . . . . .	28
1.10	Schematic of SCPB along with its first two energy levels . . . . .	30
1.11	Initial measurements to probe the quantum properties of the Cooper pair box . . . . .	31
1.12	Some representative efforts to improve measurements of the quan- tum properties of the Cooper pair box using the RF-SET and a switching Josephson junction . . . . .	34

1.13 CBA circuit schematic and its transmitted amplitude and phase near resonance . . . . .	36
1.14 S-curves of a SQUID CBA vs applied magnetic field . . . . .	37
1.15 Schematic of the Quantronium qubit with CBA readout . . . . .	39
1.16 Bloch sphere representation of Rabi and Ramsey sequences . . . . .	40
1.17 S-curves of the CBA with the qubit in its ground and excited states and the corresponding Rabi oscillations . . . . .	42
1.18 Ramsey fringe experiment and analysis of the noise limiting $T_2$ . . . . .	44
1.19 Schematic and transmitted amplitude and phase of five multiplexed CBA resonators . . . . .	45
2.1 A schematic of a driven, damped, non-linear pendulum . . . . .	50
2.2 Plots for the Duffing oscillator of the oscillation amplitude $ B ^2$ and the bifurcation powers $\beta_b^\pm$ vs reduced detuning $\Omega$ and input power $\beta$ . . . . .	51
2.3 Schematic illustrating the amplification principle based on a non-linear oscillator . . . . .	53
2.4 A schematic of a Josephson bifurcation amplifier (JBA) device . . . . .	56
2.5 Schematics of the coplanar waveguide (CPW) and coupled stripline (CS) implementations of the cavity bifurcation amplifier (CBA) . . . . .	59
2.6 Circuit schematics illustrating the series LRC equivalent model of the CBA . . . . .	60
2.7 Plot of the impedance seen by the junction in the CBA, and seen by the junction in the equivalent series LRC model . . . . .	61
2.8 Optical and SEM image of JBA device . . . . .	66
2.9 SEM image and a cartoon schematic of the resist profile used in fabricating the CPW resonators . . . . .	68

2.10	Cartoon of the CPW resonator fabrication using RIE etching . . .	69
2.11	SEM images of some typical problems encountered in resonator fabrication . . . . .	70
2.12	SEM images of resist profile and resultant Nb edge profile in the resonator etching process . . . . .	71
2.13	Optical and SEM images of a finished CBA sample . . . . .	73
2.14	Optical image of a 10 GHz resonator mounted into the sample box	77
2.15	CBA measurement setup for 2&10 GHz CBA resonators . . . . .	78
2.16	Transmitted amplitude and phase vs. $P_{in}$ and $\nu$ for sample 1 and 6	82
2.17	Reflected phase $\phi$ vs. $P_{in}$ and $\nu$ for sample 6 . . . . .	84
2.18	Schematic of CBA circuit used for calculating the steady state behavior . . . . .	85
2.19	Theoretical plots of $P_{out}$ and $\phi$ as a function of $\Omega$ for the CBA . .	86
2.20	Duffing oscillator universal plot for samples 1,2 and 6 . . . . .	88
2.21	Hysteresis measurement technique and experimental results from sample 2 . . . . .	89
2.22	Simulation of hysteresis for a CBA with $\nu_0 = 8.411$ GHz and $Q = 290$	90
2.23	Linear resonance frequency $\omega_0$ vs. applied magnetic field $B$ for sample 2 . . . . .	92
2.24	Cubic potential of Duffing oscillator in rotating frame . . . . .	95
2.25	Effect of latching on the switching histograms for sample 1 . . . .	97
2.26	Methods of measuring the escape rate of the CBA . . . . .	99
2.27	“Beta-two-thirds” plots for sample 1 . . . . .	101
2.28	Escape rate vs. detuning for sample 3 . . . . .	103
2.29	Bifurcation voltage and barrier height vs. detuning for sample 4 .	104
2.30	“Beta-two-thirds” plot and s-curve on same plot from sample 2 . .	106

2.31	Latching pulse shape with important time scales . . . . .	107
2.32	S-curves vs. wait time for sample 1 . . . . .	107
2.33	Measured and simulated s-curves for samples 1, 3 and 4c . . . . .	108
2.34	S-curves vs. detuning for sample 5a . . . . .	110
2.35	S-curves vs. magnetic field. We use this method to find the CBA's discrimination power . . . . .	111
3.1	SCPB schematic along with its energy levels and loop currents . .	116
3.2	Dependance of the energy levels of SCPB and their charge content with $E_J/E_{CP}$ ratio. . . . .	119
3.3	Anharmonicity of the SCPB energy levels . . . . .	120
3.4	Schematic and optical image of SCPB with CBA readout . . . . .	123
3.5	Images of the fabrication steps of SCPB with CBA readout . . . . .	126
3.6	A schematic of the qubit fridge measurement setup . . . . .	128
3.7	A photograph of qubit fridge measurement setup . . . . .	129
3.8	A typical qubit room temperature microwave setup . . . . .	131
3.9	Plots of the qubit gate charge and flux modulations with the read- out in both the linear and non-linear operating regime . . . . .	134
3.10	Plots illustrating the dependance of gate and flux modulations on $E_J/E_{CP}$ . . . . .	135
3.11	Plots of gate and flux modulations with an extra added tone near the qubit frequency . . . . .	136
3.12	Plots of the spectroscopy of the first two qubit energy levels while varying $N_g$ . . . . .	137
3.13	Image plot of the spectroscopy of the $ 0\rangle$ to $ 2\rangle$ transition for varying $N_g$ . . . . .	139

3.14 Bloch sphere representation of qubit state . . . . .	141
3.15 Rabi oscillations vs. pulse length $\tau_R$ and pulse height $A$ . . . . .	142
3.16 Measurement of the qubit relaxation time $T_1$ . . . . .	143
3.17 S-curves of CBA with the qubit in the ground state and the excited state . . . . .	144
3.18 Ramsey fringe experiment to extract the qubit dephasing time $T_2$	147
3.19 Ramsey fringes vs. excitation frequency $\nu_s$ . . . . .	148
3.20 Variations $T_2$ and $\nu_{Ramsey}$ from 3000 Ramsey fringes on the sweet spot along with $1/f$ noise fit . . . . .	149
3.21 Tomography of various qubit states . . . . .	151
4.1 An optical image of five multiplexed resonators . . . . .	156
4.2 An optical image of mounted multiplexed sample . . . . .	157
4.3 Plots of the transmitted amplitude and phase of five multiplexed resonators . . . . .	158
4.4 Universal phase diagrams for a chip with five multiplexed resonators	159
4.5 Magnetic field dependance of a sample with five multiplexed res- onators . . . . .	161
4.6 Cartoon of a multiplexed CBA sample with coupled qubits . . . . .	162
4.7 An optical image, SEM and schematic of a multiplexed two-qubit sample . . . . .	164
4.8 Gate and flux modulations of the two multiplexed qubit sample .	166
4.9 Spectroscopy of each qubit in the two multiplexed qubit sample .	167
4.10 $T_1$ data for a coupled qubit . . . . .	168
4.11 Ramsey fringes vs. gate charge for the coupled qubit with multi- plexed readout . . . . .	169

4.12 Ramsey data vs. frequency for a coupled qubit . . . . .	170
4.13 An optical image and schematic of the in-line Transmon geometry	172
4.14 SEM image, schematic and optical image of a capacitively coupled qubit device with coplanar stripline CBA readouts . . . . .	174
4.15 SEM images and schematics of devices implementing a bifurcation readout with flux qubits . . . . .	176
4.16 Schematic and SEM image of proposed device for counting Cooper pairs . . . . .	177
4.17 Schematic of proposed device for measuring the inductance of a carbon nanotube . . . . .	180
A.1 SEM images of resist and finished Quantronium with JBA readout	184
A.2 SEM image of resist and corresponding deposited sample with a stress tear in the PMMA. . . . .	186
A.3 SEM image of a Quantronium fabricated using multilayer junctions.	187
A.4 Optical image and schematic of $\text{Al}_2\text{O}_3$ capacitors for a Quantronium sample with JBA readout. . . . .	189
A.5 SEM image of a Quantronium with Au quasiparticle traps. . . . .	190
B.1 Plot of the attenuation in an input RF line used in a typical CBA experiment . . . . .	192
B.2 Schematic and optical image of a dissipative RF filter . . . . .	193
B.3 Measured transmission and reflection of a Eccosorb dissipative RF filter . . . . .	194
C.1 Simulation input and output . . . . .	201

# List of Tables

2.1	Examples of resonator's coupling capacitors and corresponding critical powers . . . . .	72
2.2	Summary of CBA samples measured . . . . .	76
2.3	Table of measured and predicted discrimination powers for various CBA samples . . . . .	112

# Acknowledgments

When I first arrived in the U.S. in Aug 2002, I had no idea what to expect. I had never been in the states before, nor had I been outside of Ireland for such an extended period of time. To my delight, Yale proved to be a fantastic place to live and to work, and in the past five and a half years I have made life-long friends and have collaborated with some of the best minds in science.

I would like to begin with thanking my supervisor Prof. Michel Devoret. I have always been astounded with his deep understanding of physics, attention to detail, and his ability to explain simply, the most complicated physical concepts. His guidance proved invaluable during my time here at Yale.

When I first joined Michel's group in the summer of 2003, I began to work closely with Frederic Pierre, who introduced me to the world of microfabrication, a skill which was essential throughout my graduate student career. In addition, I could always rely on the in-depth fabrication knowledge of Luigi Frunzio and Chris Wilson to help solve any fabrication issue. Without the work of these people, research in the area of superconducting quantum circuits would not have been possible.

Next, I would like to thank Etienne Boaknin who helped me understand the art of cryogenics and microwave measurements. I worked closely with Etienne on the characterization of the cavity bifurcation amplifier and on the measurement of the Qnantronium qubit.

I valued greatly the many discussions I had with Vladimir Manucharyan, Irfan Siddiqi and Rajamani Vijayaraghavan on the theoretical background of the cavity bifurcation amplifier, and whose work greatly increased the understanding of the behavior of this system. Furthermore, I had many fruitful discussions with Chad Rigetti on the behavior of qubit systems and with the more recent Qlab members, Markus Brink, Nicolas Bergeal and Philippe Hyafil. I greatly appreciated the working environment in Qlab, in which everybody was always willing to lend a hand. Finally, I am thankful for the dedicated work of Maria Gubitosi and Theresa Evangeliste, who helped keep Qlab up and running, like a well oiled machine.

An essential feature of research here at Yale is the close collaboration that exists between all the research groups. Specifically, I would like to thank Professors Dan Prober, Rob Schoelkopf, Steve Girvin and their respective groups, for providing a rich working environment for developing new ideas and solving research problems. In particular, I would like to thank Dan Prober for generously lending Qlab both his He<sup>3</sup> and dilution refrigerators. It was in these fridges that most of my experiments were carried out.

Outside of Yale, I would like to thank our collaborators in Saclay where, along with Michel, the Quantrium qubit was first measured. In particular, I would like to thank Dr. Denis Vion and Dr. Daniel Esteve who helped Qlab in the development and understanding of new concepts and projects.

Finally, I would like to thank my committee, Professors Simon Mochrie, Rob Schoelkopf, Dan Prober, Steve Girvin, my external reader Dr. Daniel Esteve and last but not least, Michel Devoret, for spending the time to carefully read through my dissertation and for providing insightful comments to strengthen it.

I would like to dedicate this thesis to my family; my wife Grace, my parents Peter and Geraldine, my brother and sister Tony and Mary, and my grandmother

Mary. Their love and support helped me to strive for my best at every stage during my studies.

# Chapter 1

## Introduction

### 1.1 Quantum computing

#### 1.1.1 History and background

This thesis aims to contribute to the growing field of quantum computation [1, 2], which combines the areas of quantum mechanics and information processing. The idea of studying the quantum mechanical properties of computers was inspired by Moore’s law (1965) [3], which, based on an industry driven by economics and the need for increased computational power, says that computer circuitry must shrink in size by a factor of two every two years. Eventually, computer circuitry will be miniaturized to the point where quantum mechanical effects must be considered (see for example Keyes [4]). The idea arose that quantum mechanics, rather than being a hindrance, might actually be useful for computations. Feynman was one of the first scientists to address the effectiveness of quantum mechanics in computation. In 1981 [5], Feynman argued that a quantum system cannot be simulated “efficiently” by a classical computer, where an efficient algorithm is one in which computational time grows in a polynomial manner with the size of the system being simulated. Feynman then suggested that a quantum mechanical system, however, such as a lattice of spins, could efficiently simulate another quantum

mechanical system. The concept of using quantum mechanics for computing was made more concrete by Deutsch, who released a theoretical paper in 1985 [6], introducing the concept of the universal quantum computer which could simulate any physical process. In this computer the fundamental carrier of information would be a quantum two-level system, with states  $|0\rangle$  and  $|1\rangle$ , known today as a qubit.

Unlike a conventional bit in a classical computer which can take only an exact value of 0 or 1, a qubit is the superposition of 2 quantum states and can be written as

$$|\psi\rangle = a|0\rangle + b|1\rangle, \quad (1.1)$$

where  $|0\rangle$  is obtained with probability  $|a|^2$ ,  $|1\rangle$  is obtained with probability  $|b|^2$  and  $|a|^2 + |b|^2 = 1$ . Any quantum system, such as ions and molecules, can be used as a qubit, if 2 levels in the system can be isolated from all other levels. An ideal quantum computer would consist of multiple qubits, which can interact with each other in a well understood and coherent manner to perform calculations, and would contain an efficient system to read the state of each qubit. A quantum computation in a quantum computer can be defined as a controlled unitary evolution of an initially prepared  $n$ -qubit state and its subsequent measurement, where a general  $n$ -qubit state can be written as a superposition of all possible  $2^n$  qubit states  $|k\rangle \equiv |i_1 i_2 i_3 \dots i_n\rangle$ ,

$$|\Psi\rangle = \sum_{k=0}^{2^n-1} a_k |k\rangle, \quad (1.2)$$

with  $i_j$  the state of the  $j^{\text{th}}$  qubit and  $i = 0$  or  $1$ . For example, a 2-qubit state can be written as

$$|\Psi\rangle = a_{00}|00\rangle + a_{01}|01\rangle + a_{10}|10\rangle + a_{11}|11\rangle. \quad (1.3)$$

Why would one wish to combine the theory of quantum mechanics with computation? Initially it seems that by using a qubit instead of a bit, one loses the important computational feature that a bit has a well defined value of exactly 0 or 1. But in fact, one gains greater computational power by using qubits instead of classical bits because any single unitary operation  $U$ , or single gate, acting on an initially prepared  $n$ -qubit state  $|\Psi\rangle$ , will simultaneously act on all (exponentially many)  $2^n$  states  $|k\rangle$ ,

$$U|\Psi\rangle = \sum_{k=0}^{2^n-1} a_k U|k\rangle. \quad (1.4)$$

This ability to simultaneously act on all states is known as “quantum parallelism,” and can result in an exponential increase in computational power (if an efficient algorithm is utilized which exploits this property (see below)). Note however, that for quantum computation to be efficient, the initialization of  $|\Psi\rangle$  and its unitary evolution need to be executed using a set of operations (gates) whose number is only polynomial in  $n$ . Furthermore one needs a universal set of unitary operations, from which all other  $n$ -qubit operations can be constructed. Fortunately, such a universal set can be constructed from just a few 1-qubit operations and only one 2-qubit operation, both of which are relatively easy to implement.

Finally, one should be careful when reading out this quantum information and attempting to harness the power of quantum parallelism. A single measurement will collapse the qubit state, projecting only one classical state which is randomly chosen, and losing all other remaining information. Fortunately, one can create algorithms which can circumvent this problem. One of the first examples of a quantum algorithm that is more efficient than any possible classical algorithm is the Deutsch-Jozsa algorithm [7]. This algorithm determines whether a function  $f(x)$  is either constant ( $f(x) = 0$  or  $f(x) = 1$  for all inputs) or balanced (returns 1

for half of the input domain and 0 for the other half). Although of little practical use, it provided inspiration for Shor's and Grover's algorithms which caused an explosion of interest in quantum computation due to their potential applications.

Derived in 1994, Shor's algorithm [8] can factorize an  $N$  digit number into its prime factors in  $O(\text{Log}(N)^3)$  time, and is by far the most well known algorithm because of its relevance in cryptography. Public-key cryptography utilizes a method known as RSA which is based on the assumption that it is computationally infeasible for a classical computer to factor a large integer in a short enough time (e.g., 1024-bit integer would take  $10^5$  years). Grover's algorithm [9, 10] is a quantum search algorithm, used to find the solution of a function  $f(x)$ , where  $x \in (1, 2, \dots, N - 1, N)$ . Grover's algorithm can perform this task in  $O(N^{1/2})$  time, as compared to the classical computation time of  $O(N)$ . This algorithm may be useful for speeding up the solution of NP-complete problems <sup>1</sup>. However, Grover's algorithm is not useful for searching pre-existing databases (e.g., internet) because this requires the existence of quantum memory or a quantum mechanical memory addressing scheme [2].

In addition to executing algorithms, quantum computers can also simulate complex quantum systems, such as in many-body physics, that are impossible to simulate on a classical computer, as we have already mentioned. Furthermore, in developing the basic elements of a quantum computer with systems such as individual atoms, photons, and spins, we can deepen our understanding of these systems and therefore develop precise control techniques.

One of the main obstacles in creating a functional quantum computer is in con-

---

<sup>1</sup>**Definition:** NP-complete problems: A problem which is both NP (verifiable in nondeterministic polynomial time - solvable in polynomial time by a nondeterministic Turing machine) and NP-hard (any NP-problem can be translated into this problem). Many significant computer-science problems belong to the NP-hard class, e.g., the traveling salesman problem, satisfiability problems, and graph-covering problems.

trolling the decoherence of qubit states due to interactions with their environment. Decoherence can be viewed as a continuous measurement applied by the environment on the qubit states. Entanglement of the qubit states with the environment causes irreversible loss of the information stored in the original superposition of states, which is needed for quantum computation. The characteristic time that this information is lost is called the decoherence time  $T_2$ . As the number of qubits increase, they decohere more rapidly due to their interactions with the environment as well as each other. The problem of decoherence led to the derivation of error-correcting codes by Shor in 1995 [11] and Steane in 1996 [12], to compensate for decoherence during transmission and storage of quantum information. However, the Shor and Steane codes require many extra qubits for the error-correction algorithm and place a stringent requirement on the number of operations needed within the decoherence time of the qubit.

The performance of a qubit system be characterized in terms of how long it can maintain its quantum coherence. This time can be broken down into two different time scales, the relaxation time  $T_1$ , and the dephasing time  $T_\phi$ . Relaxation processes involve an irreversible energy transfer between the qubit and an environmental degree of freedom, resulting in the process  $|\psi\rangle = a|0\rangle + b|1\rangle \mapsto |0\rangle$ . Excitation may also occur, where the qubit gains energy from the environment (although in our experiments we are at a sufficiently low temperature where this does not occur). Dephasing is due to random fluctuations in the control parameters of the qubit which causes random changes in its transition energy between  $|0\rangle$  and  $|1\rangle$ ,  $E_{01} = \hbar\omega_{01}$ . Hence, the qubit accumulates a random contribution to the phase  $\phi$  between  $|0\rangle$  and  $|1\rangle$ ,  $|\psi\rangle \mapsto a|0\rangle + be^{i\phi}|1\rangle$ , where  $\phi(t) = \int_0^t \omega_{01} dt'$ . The decoherence time  $T_2$  is given by a combination of the relaxation and dephasing

processes via the equation

$$\frac{1}{T_2} = \frac{1}{2T_1} + \frac{1}{T_\phi} \quad (1.5)$$

### 1.1.2 Implementations of qubit systems

Several different technologies are currently being explored to assess the possibility of constructing a quantum computer. The list of technologies investigated to perform quantum computing is continuously growing and includes ion traps, liquid state nuclear magnetic resonance (NMR), neutral atom optical lattices, cavity quantum electrodynamics (CQED) with atoms, linear optics, nitrogen vacancies in diamond, electrons in liquid helium, superconducting qubits (flux, charge, phase), 2-dimensional electron gas (2-DEG) quantum dots, self assembled quantum dots, donor impurities in silicon, quantum hall qubits and quantum wire qubits. It is still too early to determine which technology is most suited for quantum computation and whether it is even possible to build a quantum computer that can solve non-trivial problems.

In this introduction, before moving onto superconducting circuit qubits, I will describe a few of the systems which have had the greatest contributions to the development of quantum computing technology and concepts and with which superconducting qubits are competitive.

#### **Nuclear magnetic resonance**

Liquid state nuclear magnetic resonance (NMR) is the manipulation and measurement of the molecular spins suspended in a liquid. This technique is well developed and is routinely applied to chemical analysis and medical imaging. Molecular spins are known to have long decoherence times at room temperature operation, which makes them favorable candidates for qubit systems. The first

implementation of quantum algorithms, such as Grover's [13, 14] and Shor's algorithm [15], was achieved using NMR technology. The molecule shown in Fig. 1.1 is a 7 qubit system used in the largest quantum computer implemented to date and was used to factorize 15 into its prime factors, 5 by 3, with the use of Shor's algorithm.

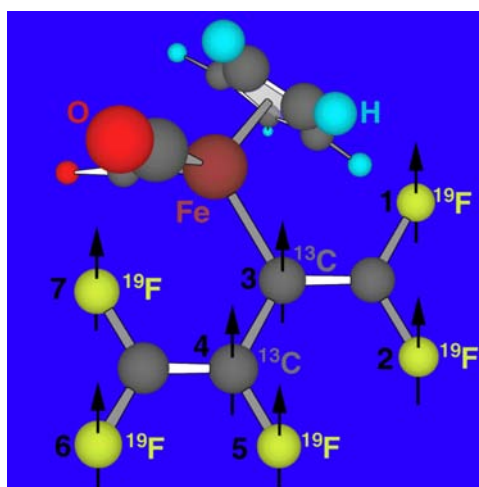


Figure 1.1: Illustration of the *dicarbonylcyclopentadienyl (perfluorobutadien-2-yl) iron* ( $C_{11}H_5F_5O_2Fe$ ) molecule used by IBM in the most complex NMR quantum computer to date to demonstrate Shor's algorithm by factorizing 15 into 5 by 3. This molecule contains 7 qubits - five fluorine and two carbon-13 atoms.[15]

First theoretically proposed by Cory et al. (1997) [16] and Gershenfeld et al. (1997) [17], NMR quantum computing does not measure the spin of a single molecule, but the expectation value of a "pseudo pure state" of an ensemble ( $\sim 10^{20-23}$ ) of molecules in liquid. A "pseudo pure state" is a slight imbalance in the density matrix of the ensemble of molecules, naturally present at thermal equilibrium, and enhanced using multiple-pulse resonance techniques. The molecular size determines the number of qubits present with the chemical bonds transmitting the interactions. RF radiation pulses are applied to manipulate the spin state of each qubit. Because of either the use of different atoms, or the dif-

ferent chemical environments of the atoms, each qubit has a different transition energy and can be selectively manipulated.

NMR quantum computing, however, has several limitations. It becomes increasingly difficult to create larger molecules with more spins (with resolvable peaks) to implement larger quantum computers. More importantly, the signal of the “pseudo pure state” decreases exponentially as the number of qubits increases. To compensate, this requires an increase in the initial net spin polarization or a decrease of the temperature (which is not compatible with the liquid state).

### **Ion traps**

First proposed by Cirac and Zoller (1995) [18], an ion trap qubit system consists of a linear array of ions, trapped by a combination of static and electric fields in high vacuum known as a Pauli trap (Fig. 1.2a). The ions act as the qubits with their common vibrational modes coupling the ions to each other. Preparation of the initial qubit state is performed using either laser cooling or optical pumping techniques. The qubit state is measured using resonance fluorescence, where the qubit absorbs incoming radiation and subsequently emits photons only if it was initially in the excited state  $|1\rangle$ .

In 1995, Monroe et al. [19] demonstrated the first implementation of the Cirac-Zoller qubit architecture, by performing a CNOT 2-qubit gate with a single trapped  ${}^9\text{Be}^+$  ion, using two hyperfine levels and 2 vibrational levels. A qubit decoherence time  $T_2$  of hundreds of microseconds and a gate operation time of  $50\mu\text{s}$  was measured. The main sources of decoherence were instabilities in laser power and RF ion trap frequency. Also the motional state coherence is limited by thermally driven voltage fluctuations in the electrodes [21].

Since pioneering experiment of Monroe et al. ion trap quantum computing

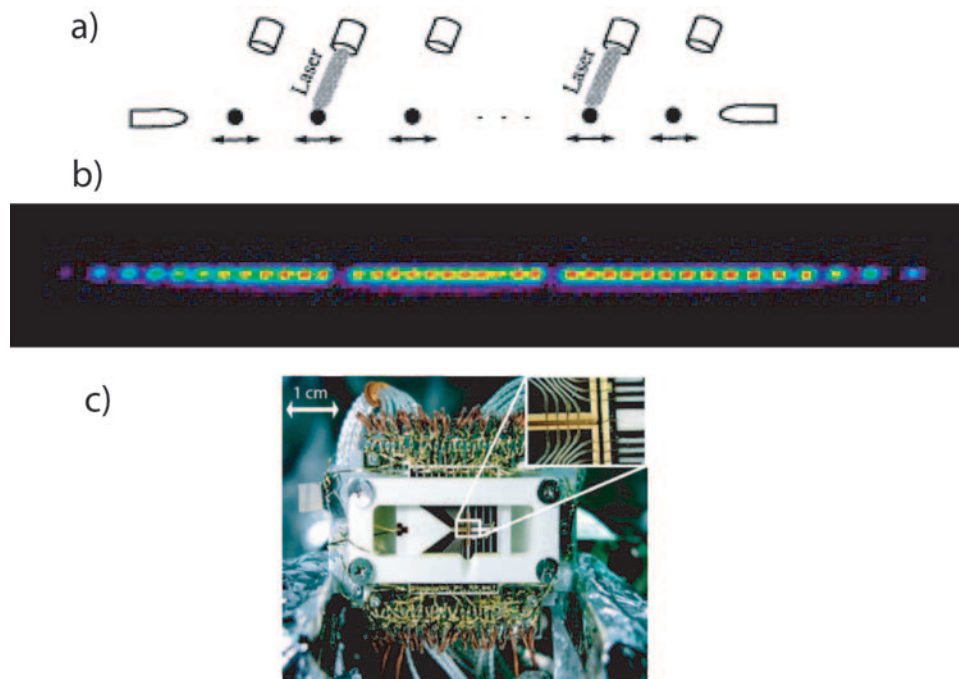


Figure 1.2: (a) A schematic of the theoretical proposal by Cirac and Zoller in 1995 [18] for trapped ion quantum computing. (b) An image of the fluorescence from a linear array of trapped ions by Wineland et al. (c) A photograph of a complicated T-junction for moving trapped ions [20].

has evolved into the most advanced contender in quantum computing research, and has led to the implementation of experiments such as quantum error correction [22], teleportation of a quantum state [23] and Grover’s quantum search algorithm [24]. However scalability has become a major technological challenge. For example, as the number of ions increases, it becomes increasingly difficult to individually address each ion. Also gate operation times get slower and noise such as thermal voltage fluctuations become more important as the traps become weaker with more ions.

In attempting to make trapped ion systems more scalable, research is currently focusing on so-called “atom chips” [25]. Ion-trap geometries which are currently being developed include symmetric high-aspect-ratio multilayer structures with

electrodes surrounding the ions, asymmetric planar structures with the ions residing above a planar array of electrodes, and symmetric ion traps fabricated from silicon electrodes with trenches etched through the chip for better optical access. Using these schemes, one can scale the system by separating the ions into different regions with communication between these regions via photons or by shuttling the ions from one region to the other. Figure 1.2(c) illustrates a T-junction for ion shuttling [20] in which a left turn, (but not a right turn), was achieved. This complex T-junction illustrates the significant technological challenge involved in trapped ion quantum computing.

### **Solid state methods**

The success of the highly developed semiconductor-based industry, which powers classical computer development, logically leads to exploring solid state methods for building a quantum computer. However, developing a well isolated solid state qubit device is challenging due to large environmental coupling. Again, I will not describe all methods proposed for solid state quantum computing and will concentrate only on quantum dot qubit systems, which are the only other solid state systems whose performance can rival superconducting qubits.

D. Loss and D. P. DiVincenzo [26] initially proposed the application of the spin states of coupled single electron quantum dots (QDs) for quantum computing in 1998 (see Fig. 1.3a). Quantum dots are electron systems confined in 3 dimensions and hence behave like artificial atoms because of the discrete energy level spectrum, from which one can construct a qubit. QDs can be fabricated in a variety of different forms, including vertical QDs [27], two-dimensional electron gas (2-DEG) QDs [28], and self-assembled QDs [29, 30, 31]. I will briefly describe only the 2-DEG implementation.

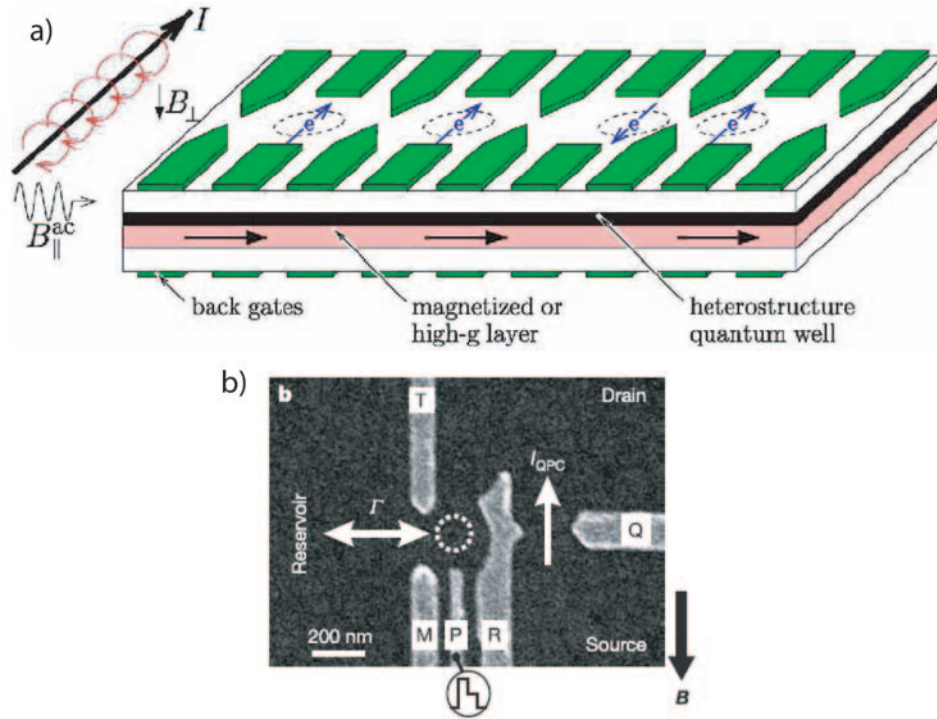


Figure 1.3: **(a)** Quantum computing proposal by D. Loss and D. P. DiVincenzo [26]. It consists of a series of exchange-coupled electron spins. Single-qubit operations could be performed in such a structure using electron spin resonance (ESR), which would require an rf transverse magnetic field. Two-qubit operations would be performed by bringing two electrons into contact, introducing a nonzero wavefunction overlap and corresponding exchange coupling for some time (two electrons on the right). In the idle state, the electrons can be separated, eliminating the overlap and corresponding exchange coupling with exponential accuracy (two electrons on the left). **(b)** A scanning electron microscope image of one of the first implementations of a single 2-DEG Quantum dot for building a quantum computer. The quantum dot is fabricated from a 2-dimensional electron gas in a GaAs/AlGaAs heterostructure [28].

### *Two-dimensional electron gas quantum dots*

One method of fabricating QDs is by manipulating a 2-DEG, which is a gas of electrons trapped in one direction by a triangular-like potential at either the surface or an interface of a semiconductor. Figure 1.3(b) displays a scanning electron microscope image of a 2-DEG QD in a GaAs/AlGaAs heterostructure

[28]. Negative voltages applied to the surface electrodes  $M$ ,  $R$  and  $T$  in Fig. 1.3a, create depletion layers which are used to trap electrons (white dotted line). With this method one can accurately control the position and size of the QD. Using an in-plane magnetic field, the spin states of a single confined electron is then split in energy. The potential is tuned such that the electron leaves or remains in the QD depending on its spin. The presence or absence (or state) of the electron (which can act as the qubit), is detected with a nearby quantum point contact (QPC). A QPC is a narrow channel of the 2-DEG between two depletion regions that has a conductance which is quantized, and is operated as a highly sensitive electrometer. Two-DEG QD systems can have energy relaxation times  $T_1$  in the millisecond range. However, random magnetic fields of nuclear spins in the substrate (hyperfine interaction) limit the coherence times  $T_2$  to a few nanoseconds. Recently, spin-echo techniques have been used to undo the dephasing due to the local random magnetic fields, enhancing the coherence time to microseconds [32], or about 7000 gate operations.

## Conclusion

The above discussions demonstrate that much more work is needed to determine which, if any, of the previously mentioned technologies is most suitable for quantum information processing. Although challenging, research into quantum computation not only offers a means for thoroughly testing the theory of quantum mechanics, but also motivates improvement of our control and understanding of quantum mechanical systems, such as atoms, photons, spins and artificial quantum structures such as quantum dots.

This thesis will now concentrate on an entirely different scheme than those previously described in this section - *superconducting quantum circuits* which,

like semiconductor qubit proposals, take advantage of modern nano-fabrication, cryogenic and microwave electronics techniques. As mentioned at the beginning of this section, these circuits can be coupled to each other as well as to the environment with simple electrical elements, such as inductors and capacitors. Like other solid state qubits, the challenging aspect of the quantum circuits method is in isolating a single quantum system from the environment while simultaneously opening channels for reading, writing and gating.

## 1.2 Superconducting quantum circuits

Currents and voltages of an electrical circuit are single macroscopic degrees of freedom and are usually treated classically, using, for example, Kirchoff's laws. Although quantum mechanics treats both microscopic and collective degrees of freedom equally, its properties are not perceived in everyday electrical circuits. In order for these macroscopic circuits to be viable qubit candidates, their collective degrees of freedom must behave according to the laws of quantum mechanics. This can be achieved by eliminating dissipation with the use of superconductors, and with sufficient isolation from environmental and thermal fluctuations (reviews: [33, 34]). In particular, A. J. Leggett and O. Caldeira [35] predicted that quantum tunneling of the superconducting phase difference across a potential barrier can be measured (see Fig. 1.5c). This effect was measured by Devoret et al. (1985) [36], who also discovered quantized energy levels in the potential well of the tunnel junction (see next section) [37]. These measurements prove that a macroscopic degree of freedom, (in this case the phase difference across a Josephson junction) in superconducting circuits, can behave in a quantum mechanical manner.

In order for these circuits to behave quantum mechanically there are some

conditions that must be satisfied. First of all, to preserve coherence there cannot be any dissipation at the energy level transition frequency,  $\nu_{01} = \omega_{01}/2\pi$ , which is often in the microwave range. Hence, we use superconductors such as Al or Nb, whose gap prevents quasiparticles from being excited by microwave photons. In order to distinguish the quantum mechanical states, we need a high enough transition frequency  $\nu_{01} = \omega_{01}/2\pi \gg k_B T_{\text{eff}}/h$ , to prevent incoherent mixing of the energy states due to thermal fluctuations.  $T_{\text{eff}}$  is used to represent the fact that the effective temperature of the electromagnetic noise coming from the input and output measurement lines, which must be sufficiently cooled and filtered, may differ from the refrigerator temperature. We typically fabricate circuits with transition energies in the gigahertz frequency range, because these are the highest frequencies that we can reliably control. Even with these gigahertz transition frequencies, we still must operate at dilution refrigeration temperatures. Note also that the transition energy must satisfy  $\hbar\omega_{01} \ll \Delta$ , where  $\Delta$  is the superconducting gap. Hence one must use superconductors with a transition temperature  $> 1$  K ( $\sim 30$  GHz).

As a basic example of such a circuit, consider briefly a parallel LC oscillator. A resonant circuit at gigahertz frequencies can easily be fabricated in the lumped element regime using micro-fabrication techniques, where we can make picofarad capacitors and nanohenry inductors whose size is much less than the wavelength at frequency angular  $\omega_{01}$ . This system can be described with flux  $\Phi$  through its inductor with inductance  $L$ , and charge  $Q$  on its capacitor plates with capacitance  $C$ . The flux  $\Phi$  and charge  $Q$  are conjugate variables, i.e.,  $[\Phi, Q] = i\hbar$ . Schrödinger's equation is easily solved for this harmonic oscillator system, and one obtains a series of equally spaced energy levels with transition energy  $\hbar\omega_{01} = \hbar/\sqrt{LC}$ . The environment, which is necessarily coupled to the oscillator because of the

measuring leads, can be modeled as a resistor,  $R$ , in parallel with the LC oscillator. This resistor introduces voltage fluctuations and damping of the oscillator. This environmental coupling introduces another constraint on the system, needed to ensure quantum mechanical behavior - the level separation must be larger than the level width or  $Q \gg 1$  where  $Q = \omega_{01}RC$  is the quality factor of the oscillator. This inequality can be re-written as  $R \gg Z_0 = \sqrt{\frac{L}{C}}$ , where  $Z_0$  is a characteristic impedance of the LC oscillator circuit.

Although this LC oscillator quantum circuit is relatively easy to fabricate and understand, a quantum LC oscillator with equally spaced energy levels is not useful for quantum information processing as it is always in the correspondence limit (behaves on average like a classical system) and so its quantum mechanical behavior is not easily measurable. Hence, this system is not useful as a qubit.

### 1.2.1 Non-linear superconducting devices: Josephson junction

In order to build a useful qubit we need a system which has two energy levels with a transition energy well separated from other transition energies of the system. Hence we need access to a non-linear circuit element which operates at the low temperatures necessary for our experiments. This element must also be non-dissipative to preserve qubit coherence.

The only element readily available today which satisfies all the above requirements is the Josephson junction (Fig. 1.4). It consists of two superconductors separated by a thin insulator (or any two superconducting electrodes coupled by a weak link). In our lab we typically use Al for the superconducting layers due to its self terminating oxidation process [38]. The oxide  $\text{Al}_2\text{O}_3$  layer is about 1 nm thick ( $\sim 10$  atoms), which is thin enough for tunneling processes. The current -

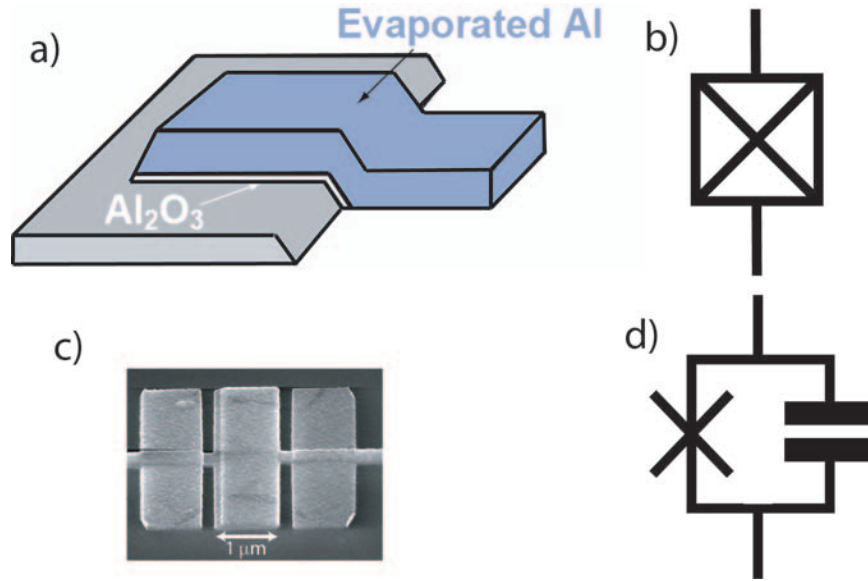


Figure 1.4: **(a)** Cartoon of the structure of a Josephson junction. A superconducting strip is first deposited to form the bottom electrode. We use Al as it can form a robust insulating oxide layer by exposure to oxygen. After oxidation a second layer of superconductor is deposited on top, forming the junction. **(b)** Circuit symbol for the Josephson junction **(c)** SEM of an Al junction fabricated in our lab. The center part of the device consists of the superconductor-insulator-superconductor sandwich. The outer electrodes are spurious electrodes formed by the fabrication process (See appendix 1.3). **(d)** The junction can be represented as a pure Josephson element in parallel with a capacitor, formed by the junctions electrodes.

voltage relations of this device are given implicitly by the two equations [39, 40]

$$\begin{aligned} I_J(t) &= I_0 \sin(\delta(t)), \\ V_J(t) &= \phi_0 \dot{\delta}(t), \end{aligned} \tag{1.6}$$

where  $\delta$  is the superconducting gauge invariant phase difference across the junction,  $V_J(t)$  is the instantaneous voltage across the junction and  $\Phi_0 = 2\pi\phi_0 = \frac{h}{2e}$  is the superconducting flux quantum.  $I_0$  is the critical current of the junction and is a measure of how strongly the phases in the two superconductors are coupled. It scales linearly with the area of the junction and the transparency of the barrier. If one defines the branch flux of this element as:  $\Phi = \int_{-\infty}^t V_J(t') dt'$  then the

Josephson relations can be written as

$$I_J(t) = I_0 \sin \left( 2\pi \frac{\Phi(t)}{\Phi_0} \right). \quad (1.7)$$

Hence, one can define a phase-dependent inductance as

$$L_J(\delta) = \left( \frac{\partial I}{\partial \Phi} \right)^{-1} = \frac{L_J}{\cos(\delta)}, \quad (1.8)$$

where  $L_J = \frac{\phi_0}{I_0}$ . One can see that the Josephson inductance has a cosine dependence on the branch flux, resulting in a non-linear behavior.

The energy stored in the junction is calculated to be

$$E(\delta(t)) = \int_{-\infty}^t I(t') V(t') dt' = -E_J \cos(\delta(t)), \quad (1.9)$$

where  $E_J = \phi_0 I_0 = \frac{\phi_0^2}{L_J}$  is the Josephson energy. Hence the inductance can also be defined as the second derivative of the energy of the circuit element

$$L_J(\delta) = \left( \left( \frac{1}{\phi_0} \right)^2 \frac{\partial^2 E(\delta(t))}{\partial \delta^2} \right)^{-1}. \quad (1.10)$$

The effective inductance of a device is an important concept that will be used in our qubit readout mechanism later (see sections 1.5.1, 3.2.3).

### 1.2.2 Superconducting qubit types

Josephson junction circuits have three main sources of noise: charge, flux and critical current noise. Circuits designed to create a two-level system from Josephson junctions must have sufficient protection from these sources of noise to maintain a high level of coherence. Three main contenders have emerged over the past few years, which may be distinguished by the variable controlling the state of the qubit: charge, flux or phase [41] (see Fig. 1.5). I now will briefly describe each of these qubit implementations.

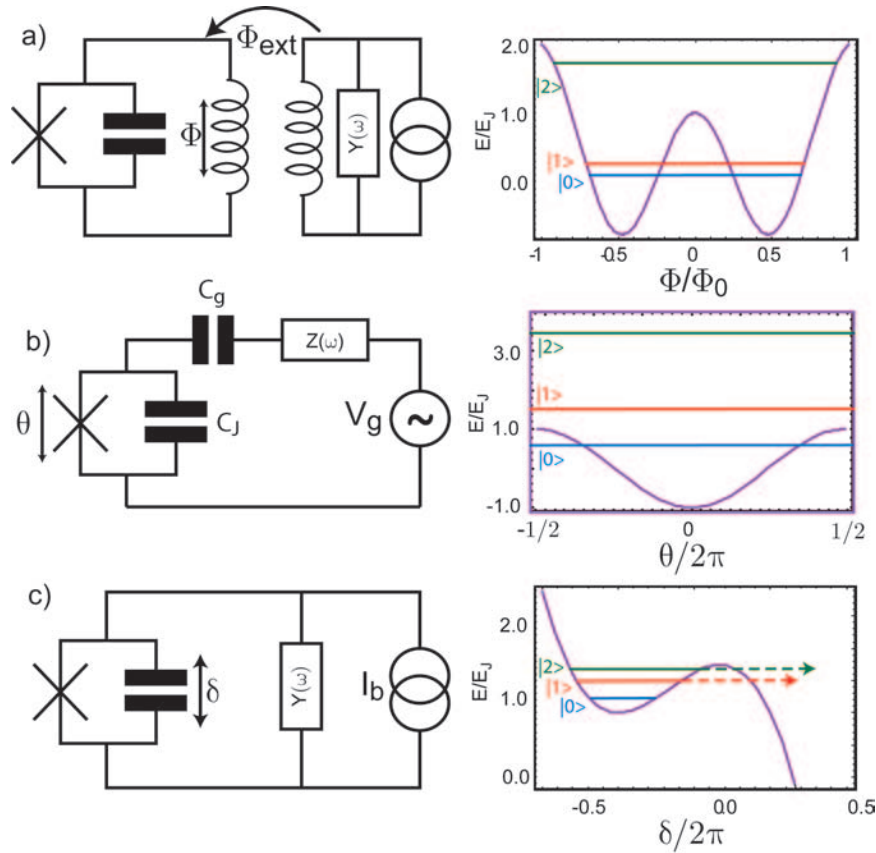


Figure 1.5: The three main types of superconducting qubit along with their potential energy landscapes. Note the Josephson junctions are represented as a parallel combination of a pure Josephson element and a parallel plate capacitor,  $C_J$  (see Fig. 1.4d). The double circle symbol in (a) and (c) represents an ideal current source. **(a)** Flux qubit with its double well potential. The first two energy levels are symmetric and anti-symmetric superpositions of the persistent current states corresponding to the two minima of the potential energy. **(b)** Cooper pair box with its cosine potential. The energy levels are superpositions of charge states of the superconducting island. **(c)** Phase qubit with its tilted washboard potential. The system tunnels through the barrier with a much higher rate when excited. The subsequent runaway down the washboard potential causes a voltage of  $2\Delta/e$  to develop across the junction.

### Flux Qubit

A flux qubit basically consists of an RF-SQUID. Its circuit schematic and a cartoon of its potential energy landscape is shown in Fig. 1.5a. The junction's electrodes

are connected via a loop with inductance  $L_{loop}$  and biased by an external magnetic field  $\Phi_{ext}$ . Large ratios of  $\frac{E_J}{E_{CP}} \sim 10 - 100$  are taken to reduce the effect of charge noise, where  $E_{CP} = \frac{(2e)^2}{2C_J}$  is the Coulomb charging energy for one Cooper pair on the junction capacitance,  $C_J$ . The resulting loss in non-linearity is compensated for by taking  $\Phi_{ext} \sim \Phi_0/2$  and  $\lambda \equiv \left(\frac{L_J}{L_{loop}} - 1\right) \sim 1$ . The first two energy levels are symmetric and anti-symmetric superpositions of the persistent current states corresponding to the two minima of the potential energy. This circuit was first implemented by Lukens et al. (2000) [42, 43]. Better control over the potential tunnel barrier can be attained by using multi-junction versions of this system. For example, a flux qubit with 3 junctions in series has been implemented by Mooij et al. (1999) [44, 45]. At the time of this writing, these samples have relaxation times,  $T_1$ , and decoherence times,  $T_2$ , of a few microseconds [46]. A main source of decoherence in these qubits is 1/f flux noise. The source of this noise is not yet understood and could come from magnetic impurities on the surface of the films or critical current fluctuations in the junctions of the SQUID readout schemes. Note also that SQUID amplifiers themselves are subject to a similar 1/f flux noise [47].

### Charge Qubit

This is our qubit of choice and is based on the Cooper pair box (CPB) (Fig. 1.5b). First described theoretically by Büttiker in 1987 [48] (although in a slightly different form), the CPB consists of a superconducting island isolated from its environment by a capacitor,  $C_g$ , leading to a voltage source  $V_g$  (via the impedance  $Z(\omega)$ ), and also by a small Josephson junction leading to a superconducting reservoir. The single degree of freedom of this circuit is the excess number of Cooper pairs of the island,  $N$ . Cooper pairs can be brought onto the island from the reservoir by controlling the gate voltage  $V_g$ . The energy level structure of this system de-

depends on the competition between its two main energy scales,  $E_{CP} = \frac{(2e)^2}{2C_\Sigma}$  the Cooper pair charging energy of the island (where  $C_\Sigma = C_g + C_J$  is the total capacitance of the island to ground) and the Josephson energy of the junction,  $E_J$ . For a wide range of  $E_J/E_{CP}$  this system can behave as a two level system. For large ratios the qubit levels become equally spaced, similar to that of an harmonic oscillator. Typically, we use  $\frac{E_J}{E_{CP}} \sim 1$ , where there is a good balance between reducing the level of  $1/f$  charge noise and retaining the desired unequal spacing of the energy levels. However, the main limitation for these qubits performance is the  $1/f$  charge noise, so that in future implementations of this qubit, the junction parameters will be tuned such that this qubit becomes immune to charge noise. Immunity to charge noise is achieved by making the energy levels of the qubit almost insensitive to charge, by using a larger  $E_J/E_{CP}$  of about 10. To date, these Cooper pair box circuits are the best performing superconducting qubit candidates in terms of relaxation times,  $T_1$ , and decoherence times,  $T_2$ , with some groups reporting  $T_1 \sim 1 - 7\mu\text{s}$  and  $T_2 \sim 0.5 - 2\mu\text{s}$  [49, 50, 51, 52].

### Phase Qubit

A phase qubit is a large current-biased Josephson junction. It is illustrated, along with its tilted washboard potential, in Fig. 1.5c. Due to its large  $\frac{E_J}{E_{CP}} \sim 10^6$ , the effect of charge noise is greatly reduced. A high impedance current source is obtained by using an inductively coupled flux bias. To increase the non-linearity of the phase qubit, the DC bias current is taken close to the junction critical current  $I_0$ . This system has the advantage of having a built-in readout mechanism. The excited state has a much higher probability of tunneling out of the well in the tilted washboard potential. This rate can be increased further by adiabatically decreasing the barrier height using a fast DC pulse. When the system tunnels, a voltage of  $2\Delta/e$  develops across the junction, which can then be measured to

determine the qubit state. The first time-resolved measurements were done by Martinis et al. (2002) [53]. These systems are exposed to large critical current noise because the junction is biased so close to the critical current. Couplings to microscopic charge motion two level systems in the barrier of the large junction has been the cause of loss in readout fidelity and reduction in coherence times. To combat these problems, the junction size has been reduced, increasing the plasma frequency, which is compensated for by shunting it with a capacitor with a high quality insulator [54]. At the time of this writing these samples have relaxation times  $T_1$  and coherence times  $T_2$  of a few  $\sim 100$  ns, substantially shorter than the best experiments involving the other two types of superconducting qubits.

## 1.3 Main fabrication technique used in this work

### 1.3.1 Dolan bridge shadow mask evaporation technique

All the superconducting circuits we fabricate have features as small as 50 – 100 nm in size, and other features as large as millimeters to centimeters in size. The larger features can be fabricated using photolithography, which has a resolution in the micrometer range. Alignment marks are usually written along with these larger features so that finer lithography can be done later, in specific areas on-chip relative to the large features. The majority of devices we study requires electron beam lithography fabrication, which has resolution down to about 10 nm, over an area of 3 mm by 3 mm. Our main fabrication procedure using electron beam lithography is known as “shadow mask evaporation,” and is described below.

The most complicated feature in our circuits is the Josephson junction, which consists of two overlapping films of superconductor with an insulator in-between (section 1.2.1). It is fabricated using the Dolan bridge shadow mask evaporation

technique [55]. This process begins with choosing a 2-inch wafer, such as Boron doped Si. This conductive substrate is chosen to avoid charging effects during the e-beam writing step (see below). In order to measure the device resistance at room temperature we often coat the substrate with an insulator (such as thermally grown  $\text{SiO}_2$ ). The wafer is spin coated with a bilayer of resist - first a layer of MMA/MAA (or MMA for short), about  $1 \mu\text{m}$  thick, followed by a thinner PMMA layer, about 200 nm thick (see Fig. 1.6a). Note our MMA is in fact a copolymer of methyl methacrylate and methacrylic acid dissolved in ethyl lactate. Polymethylmethacrylate, or PMMA, (also known as plexiglass) is made by free radical vinyl polymerization from the monomer methyl methacrylate, forming long chains of monomer molecules joined together. PMMA is typically dissolved in the solvent anisole. It has applications in beauty products, dentures, glass substitutes etc. Exposure to an electron beam creates chain scission (or de-cross-linking) within the PMMA, allowing for the selective removal of exposed areas by a chemical developer, such as MIBK (Methyl isobutyl ketone). In general, the higher the molecular weight, the slower it will dissolve in MIBK. After exposure to an electron beam, the developed contrast between the exposed and unexposed regions of the film becomes higher as the molecular weight increases, increasing the resolution [56]. MMA has a molecular weight that is about 10 times smaller than that of typical PMMA and hence gets dissolved faster in MIBK.

The resist coated wafer is baked for 30 min to remove as much solvent as possible, to form very stiff and robust PMMA structures. After baking, the sample is diced into chips with size on the order of 5 mm by 5 mm. A desired pattern is written onto the resist with an electron beam using a scanning electron microscope. The pattern illustrated in Fig. 1.6b is that required to make a Josephson junction. Exposed resist can now be removed using a MIBK solution. Diluted MIBK:IPA 1:3

mixture is used to increase the developing time to a controllable and reproducible scale of about 1 minute and to achieve higher contrast between developed and undeveloped regions than pure MIBK.

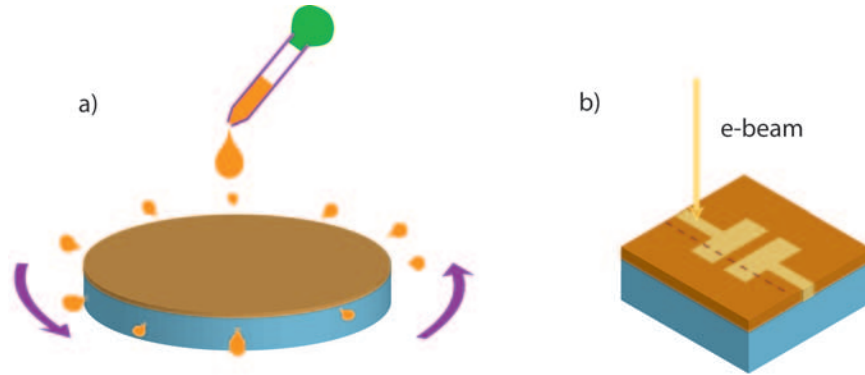


Figure 1.6: **(a)** The first step is to spin our resist bi-layer onto our substrate which is usually high resistivity Si. A layer of MMA is spun about  $1\ \mu\text{m}$  thick, followed by a layer of PMMA which is about  $150\ \text{nm}$  thick. The resist is then baked for  $1/2$  hour to ensure a stiff PMMA layer - essential for making suspended structures. **(b)** After baking the wafer is diced into smaller pieces (size depending on sample box) and the desired pattern is written in the SEM (a single junction pattern is illustrated). The dashed line is the cross section shown in Fig. 1.7.

A cartoon of the resulting cross section of the pattern (red dashed line in Fig. 1.6b) is illustrated in Fig. 1.7. Being more sensitive to an electron beam, some MMA is removed from under the PMMA along the edges of the pattern - we call this undercut. Ideally a bridge is formed where all the MMA is removed underneath a PMMA wire, but is anchored at both ends on undeveloped MMA. Baking the resist ensures that this bridge won't collapse. The suspended bridge is the essential component of the junction fabrication process.

Isopropanol (IPA), because of its low surface tension, is used to wash away the MIBK solution after development to avoid dragging down the bridge as it evaporates. Any residual resist left on the developed surface can be removed us-

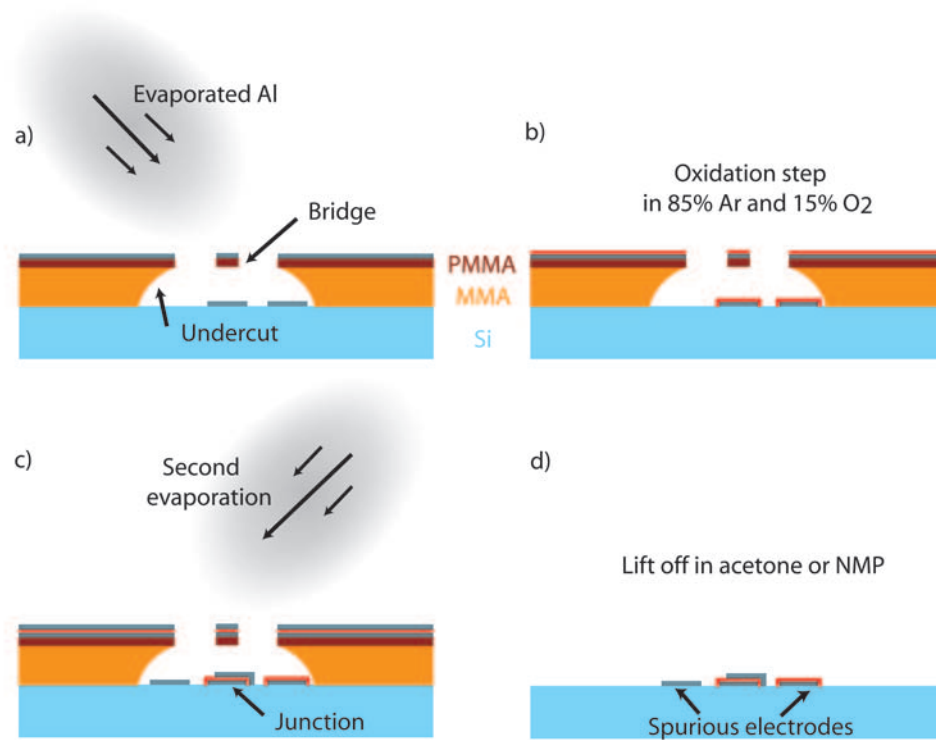


Figure 1.7: **(a)** After e-beam exposure the sample is developed to remove the exposed areas leaving undercut under the PMMA layer and a suspended bridge. Next in the e-beam evaporator a first angle of Al is deposited. **(b)** This layer of Al is then left to oxidise until the desired critical current density is reached. **(c)** Then the last layer of Al is deposited. The junction is formed at the overlap between the two evaporations. **(d)** The remaining resist and unwanted metal on top is removed by immersing the sample in either acetone or NMP followed by a cleaning in methanol.

ing an oxygen plasma or Ar ion milling. Next the sample is placed in an e-beam evaporator which is pumped down to around  $10^{-8}$  Torr. After tilting the sample between  $10^\circ$  and  $45^\circ$  (depending on the sample), we evaporate  $\sim 30 - 50\text{nm}$  of Al at  $1\text{ nm/s}$ . Al is the superconductor of choice due to its self terminating oxidation process [38]. This  $\text{Al}_2\text{O}_3$  layer is about  $1\text{ nm}$  thick, perfect for tunneling processes and is very homogeneous. We use a mixture of  $15\% \text{ O}_2$  and  $85\% \text{ Ar}$  so that we can control the pressure and oxidation time with high precision. Depending on

the sample, the pressure used was 1 – 70 T for 3 – 30 min. Following this controlled oxidation we evaporate a second layer of Al at a different angle, forming the Josephson junction at the overlap between the two layers, which is separated from the rest of the circuit by the suspended bridge (Fig. 1.7c). Spurious electrodes are formed on both sides of the junction as a consequence of this double angle evaporation process (Fig. 1.7d). Acetone is then used to wash away all the remaining resist along with the unwanted Al on top of it.

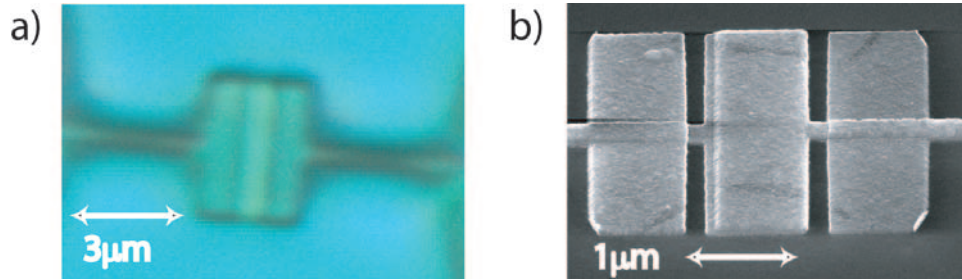


Figure 1.8: **(a)** Optical image of the pattern written by the SEM in the resist, after development in MIBK. One can clearly see the suspended PMMA bridge and junction electrodes. **(b)** SEM image of corresponding sample after double angle evaporation and lift-off in Acetone. The center part of the device is the junction sandwich. The outer two rectangular features are spurious and not involved in the device circuit. They are present as a result of the double angle evaporation.

A scanning electron micrograph of a typical junction fabricated in our lab is shown in Fig. 1.8b beside an optical image of the resist used to make it (Fig. 1.8a). The center rectangular piece consists of the overlapping Al layers, forming the Josephson junction. We can clearly see the spurious parts of the device on both sides of the junction. Also unavoidable large junctions make up the wires connecting this junction to the outside world. However, these are so large (with extremely large critical currents  $I_0$ ) that we can neglect them when describing the dynamics of our quantum circuits.

### 1.3.2 Limitations

The Dolan bridge technique is extremely versatile and robust. However, it comes with limitations, like every other process. I will briefly describe some of these limitations, along with some solutions, and in the next section I will describe in depth an example of a method used to overcome a few of these limitations.

Only metals with low evaporation temperatures can be used. Nb, for example, a commonly used superconductor, cannot be evaporated through an e-beam resist because it bakes the resist during deposition. This causes the resist to outgas and contaminate the Nb, reducing its transition temperature. This type of material is more suited to an etching process.

Insulating substrates, such as sapphire, are difficult (but not impossible) to use. During the e-beam writing step the substrate charges and deflects the on-coming e-beam, distorting the pattern. To deal with this problem we coat the PMMA layer with  $\sim 10$  nm of Al so that the e-beam has a conductive path to ground through the sample holder clips in the SEM. Before MIBK development, this Al layer is removed with a TMAH (tetramethylammonium hydroxide) solution.

E-beam lithography has excellent resolution and is essential for our fabrication process. However, it is not suited to writing large centimeter size features. With the usual current available in SEMs, it takes a long time to write such large structures. Also if the device is larger than the field of view of the SEM (2.5 mm by 2.5 mm for our microscope), then the stage motion needs to be extremely accurate (laser alignment) to stitch many fields of view together. Photolithography is more suited to such a process.

Spurious electrodes are a natural consequence of this method and do not usually create problems. However, sometimes it is desirable to get rid of these features.

This can be done by ensuring that as little undercut as possible is present along the direction of evaporation and that the evaporation angle is sufficiently sharp. Then the metal forming the extra electrode can fall completely on the MMA side wall and hence gets removed during the acetone lift-off step.

### 1.3.3 Multilayer techniques

The Dolan bridge technique forms the basic element for any device fabrication we execute in our lab. However, to make more complicated structures we can combine this process with techniques such as photolithography, reactive ion etching, plasma enhanced chemical vapor deposition etc. Throughout this thesis I will indicate when these other procedures are utilized.

As an example of a multi-step fabrication procedure, I will now describe a process which uses five layers of e-beam lithography (see Fig. 1.9) in order to fabricate a Quantronium with a Josephson bifurcation amplifier (JBA) readout (large junction shunted by a capacitor) (see section 2.2.1) with no spurious junctions, full control over circuit layout and Al-Al<sub>2</sub>O<sub>3</sub>-Cu capacitors.

The first layer consists of writing and depositing Au alignment marks using e-beam shadow mask evaporation (Fig. 1.9a). These alignment marks (crosses and rectangles) are fabricated for use in aligning all subsequent e-beam fabrication steps. A thin Ti layer ( $\sim 1$  nm) is deposited before the Au, acting as a sticking layer for the Au. The initial rough alignment is done with large markers (Fig. 1.9c) and this is followed with finer alignment with much smaller markers (Fig. 1.9a), which are accurate to about 100 nm. After depositing the Au, we re-spin a bilayer of e-beam resist, align the SEM to the markers, and write the CPB pattern using the double angle process (section 1.3.1). Then we repeat this step for the readout junction. Note that in these two layers no spurious junctions are

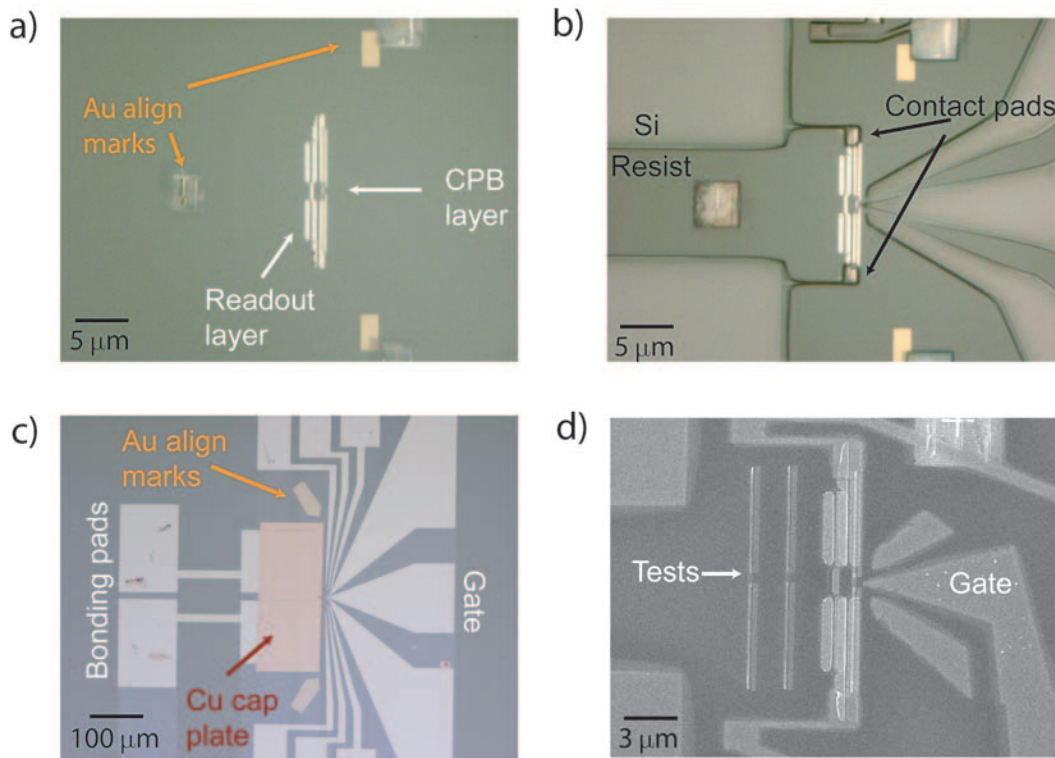


Figure 1.9: **(a)** Optical image of the first three completed fabrication layers. Au align marks are first evaporated with a Ti sticking layer. Then the CPB is deposited followed by the readout junction in the third e-beam process. **(b)** Optical image of the resist for the fourth fabrication layer. We can see the holes in the resist where the contact is made with the CPB and readout layers. Ar ion milling is used to remove the native oxide on the previous layers, forming a good ohmic contact. **(c)** Overall image of the completed device including the top Cu electrode of the capacitor which is deposited, along with the capacitor's  $\text{Al}_2\text{O}_3$  oxide, in the fifth layer. **(d)** SEM image of a finished test device.

fabricated because we haven't connected any measurement leads to these devices. Next we re-spin e-beam resist to make the contact leads and the bottom electrode of a shunting parallel plate capacitor. Before depositing this layer we ion clean, using an Ar ion gun situated inside our e-beam evaporator, to remove any native oxide on the areas of contact between the layers. Note that, because we only deposit one angle, there are no spurious junctions present. Finally, we re-spin a

bilayer of resist and write the top electrode of the capacitor. After ion cleaning we deposit  $\text{Al}_2\text{O}_3$  for the capacitor's insulator layer at an angle and while rotating the stage. Then the Cu electrode is deposited at  $0^\circ$ . This is done to ensure we have no shorts through capacitors insulator at the edges of the top electrode.

## 1.4 Cooper pair box

The work in this thesis involves the implementation of a CPB as a qubit. Hence, I will now focus on this system. I will begin by describing a modification of the CPB we use - the split Cooper pair box, and I will follow this with a short summary of previous measurements characterizing the CPB.

### 1.4.1 Split Cooper pair box energy levels

The basic CPB circuit can be slightly modified by splitting the junction into two to form a superconducting loop, resulting in a circuit called the split Cooper pair box (SCPB) (see Fig. 1.10a). A SCPB behaves like a regular CPB with a Josephson energy  $E_J(\delta)$  which depends on a magnetic flux  $\Phi$  applied through the superconducting loop. This field imposes a superconducting phase difference across the two junctions  $\delta$ , where  $\Phi = \phi_0\delta$ .

The first two energy levels are shown in Fig. 1.10b for  $E_J/E_{CP} \sim 1$ . The transition energy depends now on two external control parameters, the gate charge  $N_g = \frac{C_g V_g}{2e}$  and the externally applied loop flux  $\Phi = \phi_0\delta$ . We typically operate the SCPB at the “sweet spot” where the SCPB is immune to first order fluctuations in both charge and flux,  $\frac{\partial \nu_{01}}{\partial \delta} = \frac{\partial \nu_{01}}{\partial N_g} = 0$ . Energy states of the SCPB can be controlled via a microwave drive on the gate line,  $V_d \cos(\omega t)$ , and can be measured by either measuring the charge of the island, the current in the loop (first derivative of the energy levels), or the susceptibility of the energy levels (second derivative of the

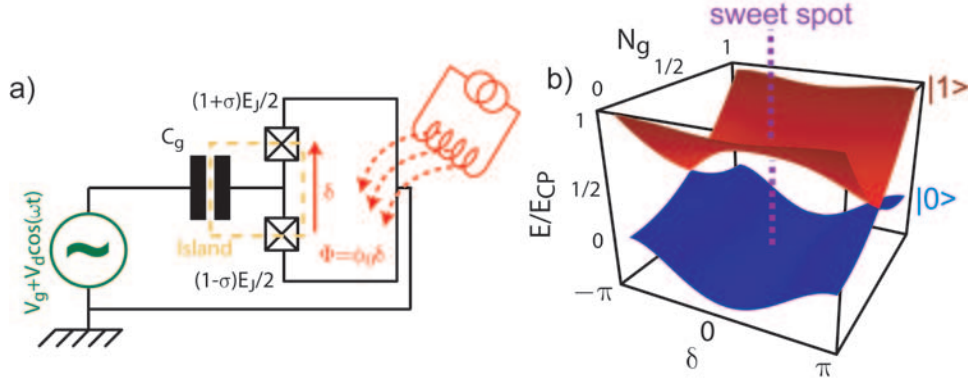


Figure 1.10: **(a)** Schematic of the split Cooper pair box (SCPB). The two small Josephson junctions, connected via a superconducting loop, behave like a single effective CPB with tunable  $E_J(\delta)$ . When there is no asymmetry between the junctions ( $\sigma = 0$ ) we have  $E_J^* = E_J \cos(\delta/2)$ . **(b)** First two energy levels of the SCPB for  $E_J/E_{CP} = 1$ . The transition frequency  $\nu_{01}$  is tuned using both the gate charge  $N_g = \frac{C_g V_g}{2e}$  and the flux through the loop  $\Phi = \phi_0 \delta$  where  $\delta$  is the superconducting phase difference across the two Josephson junctions. We typically operate at the “sweet spot” where the SCPB is immune to first order fluctuations in both  $N_g$  and  $\delta$ .

energy levels).

### 1.4.2 Initial measurements

Initial measurements carried out to characterize the CPB were performed by Bouchiat et al. (1998) [57, 58], who measured the average charge on the superconducting island, keeping the CPB in its ground state. This was done by a weak capacitive coupling of the island to a single electron transistor (SET) electrometer [59] which is sensitive to  $\frac{\partial E_k}{\partial N_g}$  or, in other words, the island potential  $V_k$

$$V_k = \langle k | \hat{V} | k \rangle = \frac{1}{2e} \frac{\partial \langle k | \hat{H} | k \rangle}{\partial N_g} = \frac{E_{CP}}{e} N_g - \langle k | \hat{N} | k \rangle, \quad (1.11)$$

where  $k = 0$  is the energy state of the CPB.

In this experiment  $E_J/E_{CP} = 0.08$  so that the energy levels become close to pure charge states, maximizing the measured signal. As the gate charge  $N_g$  is

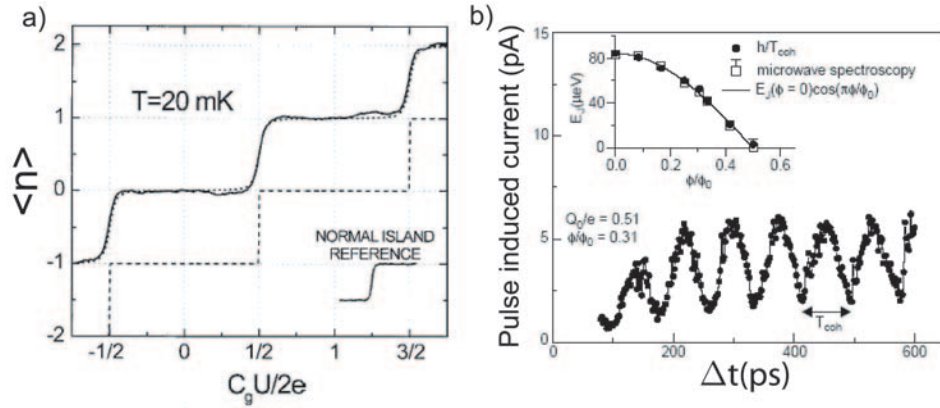


Figure 1.11: Initial measurements to probe the quantum properties of the Cooper pair box **(a)** Measurement of the average Cooper pair number on the island by Bouchiat et al. (1998) [57] using a single electron transistor [59]. The quantum superposition of charge states due to Josephson tunneling is inferred by the finite slope of the staircase. The dotted line is a fit to theory and the dashed line is the expected curve with no Josephson energy. **(b)** Measurement of a coherent quantum state evolution between two charge states of a Cooper pair box by Nakamura et. al (1999) [60] via quasiparticle tunneling of a probe junction. In these experiments the coherence times were limited to 100 ps.

swept, a staircase pattern is obtained for the average island charge, as illustrated in Fig. 1.11a. However, near  $N_g = 1/2$  the steps become rounded due to Josephson tunneling that results in the energy levels becoming superpositions of consecutive charge states near  $N_g = 1/2$ .

This experiment only probed the coherence of the CPB ground state. The next step was to probe the coherent quantum evolution between the ground state and the excited states of the CPB. Nakamura et al. (1998) [61, 60] brought two charge states of the CPB into resonance, using a voltage pulse applied to the gate capacitor  $C_g$ , where coherent evolution of the charge states could take place, called Rabi oscillations (for more information on Rabi oscillations see Fig. 1.16b). The state of the CPB was measured using the quasi-particle tunnel current through a probe junction, connected to the island and biased above the superconducting gap

$\Delta$ . Excessive decoherence was avoided by making the probe junction's resistance large to reduce the quasi-particle tunneling rate. By varying the length of the gate pulse, Rabi oscillations were observed (Fig. 1.11b) with a typical decay time of 2 ns.

Following this experiment, Nakamura et al. performed a Ramsey fringe experiment (for more information on Ramsey fringes see Fig. 1.16c) to measure the qubit's coherence time of about 100 ps. This short coherence time was initially limited by  $1/f$  charge noise [62, 63, 64] at the gate of the CPB. Then, the charge noise was compensated for using a Hahn spin echo experiment, but still only gave a decay time of up to  $\sim 2$  ns [65]. The coherence time was further limited by measurement backaction of the probe junction via quasiparticle tunneling. Furthermore, the probe junction measurement scheme continuously reads the qubit state, even during qubit manipulation pulses. Note also that the experiment is not single-shot, in the sense that the quasi-particle current needs to be averaged over many experiments to be measurable.

Hence, even though this experiment demonstrates that the CPB may be a good candidate for a qubit, because of backaction, charge noise and low signal to noise ratio, an improved readout scheme is needed. Ideally we would like a readout system which can be turned on and off and which has no effect on the qubit relaxation and decoherence times when switched off. Also a fast readout capable of a single shot measurement is desirable and which is operable with a CPB which has parameters that are insensitive to  $1/f$  charge noise.

### 1.4.3 Improved readout Schemes

In order to achieve these goals, a number of schemes were investigated. Delsing and Schoelkopf et al. (theory (2001): [66], expt. (2004): [67]) explored a method

of measuring the island charge using a capacitively coupled RF-SET (Fig. 1.12c). The RF-SET is a fast version of the sensitive SET electrometer, implemented using an RF tank circuit. This method also gives better sensitivity because one can measure away from DC and reduce the effect of  $1/f$  noise on the readout. These samples resulted in relaxation times,  $T_1$  in the  $\mu s$  range and decoherence times,  $T_2$ , of about 10 ns. However, the decoherence time was again limited by  $1/f$  charge noise and this readout system has unwanted backaction due to shot noise. Also, these samples with SET readout are often poisoned, because the SET produces non-equilibrium quasiparticles that destroys the CPB coherence.

An alternative readout method, based on measuring the loop currents of the SCPB, was developed by Cottet et al. (2002) [69] in Saclay. The readout mechanism is based on measuring the switching probability of a large readout junction into its normal state. This junction is placed into the superconducting loop of the SCPB, forming the circuit nicknamed “the Quantronium” [49] (because it behaves like a tunable artificial atom; see Fig. 1.12c). When biased near its switching point, the junction switches with a high probability when the qubit is in its excited state, but remains superconducting when the qubit is in its ground state. The readout junction is large compared to the SCPB junctions,  $E_J^0 \gg E_J$ , and hence acts like an inductive short, protecting the qubit from environmental decoherence. A switching readout has the advantage that it can be turned on and off and also the qubit remains at the “sweet spot” during qubit manipulation. Because of the “sweet spot,” this switching junction readout experiment resulted in a long decoherence time,  $T_2$ , of 500 ns.

However, there are still a number of issues to be addressed. Firstly, when the readout junction switches, it produces quasiparticles. Quasiparticles limit the repetition rate of the experiment and the resulting dissipation induces unwanted

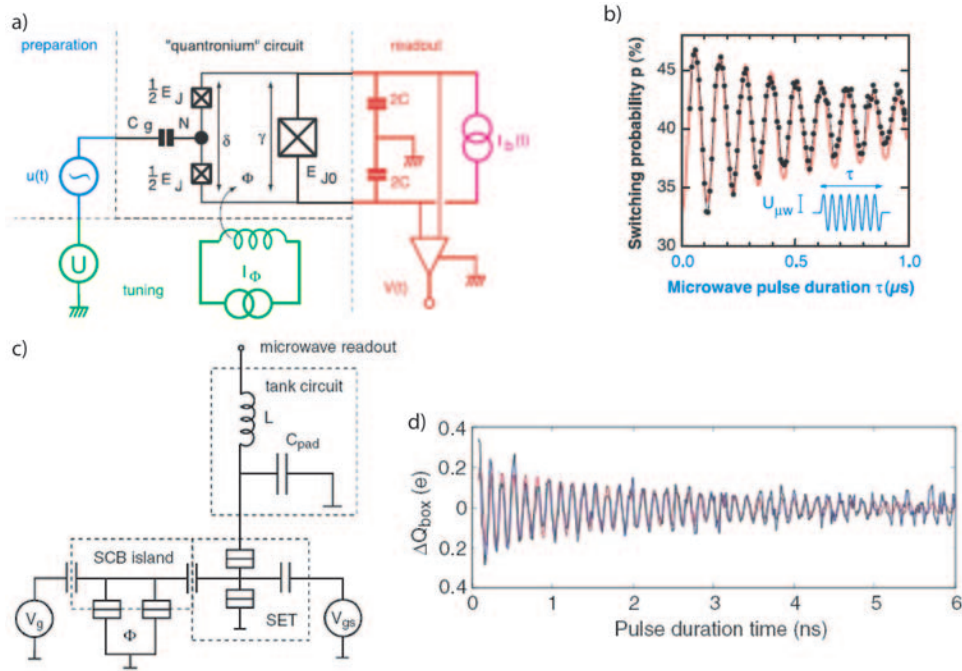


Figure 1.12: Some representative efforts to improve measurements of the quantum properties of the Cooper pair box. **(a)** In Saclay a large Josephson junction was placed in the loop of the SCPB. The states of the CPB are distinguished by measuring the switching probability of the large junction into its normal state. **(b)** Measured Rabi oscillations of this “Quantronium” at the “sweet spot” [49]. In a Ramsey fringe experiment performed on the same sample, a coherence time  $T_2$  of 500ns was measured. **(c)** Setup required to measure the charge states of the CPB using the RF-SET [66, 67, 68]. The RF-SET reads out the charge states of the CPB. **(d)** Rabi oscillations of the CPB measured at  $N_g = 0.5$ . The red curve is an exponential fit with decay time 2.7 ns

backaction. They may also affect nearby qubits on a multi-qubit sample. In an attempt to reduce the effect of these quasiparticles, Au traps were implemented, giving an improved maximum repetition rate of only 50 kHz. Furthermore, in order to get a measurable signal, the qubit needs to be moved away from the “sweet spot” in either  $N_g$  or  $\delta$  during readout, during which its transition frequency,  $\omega_{01}$ , changes by up to a factor of 2 compared with  $\omega_{01}$  at the sweet spot. During this frequency shift the qubit can come into resonance with spurious environmental

resonances [54] and relax. This probably accounts for the observed loss of readout fidelity, which in this case was limited to about 40%.

## 1.5 Dispersive readout

### 1.5.1 Cavity bifurcation amplifier

To address the problems faced by previous readout schemes, we have developed a new dispersive readout method [51, 52, 70, 71, 72, 73]. It is based on the measurement of the susceptibility of the qubit, i.e., the second derivative of the eigenstates with respect to an external parameter, such as gate charge  $N_g$  or reduced flux  $\delta$ . The experiments of Wallraff et al. [70] (or the lumped element version of Sillanpaa et. al [73]) are examples of dispersive measurements which are sensitive to the effective capacitance of the SCPB energy levels:  $C_k = \left( \frac{1}{(2e)^2} \frac{\partial^2 E_k}{\partial N_g^2} \right)^{-1}$ . In our case we exploit the effective inductance of the SCPB energy levels:  $L_k = \left( \frac{1}{\phi_0^2} \frac{\partial^2 E_k}{\partial \delta^2} \right)^{-1}$ . Unlike DC SQUID amplifiers, no resistors are required on-chip. Hence, these dispersive measurements have no on-chip dissipation, minimizing the back-action of this amplification scheme. By monitoring the frequency shifts of a resonator with resonance frequency  $\omega_0 = \frac{1}{\sqrt{LC}}$  in which a SCPB is placed, we can measure the state of the SCPB. However, the frequency change of such a resonator caused by an SCPB transition is not distinguishable in a time smaller than typical qubit relaxation times.

To achieve more sensitivity, with single shot capability, we have designed and fabricated a non-linear resonator ([74, 75, 76] (see Fig. 1.13a), the “bifurcation amplifier”. Initially we fabricated a lumped element version called the “Josephson bifurcation amplifier ” (JBA) (see R. Vijay’s thesis [77]), followed by the distributed element version called the “cavity bifurcation amplifier ” (CBA). Compared with

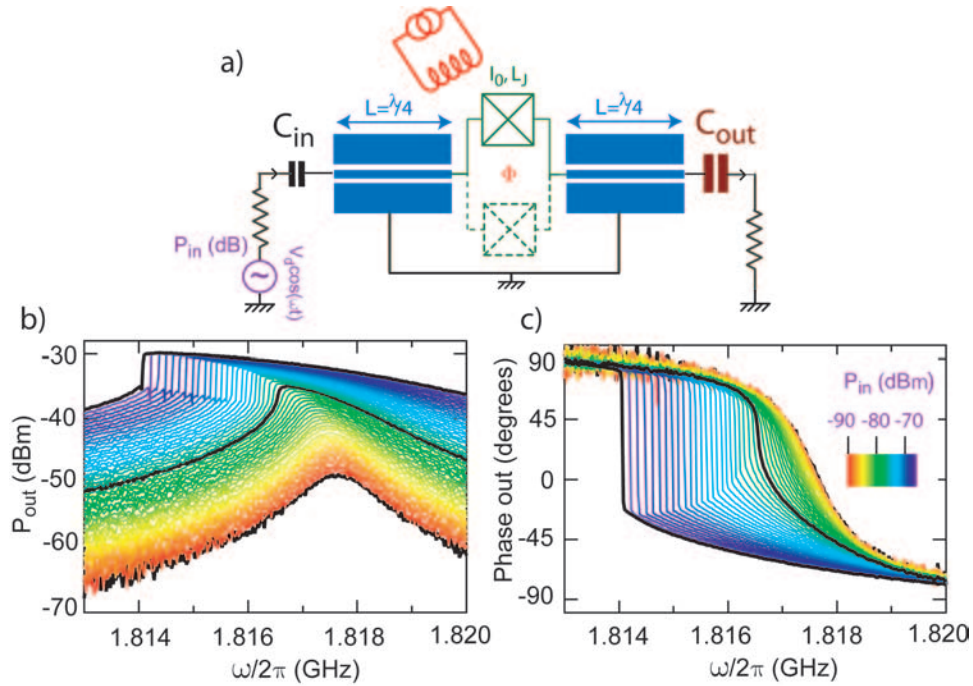


Figure 1.13: **(a)** Schematic of a CBA sample with either a single Josephson junction or two junctions placed in a SQUID geometry. The junctions are placed in the center of a  $\lambda/2$  (to first order - see Eqn. 2.37) coplanar waveguide (CPW) resonator. The SQUID is used to measure the discrimination power of the CBA by changing the effective inductance of the SQUID with an external magnetic field (see Fig. 1.14). **(b)** Transmitted microwave amplitude as a function of frequency. As the input power is increased we see the resonance shifting to lower frequencies due to the non-linear inductance provided by the junction. At high enough powers the CBA becomes bistable and we see the amplitude jump from one state to the other as we sweep the frequency. **(c)** Corresponding transmitted phase as we increase the input power. We see the expected 180 degree phase shift and again observe bifurcation at sufficiently high input powers.

the JBA, the CBA offers precise environmental control, high tunability in operation parameters such as readout frequency and bandwidth, ease of fabrication and an architecture that lends itself to multiplexing. Hence, my thesis concentrates on the CBA implementation of the bifurcation amplifier (see chapter 2 for more detail on the JBA). The CBA consists of a Josephson junction imbedded in a microwave on-chip coplanar waveguide resonator. When driven near the resonance

frequency by a sinusoidal signal with adequate amplitude, it can adopt one of two dynamical metastable states. Biasing the CBA in the vicinity of the switching point between these two states, we can obtain high sensitivity with the ability to distinguish the CPB states in a single-shot manner.

The resonator is based on a simple coplanar waveguide geometry imposing a precisely controlled environment with no stray capacitive or inductive elements. The resonance frequency  $\nu_0$  depends on the length of the resonator and the quality factor  $Q$  is determined by the large output capacitor. A Josephson junction (see section 1.2.1) is placed in the center of the resonator where the coupling with the resonator is maximum. At low temperatures this acts as a non-linear inductor so that when the CBA is driven near the resonance frequency by a sinusoidal signal with adequate amplitude, it bifurcates, adopting two metastable states.

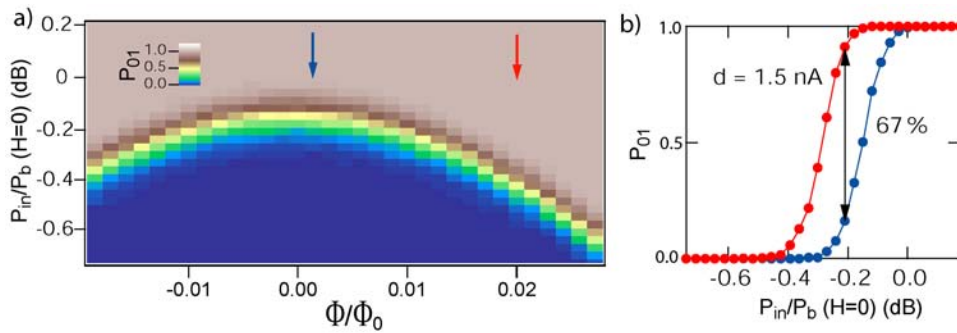


Figure 1.14: **(a)** Measured switching probability  $P_{01}$  as a function of input power  $P_{in}$  and applied magnetic field  $\Phi$  to a SQUID CBA sample. The input power is normalized to the bifurcation power  $P_b$  at zero magnetic field.  $P_b$  is the power where switching occurs in the steady state. **(b)** Two cuts of  $P_{01}$  vs  $P_{in}$  corresponding to critical currents of  $1.5000 \mu\text{A}$  and  $1.4985 \mu\text{A}$ . Their maximum separation is 67% so that the two distributions corresponding to these s-curves are separated by twice their standard deviation.

Non-linear behavior can be most easily seen by measuring the transmitted amplitude and phase as a function of input frequency  $\nu = \omega/2\pi$  and input power

$P_{in}$  (see Fig. 1.13 b&c). At low input power we see the typical Lorentzian response of the transmitted amplitude for a resonator, along with the expected  $180^\circ$  phase shift. As  $P_{in}$  is increased the resonance frequency  $\omega_0/2\pi$  bends backwards due to the non-linearity, until eventually the CBA becomes bistable. This can be seen in Fig. 1.13 b&c as jump in the transmitted amplitude and phase as the frequency is swept up.

Switching also occurs if  $P_{in}$  is ramped at fixed  $\nu$ . While ramping  $P_{in}$  we can measure the switching probability  $P_{01}$  from the lower amplitude oscillating metastable state to the higher amplitude metastable state, as shown in Fig. 1.14b. This sigmoidally shaped curve has been nicknamed “s-curve”. Any phenomenon that can be coupled to the Josephson energy will change the power at which this transition occurs. In Fig. 1.14 this is done by applying a magnetic field to the SQUID loop, changing the critical current of the SQUID. A critical current change of 1.5 nA gives the two s-curves shown in Fig. 1.14b, which are maximally separated by 67% - or twice the standard deviation of their associated distributions.

## 1.6 Quantronium with bifurcating readout

In order to use the CBA as a readout for the SCPB qubit, we place the SCPB in parallel with the large CBA junction. In this configuration, the qubit states alter the effective inductance of the junction so that the power at which the bifurcation occurs will also vary. Hence, by measuring the switching probability  $P_{01}$  of the CBA, we can sensitively discriminate the qubit energy states. Given the well known expressions for the eigenstates of the SCPB and the measured discrimination power of the CBA (e.g., Fig. 1.14b), single-shot readout should be possible.

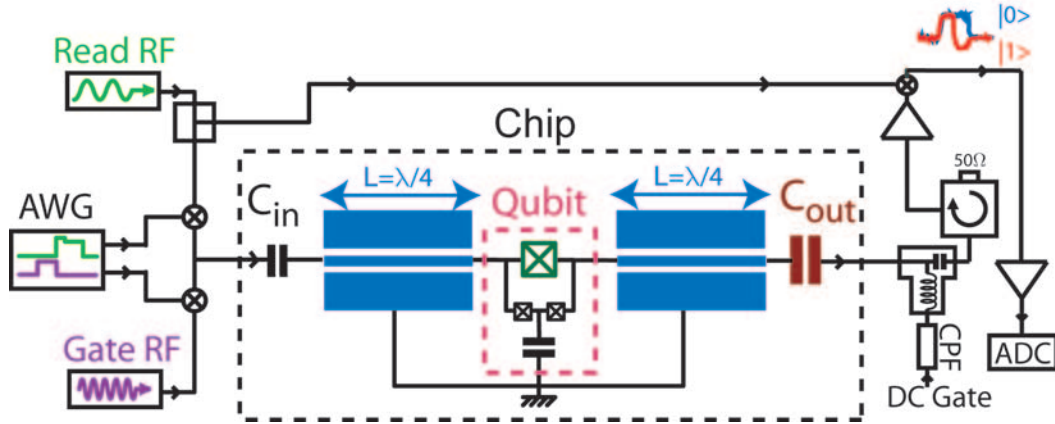


Figure 1.15: Schematic of the Quantronium qubit with CBA readout. The basic measurement schematic is also depicted. The large junction of the CBA is placed into the loop of the SCPB. The energy state of the SCPB alters the effective inductance of the CBA junction so that the power at which bifurcation occurs will also vary. By biasing the CBA near the switching point we can sensitively discriminate the SCPB energy states.

Since the CBA measures the susceptibility of the qubit (the qubit's inductance or second derivative of the energy levels) with respect to flux, the qubit remains biased (on average) at the “sweet spot” during readout, minimizing loss to spurious environmental resonances, and keeping the qubit immune to charge and flux noise (to first order) at all times. Linear resonance frequencies of 10 GHz for the CBA readout were chosen, with low quality factors  $Q$  of a few hundred to obtain a fast readout compared to the energy relaxation time of our qubits, which are typically in the microsecond range. Any qubit relaxation that occurs before readout will reduce our readout discrimination power.

The qubit chip layout and basic measurement schematic is illustrated in Fig. 1.15. The DC gate line that controls  $N_g$  is placed on the large output capacitor  $C_{out}$  of the CBA via a bias tee. The qubit state is also manipulated through the CBA readout lines by applying microwave pulses of frequency  $\nu_s$  near the qubit

transition frequency  $\nu_{01}$ , which is 14.35 GHz for the qubit sample presented below. Such pulses are used to create superpositions of the two qubit states  $|0\rangle$  and  $|1\rangle$ .

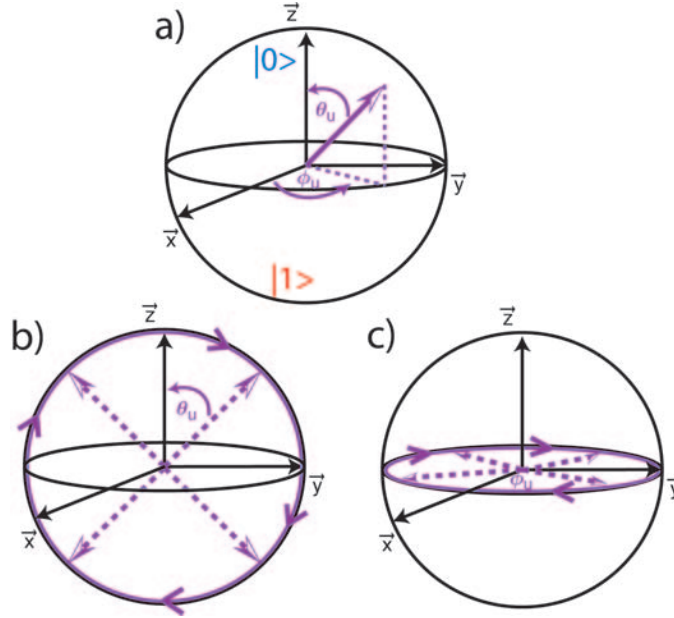


Figure 1.16: **(a)** A general qubit state is represented on the Bloch sphere with spherical polar angles  $\theta_u$  and  $\phi_u$ . **(b)** In a Rabi experiment we drive a coherent evolution between the two qubit states, which is represented on the Bloch sphere as the qubit vector rotating on a great circle with continuously increasing  $\theta_u$ . **(c)** In a Ramsey experiment we drive the qubit into a state  $(|0\rangle + |1\rangle)/\sqrt{2}$  which is in the equatorial plane of the Bloch sphere. Then it freely evolves in this plane with  $\phi_u(t) = \omega_{01}\Delta t$ .

Any superposition of states  $|\psi\rangle$ , can be represented as a vector on a unit sphere called a Bloch sphere (see Fig. 1.16a), with polar angles  $\theta_u$  and  $\phi_u$

$$|\psi\rangle = \cos(\theta_u/2)|0\rangle + \sin(\theta_u/2)e^{i\phi_u}|1\rangle. \quad (1.12)$$

Starting in the state  $|0\rangle$ , we can create a superposition  $\cos(\theta_u/2)|0\rangle + \sin(\theta_u/2)|1\rangle$  by applying a microwave pulse of amplitude  $A$  and time duration  $\tau_R$  at  $\nu_{01}$  to the qubit gate line, where  $\theta_u \propto A\tau_R$ . Any arbitrary state  $|\psi\rangle$  can then be obtained by combining these qubit manipulation pulses with a free evolution time  $\Delta t$ , where

$$\phi_u(t) = \omega_{01}\Delta t.$$

Applying a sequence of pulses at  $\nu_{01}$  of increasing duration  $\tau_R$ , we can drive coherent oscillations between these two states (see Fig. 1.16b). The resulting oscillations in the qubit excited state population are called Rabi oscillations and are plotted in Fig. 1.17b. The frequency of these oscillations varies linearly with the amplitude of the Rabi pulses  $A$ , as expected from a two-level system.

The maximally observed contrast of the Rabi oscillations is about a 50% change in  $P_{01}$  (the difference between the maximum value of  $P_{01}$  when the qubit is in the excited state and the minimum value of  $P_{01}$  when the qubit is in the ground state). For the ideal case of a non-relaxing qubit we expected a contrast of over 99.9%, given the measured parameters of the resonator. To study the contrast between the qubits states further, we again measure the s-curves of the CBA. One s-curve is measured with the qubit in the ground state  $|0\rangle$ , and the other with the qubit in the excited state  $|1\rangle$ . Before measuring the second s-curve, the qubit is excited by applying a microwave  $\pi$ -pulse to the qubit's gate line. The shift between the two curves again gives the contrast (Fig. 1.17a), which agrees with the observed contrast in the Rabi oscillations. The disagreement with the expected contrast can be attributed to three main sources. First, the transition between the two oscillating states of the CBA is broadened by more than a factor of 5 from that expected, probably due to insufficient RF filtering in the output lines. However, this broadening still doesn't account for all the loss of discrimination power. A 10% loss in contrast is obtained because the qubit relaxes before the readout takes place, due to its finite  $T_1$ . The largest contribution to the loss in contrast comes from qubit relaxation to the ground state as the readout voltage approaches the bifurcation voltage. This loss in contrast could be due to the readout pulse shifting the qubit transition frequency downwards during readout

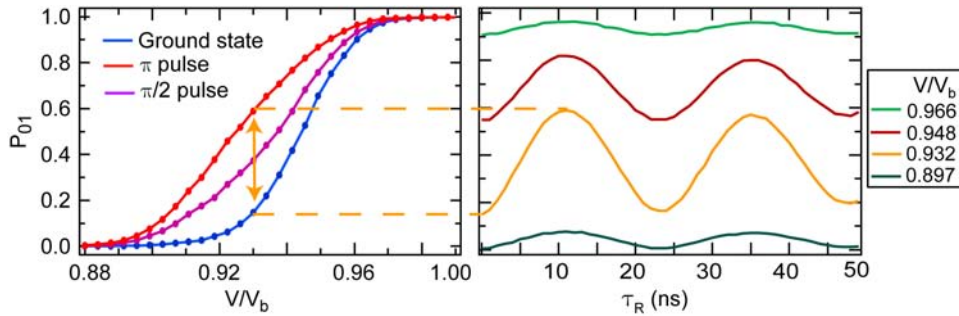


Figure 1.17: Displayed on the left panel we have the measured s-curves of the Quantonium with CBA readout. Preceding the readout pulse we apply a pulse at the qubit transition frequency to manipulate the qubit state. The right panel contains the corresponding Rabi oscillations at four different points along the s-curves. For the Rabi oscillations we apply a pulse of varying length,  $\tau_R$  to the qubit before the readout pulse. This pulse corresponds to a driven coherent evolution of the qubit state. We obtain the expected sinusoidal oscillations with pulse length with a period which depends linearly on pulse power. The contrast of these oscillations depends on the readout biasing point.

(a so-called Stark shift), where it can come in resonance with spurious transitions [54], possibly due to defects in the substrate or in the tunnel barrier.

To measure the coherence time  $T_2$  of our qubit we perform a Ramsey fringe experiment, as shown in Fig. 1.18. In this experiment, a  $\pi/2$ -pulse is used to create a state  $(|0\rangle + |1\rangle)/\sqrt{2}$ . Then the qubit is allowed to freely evolve for a time  $\Delta t$  during which it can decohere (see Fig. 1.16c). Finally, we apply a second  $\pi/2$ -pulse before reading out. We extract  $T_2$  from the exponential decay of the resulting oscillations as shown in Fig. 1.18b. This data, which takes 15 min to acquire, gives  $T_2 = 500ns$ . The Ramsey oscillations have a frequency  $\nu_{Ramsey}$  given by the difference of the pulse frequency  $\nu_s$  and  $\nu_{01}$ , as expected.

We can utilize other advantages of this CBA geometry when used as a superconducting qubit readout to study the noise sources limiting our  $T_2$ . One such advantage is that the readout junction always remains in the superconducting

state so that few QPs are created. Hence, the repetition rate is only limited by the relaxation time of the qubit and the  $Q$  of the resonator. Also since the CBA is hysteretic, we can latch its state and therefore have excellent signal to noise ratio. Hence, we can measure the fluctuations of the qubit's coherence time,  $T_2$ , on time scales as short as a second (see Fig. 1.18c,d&e). We acquire 3000 Ramsey traces over a 15 min period (corresponding to the average Ramsey fringes in Fig. 1.18b) and histogram the spread in  $T_2$  and  $\nu_{Ramsey}$ . Using this information we have determined that these fluctuations are dominated by  $1/f$  charge noise, agreeing with previous studies [62, 63, 64] and illustrating the dependence of  $T_2$  on the measurement protocol.

Another advantage of this CBA geometry is that it can easily be multiplexed on-chip (Fig. 1.19). In this multiplexed geometry, each resonator has a different length and hence a different resonance frequency. They are placed in parallel, capacitively coupled to the same input and output lines. Using this method, up to 10 CBA readouts could be implemented at once on-chip, each with a different readout frequency and separated from each other by a few linewidths to prevent crosstalk. Fig. 1.19b shows the measured transmitted amplitude for a multiplexed chip with 5 resonators. We can see that bifurcation occurs for each resonator at sufficiently high powers. Each resonator on the multiplexed chip would readout its own qubit and the island of each qubit can be capacitively coupled to a separate coupling resonator (shown in red in Fig. 1.19a). This is an important step towards scalable quantum computing.

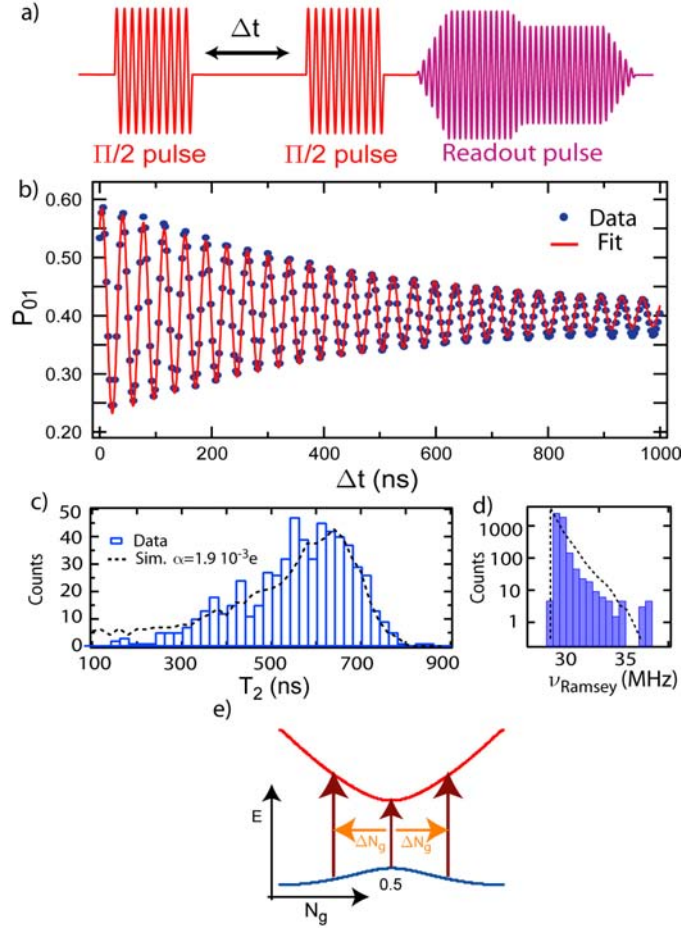


Figure 1.18: **(a)** Pulse sequence used in a Ramsey fringe experiment. **(b)** An example of a Ramsey fringe taken over a 15 min period with a decay time of  $T_2 = 500$  ns. This is the average of the data used in (c&d). **(c)** Distribution of  $T_2$  for 3000 of the Ramsey traces (600 fits) that make up the data in (b). The black dashed line is the result of a simulation of the free evolution decay of the Ramsey fringes with  $1/f$  noise fluctuations on the gate,  $S_q(\omega) = \alpha^2/|\omega|$ . In the simulation we used 10 times more points compared to the data to obtain a smoother curve. **(d)** Spread in Ramsey frequency  $\nu_{\text{Ramsey}}$  for the same data as that in (c). Again the dashed line is the result of simulation assuming  $1/f$  charge noise. **(e)** Cross-section of the qubit first two energy levels with respect to gate charge  $N_g$ . Charge noise will move the qubit away from the “sweet spot” in the direction of increasing  $\nu_{\text{Ramsey}}$ . This gives rise to the lopsided distribution shown in (d). The variation in qubit transition frequency gives rise to the observed distribution of  $T_2$ .

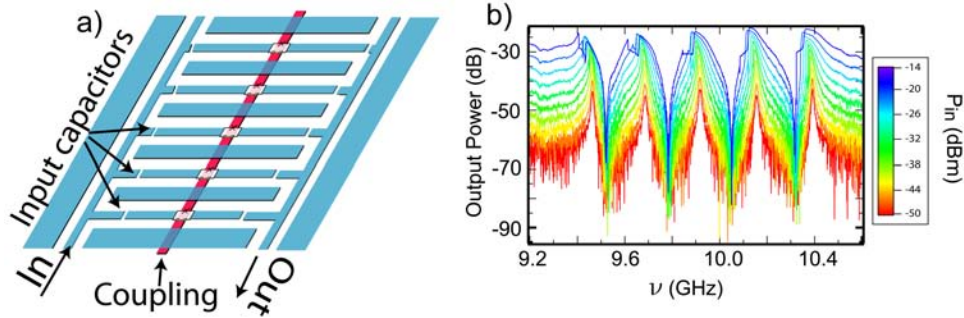


Figure 1.19: **(a)** Schematic of the multiplexed CBA design. Each resonator has a different length and so a different readout frequency. The length increases as the input and output capacitors move apart. A qubit can be placed at the center of each resonator and readout independently. The red line depicts a coupling method where each qubit island is capacitively coupled to a coupling resonator. The measurement setup is exactly the same as that used for a single resonator with only one input and output line. **(b)** Measured transmission of a chip with 5 multiplexed resonators. We can see that each resonator bifurcates as the input power is increased and each resonance is separated from its neighbor by a few linewidths to prevent crosstalk.

## 1.7 Conclusion

We have successfully implemented an improved readout method for the Quantronium qubit based on a non-linear bifurcating CPW resonator. Compared with previous readout systems it offers speed, sensitivity and ease of fabrication along with an operating environment which is precisely controlled. Because of the MHz repetition rate and large signal to noise ratio we can capture in real time the fluctuations in qubit parameters and identify the dominating external noise source. We have demonstrated that the main source of decoherence for low  $E_J/E_{CP}$  is charge noise. By using a larger  $E_J/E_{CP}$ , we could reduce the curvature with gate charge of the levels of the Cooper pair box, reducing the charge noise induced decoherence. This CBA geometry is particularly well adapted to the multiplexing of the simultaneous readout of several qubits, offering a path for scaling super-

conducting circuits up to several tens of qubits.

Furthermore, apart from the development of a quantum computer, research in the field of quantum circuits can reveal a lot of interesting physics and can lead to the development of useful tools and devices. For example, cavity bifurcation amplification has further applications outside the realm of superconducting qubits, for instance, in particle detection or analog signal detection. One can view the qubit in our experiments as a test bed for the performance of cavity bifurcation amplification in quantum measurements of mesoscopic systems. The measurement of any phenomenon that can be coupled to the Josephson energy can, in principle, benefit from this new type of amplification.

## 1.8 Dissertation overview

In chapter 2 I will begin by describing the physics of a non-linear bifurcating oscillator and how we implement this device in our lab. Following this I will describe our experiments to characterize this amplifier and to test its behavior compared to the analytical theory. In chapter 3, I move onto the measurement utilizing the CBA as a Quantronium readout. It begins with device design and fabrication and then continues with full characterization of the Quantronium. This chapter concludes with a key measurement, which capitalizes on some of the advantages of the CBA, in identifying the main source of decoherence in this qubit. Chapter 4 will describe methods for scaling the system for measuring many coupled qubits. I conclude in chapter 5 and offer a look into possible future directions.

## Chapter 2

# Principle and implementation of bifurcation readout

One of the main focuses of superconducting qubit research is creating an efficient method of reading out the qubit energy states without introducing excessive extra sources of noise. Ideally, such a readout should minimally disturb the qubit state, i.e., the readout should not cause unwanted excitation or relaxation of the qubit state, during measurement. Furthermore, while dephasing of the qubit state is required during readout, it should be avoided when not measuring, such as during qubit manipulation operations. Hence, the readout should be switchable (ON and OFF), completely decoupled from the qubit in the OFF state, and maximally coupled in the ON state.

Important parameters of any such readout system are its speed and sensitivity. Discrimination of the qubit states should occur within the relaxation time,  $T_1$ , of the qubit, so only one readout cycle is required. With this “single-shot” readout, one can measure drifts in qubit parameters in real time and either compensate for these drifts as they are detected, or simply study them to discover their source. Using this information, future generations of qubits can be adjusted to become immune to the sources of these drifts.

Some qubit systems can be biased on so-called “sweet-spots” of their external control parameters where they are immune to fluctuations in these external control parameters to first order (e.g., charge and magnetic field, c.f., section 3.1). Hence, it is important that the readout system does not require the external biasing parameters to be tuned off the “sweet-spots” to boost the readout signal. Such a readout system would need to be sensitive to the susceptibility of the qubit states with respect to the external control parameters.

In an effort to attain the above goals, we have developed a new type of dispersive bifurcating amplifier, which consists of a Josephson junction imbedded in a microwave on-chip resonator [39, 40] (see section 1.2.1). Placed in a suitable electromagnetic environment, an RF-biased Josephson junction can display a dynamical bifurcation when driven with a microwave signal of adequate amplitude. When biased near this bifurcation phenomenon, the junction can be used as a high gain amplifier, sensitive to small changes in its susceptibility (inductance), and can be potentially applied as a “single-shot” readout. The Josephson junction is the only electronic circuit element known today which is both non-linear and dissipation-free at low (mK) temperatures.

In this chapter, I will begin with a theoretical description of the bifurcation amplifier by approximating it as a Duffing oscillator. I will then describe how we implement this non-linear oscillator in our experiment, along with the fabrication procedures used for each implementation. I will concentrate on the optimum implementation, the cavity bifurcation amplifier (CBA), and describe its behavior as a Duffing oscillator. Finally, I will discuss the temporal dynamics of the CBA and measure its sensitivity to small changes in the susceptibility of any phenomenon that can be coupled to the Josephson junction’s  $E_J$ .

## 2.1 Dynamics of a non-linear oscillator

I begin with a description of a general non-linear oscillator and the conditions in which this oscillator can display a bifurcation [78, 79]. Following this, I show how this non-linear oscillator can be implemented as an amplification scheme. Finally, I describe how we realize this device in our experiment using Josephson junction circuits, which can be used to readout the state of a superconducting qubit.

### 2.1.1 Physics of a Duffing oscillator

The prototypical example of a non-linear oscillator is the simple pendulum (see Fig. 2.1). It follows the equation of motion

$$ml^2\ddot{\vartheta} + \gamma\dot{\vartheta} + mgl\sin(\vartheta) = F\cos(\omega t) + F_N, \quad (2.1)$$

where the dots represent derivatives with respect to time  $t$ ,  $l$  is the length of the pendulum,  $\vartheta$  is the angle of deflection,  $m$  is the mass,  $g$  is the acceleration due to gravity, and  $F$  is an externally applied force at frequency  $\omega$ .  $F_N$  is an external noise source applied to the pendulum.

In the limit of small oscillations,  $\vartheta \ll 1$  rad, we can expand  $\sin(\vartheta) \simeq \vartheta - \frac{1}{3!}\vartheta^3 + O(\vartheta^5)$  to obtain

$$\ddot{\vartheta}(t) + 2\Gamma\dot{\vartheta}(t) + \omega_0^2\vartheta(1 - \frac{1}{3!}\vartheta^2) = \frac{F}{ml^2}\cos(\omega t) + \frac{F_N}{ml^2}, \quad (2.2)$$

where  $2\Gamma = \frac{\gamma}{ml^2}$  is the resonance bandwidth and  $\omega_0 = \sqrt{\frac{g}{l}}$  is the resonance frequency. This is the minimum model of an oscillator which displays a bifurcation [80], and is often called the ‘‘Duffing oscillator’’. Assuming a weak non-linearity, we solve for only the first harmonic of the oscillation amplitude  $\vartheta$  and substitute

$$\vartheta(t) = A(t)e^{i\omega t} + c.c \quad (2.3)$$

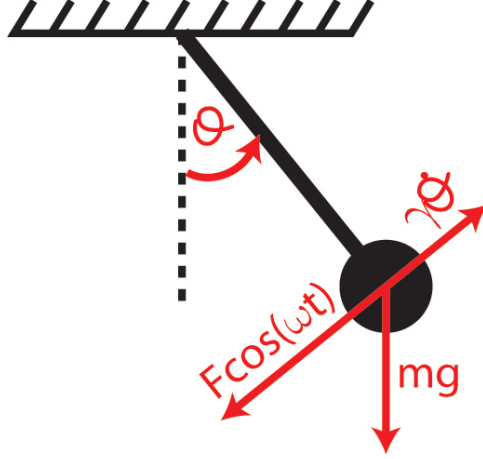


Figure 2.1: Schematic of a driven, damped, non-linear pendulum, the prototypical example of a non-linear oscillator. It is subject to a driving force  $F \cos \omega t$ , damping  $-\gamma \dot{\vartheta}$ , and acceleration due to gravity  $g$ .

into Eqn. 2.2, where  $A(t)$  changes slowly on the time scale of  $1/\omega$ . This approximation is often known as the rotating wave approximation. Then averaging over the period  $2\pi/\omega$  and neglecting  $\ddot{A}(t)$ , we obtain, after some rescaling,

$$\dot{B}(\tau) + \left( \frac{1}{\Omega} - i \frac{\zeta}{\Omega} + i |B|^2 \right) B = -i \sqrt{\beta} + \tilde{\nu}_N(\tau), \quad (2.4)$$

where  $B(\tau)$  is the rescaled slow oscillation amplitude  $A(\tau)$  with

$$B(\tau) = \sqrt{\frac{\omega_0^2}{4\omega\delta\omega}} A(\tau), \quad (2.5)$$

$\Omega = \delta\omega/\Gamma$  is the reduced detuning,  $\zeta = \frac{\omega+\omega_0}{2\omega}\Omega \sim \Omega$ ,  $\delta\omega = \omega_0 - \omega$  is the absolute detuning,  $\beta$  is the rescaled drive power with

$$\beta = \frac{gF^2}{64m^2l^5\omega^3\delta\omega^3}, \quad (2.6)$$

$\tilde{\nu}_N(\tau)$  is the rescaled noise, and the derivatives are with respect to  $\tau = \delta\omega t$ .

The steady state solution of Eqn. 2.4 can be obtained by setting  $\dot{B}(\tau) = 0$ , ignoring the noise and taking the modulus squared of both sides. This gives

$$|B|^2 \left( \frac{1}{\Omega} + \left( \frac{\zeta}{\Omega} - |B|^2 \right)^2 \right) = \beta \quad (2.7)$$

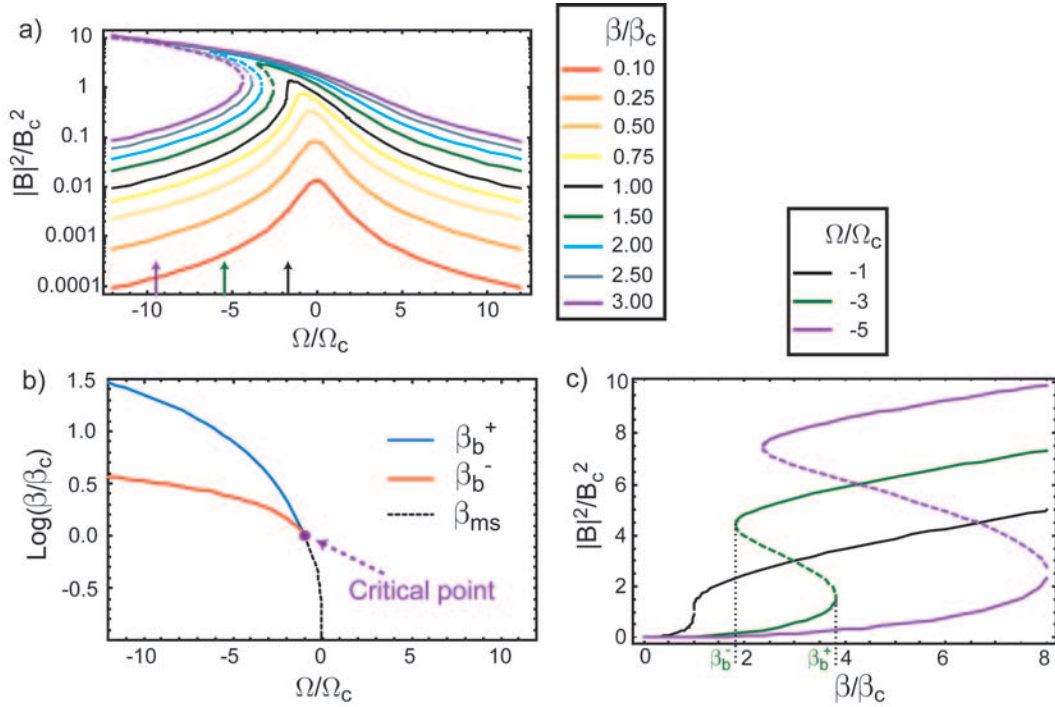


Figure 2.2: **(a)** Plot of the oscillation amplitude  $|B|^2$  normalized to the oscillation amplitude at the critical point  $B_c^2$  vs. reduced detuning  $\Omega$  normalized to the detuning at the critical point  $\Omega_c$ . Each curve corresponds to a different input power  $\beta$ , which is again normalized to the input power at the critical point  $\beta_c$ . The black curve corresponds to the critical input power  $\beta_c$ . The dashed part of each of the curves represents the unstable solution. **(b)** Upper (blue) and lower (red) bifurcation points  $\beta_b^+, \beta_b^-$  as a function of the normalized reduced detuning  $\Omega/\Omega_c$ . Also plotted is the line of maximum susceptibility  $\beta_{ms}(\Omega) = \frac{\partial B}{\partial \beta}$  (black dashed line) below the critical point. **(c)** Cuts of normalized oscillation amplitude  $|B|^2/B_c^2$  vs. normalized input power  $\beta/\beta_c$ . These cuts correspond to the arrows shown in (a). Again, the dashed parts of these curves represent the unstable solution.

The solutions of this equation are plotted in Fig. 2.2a, showing the dependence of the modulus squared of the dimensionless oscillation amplitude  $|B|^2$  on the reduced detuning  $\Omega$ . At low input powers  $\beta$ , we obtain the typical Lorentzian response of a resonator centered around the resonance frequency  $\omega_0$ . As we increase the input power  $\beta$ , the resonance frequency bends backwards due to the

non-linearity present in the system. After we reach the critical power  $\beta_c = \frac{8}{27}$  and critical detuning  $\Omega_c = \sqrt{3}$ , an overhang develops in the resonance curve, indicating that we now have three possible oscillating states. The dashed part of the resonance curve in Fig. 2.2a&c represents the unstable middle solution. The other two solutions illustrated in Fig. 2.2b represent two metastable oscillating states of the system and are given by

$$\beta_b^\mp = \frac{2}{27\Omega^3} (\zeta^3 + 9\zeta \mp (-3 + \zeta^2)^{3/2}). \quad (2.8)$$

As the input power  $\beta$  is ramped up at fixed frequency  $\nu$  (Fig. 2.2c), the system will switch from a low oscillation state to a high oscillation state at  $\beta_b^+$ . If the power is subsequently ramped down, the system will switch back from this state at  $\beta_b^-$ .

The behavior of the non-linear oscillator described above is universal and applies to any linear oscillator to which a cubic nonlinearity is added in any combination of the “position” coordinate and its derivatives. All such systems can be plotted on Fig. 2.2b without any fitting parameters. Only knowledge of the measured system parameters  $\omega_0, \Gamma$  and  $\beta_c$  is required. For example, a linear LRC oscillator, as shown in Fig. 2.3, will obey these equations if we add, for example, a non-linear element into the circuit, such as a non-linear inductor. As mentioned before, such a non-linearity is provided by the Josephson at low temperatures (see section 2.2).

### 2.1.2 Readout principle

The readout principle of the Duffing oscillator system is based on the measurement of the switching probability,  $P_{01}$ , of the oscillator from the low oscillation amplitude state to the high oscillation amplitude state. Any device which is cou-

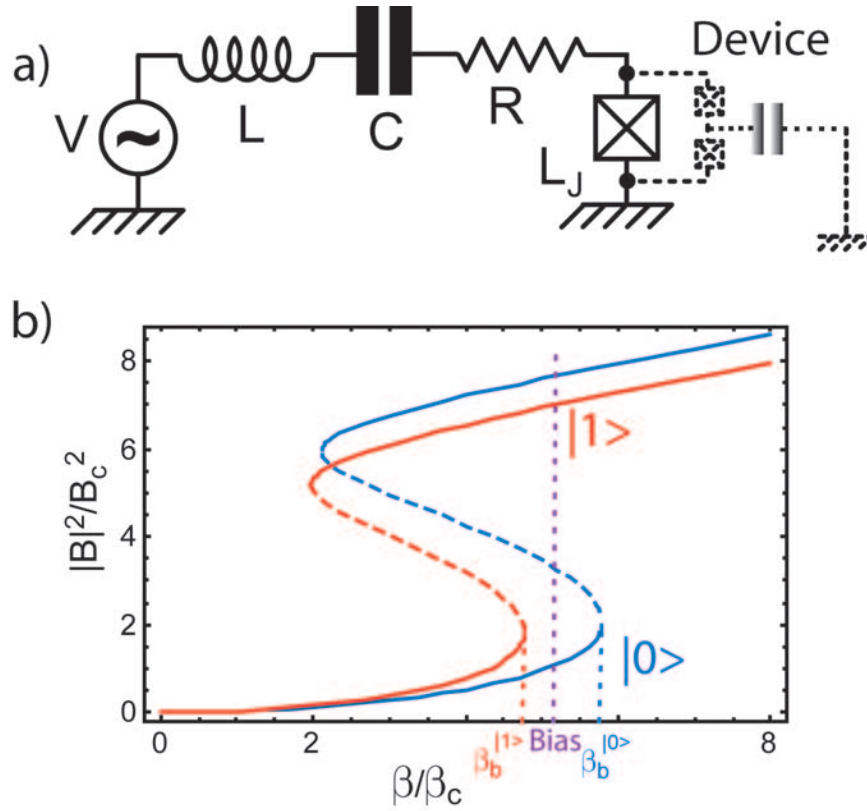


Figure 2.3: **(a)** Schematic of a series LRC circuit with a microwave drive  $V$ . The device to be measured (here illustrated as a qubit) must be coupled to a circuit element. **(b)** Cartoon of the oscillation amplitude  $B$  vs. drive power  $\beta$  of the non-linear series LRC circuit for two different states, say  $|0\rangle$  and  $|1\rangle$ , of the device being measured.  $B$  in this case is the slow amplitude of charge flowing through the LRC circuit and  $\beta$  can be related to the microwave drive power  $P = V^2$ . When measuring, the non-linear LRC oscillator is biased just below the bifurcation point  $\beta_b^+$ . Therefore, the non-linear oscillator can switch from the low oscillating state to the high oscillating state if the device we are measuring switches from state  $|0\rangle$  to state  $|1\rangle$ . Otherwise, if the device remains in  $|0\rangle$ , the LRC oscillator will remain in the low oscillating state.

pled to the oscillator's parameters can induce a variation in the switching point and, hence, large variations in the switching probability  $P_{01}$ . Note that this amplifier can also be operated in a continuous, reversible mode by biasing at low input powers, where the oscillator is linear.

A schematic showing an example of a device coupled to a series LRC non-linear oscillator is shown in Fig. 2.3a. In this case, the device is a SCPB qubit (see section 3.1) with energy states  $|0\rangle$  and  $|1\rangle$ . It is coupled to the junction of the oscillator by placing the junction in the superconducting loop of the SCPB, forming a circuit known as the Quantronium. This gives the oscillator two bifurcation powers  $\beta_b^{(0)}$  and  $\beta_b^{(1)} < \beta_b^{(0)}$ , depending on the state of the qubit,  $|0\rangle$  or  $|1\rangle$  (see Fig. 2.3b). The power  $\beta$  is quickly ramped to a level between  $\beta_b^{(0)}$  and  $\beta_b^{(1)}$  so that if the Quantronium qubit is in  $|1\rangle$ , the non-linear oscillator will switch to the high oscillating state, whereas if it is in  $|0\rangle$ , the non-linear oscillator will remain in the low oscillating state.

## 2.2 Implementations

As mentioned above, we wish to build a non-linear oscillator that is compatible with measuring a superconducting qubit at low temperatures. We achieve this by imbedding a Josephson junction into a well controlled resonant electromagnetic environment. All circuit elements are constructed from superconductors which are dissipation-free at low temperatures, and the non-linearity is provided by the non-linear inductance of the Josephson junction. There are many options available in constructing this resonant electromagnetic environment. We can use either lumped element capacitors and inductors and/or distributed element transmission line resonators. Our choice depends on ease of fabrication, control over spurious resonances, tunability of electromagnetic parameters and compatibility with the device to be measured (e.g., superconducting qubit). The lumped circuit elements must be much smaller than the characteristic wavelengths associated with the resonant circuit, otherwise problems may arise from radiation and par-

asitic resonances. Precise microwave engineering is required to understand these parasitics. In this regime, it is more convenient to use distributed element structures such as coplanar waveguides (CPW) or microstrip lines [81], which have well defined behavior without significant parasitics.

### 2.2.1 Josephson bifurcation amplifier

Our first attempt at implementing the non-linear oscillator involved constructing a parallel lumped element LC circuit, forming the so-called Josephson bifurcation amplifier (JBA), with the junction itself acting as the inductor  $L_J$ . The junction has a parallel plate capacitance,  $C_J$ , in parallel with  $L_J$ , with an associated resonance frequency of  $\omega_p/2\pi = 1/2\pi\sqrt{L_J C_J} \sim 20 - 100$  GHz (depending on the oxidation parameters of the junction). This frequency is too high to enable precise microwave engineering of the on-chip environment and external circuitry. By placing a capacitor in parallel with the junction, we can reduce this plasma frequency,  $\omega_p$ , to a more convenient lower frequency range. We typically aim for 1 – 2 GHz by using a 10 – 100 pF capacitor. In this frequency range, the circuit is still safely in the lumped element regime, resulting in a simple on-chip environment with minimum parasitic elements. Additionally, the microwave circuitry and hardware for this frequency range is well developed and readily available.

Figure 2.4 displays a schematic of the device. The oscillation state of the JBA is probed by measuring the phase difference  $\phi$  of the reflected microwave drive  $I_d \cos(\omega t)$ . Using Kirchoff's laws, we get the equation of motion for this circuit as

$$C_s \dot{V}_J(t) + \frac{V_J(t)}{R} + I_0 \sin(\delta(t)) = I_d \cos(\omega t) + I_N, \quad (2.9)$$

where  $V_J$  is the voltage across the Josephson junction,  $\delta(t)$  is the superconducting phase difference across the junction, and the current noise  $I_N$  produced by the

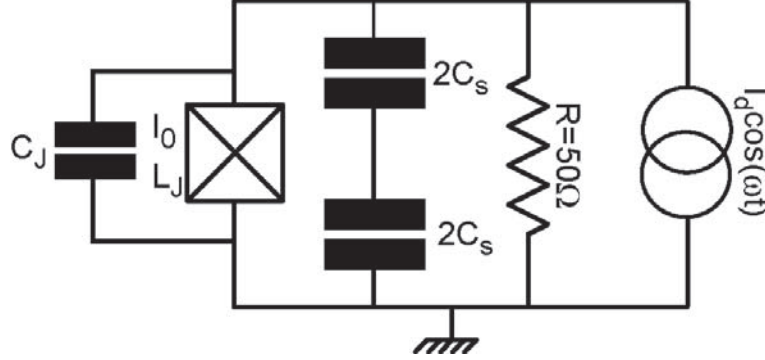


Figure 2.4: A schematic of a Josephson bifurcation amplifier (JBA) device. A lumped element capacitor of about  $C_s \sim 30$  pf is placed in parallel with the Josephson Junction to reduce the junction's resonance frequency to the 1 – 2 GHz range. This parallel LC implementation is known as the Josephson bifurcation amplifier (JBA). The state of the JBA is deduced from measuring the phase difference,  $\phi$ , of the reflected microwave drive.

resistance  $R$  obeys

$$\langle I_N(t)I_N(0) \rangle = \frac{2k_B T}{R} \delta(t). \quad (2.10)$$

From the Josephson relations (Eqn. 1.6), we know that  $V_J(t) = \phi_0 \dot{\delta}(t)$ , where  $\phi_0 = \frac{\hbar}{2e}$  is the reduced flux quantum. Hence, the JBA equation of motion becomes

$$\phi_0 C_s \ddot{\delta}(t) + \frac{\phi_0}{R} \dot{\delta}(t) + I_0 \sin(\delta(t)) = I_d \cos(\omega t) + I_N. \quad (2.11)$$

Taylor expanding the non-linear part of this equation,  $\sin(\delta(t))$ , for small  $\delta(t)$  and keeping only the first two terms, we obtain

$$\ddot{\delta}(t) + 2\Gamma \dot{\delta}(t) + \omega_p^2 \left( \delta - \frac{1}{3!} \delta^3 \right) = \frac{I_d}{C_s \phi_0} \cos(\omega t) + \frac{I_N}{C_s \phi_0}, \quad (2.12)$$

where  $\Gamma = 1/2RC_s$  is the linear resonance bandwidth, and  $\omega_p^2 = I_0/\phi_0 C_s$  is the junction plasma frequency. This equation has the same form as that for the driven, damped pendulum (see Eqn. 2.2). Following the same procedure as for the pendulum, we move to a rotating frame with  $\delta(t) = A(t)e^{i\omega t} + c.c.$  and re-scale. Again, averaging over the period  $2\pi/\omega$ , we get the reduced Duffing oscillator

equation

$$B(\dot{\tau}) + \left( \frac{1}{\Omega} - i + i |B(\tau)|^2 \right) B(\tau) = -i\sqrt{\beta} + \tilde{I}_N(\tau). \quad (2.13)$$

However, in this case we have the transformations

$$B(\tau) = \sqrt{\frac{\omega_p^2}{4\omega\Delta\omega}} A(\tau), \quad (2.14)$$

$$\beta = \frac{\omega_p^6 I_d^2}{64 I_0^2 \omega^3 \Delta \omega^3}, \quad (2.15)$$

with

$$\tau = \Delta\omega t, \quad \Delta\omega = \omega_p - \omega. \quad (2.16)$$

Similar to the pendulum case, the system bifurcates for detuning  $\Omega > \Omega_c = \sqrt{3}$  and input power  $\beta > \beta_c = 8/27$ . Furthermore, to observe bifurcation, the current through the junction at the critical point  $I_c$  must be less than the critical current  $I_0$  of the junction:

$$I_c \equiv \frac{4}{3^{1/4}} \sqrt{\frac{1}{Q} \frac{L_J}{L_T^p}} = \frac{4}{3^{1/4}} \sqrt{\frac{1}{p^p Q}} < I_0, \quad (2.17)$$

where  $L_T^p$  is the parallel sum of the effective inductance of the junction,  $L_J$ , and any stray inductance,  $L_p$ , in parallel with it

$$L_T^p = \frac{L_J L_p}{L_J + L_p}, \quad (2.18)$$

and  $p^p = \frac{L_T^p}{L_J}$  is the parallel participation ratio. The presence of a finite stray inductance shifts the current at the critical point upwards, causing the above condition to be violated. If this condition is violated and the RF current approaches  $I_0$ , the system becomes unstable and adopts a chaotic-like behavior. Even if the above inequality is obeyed, the system will eventually reach this chaotic region at sufficiently high input powers. In this region, the phase jumps randomly about an average of  $0^\circ$  and the junction adopts a measured AC resistance (see [79, 77] for more details).

### 2.2.2 Cavity bifurcation amplifier

Cavity bifurcation amplifier (CBA) refers to the implementation of the non-linear bifurcation amplifier that uses distributed element resonators. These distributed element resonators can be fabricated in many different geometries, including coplanar waveguides (CPW) or coupled striplines (CS) [81] (Fig. 2.5). These resonators have the advantages of not requiring the deposition of extra insulators and of having a simple two-dimensional structure. For the frequencies we are interested in, the behavior of these structures are well understood, with no stray capacitive or inductive elements. The resonance frequency  $\nu_0$  is determined only by the geometry of the resonator, and the quality factor  $Q$  is set by input and output capacitors,  $C_{in}$  and  $C_{out}$ . The coupled stripline resonators have the advantage that they can be quickly fabricated using e-beam lithography and be easily aligned with pre-fabricated on-chip structures (see section 4.4). On the other hand, CPW structures, which need photolithography to fabricate, have modes which are more easily launched and controlled. Also, since the CPW resonators have demonstrated internal  $Q$  values of up to  $10^6$  [82, 83], we began with this implementation.

The CPW consists of a narrow center conductor and two nearby ground planes, all of which are deposited as two dimensional films on a planar substrate. A Fabry-Perot like resonator is created by confining a length,  $2L$ , of the CPW using input and output coupling capacitors,  $C_{in}$  and  $C_{out}$ . These capacitors act as the Fabry-Perot cavity mirrors. The fundamental resonance frequency  $\nu_0$  is determined by the resonator length,  $2L = \lambda/2$ . To make this resonator non-linear, we place a Josephson junction in the center where it is maximally coupled to the resonator's fundamental mode, which has a current maximum at the resonator's center. The

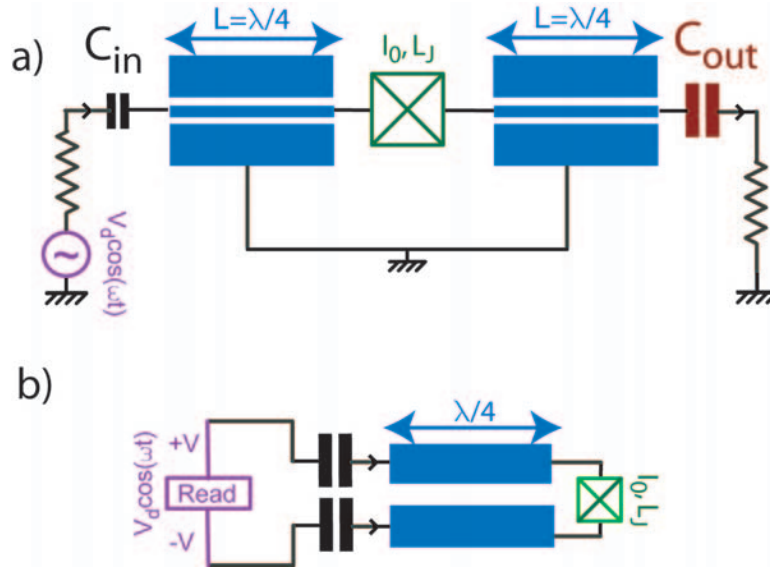


Figure 2.5: Schematics of the coplanar waveguide and coupled stripline (CS) implementations of the cavity bifurcation amplifier (CBA). The resonator length determines the resonance frequency  $\nu_0$ , and the coupling capacitors determine the device bandwidth  $\Gamma$ . In (a) we place the junction in the center of a  $\frac{\lambda}{2}$  co-planar waveguide resonator and measure both reflection and transmission. In (b) we place the junction at the end of a  $\frac{\lambda}{4}$  coupled stripline resonator (CS) and measure only in reflection.

junction's inductance will pull  $\nu_0$  to lower frequencies and can cause the system to bifurcate at sufficiently high input powers. By measuring the amplitude and phase of a transmitted microwave signal through the resonator, we can infer the oscillation state of the CBA.

To quantitatively describe the dynamics of this distributed element oscillator, we can model it as a lumped element series LRC circuit for frequencies near its fundamental resonance frequency,  $\nu_0$  (see Figs. 2.6 & 2.7). We will only model the behavior of the circuit near the fundamental resonance frequency,  $\nu_0$ , so only a single series LRC circuit is needed. More series LRC circuits can be added in parallel to model higher harmonics. The impedance seen by the series LRC

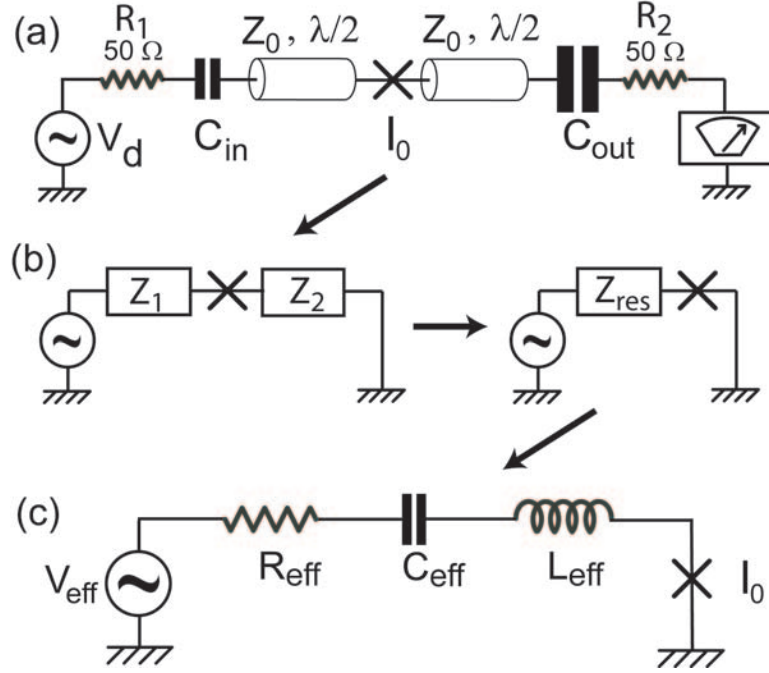


Figure 2.6: Circuit schematics illustrating the impedance modeling used in describing the dynamics of the CBA. **(a)** This is a schematic of the CPW CBA implementation. **(b)** The impedance seen by the junction in the resonator can be computed as the sum of impedances on the left and right hand sides of the junction  $Z_{res} = Z_1 + Z_2$ . **(c)** Near the fundamental resonance frequency,  $\nu_0$ , we map the junction's environment to a series LRC circuit. With this circuit we can model the dynamics of the system.

oscillator is

$$Z_{series} = R_{eff} + i\omega L_{eff} - \frac{i}{\omega C_{eff}}. \quad (2.19)$$

The impedance seen by the junction inside the  $\lambda/2$  resonator can be written as a sum of the impedances seen on the left-hand side of the circuit,  $Z_1$ , and the right-hand side,  $Z_2$  (see Fig. 2.6b). We choose our coordinate  $x$  along the transmission line such that the junction is placed at  $x = 0$  and the capacitors  $C_{in}$  and  $C_{out}$  are placed at  $|x| = L$ . Hence, the impedance seen by the junction on each side is given by

$$Z_{1(2)} = Z_0 \frac{e^{2ikL} - \Gamma_{1(2)}}{e^{2ikL} + \Gamma_{1(2)}}, \quad (2.20)$$

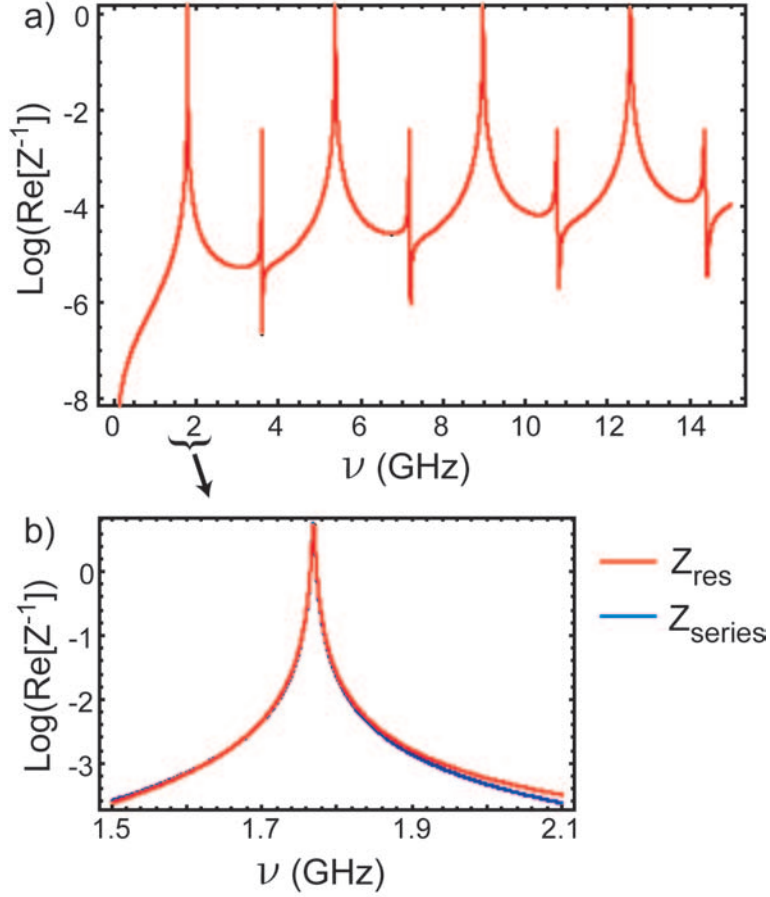


Figure 2.7: **(a)** Theoretical plot of the the real part of the inverse of the impedance seen by the junction in the center of a  $\lambda/2$  resonator (see Eqns. 2.20, 2.21). **(b)** Zoom in of (a) near the fundamental resonance frequency  $\nu_0$  with the impedance seen by the junction for the series circuit model for comparison (see Eqn. 2.19). The series circuit is a single mode model with values based on Eqns. 2.22. We get some disagreement between the two impedances for higher frequencies where the second harmonic begins to have some influence. The parameters of the resonator in these curves are  $\nu_0 = 1.8$  GHz,  $C_{in} = 7$  fF,  $C_{out} = 110$  fF and  $R_1 = R_2 = Z_0 = 50 \Omega$ . The series LRC fit has the parameters  $C_{eff} = 1.12$  pF,  $L_{eff} = 7.2$  nH and  $R_{eff} = 0.125 \Omega$ .

where  $Z_0 = 50 \Omega$ ,  $2kL = 2\frac{2\pi}{\lambda} \frac{\lambda_0}{4} = \pi \frac{\omega}{\omega_0}$ , and  $\Gamma_{1(2)} = \frac{Z_0 - Z_{L1(2)}}{Z_0 + Z_{L1(2)}}$ . The load impedance at each end of the CPW resonator is given by

$$Z_{L1(2)} = R_{in(out)} + \frac{1}{i\omega C_{in(out)}}. \quad (2.21)$$

The resulting impedance of the resonator  $Z_{res} = Z_1 + Z_2$  is plotted in Fig. 2.7 and compared with the matching impedance of a series LRC circuit  $Z_{series}$ . Good agreement is achieved only near the fundamental resonance frequency of the resonator, far from the higher harmonics which are not included in the model. Expanding Eqn. 2.20 we can make an analytical map between  $Z_{res}$  and  $Z_{series}$ . If we assume  $C_{in} \ll C_{out}$ , we obtain

$$\begin{aligned} V_{\text{eff}} &= Z_0 \omega_0 C_{in} V_d, & R_{\text{eff}} &= Z_0^2 R_L \omega_0^2 C_{out}^2, \\ L_{\text{eff}} &= \frac{Z_0}{4\omega_0/2\pi}, & C_{\text{eff}} &= \frac{1}{\pi^2 Z_0 \omega_0 / 2\pi}. \end{aligned} \quad (2.22)$$

The quality factor of a series LRC circuit is given by  $Q = 1/\omega_0 R_{\text{eff}} C_{\text{eff}}$ . Using Eqns. 2.22, we obtain

$$Q_{ext} = \frac{\pi}{2Z_0 R_L \omega_0^2 (C_{out}^2 + C_{in}^2)}, \quad (2.23)$$

which agrees with the quality factor calculated directly from a capacitively loaded resonator. In the limit  $C_{out} \gg C_{in}$ , we can tune  $Q$  simply by choosing an appropriate  $C_{out}$ . If there are internal losses in the cavity due to dielectrics or radiation, then the total quality factor of the resonator becomes

$$\frac{1}{Q} = \frac{1}{Q_{ext}} + \frac{1}{Q_{int}}, \quad (2.24)$$

where  $Q_{ext}$  is given by Eqn. 2.23 and  $Q_{int}$  is determined by the internal losses.

Hence, we can quantitatively study the dynamics of the CBA near  $\nu_0$  using this equivalent circuit. We begin by writing down the equation of motion using Kirchoff's laws:

$$L_{\text{eff}} \ddot{q}(t) + R_{\text{eff}} \dot{q}(t) + \frac{q(t)}{C_{\text{eff}}} + \phi_0 \dot{\delta}(t) = V_d \cos(\omega t) + V_N(t) \quad (2.25)$$

where  $q(t)$  is the charge on the capacitor and  $V_N(t)$  is the thermal noise produced by the resistor,  $\langle V_N(t) V_N(0) \rangle = 2k_B T R_{\text{eff}} \delta(t)$ . Using the Josephson relations

(Eqn. 1.6) for the voltage across a junction  $V(t) = \phi_0 \dot{\delta}(t)$  and the current through a junction  $\dot{q}(t) = I_0 \sin(\delta(t))$ , we obtain

$$\left( L_{\text{eff}} + \frac{L_J}{\sqrt{1 - \dot{q}^2/I_0^2}} \right) \ddot{q} + R_{\text{eff}} \dot{q} + \frac{q}{C_{\text{eff}}} = V_d \cos(\omega t) + V_N(t). \quad (2.26)$$

At first glance, this equation does not appear as if it behaves like a Duffing oscillator, because the non-linearity is contained in the  $\ddot{q}(t)$  term. However, in the weak non-linear regime and for the single harmonic approximation, the Duffing oscillator behavior is recovered. This is not a coincidence, because any cubic non-linearity added to a linear oscillator will obey the Duffing oscillator equation 2.13 in the weak non-linear limit. We begin by expanding the non-linearity to lowest order

$$\frac{1}{\sqrt{1 - \dot{q}^2/I_0^2}} \simeq 1 + \frac{\dot{q}^2}{2I_0^2}, \quad (2.27)$$

and then again make the rotating wave approximation:

$$q(t) = A(t)e^{i\omega t} + c.c., \quad (2.28)$$

where  $|\dot{A}/\omega A| \ll 1$ , keeping only first order terms in this quantity. Averaging over the period  $2\pi/\omega$  and re-scaling to dimensionless variables, we again obtain the Duffing oscillator equation 2.13.

$$B(\tau) + \left( \frac{1}{\Omega} - i + i|B(\tau)|^2 \right) B(\tau) = -i\sqrt{\beta} + \tilde{v}_N(\tau). \quad (2.29)$$

However, in this case, the slow amplitude dimensionless charge  $B(\tau)$  and dimensionless drive  $\beta$  are given by

$$B(\tau) = \frac{A(\tau)\omega}{I_0} \sqrt{\frac{1}{2\Omega\epsilon^2}}, \quad (2.30)$$

$$\beta = \frac{V_d^2}{\phi_0^2 \omega^2} \left( \frac{1}{2\Omega\epsilon^2} \right)^3, \quad (2.31)$$

where  $\tau = t\delta\omega = t(\omega_0 - \omega_d)$  is the dimensionless time,  $\Omega = \delta\omega/\Gamma$  is the dimensionless detuning,  $\epsilon = \sqrt{\frac{L_T}{L_J} \frac{1}{Q}}$  and  $L_T = L_{\text{eff}} + L_J$  is the total inductance. The correlation function of the noise is now given by

$$\begin{aligned}\langle \tilde{v}_N(\tau) \tilde{v}_N^\dagger(0) \rangle &= \frac{k_B T}{E_J} \left( \frac{L_J}{L_T} \right)^2 \frac{Q}{2\Omega^2} \delta(\tau), \\ \langle \tilde{v}_N(\tau) \tilde{v}_N(0) \rangle &= 0.\end{aligned}\tag{2.32}$$

Similar to the JBA implementation, the RF current through the junction must not exceed the junction's critical current,  $I_0$ , or the dynamics will become chaotic. In other words, the current through the junction at the critical point must be lower than  $I_0$  to observe a clean bifurcation:

$$I_c = 2|A_c|\omega = 2I_0 \sqrt{2\Omega_c \frac{L_T}{L_J} \frac{1}{Q}} |B_c| < I_0,\tag{2.33}$$

or, equivalently,

$$\frac{4}{3^{1/4}} \sqrt{\frac{L_T}{L_J} \frac{1}{Q}} = \frac{4}{3^{1/4}} \sqrt{\frac{1}{pQ}} < 1\tag{2.33'}$$

where  $p = \frac{L_J}{L_T}$  is the series participation ratio. When  $p$  is reduced,  $Q$  needs to be increased, decreasing the operation speed of the CBA. When measuring a system with a finite lifetime, such as a qubit,  $Q$  must be as low as possible in order to measure the system before it decays. Both the JBA and CBA have been implemented in our experiments. Each design has its own advantages and disadvantages. So the question arises - which is the most useful and versatile? To begin this discussion, in the next section I will describe how these two devices are fabricated, along with their range of operating parameters.

## 2.3 JBA lumped element fabrication

The JBA is made from lumped elements and with the use of microfabrication we can make its circuit elements much smaller than the wavelength at  $\omega_0$  to reduce

any parasitics (for schematic, see Fig. 2.4). The JBA parallel LC circuit is made by shunting a large Josephson junction (which acts as the inductor  $L_J$ ) with a parallel plate capacitor  $C_s$ . A Cu plane, used as the bottom electrode of  $C_s$ , is fabricated first and is then followed by the capacitor's insulator, which is deposited everywhere on-chip. In a subsequent layer, both the top electrodes of  $C_s$  and the junction are fabricated together.

### 2.3.1 Cu ground plane fabrication

First, a bilayer of resist is spun on a full two-inch low resistivity Si wafer. At least  $1\ \mu\text{m}$  of MMA is spun, followed by 200 nm of PMMA. This resist is used to fabricate the Cu ground planes for the bottom electrode of the capacitor  $C_s$ . About 30 rectangular ground planes, each  $500\ \mu\text{m}$  by 1 mm in size, are then written on the full two-inch wafer using an SEM. After developing, the chip is placed into an e-beam evaporator. Similar to the lift-off process used in making the Al CPW resonators (see section 2.4.1), the stage is rotated at about  $10^\circ\ \text{sec}^{-1}$  and tilted to about  $5^\circ$  during the Cu evaporation to ensure a good sloped edge profile. About 500 – 1000 nm of Cu is deposited to reduce stray inductance in the Cu plane and dissipation. To ensure the thick plane of Cu adheres to the Si substrate without peeling off during the following lift-off procedure, a thin Cr sticking layer is deposited between the Si and Cu layers.

### 2.3.2 Capacitor and junction fabrication

After fabricating the Cu ground planes, we next deposit the insulator  $\text{Si}_3\text{N}_4$  over them using plasma enhanced chemical vapor deposition (PECVD). During this process, the wafer is heated to  $400\ ^\circ\text{C}$ , causing the substrate to outgas and create bubbles in the Cu ground plane, if no precautions are taken. A Cr sticking layer

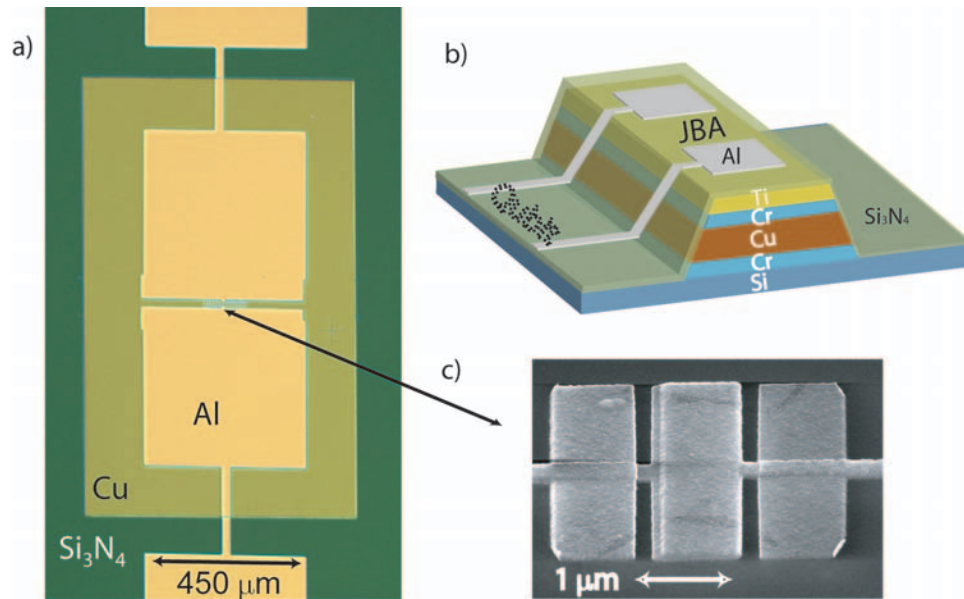


Figure 2.8: **(a)** Optical image of a complete JBA device. The junction is placed in the center of the copper ground plane and the bonding pads are placed off to the side of the capacitor so that the wirebonder doesn't damage the capacitors. **(b)** Cartoon of capacitor structure. In a qubit device, the quantum dot is placed off to the side of the ground plane. In a JBA device with no qubit, the junction is placed in the middle of the ground plane. **(c)** SEM image of Josephson junction in center of JBA device

below the Cu and a second Cr layer on top of the Cu are used to prevent the outgassing from damaging the surface of the Cu. Furthermore,  $\text{Si}_3\text{N}_4$  does not adhere well to Cu or Cr and therefore an extra sticking layer of Ti is added on top. About 200 nm of  $\text{Si}_3\text{N}_4$  is deposited, giving about  $0.3 \text{ fF}/\mu\text{m}^2$ . Finally, a new bilayer of e-beam resist is spun onto the full two-inch wafer for fabricating the Josephson junction with e-beam lithography. The wafer is manually diced into chips of about 5 mm by 5 mm in size, each with a single ground plane. The top electrodes of  $C_s$  and the bonding pads are then deposited along with the junction.

The Josephson junctions have critical currents,  $I_0$ , in the  $\mu\text{A}$  range. The intrinsic plasma frequencies are determined by the parallel combination of the

pure Josephson element and the junction capacitance  $C_J$ , and are typically in the range 20 – 100 GHz. The plasma frequency can only be adjusted by changing the oxidation pressure and time during the junction evaporation.

## 2.4 CBA fabrication

The first step in making a CBA device involves fabricating the CPW resonators with photolithography. The resonator design can either be etched into a pre-deposited superconductor or the pattern can be lifted-off using a shadow mask. The method chosen depends on which superconducting material is desired for the resonator. In either case, photolithography is used to define the resonator's design on a full two-inch wafer which is subsequently diced. The junction is then fabricated using e-beam lithography, one chip at a time.

### 2.4.1 Resonator lift-off process

Al resonators are typically fabricated using a shadow mask lift-off process. A bilayer of optical resist is used as the mask, through which we evaporate the Al. Nb resonators cannot be fabricated in this manner because the resist is baked during deposition due to the high evaporation temperature of Nb. This causes the resist to outgas and to contaminate the Nb film, decreasing its superconducting transition temperature. LOR5A is used as the bottom layer (400 nm thick) and S1808 as the top layer (800 nm thick) (Fig. 2.9a). We use a bilayer to prevent flagging on the edge of the deposited films. Hard contact mode is used during U.V. exposure to obtain a vertical profile in the S1808 resist layer. The optical mask must be extremely clean for this exposure mode to prevent interference fringes appearing on the edges of the pattern. After exposure, we develop in an ammonium hydroxide solution, typically MF319, for about 2 min until at least

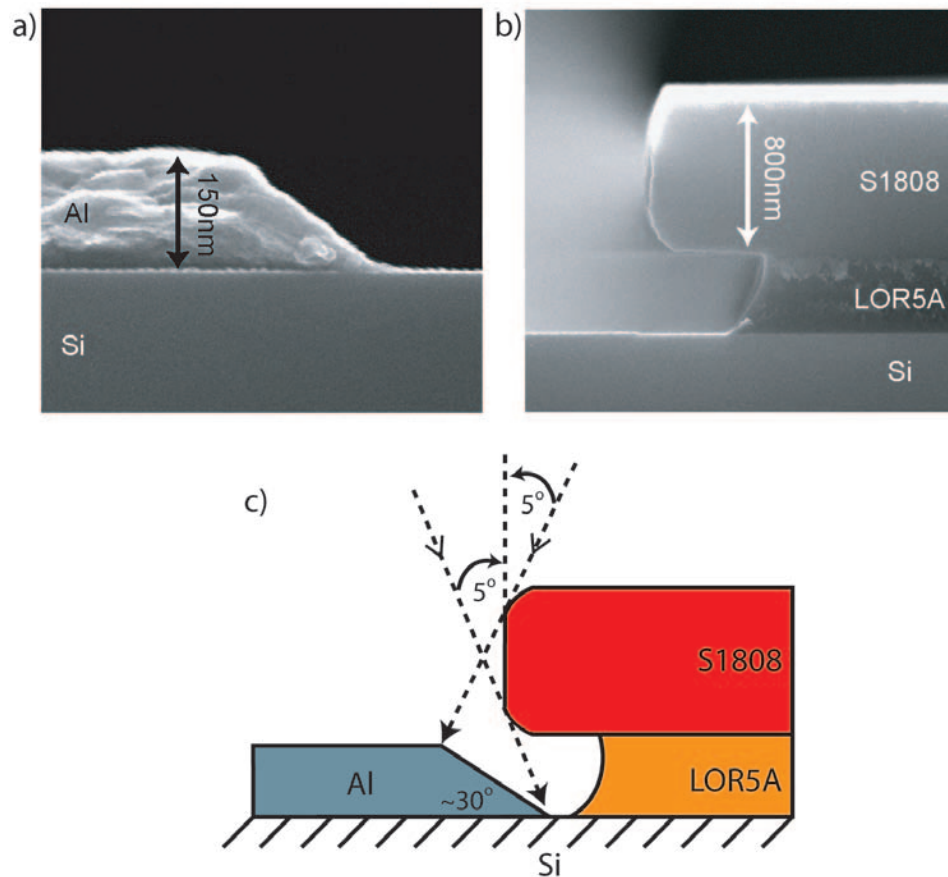


Figure 2.9: (a) SEM image of resist profile used in the CPW fabrication. The undercut is needed to get the sloped Al edge. (b) SEM image of the resultant Al edge after evaporation at  $5^\circ$  and with a substrate rotation of  $10^\circ/\text{sec}$ . In this case we have an edge slope of  $30^\circ$ . (c) Cartoon of the evaporation process which leads to sloped Al edge.

100 nm of undercut is obtained under the S1808 layer. The LOR5A layer is insensitive to optical exposure, but is continuously dissolved by the developer. Hence, the amount of undercut obtained only depends on the development time. After development, the wafer is washed in de-ionised water for about a minute and then air-blown dried.

Next, the full wafer is placed in an e-beam evaporator. To ensure a sloped edge on the Al film is obtained, as shown in Fig. 2.9b, the stage is rotated at about

$10^\circ\text{s}^{-1}$  and tilted to about  $5^\circ$  during the Al evaporation. Fig. 2.9c illustrates the process involved in getting the resulting  $30^\circ$  profile of the Al film. This detail ensures a clean and continuous contact between this resonator and any subsequent fabrication layers. After evaporation, lift-off is done using NMP at about  $100^\circ\text{C}$  for around half an hour. Finally, the finished resonators are cleaned with methanol.

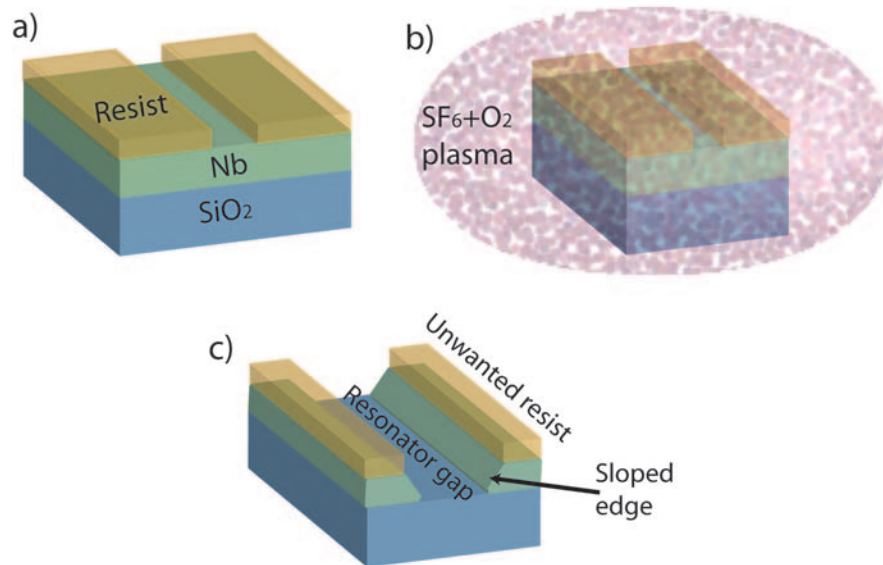


Figure 2.10: Cartoon of the CPW resonator fabrication using RIE etching. A plasma of  $\text{SF}_6$  is typically used to etch the Nb film. In order to get sloped edges we use  $\text{O}_2$  in the plasma which slowly etches back the resist (Note, oxygen should be avoided if high  $Q$  resonators are required). **(a)** S1808 is spun on and baked at  $115^\circ\text{C}$  for 1 min. We then optically expose the sample and develop in MF319. **(b)** The sample is etched in an  $\text{SF}_6$  and  $\text{O}_2$  plasma in an RIE. **(c)** Cartoon of the resulting sloped profile with remaining resist that is finally removed with NMP.

## 2.4.2 Resonator etching process

The main steps involved in fabricating the CBA resonators using the etching process are shown in Fig. 2.10. We begin with a new, clean substrate of either Si,  $\text{SiO}_2$  or Sapphire ( $\text{Al}_2\text{O}_3$ ) and deposit the desired metal over the full 2 inch

wafer. Then we spin on a single layer of photoresist and expose the resonator pattern. Contrary to the pattern exposed for the lift-off process, we expose the resonator gaps where we do not want any metal in the finished sample. After development, the wafer is placed into a reactive ion etcher (RIE) and the metal under the previously exposed resist is etched away using an appropriate plasma. Oxygen can be added to the plasma to also etch the resist (Note, oxygen should be avoided if high  $Q$  resonators are required). As the etching process continues, the resist is etched back from the edges of the pattern, resulting in a sloped edge profile on the metal films. When the etching is completed, the wafer is placed into NMP to remove the remaining photoresist, leaving a full wafer of etched resonators.

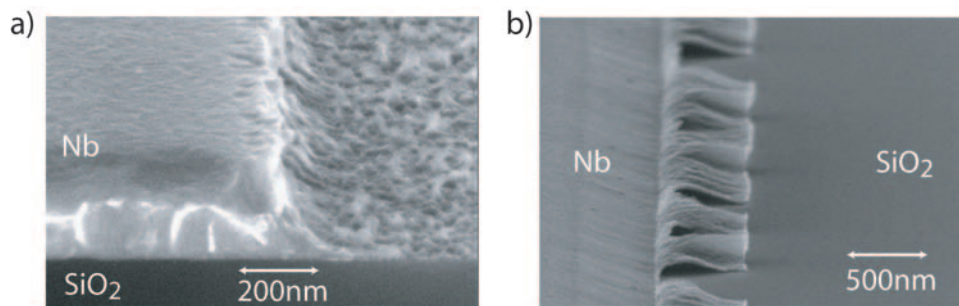
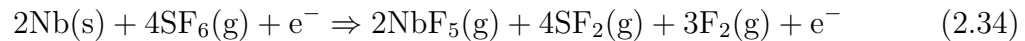


Figure 2.11: SEM images of some typical problems encountered in resonator fabrication. **(a)** During the Nb etching process, the etched metal can become redeposited and can then cause inhomogeneous etching of the film. This results in an uneven, bumpy, substrate after etching which is unsuitable for junction fabrication. To avoid this problem, Ar gas is used in the plasma to help suck out the etched products. **(b)** If Nb is sputtered through a lift-off mask the Nb covers the walls of the resist. Then, after lift-off this Nb sticks to the substrate and falls back, forming flags. These flags can also break loose during sonication, leaving a rough edge behind.

Etching the resonators has several advantages over the lift-off process. First, the metal is deposited on a clean wafer with no previous fabrication steps. In the lift-off process there could be residual resist left on the substrate after exposure.

Also, during the deposition in the lift-off process, the resist can outgas and contaminate the metal. Sputtering the metal through the mask avoids this problem; however, sputtering is non-directional and flags are obtained on the edges of the sputtered film, as shown in Fig. 2.11b. During the etching process, one must be careful to avoid redeposition of etched materials. The area where the material is redeposited is etched more slowly, and hence, the exposed substrate can become bumpy and can even have grass like structures (Fig. 2.11a). To avoid this problem, another gas such as Ar is added to the plasma to help remove the etched products in its flow stream.

Nb is typically etched by  $\text{SF}_6$  and follows the reaction



However,  $\text{SF}_6$  also etches Si and makes it difficult to stop at the correct point

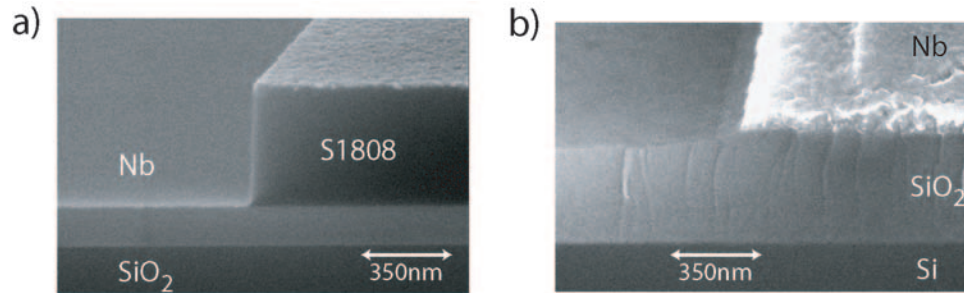


Figure 2.12: **(a)** S1808 resist profile on  $\text{SiO}_2$ . Typically we spin S1808 at about 4000 rpm to get  $\sim 800$  nm thickness. **(b)** Resultant slope profile for Nb on  $\text{SiO}_2$ . This sample was etched in a  $\text{CF}_4$ , Ar and  $\text{O}_2$  plasma. This plasma also etches the substrate and so, in this case, we have etched  $\sim 30$  nm into the substrate.

when using Si as the substrate.  $\text{SiO}_2$  has a better selectivity with respect to Nb than Si, so we initially used this substrate for the etched resonators. Figure 2.12 shows the S1808 resist used in this process along with the resulting Nb profile after lift-off. Note that in this case, we etched about 30 nm into the substrate, but since

the surface is flat, we can fabricate Josephson junctions on it (see sections 1.2.1 and 1.3.1). Sapphire is not etched at all by  $\text{SF}_6$ , which allows us to over-etch when using this substrate to ensure a smooth, clean surface.

### 2.4.3 Finished CBA resonator and junction fabrication

An optical image of an example of a finished resonator is shown in Fig. 2.13. This resonator has been etched out of Nb on  $\text{SiO}_2$ . The chip size is 10 mm by 3 mm with a 300  $\mu\text{m}$  thick substrate. The center pin of the CPW resonator shrinks down to a 10  $\mu\text{m}$  width, with a gap of 5.3  $\mu\text{m}$  to the ground planes in order to achieve an impedance  $Z_0 = 50 \Omega$ . The length of the resonator between the input capacitor  $C_{in}$  and output capacitor  $C_{out}$  determines the resonance frequency  $\nu_0$ . Hence, the resonator has to be meandered to attain a resonance frequency of about 2 GHz, whereas for  $\omega_0 = 2\pi \cdot 10 \text{ GHz}$ , a simple straight line is needed between  $C_{in}$  and  $C_{out}$ . The input and output capacitors  $C_{in}$  and  $C_{out}$  are 2-dimensional finger capacitors which interrupt the center pin of the CPW.  $C_{in}$  is usually around 1 – 7 fF and sets the input voltage,  $V_c$ , at the critical point via the equation

$$V_c = \frac{8}{3^{3/4}} \left( \frac{\omega_0 - \Gamma\Omega}{\omega_0} \right) \left( \frac{L_T}{L_J Q} \right)^{3/4} \frac{\phi_0}{Z_0 C_{in}} \quad (2.35)$$

$C_{out}$  determines the quality factor,  $Q$ , of the resonator (see Eqn. 2.23). Typically we choose a  $C_{out}$  of about 30 fF, so that for a linear resonance frequency of  $\omega_0/2\pi \sim 10 \text{ GHz}$ , we have a  $Q$  of a few hundred (see table 2.1).

$\nu_0$ (GHz)	$C_{in}$ (fF)	$C_{out}$ (fF)	$P_c = V_c^2/50\Omega$ (dBm)
1.8293	2	45	-87.5
1.8177	1.6	56	-76.5
10.154	2.3	13	-80.5

Table 2.1: Examples of resonator's coupling capacitors and corresponding critical powers

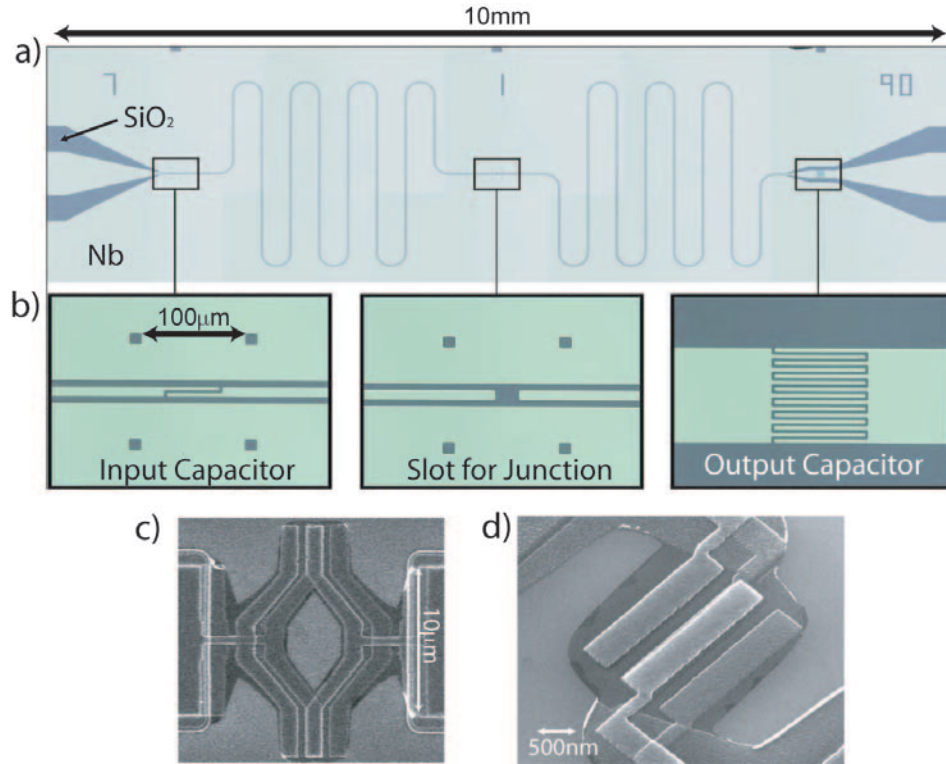


Figure 2.13: **(a)** Optical image of a 2 GHz Nb resonator on SiO<sub>2</sub>. **(b)** Zoom in of the input capacitor, the gap at the center for the junction, and the output capacitor. The four holes in the Nb ground plane is used for alignment purposes in subsequent e-beam fabrication steps. **(c)** SEM image of a SQUID which is placed in the center gap of the resonator. Contact is made between the SQUID and the resonator using 2 min of Ar ion milling. **(d)** SEM image of single junction which is also placed in the center of the resonator. The picture has a viewing angle of 35°

A 20 μm gap is left in the center of the resonator to place the Josephson junction or SQUID. A SQUID geometry is chosen if we wish to vary the junction inductance  $L_J$  with an external magnetic field. After aligning to the gap in the center pin using four holes in the Nb ground planes (see Fig. 2.13b), we use the Dolan bridge double angle evaporation technique to make the junction (section 1.3.1). With a hollow cathode Ar ion gun, we make an ohmic contact between the e-beam layer and the resonator.

The size of the junction will determine the amount of non-linearity present in the CBA. If the junction is too small, the voltage at which the critical point occurs will be very small (Eqn. 2.35) and hence we would have small signal to noise ratio. However, the junction cannot be too large either because, in order to see bistability, the RF current through the junction at the critical point must be less than the critical current of the junction (see Eqn. 2.33). This places a limitation on the Josephson inductance  $L_J$  that is given by

$$L_J \gg 10 \frac{L_T}{Q} \quad (2.36)$$

If the junction is too large, the system becomes chaotic before bistability occurs.

#### 2.4.4 Comparison of JBA and CBA implementations

From the point of view of fabrication, both implementations of the bifurcation amplifier have advantages and disadvantages. The JBA has the advantage that it can be completely fabricated using e-beam lithography and one does not have to worry about precise alignment between different layers. Also, the chip size is completely up to the experimenter and dicing is easy and can be done manually using just tweezers. The CBA on the other hand, needs photolithography in order to fabricate the large resonators, which then require precise alignment with the wafers crystal axis to facilitate dicing. Dicing also needs to be accurate and requires the use of a dicing saw or a precise scribe. Nonetheless, the resonator's structure is much simpler than the complicated thick Cu ground plane of the JBA which incorporates sticking and protection layers along with a  $\text{Si}_3\text{N}_4$  insulating layer. Once the resonators are fabricated, although precise alignment is needed, junction fabrication is very easy.

The JBA and CBA have different parameter ranges in which they are most

easily implemented. Overall the CBA is more tunable. The  $Q$  depends mainly on  $C_{out}$  and the length of the resonator between  $C_{in}$  and  $C_{out}$  determines  $\omega_0$ . Also, with the distributed element CPW resonator, no stray environmental parasitic elements are present. The CBA has been implemented with  $Q = 160 - 2000$  and  $\nu_0 = \omega_0/2\pi = 1.7 - 10.1$  GHz. In contrast, the JBA has the advantage that low  $Q$ 's are more easily attainable, whereas high  $Q$  values are difficult to construct. However,  $\omega_0$  is constrained to a low frequency range where the circuit elements remain in the lumped element regime with simple microwave behavior. More precise microwave engineering is needed for larger frequencies (such as in the CBA). The presence of stray inductance and resistance in the Cu ground plane will alter the behavior of the system. The stray inductance will shift the RF current at the critical point higher in power, bringing the system closer to the chaotic region. Furthermore, any stray resistance in the ground plane will reduce the phase shift of the reflected microwave signal from the expected  $360^\circ$ . To avoid these two effects, the Cu ground plane is made very thick, about  $1 \mu\text{m}$ , resulting in complications in further fabrication steps due to inhomogeneous resist height and strain in the resist at the edge of the ground plane where the qubits will be fabricated.

## 2.5 CBA - Experimental demonstration of bistability

Considering the CBA's ease of fabrication, greater range of operating parameters and future multiplexing possibilities, I have decided to concentrate on this implementation for the remainder of this thesis. Hence, I will begin with a description of the measurements characterizing the CBA's behavior and I will discuss its agree-

ment with the above Duffing oscillator bifurcation theory. Also, I will characterize its ability to discriminate small changes in the readout junction's inductance,  $L_J$ , in order to evaluate its amplification capabilities. For future reference, I list all the measured CBA devices (with no qubit yet - see chapter 3) in Table 2.2.

Label	Name	Type	$\omega_0$ (GHz)	$2\Gamma$ (MHz)	Q	$I_0$ ( $\mu\text{A}$ )	$\frac{L_J}{L_T}$
1	7-1-110	Single J.J.	1.8293	0.8	2286	1.3	0.03
2	1-1-140	SQUID	1.8177	1.28	1398	1.6	0.03
3	7-1-90	Single J.J.	1.7235	1.43	1200	0.3	0.13
4a	5-10-15	Muti- plexed SQUID	10.370	8.69	1193	5	0.07
4b	-0-1		10.154	11.71	867	5	0.06
4c			9.928	10.60	936	5	0.05
4d			9.690	11.7	828	5	0.05
4e			9.456	8.42	1123	5	0.05
5a	5-10-20	Muti- plexed SQUID	10.059	14.58	690	6.3	0.04
5b	-1-0		9.847	-	-	6.3	0.04
5c			9.625	-	-	6.3	0.06
5d			9.395	-	-	6.3	0.06
5e			8.93	14.60	612	6.3	-
6	1-1-30	SQUID	9.5872	20.12	436	3.4	0.07

Table 2.2: Summary of CBA samples measured

Resonators with resonance frequencies in the range  $\nu_0 \sim 2-10$  GHz and quality factors of  $Q \sim 400 - 2300$  were measured, which included four single resonator CBA devices (samples 1, 2, 3 and 6) and two chips with five multiplexed resonators (samples 4 and 5) (see section 4.1).

### 2.5.1 Experimental setup

Most of the CBA experiments were carried out in an Oxford Heliox pumped  $^3\text{He}$  refrigerator with a base temperature of 220 mK. Only sample 3 was measured in a dilution refrigerator with a base temperature of 12 mK (see [84] for a good review of low temperature techniques). Nevertheless, the same basic measurement setup was used for all experiments, an example of which is shown in Fig. 2.15. The

sample is mounted in a Cu box with a CPW printed circuit board (PCB) launch (see Fig. 2.14). The CPW PCB has vias built into the ground planes to connect them to the common ground of the Cu box. These ground connections help to damp out any spurious resonance modes. The PCB also has a slot cut out of its center to fit the sample chip, which has a size of 10 mm by 3 mm. After sticking

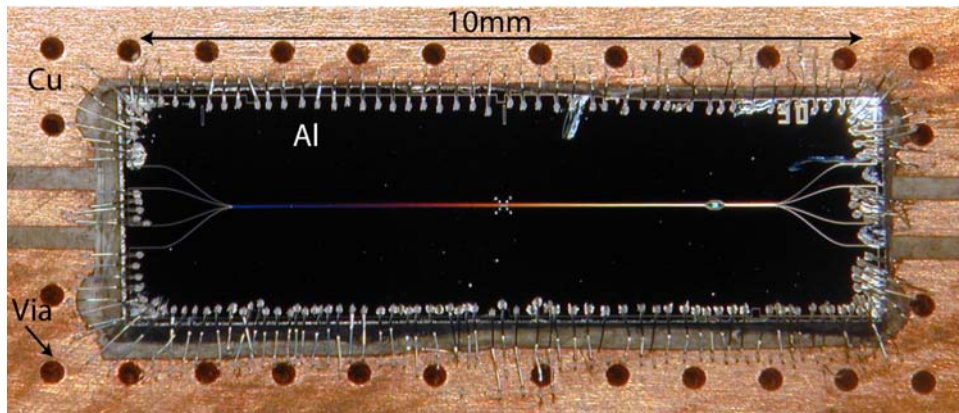


Figure 2.14: Optical image of a 10 GHz resonator mounted into the sample box. The chip is held down using “G-varnish” in a slot in the PCB on which a Cu CPW launch is pre-fabricated.

down the chip with some “G-varnish” (GE 7031), we wirebond the sample to the Cu PCB using as many bonds as possible (see Fig. 2.14) to reduce any stray series inductance and to again damp out any spurious resonances. The resonator itself was initially tested using Nb resonators with no junctions (or gap) by simply dunking the mounted sample into a dewar of liquid helium. Since the transition temperature of Nb is  $T_c = 9$  K, we can characterize the bare resonators in liquid helium without the time consuming step of cooling to the base temperature of a refrigerator. After finding a resonator with the desired fundamental frequency  $\nu_0$  and quality factor  $Q$ , we can choose an equivalent resonator with a gap in which we fabricate the CBA’s junction.

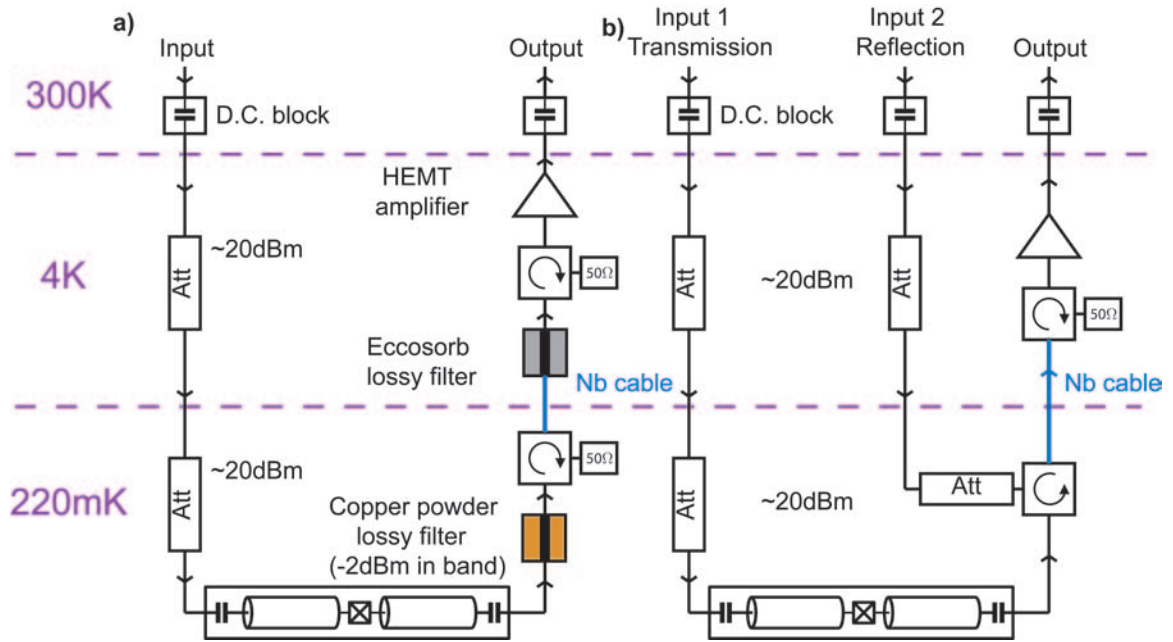


Figure 2.15: (a) A typical Heliox fridge setup used for the measurement of a 2 GHz CBA sample. Large attenuation is placed on the input line to avoid excess noise affecting the sample from warmer temperature stages. Isolators are placed on the output side to protect from in-band noise, while lossy transmission line filters are used to reduce out of band noise. In addition, a Nb cable is used to bridge the 4 K and 220 mK stage. At 4 K we have a cold HEMT amplifier with a noise temperature of around 10 K. (a) Typical fridge setup used for measurement of a 10 GHz CBA sample. We couldn't fabricate lossy filters in this frequency range to filter out of band noise. We added an extra input line on the  $C_{out}$  side to perform reflection measurements along with transmission measurements.

## RF lines

A typical measurement setup is shown in Fig. 2.15 for both a 2 GHz and a 10 GHz resonator experiment. Thermal white noise coming down the microwave lines from higher temperature stages could limit the ultimate sensitivity of the CBA, necessitating sufficient filtering on both the input and output lines. On the input lines we can simply use attenuators which are anchored to each temperature stage. The amount of attenuation we can use is only limited by the amount of avail-

able power we have at the top of the fridge. The attenuation,  $Att$ , will produce thermal noise at the temperature to which is anchored, with a voltage spectral density  $S_V(\omega) = 2k_B RT$ , with  $R = 50 \Omega$ . However, this attenuation will also reduce the effective noise temperature  $T_{\text{eff}}$  from higher temperature stages by a factor of  $Att$ . We cannot use this simple method on the output lines because we would also attenuate our signal of interest. Ideally, we would like to attenuate all signals outside our measurement band. This can be done using commercial bandpass LC filters. However, at higher frequencies such lumped element filters develop resonances and cease to be effective. As a result, we have developed lossy RF bandpass filters to eliminate higher frequency modes. They consist of a transmission line on a lossy dielectric made up of either a copper powder suspension or a microwave absorber called Eccosorb. In-band, these filters have a characteristic impedance of  $50 \Omega$  and can easily transmit our signal. At higher frequencies they are very lossy, eliminating higher frequency noise. These filters were only fabricated for the low frequency resonators  $\sim 2$  GHz and hence the resonators near  $\sim 10$  GHz had a larger  $T_{\text{eff}}$  (see section 2.6.2). To increase the cutoff frequency of these filters to 10 GHz, we would need to make them 5 times shorter which proved impossible with the current design, hence, alternative designs are currently being investigated (see Appendix B).

In-band filtering without attenuation is provided by circulators. These are a three-port devices which allow microwave transmission in one direction only (e.g., clockwise). They achieve this by using a ferrite material to break time reversal symmetry. The sample is only subject to the noise coming from a thermalized  $50 \Omega$  resistor on the third port of the circulator, while the noise coming down the line from higher temperatures goes straight to into the same  $50 \Omega$ . About 20 dB isolation can be obtained between the sample and the noisy lines, and can

be improved by placing multiple circulators in series.

Amplification at low temperatures is done using low noise HEMT (high electron mobility transistor) amplifiers, which are typically anchored to the 4 K stage. These amplifiers are made from a two dimensional electron gas heterostructure. The electrons in this layer have high mobility due to the low density of impurities and hence these amplifiers have higher gains and lower noise compared with conventional FET transistor based amplifiers. The noise temperature of these amplifiers is filtered using the circulators mentioned above. In addition to this filtering, we need thermal isolation between the amplifier and the sample. This is achieved using a superconducting Nb cable which has small thermal conductance but great electrical conductance so that none of the signal is lost before amplification.

All the temperature stages need to be sufficiently thermally isolated from each other to ensure the efficient operation of the fridge. Hence stainless steel cables are used to bridge different temperature stages on the input lines and either superconducting or stainless steel cables are used on the output lines. The center pin of these cables needs to be well thermalized at each temperature stage by using either attenuators or circulators.

### 2.5.2 Phase diagram

The first step of this experiment is to characterize the average transmission properties of the resonator [76] in order to determine whether it follows Duffing oscillator physics and to extract the CBA resonator parameters such as  $\omega_0$  and  $Q$ . We input a continuous microwave signal and measure the transmitted amplitude  $P_{out}$  and phase difference  $\phi$  as a function of input frequency  $\nu$  using a vector network analyser. Note that this instrument can only sweep  $\nu$  upwards and does not probe

the device's hysteresis (see later for hysteresis method). For a linear resonator, we expect a lorentzian lineshape for the transmitted amplitude with  $Q$  given by Eqn. 2.23 and with scattering matrix  $S_{21} = \frac{V_{out}}{V_{in}}$  given by [81], [85]

$$S_{21} = \frac{T}{1 - i \frac{2(\omega - \omega'_0)}{\kappa_{in} + \kappa_{out}}}, \quad (2.37)$$

where the input/output coupling,  $\kappa_{in/out}$ , is given by  $\kappa_{in/out} = \frac{2}{\pi} \omega^2 C_{in/out}^2 Z_0^2 \omega'_0$  and the transmission on resonance,  $T$ , is given by  $T = \frac{2\sqrt{\kappa_{in}\kappa_{out}}}{\kappa_{in} + \kappa_{out}}$ .  $S_{21}$  has a peak at the resonance frequency  $\omega = \omega'_0$ , which is slightly shifted to frequencies lower than the  $\lambda/2$  fundamental resonance frequency  $\omega_0$  by  $C_{in}$  and  $C_{out}$  via the equation  $\omega'_0 = \omega_0(1 - \omega Z_0(C_{in} - C_{out}))$ . When the resonator has symmetric input and output capacitors  $C_{in} = C_{out}$ , it attains unity transmission,  $T = 1$ , on resonance. Typically we have  $C_{out} \gg C_{in}$  which causes some of the input power to be reflected and hence reduces the transmission on resonance. Along with this transmitted amplitude there is also an associated phase change,  $\phi$ , of the transmitted microwave signal near  $\omega_0$  which is given by

$$\phi = \arctan\left(\frac{\text{Im}(S_{21})}{\text{Re}(S_{21})}\right) = \arctan\left(\frac{2(\omega - \omega_0)}{\kappa_{in} + \kappa_{out}}\right). \quad (2.38)$$

Across the resonance frequency  $\omega_0$  we expect a phase change of  $180^\circ$

$$\phi_{\omega \ll \omega_0} - \phi_{\omega \gg \omega_0} = -\pi. \quad (2.39)$$

The state of a superconducting qubit can be measured with just a linear resonator described above by either capacitively [86, 70, 87] or inductively coupling the qubit to the resonator. However, in order to get more sensitivity, we make the resonator non-linear by placing a Josephson junction in the center of the resonator, as explained above (see section 2.2.2). To characterize the amount of non-linearity in this system we measure the transmitted amplitude  $P_{out}$  and

phase  $\phi$ , as a function of both input frequency  $\nu = \omega/2\pi$  and input power  $P_{in}$ . The Duffing oscillator model of this system (section 2.2.2) shows us that the resonance frequency  $\omega_0$  should bend backwards as  $P_{in}$  is increased, until eventually it bifurcates, attaining two stable oscillating states.

Representative data from a 1.83 GHz and a 9.25 GHz resonator is plotted in Fig. 2.16. One can clearly see the back-bending of the resonance as  $P_{in}$  is increased. When  $P_{in}$  reaches a critical power  $P_c$  (black curve) the system becomes bistable and we can see a jump in both the amplitude and phase as the power is swept up. Qualitatively, we can immediately see the agreement with the theoretical prediction of Fig. 2.2a. Note that these curves are not offset. The fact that the

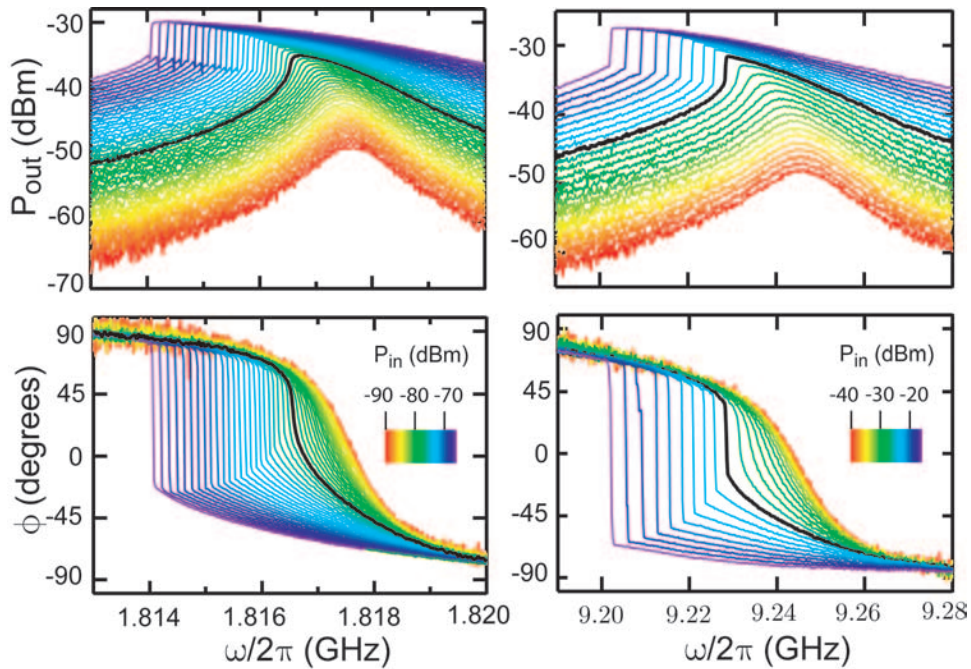


Figure 2.16: Resonance curves for both a 1.83 GHz resonator, sample 1, and a 9.25 GHz resonator, sample 6. Using a network analyzer the transmitted amplitude and phase are measured for each resonator, while the frequency is swept upwards. The input power is then increased in steps and at sufficiently high powers, bifurcation is reached (center black curves).

curves don't intersect at any point is a sign that the non-linearity originates from a non-dissipative source. For instance, if the dissipation in the resonator increased with power, the resonance would become broader, its maximum would decrease and the resonance curves would eventually cross each other [88, 89], an effect never observed in our experiment.

Note that by adding an extra input line (via a directional coupler on the output) on the large capacitor side  $C_{out}$ , we can also measure these samples in reflection from the small capacitor  $C_{in}$  (this was done with some 10 GHz samples). In this case, we have no amplitude response (most power is reflected) and a linear phase shift of  $\phi_{\omega \ll \omega_0} - \phi_{\omega \gg \omega_0} = -2\pi$ . The resulting reflected phase data from sample 6 is plotted in Fig. 2.17. In this figure, instead of plotting each individual trace like in Fig. 2.16, the phase  $\phi$  is plotted with a color scale where dark green corresponds to  $180^\circ$ , dark red corresponds to  $-180^\circ$  and yellow corresponds to the resonance frequency  $\omega_0$  at  $0^\circ$ . The disappearance of the yellow region signifies the onset of bifurcation. Note, we can now also see the appearance of a different behavior at higher  $P_{in}$ . The bifurcation line branches in a V-like shape around a black region. In this region we are strongly driving the junction with an RF current close to its critical current  $I_0$ , causing the system to behave in a chaotic manner (see Eqn. 2.33).

To quantitatively describe this steady state data in Figs. 2.16&2.17, we can use a simple calculation based on the full circuit (see Fig. 2.18) and using no approximations (the Duffing oscillator model predictions will be examined later).

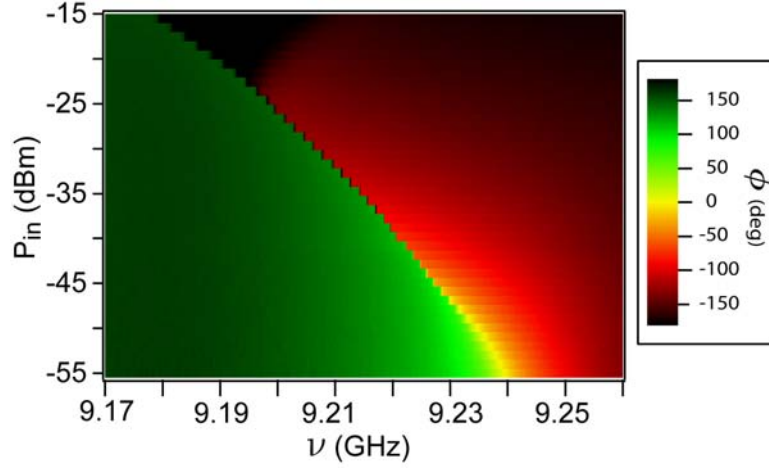


Figure 2.17: Resonance curves for sample 6 measured in reflection with the output port. Using a network analyzer we measure the reflected phase as the frequency is swept upwards. Then we step the power and repeat. Hysteresis can't be measured with this method as we cannot sweep down the frequency. We see a  $360^\circ$  phase shift as expected for reflection from a lossless resonator. At higher powers we enter a “chaotic” region.

We begin with Kirchoff's laws for the input voltage  $V_{in}$  and output voltage  $V_{out}$

$$\begin{aligned}
 V_{in}(t) &= V_d(t) - RI_{in} - \frac{q_{in}(t)}{C_{in}}, \\
 \text{where, } q_{in}(t) &= \int_{-\infty}^t I_{in}(t') dt', \\
 \text{and, } V_{out}(t) &= RI_{out} + \frac{q_{out}(t)}{C_{out}}, \\
 \text{where, } q_{out}(t) &= \int_{-\infty}^t I_{out}(t') dt'.
 \end{aligned} \tag{2.40}$$

Since we want the frequency dependence for the amplitude and phase of the output current  $I_{out}$ , we move to frequency space by getting the Fourier transform of Eqns. 2.40

$$\begin{aligned}
 V_{in}[\omega] &= V_d[\omega] - RI_{in}[\omega] - \frac{iI_{in}[\omega]}{\omega C_{in}}, \\
 V_{out}[\omega] &= RI_{out}[\omega] + \frac{iI_{out}[\omega]}{\omega C_{out}},
 \end{aligned} \tag{2.41}$$

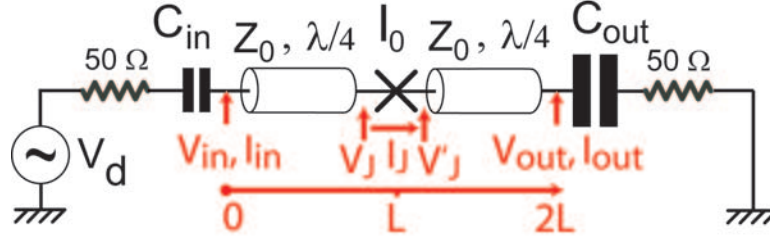


Figure 2.18: We can get the steady state solution of the CBA from the full system model of a junction inside a  $\lambda/2$  resonator. At the end we will want the frequency dependance of the amplitude and phase of the output current  $I_{out}$  through  $R$  (Thanks to S. Fissette for this calculation).

where the square brackets denotes the Fourier transform. Next, we calculate the voltages and currents along the transmission lines, which can be written as a sum of incident and reflected waves [81]

$$\begin{aligned} V(z) &= V_0^+ e^{-i\beta z} + V_0^- e^{i\beta z}, \\ I(z) &= \frac{V_0^+}{Z_0} e^{-i\beta z} + \frac{V_0^-}{Z_0} e^{i\beta z}, \end{aligned} \quad (2.42)$$

where  $z$  is the coordinate system along the axis of the resonator, chosen so that the center of the resonator is given by  $z = L$ , where  $2L$  is the length of the resonator. Using Eqns., 2.42 we can solve for  $V_J$  and  $I_J$  in terms of  $V_0$  and  $I_0$  and, also, we can solve for  $V_{out}$  and  $I_{out}$  in terms of  $V_J'$  and  $I_J$

$$\begin{aligned} V_J \pm Z_0 I_J &= (V_0 \pm Z_0 I_0) e^{\pm i\beta L}, \\ V_{out} \pm Z_0 I_{out} &= (V_J' \pm Z_0 I_J) e^{\mp i\beta L}. \end{aligned} \quad (2.43)$$

Note for a TEM line  $\beta = \omega/\nu_p$  (neglecting dispersion due to kinetic inductance), where  $\nu_p$  is the phase velocity of the transmission line. Since  $2L \simeq \lambda/2$  we have  $\beta L = \frac{\pi\omega}{2\omega_0}$ . Finally, to complete the calculation we require relations between the current and voltages across the Josephson junction, i.e., the Josephson relations

1.6

$$\begin{aligned} I_J(t) &= I_0 \sin(\delta(t)), \\ V_J'(t) - V_J(t) &= \phi_0 \dot{\delta}(t). \end{aligned} \quad (2.44)$$

We Taylor expand  $\sin(\delta(t))$  and keep only the first two terms. Then we make the

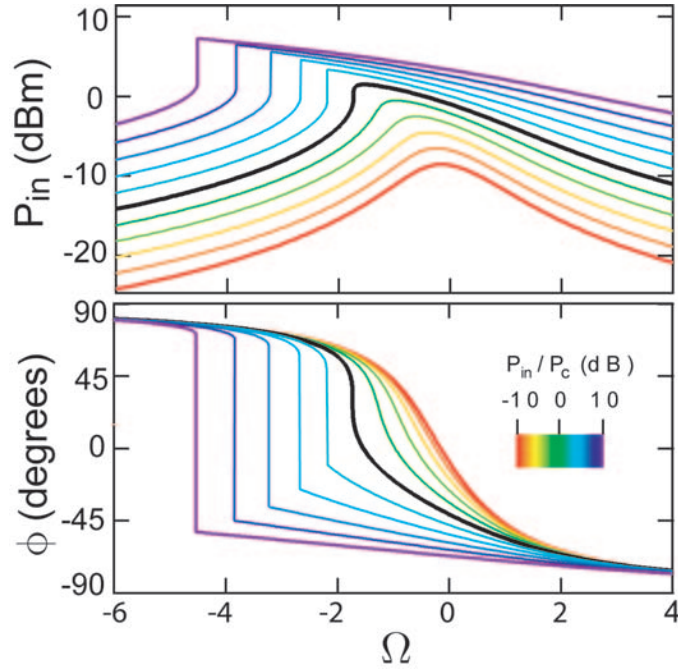


Figure 2.19: Theoretical plots of output power and phase as a function of reduced detuning,  $\Omega = 2Q(\omega_d - \omega_0)/\omega_0$ . Note that the real data is not plotted here because the presence of nearby spurious resonances distorts the resonance shape. For a more detailed analysis of theory vs. experiment for the dependence of resonance frequency and bifurcation points vs. input power see the next section.

substitution  $\delta(t) = 0.5 [Ae^{i\omega t} + A^*e^{-i\omega t}]$  and keep only the first harmonic terms.

Following the transformation to frequency space we finally get

$$\begin{aligned} I_J &= AI_0 \left(1 - \frac{a^2}{8}\right), \\ V_J &= V'_J - i\omega\phi_0 A, \end{aligned} \quad (2.45)$$

$$\text{where, } A = ae^{i\theta}.$$

Substituting Eqns. 2.45 into Eqns. 2.43 and Eqns. 2.41 we can now solve for the amplitude and phase of  $I_{out}$  given  $V_{in}$ . The results are shown in Fig. 2.19 and give excellent qualitative agreement with the measurements

### 2.5.3 Universal Duffing oscillator behavior

To gain further insight into the behavior of the CBA we now analyze these results using the Duffing oscillator model. If this model is valid, all the measured samples, each with different values of the parameters  $\omega_0$ ,  $Q$  and  $I_0$ , should fit on a universal curve of  $P_{out}$  or  $\phi$  vs.  $P_{in}/P_c$  and  $\Omega$ . To test this hypothesis, we plot in Fig. 2.20 the positions of the upper and lower bifurcation points  $P_b^\pm$  vs.  $P_{in}/P_c$  and  $\Omega$  for samples 1, 2 and 6 (see table 2.2). These bifurcation points can be easily extracted from the data by calculating the highest derivative of the output with respect to  $\nu$ ,  $\partial P_{out}/\partial\omega$ . We also plot for comparison the theoretical positions of these lines which we can calculate from Eqn. 2.8

$$\frac{P_b(\Omega)}{P_c} = \frac{1}{12\sqrt{3}}\Omega^3 \left( 1 + \frac{9}{\Omega^3} \pm \left( 1 - \frac{3}{\Omega^2} \right)^{3/2} \right), \quad (2.46)$$

(red and blue lines). Furthermore, below the critical power  $P_c$ , in the non-hysteretic region, we plot the highest first derivative of the data, which is predicted to follow

$$\frac{P_{HD}}{P_c} = \frac{\sqrt{3}}{2}\Omega - \frac{1}{2}, \quad (2.47)$$

(black dashed line). All of these theoretical lines are also plotted on the inset in Fig. 2.20. There,  $\partial P_{out}/\partial\omega$  is normalized to its maximum and plotted as a function of the absolute drive frequency  $\omega$  and input power  $P_{in}$ . The maximum output power  $P_{out}$  (below  $P_c$ ) is shown as a white line which is defined by  $P_{max}/P_c = \frac{9}{8\sqrt{3}}$  and coincides with the change of sign of  $\partial P_{out}/\partial\omega$ . We obtain excellent overall agreement between experimental results and theoretical predictions. This agreement validates our Duffing oscillator description of the CBA, demonstrates our level of control of the junction's environment and allows us to eliminate non-linear dissipative effects as the cause for the bifurcation.

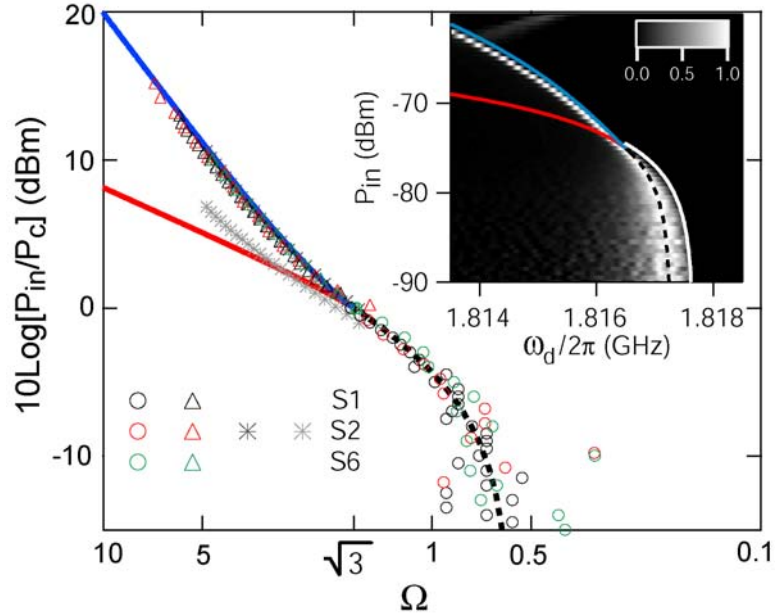


Figure 2.20: Logarithmic plot of the highest derivative  $\partial P_{out}/\partial \omega$  as a function of reduced parameters  $\Omega$  and  $P_{in}/P_c$ . The lines depict theoretical predictions from the Duffing model. Triangles, circles and crosses represent respectively the measured bifurcation power, its highest derivative (below  $P_c$ ), and the data from a hysteresis measurement. **Inset:** Plot of the derivative of the output power with respect to drive frequency, normalized to its maximum, as a function of  $\nu$  and  $P_{in}$ . Note the white line indicates the point where the output power is maximum (the derivative changes sign).

### 2.5.4 Hysteresis

As mentioned before, these measurements do not probe the hysteresis since the frequency is swept only in the forward direction. To verify the hysteretic behavior of the phenomenon, we instead swept the power up and down while keeping the frequency fixed (see Fig. 2.21). We made these power sweeps by multiplying a continuous RF signal at frequency  $\nu$  by a DC voltage triangle. The output signal from the CBA was then mixed back down to a few megahertz using another RF signal which is phase locked to the input signal and slightly detuned from  $\nu$ . Using this method, we were able to probe the power and frequency dependence of both

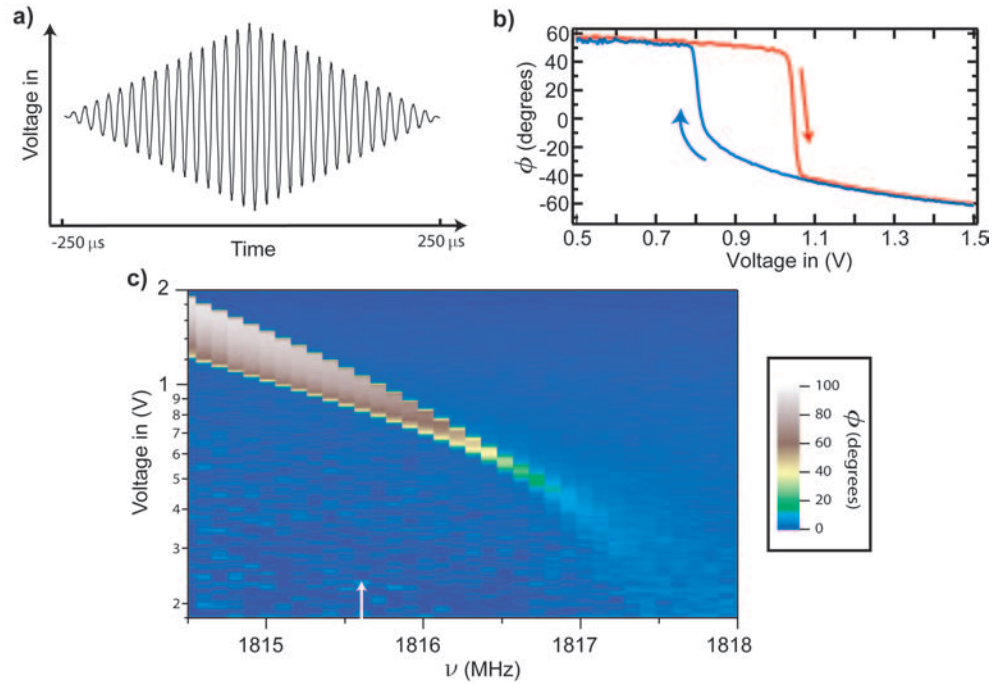


Figure 2.21: **(a)** A schematic of the waveform used in measuring the sample hysteresis. We mix together a triangle waveform and the microwave signal at a fixed frequency. For the following data from sample 2, the total triangle pulse length was  $500 \mu\text{s}$ . **(b)** Plot of the resulting phase response for sample 2 at 1815.6 MHz. The voltage is ramped up for the red trace and ramped back for the blue trace. The CBA switches back at a lower voltage compared to the up ramp. This hysteresis can be used to latch in the state of the CBA and hence we can increase the signal to noise by measuring longer. **(c)** We repeat the measurement in (b) while stepping the frequency. The color scale is the phase difference between the up voltage ramp and the down voltage ramp. The white arrow corresponds to the data shown in (b)

the upper and lower bifurcation points. The resulting data is shown in Fig. 2.21 and is also plotted as stars on the universal Duffing oscillator results in Fig. 2.20. The measured hysteresis deviates from predictions based on the Duffing model, but it is reproduced by simulating the full single mode series LRC equation (see Eqn. 2.26). The color scale in Fig. 2.22 illustrates the results of such a simulation, solved using a fourth order Runge Kutta algorithm (see appendix C.1). The black

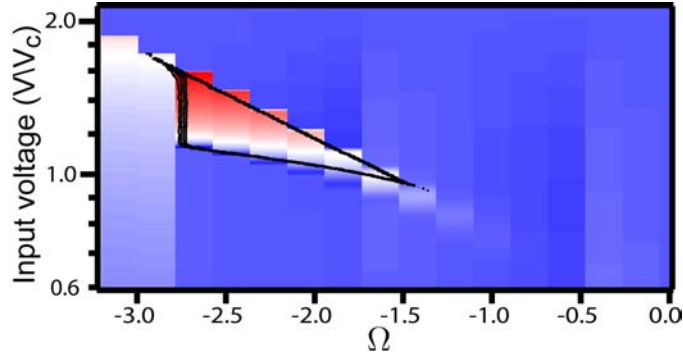


Figure 2.22: The color scale is the simulation of the hysteresis for a CBA with  $\nu_0 = 8.411$  GHz and  $Q = 290$ . The black contours are the corresponding experimental results.

contours, overlaid on the simulation, are the experimental results, and have excellent agreement with the simulation at both the upper and lower bifurcation points. The lower bifurcation point vanishes at larger detuning because the voltage ramp reaches the chaotic region before ramping back down. Note that the upper and lower bifurcation current in this RF experiment is analogous to the switching and retrapping current, respectively, in DC Josephson IV measurement.

### 2.5.5 Parameter extraction

From the above described measurements of the transmitted and reflected amplitude and phase we can extract the CBA parameters  $\omega_0$ ,  $Q$ ,  $I_0$ ,  $C_{in}$ ,  $C_{out}$ , and  $L_{eff}$ . We begin with the simple measurement of  $\omega_0$  and  $Q$  by fitting the peak in the transmitted amplitude with a lorentzian. After extracting the value of  $\omega_0$  and  $Q$  and with the use of Eqn. 2.23 for the quality factor of a capacitively coupled resonator, we obtain a relationship between the values of  $C_{out}$  and  $C_{in}$ . A further relationship is obtained from the transmission  $T$  of the resonator on resonance, which is given by Eqn. 2.37. Hence using these two equations we can infer the values of  $C_{out}$  and  $C_{in}$ . Note that  $C_{in}$  and  $C_{out}$  can be measured more accurately

if we add an extra input line on the  $C_{out}$  side of the resonator and take measurements of the reflected amplitude and phase. Then, using the ratio of the power at the critical point  $P_c$  in both transmission and reflection, we can obtain a further relationship between  $C_{in}$  and  $C_{out}$ .

The most difficult parameter to extract is the critical current of the junction,  $I_0$ . If we had DC access to the device we could easily get  $I_0$  from measurements of the junction's switching rate into its normal state. The basic method to get  $I_0$  for the CBA is to measure the input voltage at the critical point  $V_c$ , given by Eqn. 2.35. Using the value of the attenuation in the input lines, and the inferred value of  $C_{in}$ , we can then extract  $L_T/L_J$  from this formula. Finally, the resonator's inductance  $L_{eff}$  can be calculated from Eqn. 2.22, allowing us to calculate  $L_J$  from  $L_T/L_J$ . The main difficulty in this calculation is in accurately measuring the attenuation in the input lines. It is only measured at room temperature and certainly changes as the fridge is cooled to base temperature and as the liquid He level in the fridge changes. Hence, this attenuation is only known to within a factor of 2 or 3 dB and so  $I_0$  is therefore known, at best, to within a factor of two.

To gain more accuracy in extracting  $I_0$  we can replace the single junction by two junctions in parallel or, in other words, a SQUID. This SQUID behaves like an effective single junction whose critical current  $I_0$  can be varied by applying a magnetic field,  $B$ , through the loop of the SQUID. The inductance of a SQUID changes with  $B$  according to the equation

$$L_J(B) = L_J(0) \left| \cos \left( \pi \frac{I_{coil} - I_{off}}{\Delta I} \right) \right|^{-1}, \quad (2.48)$$

where  $I_{coil}$  is the current through the magnetic field coil,  $I_{off}$  is an offset current and  $\Delta I$  is the period of the modulation.  $I_{off}$  is required in this equation because the zero field point doesn't correspond to the modulation maximum. This is could

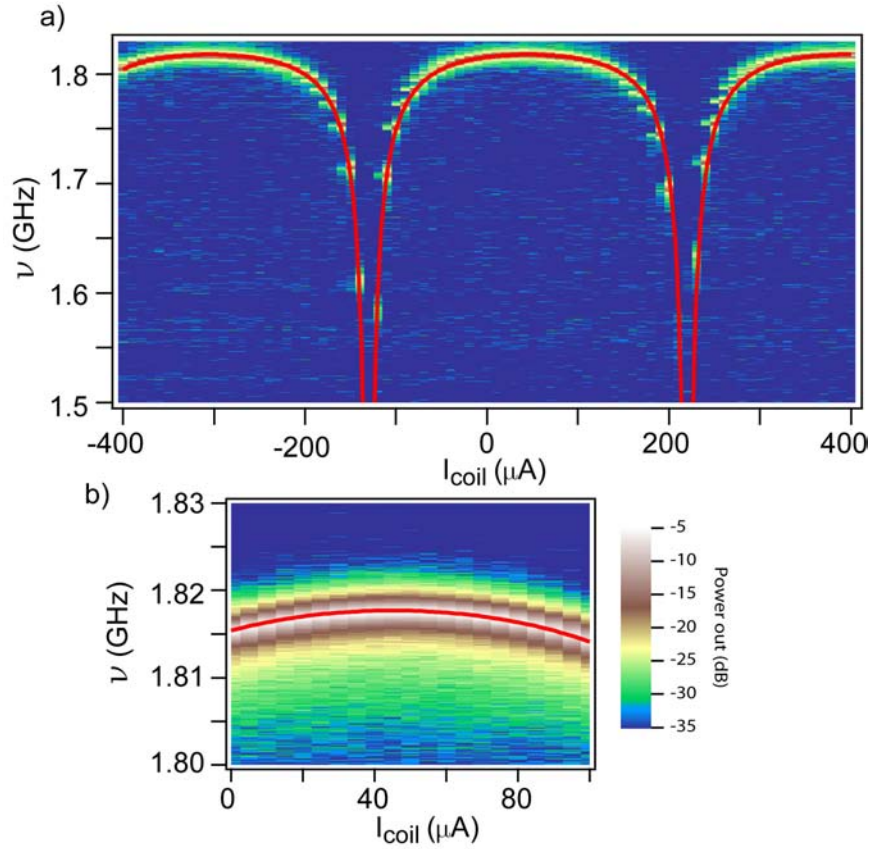


Figure 2.23: **(a)** At a fixed magnetic field we measure the transmitted amplitude,  $P_{out}$ , at low input power,  $P_{in}$  (linear resonance) and sweep the frequency,  $\nu$ . Then, we repeat for different magnetic fields,  $B$ . The red line is a fit used to extract the participation ratio with Eqn. 2.50. In this case we are measuring sample 2 and find a participation ratio of  $L_J/L_T = 0.03$ . **(b)** Zoom in of the fit near the maximum of one of the modulations.

be due to a constant global magnetic field due to, for example, the circulators in the measurement setup. It could also be caused by local magnetic fields which are caused by, for example, a vortex trapped in the superconducting film nearby the SQUID loop. The change in inductance of the junction will result in a shift of the resonance frequency  $\omega_0$ . This is illustrated in Fig. 2.23 where I have plotted the linear resonance peak vs. applied magnetic field  $B$ . The resonant frequency

will change according to the equation

$$\frac{\omega_0(B)}{\omega_0(0)} = \sqrt{\frac{L_T(0)}{L_T(B)}} \simeq \sqrt{\frac{1 + \frac{L_J}{L_T}(0)}{1 + \frac{L_J}{L_T}(B)}}. \quad (2.49)$$

Hence inserting Eqn. 2.48 into Eqn. 2.49 we get

$$\omega_0(B) = \omega_0(0) \sqrt{\frac{1 + \frac{L_J}{L_T}}{1 + \frac{L_J}{L_T} / \left| \cos\left(\pi \frac{I_{coil} - I_{off}}{\Delta I}\right) \right|}}. \quad (2.50)$$

By fitting the modulation of the resonance frequency  $\omega_0$  with this equation we can extract the participation ratio  $L_J/L_T$  with high accuracy (see red line in Fig. 2.23).

Apart from being useful in extracting  $I_0$ , a SQUID will prove useful later in this chapter in calculating the sensitivity of the CBA to changes in the effective inductance  $L_J$  of the Josephson junction. Using this information we can predict whether the CBA will be able to readout a superconducting qubit state in single shot manner.

## 2.6 Time domain measurements

In order to access the CBA's effectiveness as an amplifier, I will now study the dynamics of the switching mechanism from the lower oscillating state to the higher oscillating state. The switching rate,  $\gamma$ , depends on how close we drive the system to the bifurcation point  $V_b$  with RF voltage  $V_d$ . It increases as we move closer to  $V_b$  and has a transition width which depends on the noise present in the system. For high bath temperatures,  $T$ , the transition will be dominated by thermal fluctuations and at low temperatures we expect quantum effects to come into play. This width will determine the ultimate limit on the CBA's sensitivity.

### 2.6.1 Theoretical escape rate

The following derivation of the escape rates is taken from Dykman et al. (1980)[78]. We begin with the reduced Duffing oscillator equation in a rotating frame at the drive frequency, Eqn. 2.4. Near the bifurcation point  $\beta_b$ , we can approximate Eqn. 2.4 as

$$\dot{x} = -bx^2 + \varepsilon x + \nu_N(\tau), \quad (2.51)$$

where

$$b(\Omega) = \frac{1}{27\sqrt{\beta_b}} \left( \Omega^2 \left( 1 + \sqrt{1 - \frac{3}{\Omega^2}} \right) + 9\sqrt{1 - \frac{3}{\Omega^2}} - 6 + \frac{9}{\Omega^2} \right), \quad (2.52)$$

and

$$\varepsilon = \frac{1}{2} \frac{\beta_b(\Omega) - \beta}{\sqrt{\beta_b(\Omega)}}. \quad (2.53)$$

The above equation describes a system which behaves like a 1-D massless Brownian particle subject to a random force  $\nu_N(\tau)$ , and diffusing in a cubic “meta-potential”  $V(x)$

$$V(x) = -\frac{bx^3}{3} + \varepsilon x. \quad (2.54)$$

We can define an attempt frequency (or inverse equilibration time)  $\omega_a$  of the particle in the meta-stable state of the cubic potential by

$$\omega_a = 2\sqrt{b\varepsilon} = \frac{2}{3\sqrt{3}} \Gamma \Omega^2 \left| 1 - \frac{V_d^2}{V_b^2} \right|^{1/2}. \quad (2.55)$$

In order for the above Langevin equation to be valid, we need this attempt frequency  $\omega_a$  to be less than the linear resonance bandwidth  $\omega_a \ll \Gamma$ . The switching of the CBA from the low oscillating state to the high oscillating state can be thought of as the escape of this fictitious particle out of the minimum of the cubic potential, with barrier height  $U(V_d)$  given by

$$U(V_d) = \frac{8\sqrt{2}}{3} E_J \left( \frac{L_T}{L_J} \right)^2 \frac{1}{Q} \frac{(\beta_b)^3 \Omega^2}{b(\Omega)^{1/2}} \left| 1 - \frac{V_d^2}{V_b^2} \right|^{3/2} \equiv U_0 \left| 1 - \frac{V_d^2}{V_b^2} \right|^{3/2}. \quad (2.56)$$

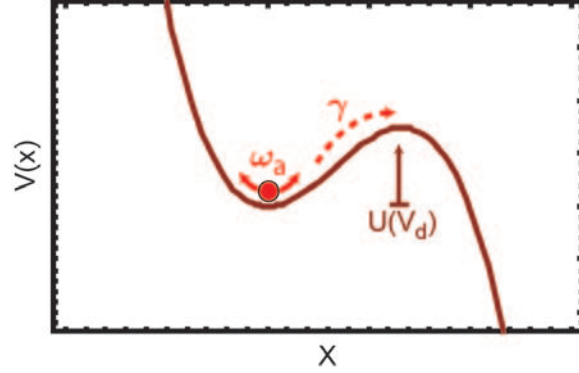


Figure 2.24: Cubic potential  $V(x)$  of Duffing oscillator in rotating frame. A fictitious particle of zero mass diffusing inside the metastable state with the potential barrier  $U(V_d)$  and escape rate  $\gamma$

As we increase the RF drive  $V_d$ , this barrier height  $U(V_d)$  decreases and the escape rate  $\gamma$  increases. If we are at low enough temperatures such that  $U/k_B T \gg 1$ , then the system obeys an Arrhenius-like law for the escape rate i.e.

$$\gamma = \frac{\omega_a}{2\pi} \exp\left(-\frac{U(V_d)}{k_B T_{\text{esc}}}\right). \quad (2.57)$$

In a typical experiment, we measure  $\gamma$  vs.  $V_d$  at fixed  $\Omega$ , from which we extract  $T_{\text{esc}}$ . This is achieved by getting the logarithm of both sides of Eqn. 2.57 to get

$$\beta^{2/3} = \left(\ln\left(\frac{\omega_a}{2\pi\gamma}\right)\right)^{2/3} = \left(\frac{U_0}{k_B T_{\text{esc}}}\right)^{2/3} \left|1 - \frac{V_d^2}{V_b^2}\right| \quad (2.58)$$

A plot of  $\beta^{2/3}$  vs.  $V_d^2$  is nicknamed a “beta-two-thirds” plot, and with the use of Eqn. 2.58, we can fit the data to a straight line with slope  $-\frac{1}{V_b^2} \left(\frac{U_0}{k_B T_{\text{esc}}}\right)^{3/2}$ , y-intercept  $\left(\frac{U_0}{k_B T_{\text{esc}}}\right)^{3/2}$  and x-intercept  $V_b^2$ . From these parameters, we can extract the effective temperature  $T_{\text{esc}}$ . If the escape temperature matches the fridge bath temperature, we know that our escape process is thermally activated. However, if  $T_{\text{esc}} > T$ , then we have extra noise playing a role. This extra noise could be due to insufficient filtering in the microwave lines. However, it could also be due to a quantum escape process, an effect which would have to be verified by showing

that this escape temperature scales with drive frequency  $\omega$  (see R. Vijay thesis, [77]).

### 2.6.2 Experimental demonstration of switching between metastable states

In the previous section we used continuous microwave signals to study the frequency dependence of the time averaged steady state response of the CBA. However, now we would like to study the time dynamics of the CBA and so we will need to construct fast microwave pulses whose rise times are constructed on the same time scale as the response time of the resonator. These pulses are constructed by multiplying continuous RF signals at frequency  $\nu$ , by a DC pulse with the desired envelope shape. The output of the CBA is mixed down to either DC or to a frequency in the megahertz range which can be easily be digitized and analyzed.

A typical experiment to measure the switching probability,  $P_{01}$ , of the CBA is shown in Fig. 2.25a. We pick an RF frequency which is sufficiently detuned from the linear resonance frequency  $\omega_0$  so that  $\Omega > \sqrt{3}$ , and then we mix this continuous signal with the DC pulse shown in the inset. The power is initially ramped to a voltage,  $V$ , just below the bifurcation voltage,  $V_b$ . This initial ramp time is set by resonator's bandwidth. For example, if the bandwidth of the resonator is 10 MHz, we typically ramp with a time on the order of 100 ns. After the ramp we wait some time to allow the resonator to decide whether to switch into the higher oscillation state or not. Then we measure and average over a time  $t_{meas}$ . After repeating the measurement 10,000 times we make a histogram of the data, as shown in Fig. 2.25a & c. In these plots, the length of the vector from the origin to each pixel denotes the amplitude  $A$  of the mixed down transmitted signal and the angle

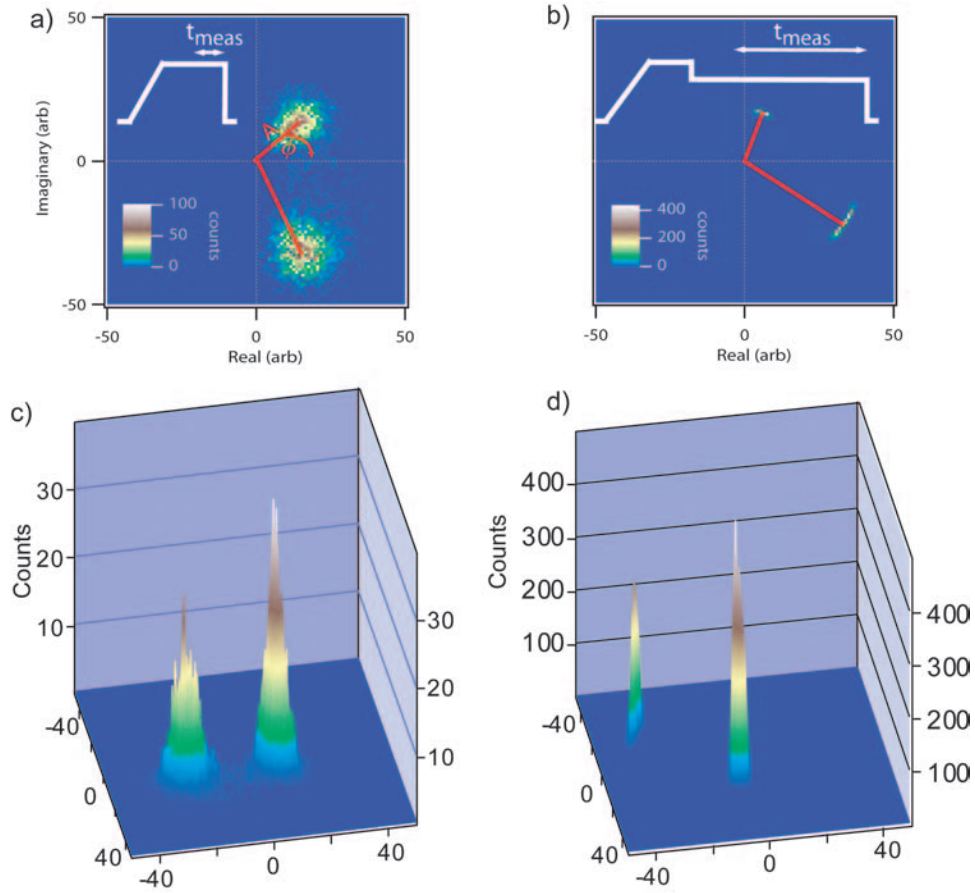


Figure 2.25: **(a)** (Sample 1) Histograms of 10000 switching events. In this plot the length of the vector to each pixel is the measured transmitted amplitude,  $A$ , and the angle is the measured transmitted phase,  $\phi$ . For this experiment we used a measurement time  $t_{meas} = 0.5 \mu s$ . **(b)** Using the CBA's hysteresis we can latch in the state and measure it with arbitrary precision. After the wait time we latch in the state by quickly ramping down the power past the upper bifurcation point, but still above the lower bifurcation point. We can then measure for as long as is needed - in this case  $t_{meas} = 200 \mu s$ . **(c & d)** 3-D histograms with the same data as in (a) and (b). Both sets of data had an initial ramp time and wait time before measurement of  $2 \mu s$

represents the phase  $\phi$  of the mixed down transmitted signal. For this particular experiment, the ramp voltage  $V$  was chosen so that the oscillator switches about 50 % of the time.  $P_{01}$  is calculated by simply dividing the number of counts in one histogram with the total number of counts (measurements).

With the above method we cannot simply average over a longer time,  $t_{meas}$ , in order to increase the signal to noise ratio. This is because while averaging, the CBA may switch state, resulting in a false reading of the state of the CBA. This gives extra counts between the two histograms and hence a reduction of the signal to noise ratio. To avoid this problem we can use the hysteretic property of the CBA. After ramping to the initial voltage and waiting for the CBA to switch, we then rapidly ramp the voltage amplitude back down by a few percent (see inset in Fig. 2.25b). This has the effect of locking-in the CBA's state. If the CBA was in the higher oscillating state, it remains there because of the hysteresis. If it was in the lower oscillating state, then it also remains fixed because the quick ramp down takes the CBA away from the switching point. Hence, we can measure over a longer time to reduce the width of the histograms without the fear of obtaining false counts (see false counts in between histograms in Fig. 2.25a and c).

### 2.6.3 Escape rate measurement methods

We measure the escape rate  $\gamma$  out of the metastable well with two different methods - the “flat top” method and the “ramp” method, as illustrated in Fig. 2.26. In the “ramp” method, a slow RF voltage ramp is input into the sample. The ramp is divided into bins around the region where switching occurs. The bin in which switching occurs is recorded and then the measurement is repeated a few thousand times. Switching events are histogrammed, giving a lopsided distribution with a long tail on the low voltage side and a sharp cutoff on the high voltage side. This occurs because, as the voltage is ramped up towards the bifurcation voltage  $V_b$ , the potential barrier  $U(V_d)$  decreases and hence the switching probability  $P_{01}$  increases. However, if it is more probable for the system to switch now, it is less probable that it will switch at a later time. This effect causes a sharp drop-off in

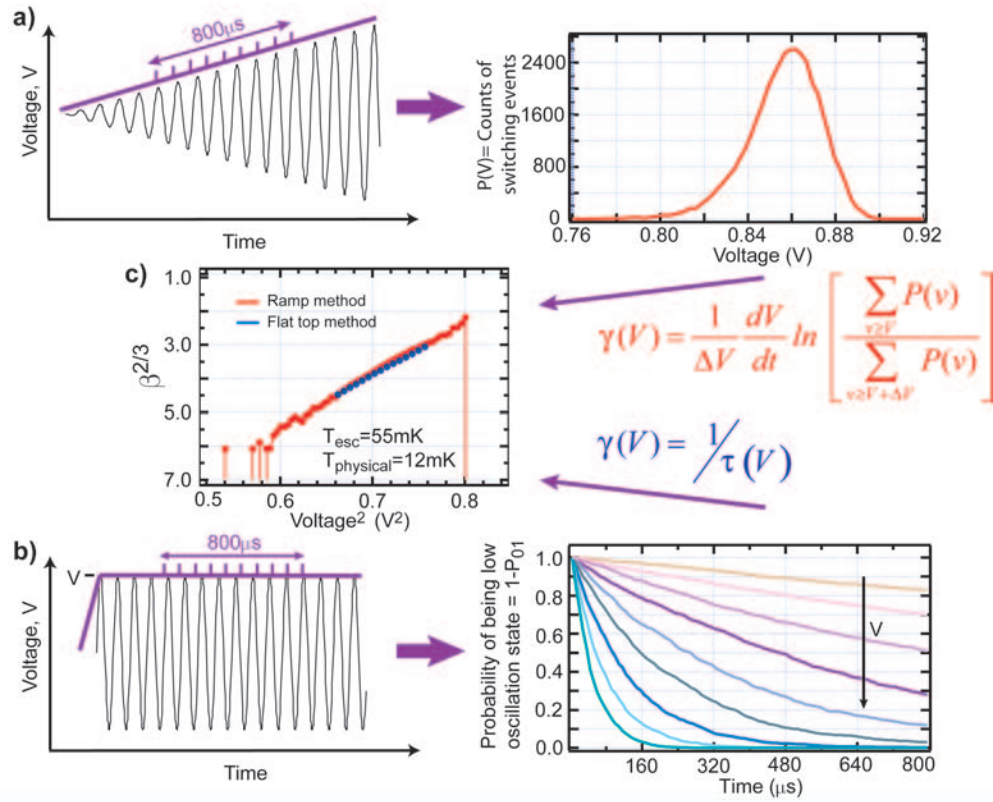


Figure 2.26: (a) In the ramp method of measuring the escape rate, we monitor the phase and we increase the input voltage until we see a switching event. After repeating a few thousand times we histogram the number of switching events as a function of voltage. From this data we can calculate the escape rate with the formula shown, giving the red data shown in (c). (b) An alternative method is to directly measure the probability of escape out of the metastable state as a function of time at a fixed input voltage. Then, by fitting the resulting exponential curve we extract the lifetime. Next we repeat for different input voltages. This data is shown in blue in (c). All the data shown is from sample 3.

the switching probability at higher voltages. Using this histogram one can extract the lifetimes  $\gamma(V)$  with the following equation [90]

$$\gamma(V) = \frac{1}{\Delta V} \frac{dV}{dt} \ln \left[ \frac{\sum_{v \geq V} P(v)}{\sum_{v \geq V + \Delta V} P(v)} \right] \quad (2.59)$$

where  $\Delta V$  is the bin size,  $\frac{dV}{dt}$  is the slope of the voltage ramp and  $P(v)$  is the number of switching events in voltage bin  $v$ . Once  $\gamma(v)$  is calculated, we can then

make the “beta-two-thirds” plot (see Eqn. 2.58) and extract  $T_{\text{esc}}$  and  $V_b$ .

The “flat top” method of measuring  $\gamma(V)$  involves the use of a microwave signal at a fixed voltage  $V$  (see Fig. 2.26b). At this fixed voltage, we measure the time at which switching occurs and then we repeat this measurement a few thousand times. On average we obtain an exponential rise vs. time for the probability of switching into the higher oscillating state. Fitting this curve to an exponential gives a direct measurement of the lifetime  $\tau(V)$  of the lower oscillating state at a fixed voltage  $V$ . Repeating for different voltages and calculating  $\gamma(V) = \frac{1}{\tau(V)}$ , gives the escape rate as a function of voltage.

Both of these measurement methods should end up with the same “beta-two-thirds” plot, as shown in Fig. 2.26c. However, they access different ranges of the escape rate  $\gamma$ . Using the “ramp” method we can measure  $\gamma(V)$  very close to the bifurcation point  $V_b$  by increasing the ramp time. The “flat top” method can be viewed as the extreme limit of the ramp method for zero ramp speed. An advantage of the “flat top” method is that it is easy to see if more than one decay process is involved in the measured signal. For example, if back-switching of the CBA from the high oscillation state to the low oscillating state occurs, we would see a second exponential in “flat top” method, with the signal decaying to a finite value - not to zero. This signal can be fitted with a double exponential in order to extract both decay constants.

These measurements can be used to investigate whether the ultimate sensitivity of our amplifier is limited by thermal fluctuations, electromagnetic noise from the RF lines or quantum fluctuations by measuring the escape rate of the CBA out of the metastable state as a function of bath temperature  $T$  and excitation frequency  $\omega$ . We can also perform a stringent test of the Duffing oscillator model by measuring the escape rate  $\gamma$  as a function of voltage  $V$  and detuning  $\Omega$ .

### 2.6.4 Experimentally measured escape rates

We begin with measuring the escape rates of sample 1. This was a single junction sample with a resonance frequency of 1.8283 GHz at 200 mK at the time of the following measurements. The input lines were heavily attenuated to reduce the

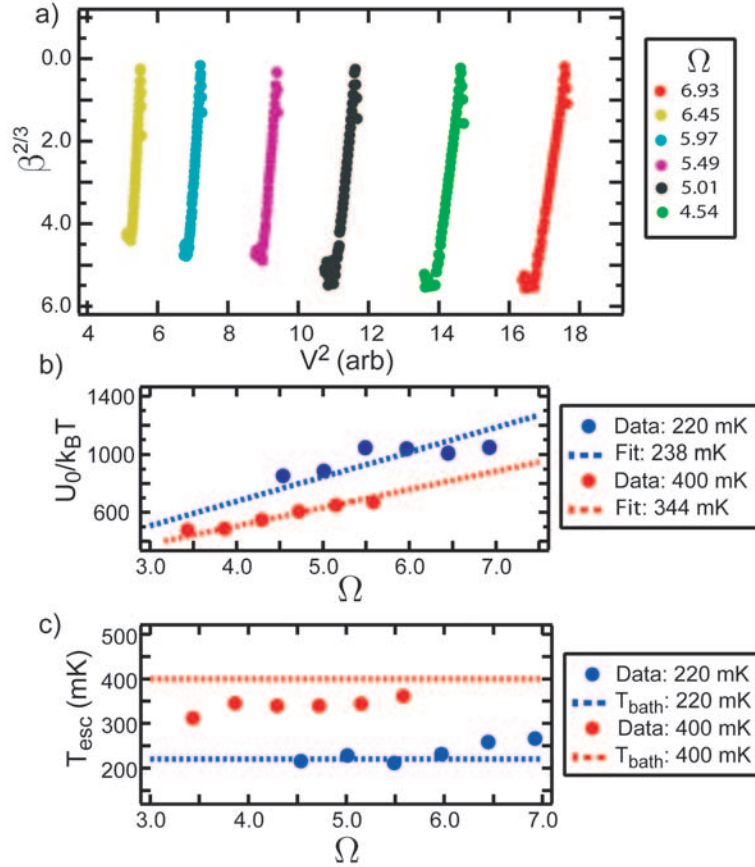


Figure 2.27: **(a)** “Beta-two-thirds” plot for sample 1 at 220 mK for different values of detuning  $\Omega$ . **(b)** Extracted values of  $U_0/k_B T$  for the same data as in (a) and also for 400 mK. The fit is from the Duffing oscillator theory for an escape temperature of 238 mK and 344 mK. **(c)** Extracted escape temperature  $T_{\text{esc}}$  vs. detuning  $\Omega$  for the fits shown in (a) at 200 mK and for the data at 400 mK shown in (b). When extracting  $T_{\text{esc}}$  from the 400 mK data we had to re-measure  $\omega_0$  and  $Q$  and estimate the change in  $I_0$  with temperature. The procedure for extracting  $T_{\text{esc}}$  is very sensitive to changes in the resonator’s parameters.

effect of any electromagnetic noise on  $T_{\text{esc}}$ . In addition, the output lines had cir-

culators to filter in-band noise and dissipative RF filters to filter out of band noise (see Fig. 2.15a and appendix B). Using the “ramp” method, we measured  $\gamma(V)$  vs.  $\Omega$ , as shown in Fig. 2.27. The value of  $U_0$  scales approximately linearly with detuning (Fig. 2.27b), as expected from the Duffing oscillator escape theory (see Eqn. 2.56). We also see from this data that  $T_{\text{esc}}$  increases as the bath temperature (Fig. 2.27c) increases, indicating that the escape process is dominated by thermal fluctuations.

This procedure for extracting  $T_{\text{esc}}$  is very sensitive to changes in the resonator’s parameters. For example, a slight shift in  $\omega_0$  will greatly change the extracted  $T_{\text{esc}}$  and this parameter can vary from day to day if, for example, the resonator traps flux. Furthermore,  $T_{\text{esc}}$  is very sensitive to the value of the critical current  $I_0$ . However, because we do not have any DC access in these samples,  $I_0$  has to be inferred from test samples fabricated at the same time, or, it can be extracted from the input power at the critical point  $P_c$ , to within a factor of 2 (see section 2.5.5). The critical current was used as a fitting parameter for the fits shown in Fig. 2.27 which give  $I_0 = 1.6 \mu\text{A}$ . This is close to the value we aimed for during fabrication of  $1.3 \mu\text{A}$ . When taking data at 400 mK, we re-measured  $\omega_0$  and  $Q$  because they change value significantly between 200 mK and 400 mK. Furthermore, we have to estimate the change in  $I_0$  with temperature, by measuring how the linear resonance frequency moves with temperature.

In order to test if  $T_{\text{esc}}$  follows the bath temperature as the temperature is lowered, we cooled a sample down to 12 mK in a dilution refrigerator (sample 3). At each detuning I extract the bifurcation voltage  $V_b$  and the barrier height  $U_0/K_B T$  from the “beta-two-thirds” plots (Fig. 2.28a). In the fits I use the switching histograms as weights. This procedure gives preference to the points which have more statistics and which are closer to the bifurcation voltage, where the Duffing

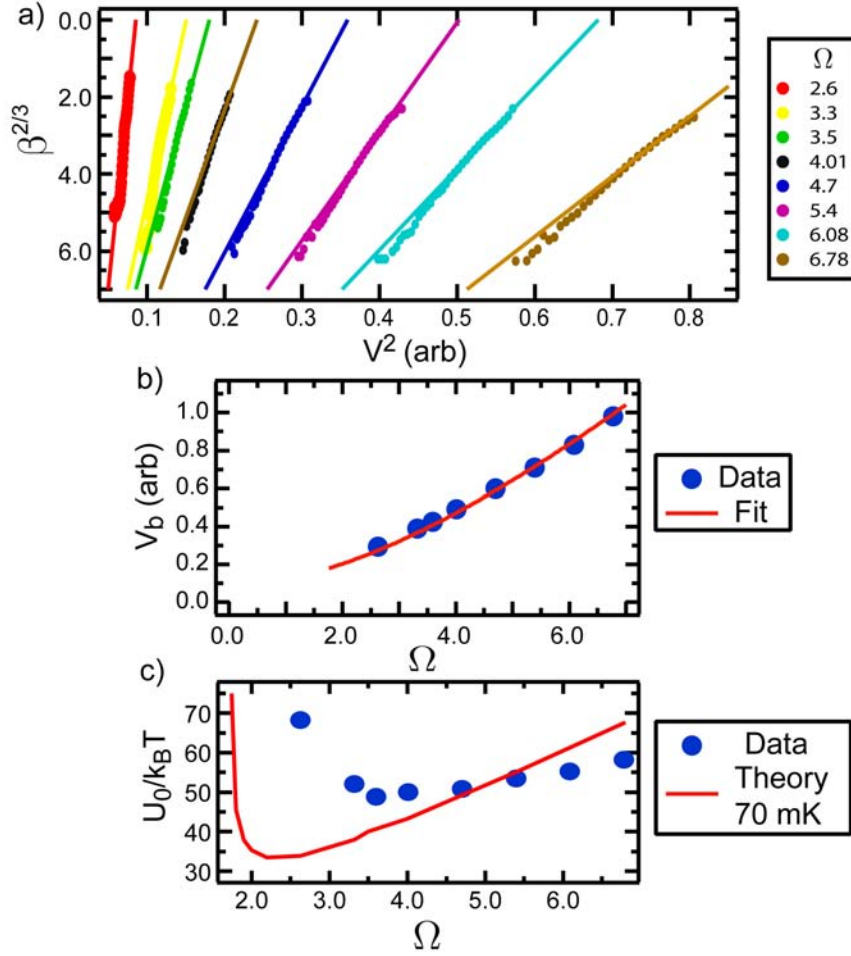


Figure 2.28: (a) “Beta-two-thirds” plots for sample 3 and different detunings  $\Omega$ . (b) Bifurcation voltage extracted from (a). The fit uses Eqn. 2.60 with the attenuation in the input line used as the fitting parameter. (c) Extracted values of  $U_0/k_B T$  for the same data as in (a) and (b). As expected from the theory we see an upturn as we approach the critical point. However, the functional dependence deviates from the Duffing oscillator theory.

oscillator escape theory is more accurate.

The bifurcation voltage behaves as expected from the Duffing oscillator theory, following the equation

$$V_b = \text{Att} \phi_0 \omega_0 \sqrt{8\beta_b(\Omega)\Omega^3\epsilon^3}, \quad (2.60)$$

where  $\beta_b(\Omega)$  is given by Eqn. 2.8 and  $\epsilon = \sqrt{\frac{1}{Q} \frac{L_T}{L_J}}$ . The attenuation in the input line,  $\text{Att}$ , is the only fitting parameter in Fig. 2.28b. However, we find that the extracted escape temperature,  $T_{\text{esc}}$ , is not constant as  $\Omega$  changes. In other words, as shown in Fig. 2.28b,  $\frac{U_0}{k_B T}$  disagrees with the Duffing oscillator escape theory. As predicted in the theory, we see an increase in  $\frac{U_0}{k_B T}$  as we approach the critical point, however, it has a different functional dependance with  $\Omega$ . For large  $\Omega$ ,  $U_0/k_B T$  becomes linear in  $\Omega$ , but with a slope different from what we expect, given an estimated critical current of  $I_0 = 0.3 \mu\text{A}$ .

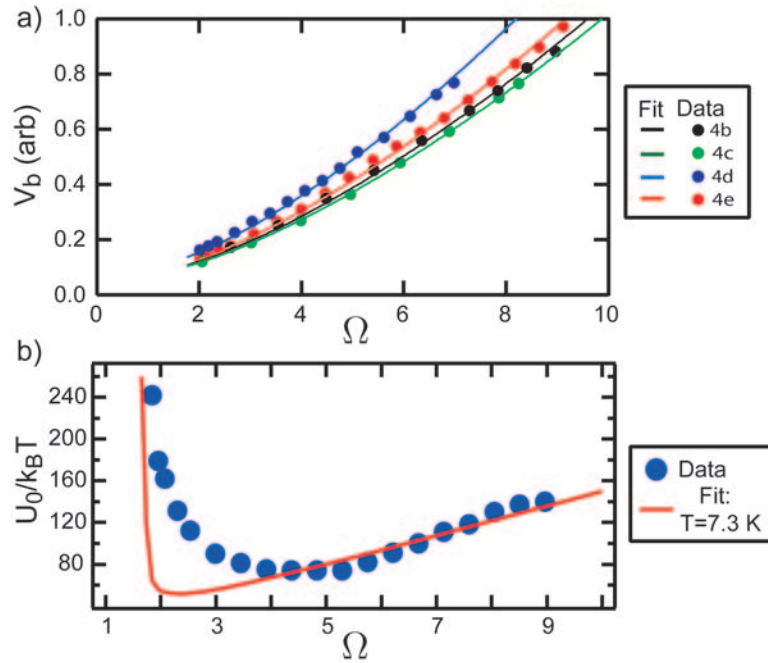


Figure 2.29: **(a)** Bifurcation voltage  $V_b$  vs. detuning, extracted from escape rate data for sample 4 at 240 mK. The solid lines are fits using Eqn. 2.60. **(b)** Extracted barrier height  $U_0/k_B T$  vs. detuning. The red solid line is the expected behavior from Eqn. 2.56 at 7.3 K.

To achieve better accuracy in determining  $I_0$ , we have measured CBA samples with SQUIDS (for more details on parameter extraction see section 2.5.5). The results shown in Fig. 2.29 are from such a sample (sample 4), which consists of

five multiplexed resonators (multiplexing is described in section 4.1) near 10 GHz and was measured at 0.23 K. As before, the extracted bifurcation voltage behaves as expected with detuning (Fig. 2.29a). The barrier height,  $U_0/k_B T$ , increases at low detuning as expected, but deviates from the expected behavior based on the Duffing oscillator escape theory (see Eqn. 2.56). At large detuning,  $U_0/k_B T$  increases linearly with detuning as expected, but has an elevated escape temperature of 7.3 K. This could be due to insufficient filtering in the output lines, which did not have any filtering in the circulator’s band (see appendix B).

### 2.6.5 S-curves and predicted contrast

We can study  $T_{\text{esc}}$  on a much faster time-scale than the “Beta-two-thirds” plots described in the previous section by measuring the switching probability,  $P_{01}(V_d, I_0)$ , of the CBA from the lower amplitude oscillating state to the higher amplitude state at input voltage  $V_d$ . This is done by measuring the CBA’s state after quickly ramping the input to a fixed voltage,  $V_d$ , close to the bifurcation point,  $V_b$ , and then repeating this sequence a few thousand times to calculate  $P_{01}(V_d, I_0)$ . We repeat this measurement for different input voltages  $V_d$ , resulting in a sigmoidal shaped curve of  $P_{01}$  vs.  $V_d$  that has been nicknamed an “s-curve”. The CBA completely switches at the bifurcation voltage  $V_b$  ( $P_{01} = 1$ , see Fig. 2.30), corresponding to the point at which the “beta-two-thirds” plot crosses the x-axis (see Eqn. 2.60). An “s-curve” measurement can be thought of as the extreme limit of the “ramp” method, with ramp times that are only limited by the  $Q$  of the resonator, enabling us to get closer to the bifurcation point  $V_b$ . Because of this, an “s-curve” measurement is less prone to low frequency noises, but is more difficult to describe theoretically (The Arrhenius law breaks down for low barrier heights where the escape rate is too high) and we need a simulation to understand it (see

Fig. 2.33 and appendix C.1 for more detail on the simulations).

The width of the transition from the low oscillation state to the high oscillation state is again limited by  $T_{\text{esc}}$ . Therefore, this measurement can be used to characterize the ultimate sensitivity of the CBA. A schematic of the pulse shape

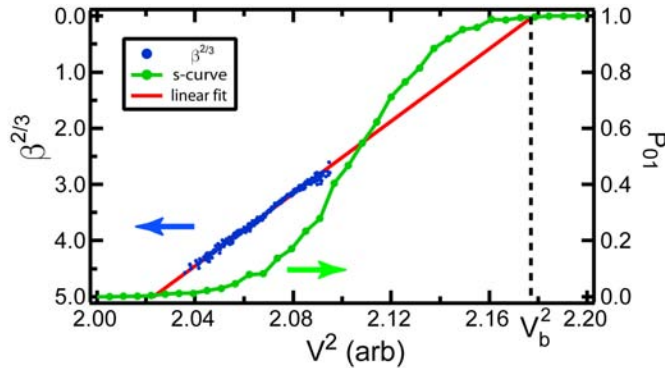


Figure 2.30: “Beta-two-thirds” plot and s-curve on same plot from sample 2. The switching probability,  $P_{01}$ , reaches 1 at the bifurcation voltage,  $V_b$ , which is also the point where the “beta-two-thirds” plot crosses the x-axis. The escape rate in the “beta-two-thirds” plot is determined by the voltage ramp rate used in the experiment, which in this case was 1 ms. The pulse used in taking the s-curve (see Fig. 2.31) had a ramp time and a wait time of 2.5  $\mu\text{s}$ .

used to measure the “s-curves” is shown in Fig. 2.31. As mentioned above, the initial ramp time,  $t_{\text{ramp}}$ , is limited by the  $Q$  of the resonator. Following this ramp, we wait for a time  $t_{\text{wait}}$ , during which the CBA can switch states with a switching probability given by

$$P_{01}(V_d, I_0) = 1 - \exp(-t_{\text{wait}}\gamma(I_0)) \quad (2.61)$$

When  $t_{\text{wait}}$  is too short, the s-curves are widened and shifted to higher input voltages (see Fig. 2.32). At longer  $t_{\text{wait}}$ , the s-curves converge and hence we try to minimize  $t_{\text{wait}}$  in order to maximize the CBA’s measurement repetition time. Following  $t_{\text{wait}}$ , we decrease the input voltage slightly in order to latch in the

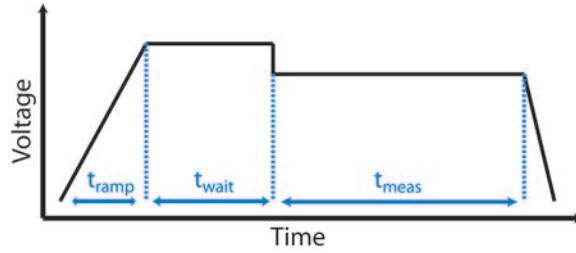


Figure 2.31: Readout pulse shape used to measure the s-curves of the CBA. The ramp time is limited by the  $Q$  of the device and the wait time must be adjusted to optimize the width of the s-curve. If the wait time is too short the s-curve will be shifted to higher voltages and will be artificially widened and for longer wait times the s-curves converge. The measuring time is chosen based on the needed signal to noise.

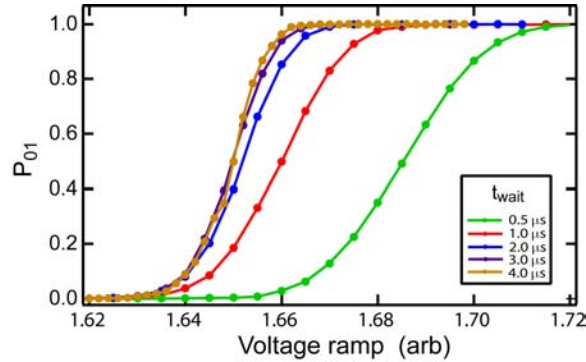


Figure 2.32: S-curves versus wait time,  $t_{wait}$ , for sample 1 with  $\omega_0 = 1.829$  GHz and  $\Gamma = 0.4$  MHz (see table 2.2). In this case  $t_{ramp} = 2 \mu s$  and  $t_{meas} = 4 \mu s$ . They were measured with an intermediate frequency (IF or mixed-down) frequency of 5 MHz, 20 ns sampling interval and 2000 averages per point. For this data, the de-tuning is  $\Omega = 9.75$  with a base temperature of  $T = 220$  mK

CBA's state. The final measuring time,  $t_{meas}$ , can then be increased indefinitely depending on the needed signal to noise and measurement repetition time.

S-curves for three of the samples measured are shown in Fig. 2.33b, along with corresponding simulations of their series LRC model (Eqn. 2.26) using a fourth order Runge-Kutta algorithm (see appendix C.1). The data's voltage scale has been re-normalized by the bifurcation voltage,  $V_b$ , in order to fit the simulated

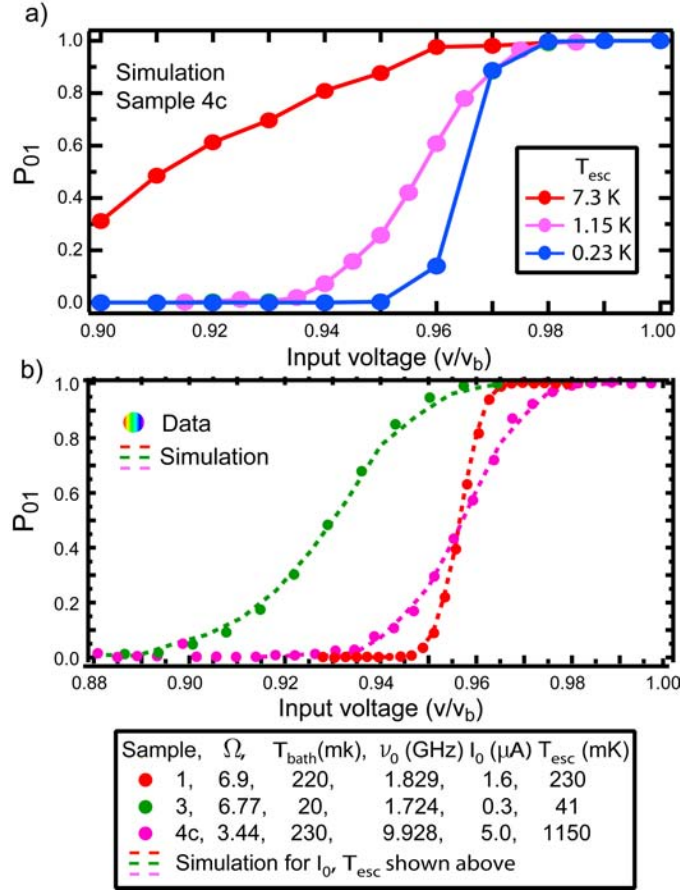


Figure 2.33: **(a)** Simulated s-curves for the parameters of sample 4c for 3 different escape temperatures,  $T_{\text{esc}}$ . The latching pulse has a 300 ns ramp and wait time. Each simulated point in switching probability,  $P_{01}$ , is estimated from approximately 300 switching events, each of which takes approximately 3 seconds to simulate. Hence, a full s-curve of 20 points takes 5 hours to simulate. **(b)** Measured (dots) and simulated (dashed lines) s-curves for samples 1, 3 and 4c. The width of the s-curves for samples 1 and 3 are as expected. However, sample 4c has a width which can only be explained with an effective temperature that is five times higher than expected (similar to all samples with  $\nu_0 \sim 10$  GHz).

curves. When a single junction sample is being measured (e.g., sample 1 and 3), the critical current is estimated based on fabrication and fits from the escape rate experiments described in the previous section. The width of the s-curve for sample 1 is consistent with the fridge bath temperature of 220 mK. The width of

the s-curve for sample 3 is consistent with the expected escape temperature based on escape via quantum activation  $T_{\text{esc}} = \frac{\hbar\omega}{2k_B} = 41$  mK (see R. Vijay's thesis [77] for more details on this point). However, sample 4c has a width much wider than expected based on the fridge bath temperature and on the quantum limited escape temperature, both of which were approximately 220 mK. In order to reproduce the data, I needed to use an effective temperature five times higher than expected,  $T_{\text{esc}} = 1.15$  K.

The expected width of these s-curves can also be analytically estimated from the escape theory based on the Duffing oscillator, described above in section 2.6.1. We can define the width of an s-curve as the difference between the bifurcation voltage  $V_b$  and the voltage at which  $U = k_B T_{\text{esc}}$ , where we have an appreciable escape rate  $\gamma$ . Hence the width is given by

$$\delta V = V_b - V_d|_{U=k_B T_{\text{esc}}}. \quad (2.62)$$

Using Eqn. 2.56 in Eqn. 2.62 we get

$$\frac{\delta V}{V_b} = \left( \frac{k_B T_{\text{esc}}}{U_0} \right)^{(2/3)}. \quad (2.63)$$

Using this equation for the width of the s-curves, we can again test the escape theory based on the Duffing oscillator by measuring the width of the s-curves and extracting  $\frac{U_0}{k_B T_{\text{esc}}}$  to test its dependence on reduced detuning  $\Omega$ . The results are shown in Fig. 2.34, where we again see a linear scaling at large  $\Omega$  as expected. Note again however, that especially for the 10 GHz resonators,  $T_{\text{esc}}$  is a few times higher than expected. As explained in the previous section, this is probably due to insufficient filtering in the output lines <sup>1</sup>.

---

<sup>1</sup>This hypothesis was tested by inputting extra external noise on the RF lines which resulted in an increase in  $T_{\text{esc}}$ . The best test is to develop better RF filters and measure a decrease in  $T_{\text{esc}}$  (see appendix B).

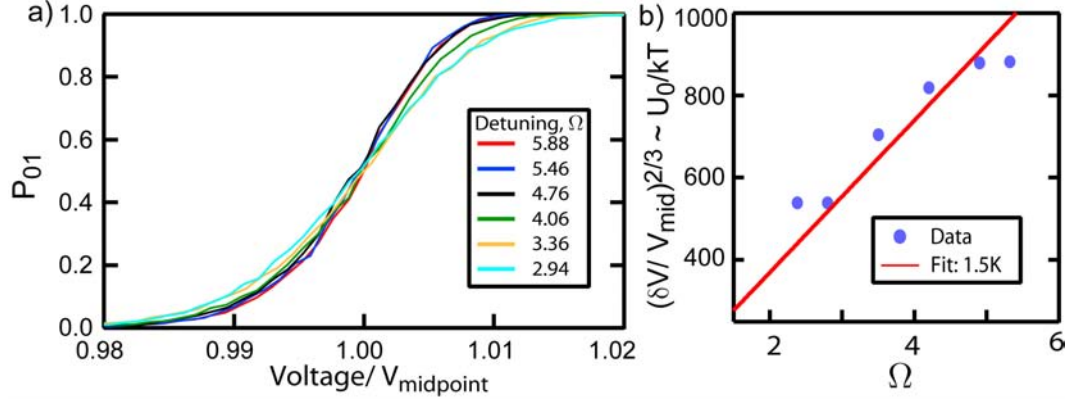


Figure 2.34: (a) S-curves vs. detuning for sample 5a. (b) Extracted s-curve width vs. detuning. It shows the expected 2/3 behavior with de-tuning.

Any phenomenon that can be coupled to the Josephson energy will change the power at which the transition occurs. Hence, we can measure the smallest critical current change that the CBA can discriminate by measuring the shift in the s-curves. To facilitate this measurement, we construct the Josephson junction in a SQUID geometry. Then, by applying a magnetic field to the SQUID loop we can change the critical current of the SQUID and hence, the bifurcation voltage  $V_b$ . An example of data from such an experiment is shown in Fig. 2.35, where I have plotted the s-curves of sample 2 vs. applied magnetic field. In particular, a critical current change of 1.5 nA gives two the s-curves shown in Fig. 2.35c, which are maximally separated by 67% - or twice the standard deviation of their distributions.

For comparison, we can use the Duffing oscillator escape theory to calculate the expected discrimination power of the CBA. We define the discrimination power of the CBA as the smallest current change,  $\Delta I_0$ , that shifts the s-curve by its width  $\delta V$ , i.e.,

$$\Delta I_0 = \frac{\delta V}{dV_b/dI_0}. \quad (2.64)$$

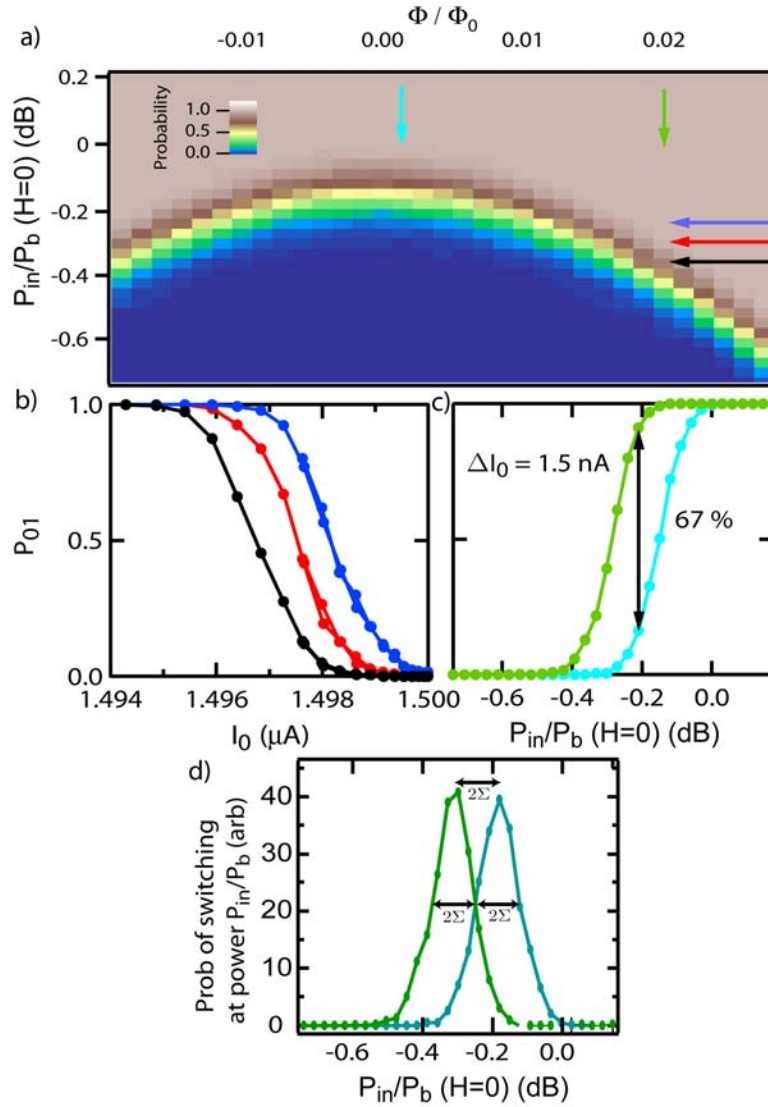


Figure 2.35: **(a)** For each magnetic field we measure an s-curve, i.e., the probability of the CBA switching out of the low oscillating state as a function of applied power. The data shown is for sample 2 which has a SQUID configuration. **(b)** These are cuts versus magnetic field where the field has been converted to the corresponding value of critical current. From this data we see we can discriminate a current change of about 2 nA, close to the theoretically predicted value of 1.5 nA. **(c)** These are two s-curves at 1.5000  $\mu A$  and 1.4985  $\mu A$ . Their maximum separation is 67%. **(d)** The two distributions corresponding to the s-curves in (c) are separated by twice their standard deviation.

Sample	1	2	3	4b	5d
$\omega_0$ (GHz)	1.8293	1.8177	1.724	10.154	9.395
$\Delta I_0^{meas}$ (nA)	0.75	1.5	0.4	7	6.4
$\Delta I_0^{thy}$ (nA)	0.9	1.1	0.3	2.3	2.7

Table 2.3: Table of measured and predicted discrimination powers for various CBA samples

Hence, using Eqn. 2.63 in Eqn. 2.64, the smallest current we can discriminate is given by

$$\Delta I_0 = \frac{2}{3} \left( \frac{9\sqrt{3}}{32} \right)^{2/3} \left( \frac{K_B T_{esc}}{\phi_0^2/L} \right)^{2/3} \left( \frac{\Omega}{Q} \right)^{1/3} \frac{\phi_0}{L} \quad (2.65)$$

The theoretical and experimental results for most of the measured samples are given in table 2.3. Good agreement is obtained for the 2 GHz resonators. However, we see again that the 10 GHz resonators have excess noise which reduces their sensitivity.

## 2.7 Conclusions

In conclusion, we have observed the dynamical bifurcation of a superconducting microwave resonator incorporating a non-linear element in the form a Josephson tunnel junction. We have implemented this resonator using, at first, lumped circuit elements, known as the Josephson bifurcation amplifier (JBA) and, later, distributed circuit elements, known as the cavity bifurcation amplifier (CBA). Comparing the two devices, the distributed element implementation offers ease of fabrication, greater range of operating parameters and future multiplexing possibilities. Therefore, I have decided to concentrate on this implementation for future applications such as in reading the state of a superconducting qubit.

The CBA was shown to agree with the steady state Duffing oscillator theory with great precision, demonstrating our precise control of the on-chip circuit environment and our understanding of the behavior of this system. However, the escape dynamics of the CBA demonstrated some discrepancies with the expected behavior. Nonetheless, the measured sensitivity of the CBA is still sufficient to readout the state of SCPB qubit with single-shot capability.

## Chapter 3

# The Quantronium qubit with CBA readout

Having described the performance of the cavity bifurcation amplifier (CBA) in the previous chapter, I will now apply it to the readout of the state of a superconducting qubit. The qubit of choice is the split Cooper pair box (SCPB), which is the superconducting qubit with some of the longest measured relaxation and decoherence times to date [70], [49] (see section 4.5.1 for implementations with other superconducting qubit types). Charge noise with a  $1/f$  spectrum is the main factor limiting this qubit's decoherence time  $T_2$  (see section 1.4.2). However, the CBA readout scheme is compatible with operating the SCPB with higher  $E_J/E_{CP}$  ratios where the qubit is more immune to this noise. Also, one can manipulate and measure the qubit state without displacing it from the so-called "sweet spot". At this point, the qubit is immune to first order fluctuations in both charge and flux. Other advantages of the CBA are its speed and sensitivity, which we can exploit to investigate the main source of the noise present in this superconducting qubit.

In this chapter, I will begin with a short theoretical description of the SCPB and then continue with a detailed study of the implementation of the CBA as a

readout for the SCPB.

### 3.1 Superconducting qubit: split Cooper pair box (SCPB)

A Cooper pair box (CPB) [48, 57] consists of a small superconducting island that is isolated from its environment by a capacitor  $C_g$ , which is connected to a voltage source  $V_g$ , and also by a small Josephson junction with self capacitance  $C_J$ , which leads to a superconducting reservoir. The single degree of freedom of this circuit is the excess number of Cooper pairs of the island,  $N$ . Cooper pairs can be brought onto the island from the reservoir by controlling the gate voltage  $V_g$ . The behavior of this system is dependent on its two main energy scales - the Josephson energy of the junction  $E_J$ , and the Cooper pair Coulomb energy  $E_{CP}$ .  $E_{CP}$  is the characteristic energy cost of a Cooper pair entering the island and is given by

$$E_{CP} = \frac{(2e)^2}{2C_\Sigma}, \quad (3.1)$$

where  $C_\Sigma = C_g + C_J$  is the total capacitance of the island. Typically,  $C_g$  is on the order of a few attofarads so that  $C_\Sigma$  is dominated by  $C_J$ , which is of the order of a few femtofarads. For a wide range of  $E_J/E_{CP}$ , this system can behave as a two level system and hence can be utilized as a qubit. This ratio can easily be tuned by varying the area of the qubit, because,  $E_{CP} \propto 1/C_J \propto 1/area$ , and  $E_J \propto area$ , giving  $E_J/E_{CP} \propto area^2$  (see section 4.3 for more discussion on this point).

The  $E_J/E_{CP}$  ratio can actually be altered in situ during an experiment by using a slightly modified version of the CPB, in which the junction is split into two. The superconducting island now lies in-between the two junctions and their outer electrodes are connected with a superconducting loop (see Fig. 3.1a). This

modified circuit is known as a split Cooper pair box and it behaves like a regular CPB with a Josephson energy  $E_J^*(\delta)$  that depends on a magnetic field  $\Phi$  applied through the superconducting loop. The field imposes a superconducting phase difference across the two junctions  $\delta$ , where  $\Phi = \phi_0 \delta$ .

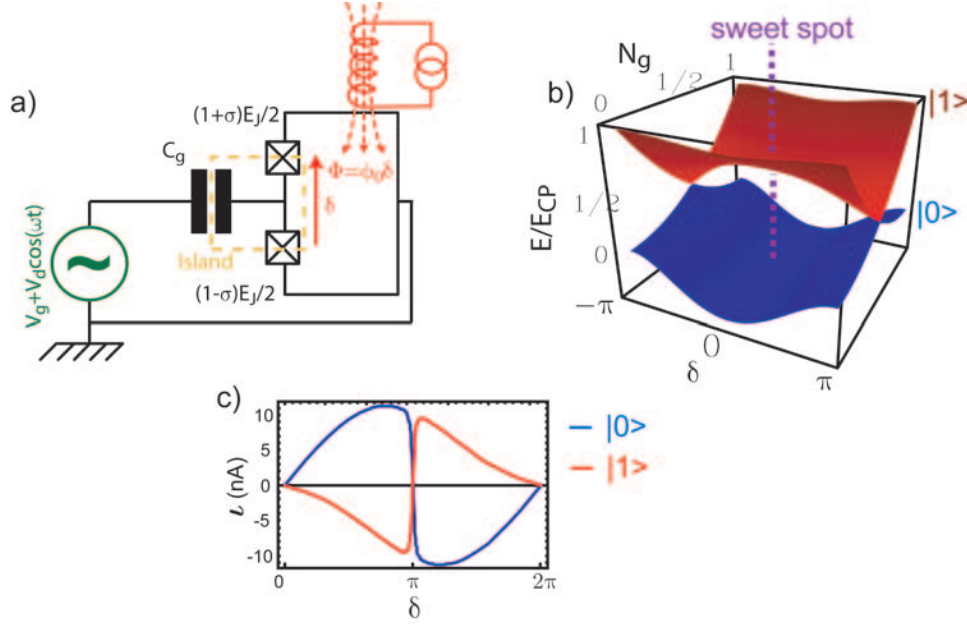


Figure 3.1: **(a)** Schematic of the split Cooper pair box (SCPB). The two small Josephson junctions, connected via a superconducting loop, behave like a single effective CPB with tunable  $E_J(\delta)$ . When there is no asymmetry between the junctions ( $\sigma = 0$ ),  $E_J^* = E_J \cos(\delta/2)$ . **(b)** Plot of the first two energy levels of the SCPB for  $E_J/E_{CP} = 1$ . The transition frequency  $\nu_{01}$  is tuned using both the gate charge  $N_g = \frac{C_g V_g}{2e}$  and the flux through the loop  $\Phi = \phi_0 \delta$ , where  $\delta$  is the superconducting phase difference across the two Josephson junctions. We typically operate on the “sweet spot” where the SCPB is immune to first order fluctuations in both  $N_g$  and  $\delta$ . **(c)** Plot of the loop currents in the SCPB superconducting loop (for  $E_J/E_{CP} = 1$ ) for the ground and first excited state at  $N_g = 0.5$ .

### 3.1.1 Hamiltonian of SCPB

To calculate the energy levels of this system, one begins with the Hamiltonian of this system in the charge representation, i.e., using the excess number of Cooper

pairs on the island  $N$ , where  $\hat{N}|N\rangle = N|N\rangle$ . At energies lower than  $\Delta$ , there are no quasiparticles present so that the eigenstates  $|N\rangle$  are a complete basis of states.

The Hamiltonian consists of two main parts - the electrostatic Hamiltonian  $\hat{H}_{el}$ , and the Josephson Hamiltonian  $\hat{H}_J$ . The electrostatic part of the Hamiltonian can be written as

$$\hat{H}_{el} = E_{CP}(\hat{N} - N_g)^2, \quad (3.2)$$

where  $N_g = \frac{C_g V_g}{2e}$  is the reduced gate charge in units of Cooper pairs. The Josephson energy part of the Hamiltonian couples consecutive charge states. For simplicity, assume the situation where the junctions are perfectly symmetric  $\sigma = 0$ , so that the Josephson term is given by

$$\hat{H}_J = -\frac{E_J^*}{2} \left( \sum_{N \in \mathbb{Z}} |N\rangle\langle N+1| + |N+1\rangle\langle N| \right), \quad (3.3)$$

where  $E_J^* = E_J \cos(\delta/2)$  (i.e., tunable with an applied magnetic field). Note that an asymmetry, i.e.,  $\sigma \neq 0$ , would lift the energy level degeneracy between the ground and first excited states at  $\delta = \pi, N_g = 1/2$ . This Hamiltonian can be rewritten in the phase representation  $\hat{\theta}$ , where  $\hat{\theta}$  is the superconducting phase of the island, conjugate to the charge operator  $\hat{N}$ , giving

$$\hat{N} = \frac{1}{i} \frac{\partial}{\partial \hat{\theta}}. \quad (3.4)$$

Hence, in the phase representation the total Hamiltonian of the SCPB is given by

$$\hat{H}(N_g, \delta) = E_{CP} \left( \frac{1}{i} \frac{\partial}{\partial \hat{\theta}} - N_g \right)^2 - E_J^*(\delta) \cos(\hat{\theta}). \quad (3.5)$$

### 3.1.2 Energy levels

Full analytical expressions for the energy levels of the SCPB can be obtained in the phase representation (see [91] for more details) with the Schrödinger equation

$$E_{CP} \left( \frac{1}{i} \frac{\partial}{\partial \theta} - N_g \right)^2 \Psi_k(\theta) - E_J^* \cos(\theta) \Psi_k(\theta) = E_k \Psi_k(\theta), \quad (3.6)$$

where  $E_k$  is the  $k^{\text{th}}$  energy level with energy eigenstate  $|k\rangle$ , and wavefunction  $\Psi_k(\theta) = \langle \theta | k \rangle$  that follows the boundary condition

$$\Psi_k(\theta) \equiv \Psi_k(\theta + 2\pi). \quad (3.7)$$

This Schrödinger equation has been solved in terms of the well known Mathieu functions [92], giving the eigenstates and eigenfunctions,

$$E_k = \frac{E_{CP}}{4} \mathcal{M}_A \left( r_k, -\frac{2E_J^*}{E_{CP}} \right), \quad (3.8)$$

$$\Psi_k(\theta) = \frac{e^{iN_g\theta}}{\sqrt{2\pi}} \left[ \mathcal{M}_C \left( \frac{4E_k}{E_{CP}}, -\frac{2E_J^*}{E_{CP}}, \frac{\theta}{2} \right) + i(-1)^{k+1} \mathcal{M}_S \left( \frac{4E_k}{E_{CP}}, -\frac{2E_J^*}{E_{CP}}, \frac{\theta}{2} \right) \right],$$

where  $r_k = k + 1 - (k + 1)[\text{mod } 2] + 2N_g(-1)^k$ ,  $\mathcal{M}_{C,S}$  are the Mathieu functions and  $\mathcal{M}_A$  is known as a Mathieu characteristic function, an eigenvalue of  $\mathcal{M}_C$ . An example of the energy levels  $E_k$  vs.  $N_g$  and  $\delta$  for  $k = 0$  &  $1$  is shown in Fig. 3.1b. We typically operate this qubit at the indicated “sweet spot”  $N_g = 0.5$ ,  $\delta = 0$ , where

$$\frac{\partial(E_1 - E_0)}{\partial N_g} = \frac{\partial(E_1 - E_0)}{\partial \delta} = 0. \quad (3.9)$$

Having a “sweet spot” is an essential feature of this qubit system because, at this operating point, the qubit is immune to first order fluctuations in both of the parameters  $N_g$  and  $\delta$ .

The ratio  $E_J/E_{CP}$  determines the charge content of the energy levels, as shown in Fig. 3.2. If  $E_J/E_{CP} \ll 1$ , the energy levels  $|k\rangle$  approach pure charge states  $|N\rangle$ ,

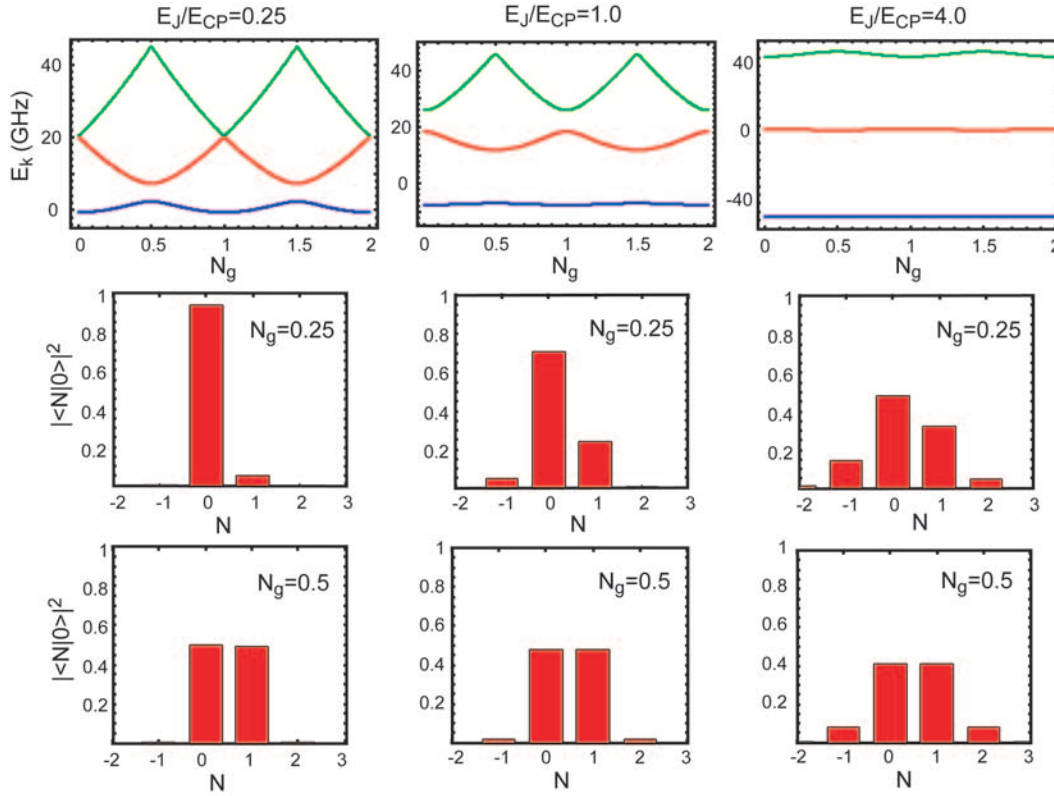


Figure 3.2: The first three energy levels of the SCPB for three different ratios of  $E_J/E_{CP}$ . As this ratio increases, the levels flatten out and resemble a harmonic oscillator for large values. The energy levels look more like charge states for low values of this ratio. Note, as  $E_J/E_{CP}$  increases, the charge content dependence of the energy levels on  $N_g$  diminishes.

except for the region in the vicinity of the “sweet spot”, where the electrostatic energy difference between the two charge states  $|N\rangle$  &  $|N+1\rangle$  is on the order of, or smaller than,  $E_J$ . In this region, the ground state of the system is a superposition of these two charge states  $(|N\rangle + |N+1\rangle)/\sqrt{2}$ , and exactly at the “sweet spot,” the transition energy is given by  $E_{01} = \hbar\omega_{01} = E_J$ .

For larger  $E_J/E_{CP}$  ratios, the system’s energy levels flatten out with respect to charge  $N_g$  and resembles an harmonic oscillator with equally spaced energy levels. The phase  $\theta$  of the island becomes a good quantum number, and due

to the Heisenberg uncertainty relation, we get large quantum fluctuations of the island charge  $N$ . Because  $E_{01}$  is insensitive to changes in  $N$ , this could be a useful region to operate the SCPB if there is a large amount of charge noise present in the sample. In the limit of large  $E_J/E_{CP}$ , the transition energy  $E_{01} = \hbar\omega_{01}$  converges to  $\hbar\omega_p = \sqrt{2E_J E_{CP}}$ .

The equality between the energy level transitions can be quantified using the anharmonicity  $\mathcal{A}$ , which is defined as

$$\mathcal{A} = 2 \frac{\nu_{12} - \nu_{01}}{\nu_{12} + \nu_{01}}. \quad (3.10)$$

An anharmonicity of zero means that one can not individually address the energy level transitions. Consequently, a device with this property would not be useful as a qubit. Figure 3.3 shows that for  $E_J/E_{CP} = 2$  and operating at the “sweet spot”, the first three energy levels are equally spaced. A good working point

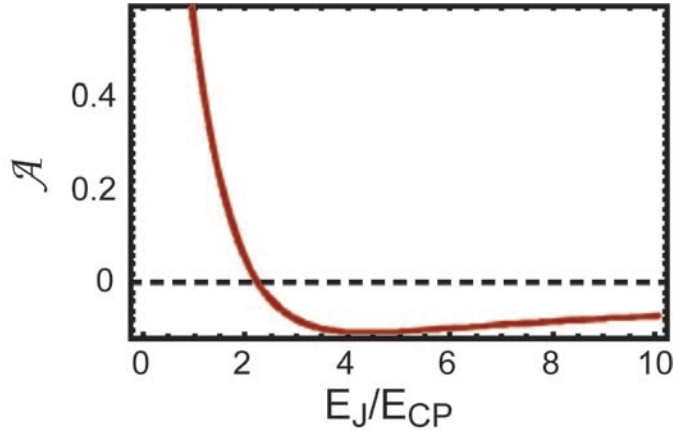


Figure 3.3: Anharmonicity of the SCPB energy levels at  $N_g = 0.5$ ,  $\delta = 0$ .

would be  $E_J/E_{CP} = 4$ , where the system is still sufficiently anharmonic and has good charge noise immunity. The choice of  $E_J/E_{CP}$  results from a competition between how much one can tolerate charge noise, the SCPB parameter you are

measuring (see next section), the desired transition frequency  $\nu_{01}$ , and the needed anharmonicity  $\mathcal{A}$  of the energy levels.

## 3.2 SCPB readout scheme

### 3.2.1 Charge readout

The ground and first excited states of the SCPB have different charge content, especially for low  $E_J/E_{CP}$ . Hence, one can distinguish between the energy states by measuring their charge content. This was the first method used to measure the state of the CPB [58] (see section 1.4.2). The measurement used a single electron transistor (SET) capacitively coupled to the island, and was thus sensitive to the average island potential  $V$ . An expression for this potential can be derived from the generalized Josephson relation

$$\hat{V} = \phi_0 \frac{d\hat{\theta}}{dt} = -\frac{1}{2e} \frac{\partial \hat{H}}{\partial N}. \quad (3.11)$$

Hence,

$$\hat{V} = \frac{1}{2e} \frac{\partial \hat{H}}{\partial N_g} = \frac{2e(N_g - \hat{N})}{C_\Sigma}. \quad (3.12)$$

A measure of the average potential of the island is therefore related to the average charge of the island, which is proportional to the first derivative of the energy levels with respect to charge:

$$\langle k | \hat{V} | k \rangle = \frac{E_{CP}}{e} \left( N_g - \langle k | \hat{N} | k \rangle \right) = \frac{1}{2e} \frac{\partial E_k(N_g)}{\partial N_g} \quad (3.13)$$

However, note from Eqn. 3.13 that the signal is proportional to  $\frac{\partial E_k}{\partial N_g}$ , which is zero at the “sweet spot”. Hence, to get a measurable signal, the qubit must be moved to a more sensitive point before measurement. Also, the signal increases as  $E_J/E_{CP}$  decreases, making the system more anharmonic and more sensitive to charge noise.

### 3.2.2 Current measurement

An alternative to the charge readout method of the qubit energy states is to measure the currents in the superconducting loop of the SCPB. These currents differ in both magnitude and direction depending on the qubit energy state and biasing conditions (see Fig. 3.1c). The current measurement has the benefit of being sensitive for larger  $E_J/E_{CP}$  ratios compared to the charge readout method. If  $N_1$  is the number of Cooper pairs tunneling through junction 1 and  $N_2$  is the number for junction 2, then the operator for the loop current is given by

$$\hat{I}(N_g, \delta) = -2e \frac{d\hat{K}}{dt}, \quad (3.14)$$

where  $\hat{K} = (\hat{N}_1 + \hat{N}_2)/2$ . Hence, the average loop current for the energy eigenstate  $|k\rangle$  is given by

$$\iota_k(N_g, \delta) = \frac{1}{\phi_0} \frac{\partial E_k(N_g, \delta)}{\partial \delta}. \quad (3.15)$$

Figure 3.1c shows an example of these currents for  $\delta = 0$  and  $E_J/E_{CP} = 1$ . Similar to the charge readout, which has no signal at the charge optimal point, this scheme has no signal at the flux optimal biasing point, where  $\frac{\partial E_k}{\partial \delta} = 0$ . However, as mentioned before, the signal is now proportional to  $E_J$  and hence, the SCPB can operate in a regime which is more immune to charge noise.

### 3.2.3 SCPB with CBA readout

The rest of this chapter describes the implementation of the SCPB with CBA readout [52]. Unlike the above two readout schemes (charge and current), this readout is sensitive to the second derivative of the energy levels of the SCPB and hence, the SCPB never needs to be moved away from the optimum biasing point.

From Eqn. 3.15, one obtains

$$L_k(N_g, \delta) = \left( \frac{1}{\phi_0} \frac{\partial \nu_k}{\partial \delta} \right)^{-1} = \left( \frac{1}{\phi_0^2} \frac{\partial^2 E_k}{\partial \delta^2} \right)^{-1}, \quad (3.16)$$

for the effective inductance  $L_k$  of the energy level  $|k\rangle$ . When the SCPB is placed

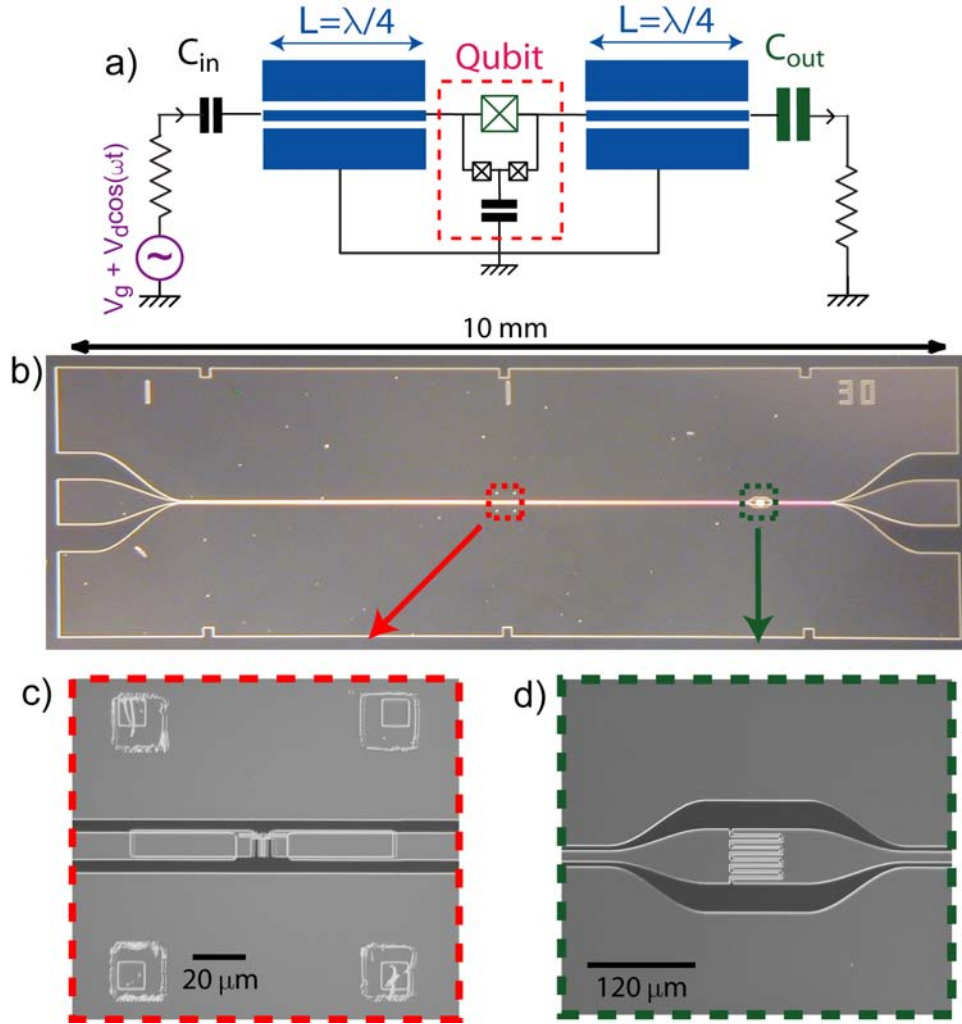


Figure 3.4: **(a)** Schematic of the quantronium with CBA readout device. **(b)** Optical image of resonator used in qubit readout. No meander of the resonator is needed due to its resonance frequency of about 10 GHz. **(c)** Optical image of center of resonator. We can see the four alignment marks surrounding the finished qubit sample. The marks have been exposed during the e-beam steps. **(d)** Optical image close up of large output finger capacitor  $C_{out}$ .

in parallel with the CBA's junction to form a circuit, known as the quantronium

(for schematic see Fig. 3.4a), the effective inductance of the ground state  $L_0$  and excited state  $L_1$  gives the resonator two bifurcation powers,  $P_b^{(0)}$  and  $P_b^{(1)} < P_b^{(0)}$ , depending on the state of the qubit  $|0\rangle$  or  $|1\rangle$ . The two qubit states are mapped into the two metastable states of the CBA by quickly ramping the power  $P$  to a level intermediate between  $P_b^{(0)}$  and  $P_b^{(1)}$ . If the quantronium qubit is in  $|1\rangle$ , the CBA will switch to the high oscillating state; whereas, if it is in  $|0\rangle$ , the CBA will remain in the low oscillating state. Note that the previous descriptions make the assumption of the adiabatic limit, where the readout frequency is much less than the qubit frequency. The qubit is assumed to remain in its instantaneous state during readout. For higher readout frequencies one must treat the full system quantum mechanically and could result in effects such as readout induced qubit excitations.

For completeness, I will now summarize the main motivations in developing the CBA readout scheme, some of which have been discussed in detail in the introduction and chapter 1 (see for example 2.4.4, 1.5.1). Firstly, this readout has the advantage of being non-dissipative as the readout junction never switches into the normal state, unlike the original DC-biased quantronium readout [49]. This dispersive readout minimally disturbs the qubit state. Since one does not need to wait for quasiparticles to relax after switching, the repetition rate is only limited by the relaxation time  $T_1$  of our qubit and the  $Q$  of our resonator. Like the DC readout, the CBA readout can latch [74], allowing enough time for the measurement of the complex amplitude of the transmitted wave, and therefore, excellent signal to noise ratio. These characteristics were also present in the Josephson bifurcation amplifier [74, 75, 51], which implemented a bifurcating non-linear oscillator using a lumped element capacitor in parallel with the junction (see section 2.2.1). However, this capacitor was fabricated using a Cu/Si<sub>3</sub>N<sub>4</sub>/Al

multilayer structure, which was difficult to fabricate and integrate with more than one qubit. Also, the parallel plate geometry suffered from inherent stray inductive elements. In contrast, the CBA is fabricated using a simple coplanar waveguide geometry with no stray elements. The resonance frequency  $\nu_0$  and the quality factor  $Q$  are controlled by the resonator length and output capacitor, respectively. The CBA geometry thus offers the possibility of designing a multi-resonator chip with multiplexed readouts, which could accommodate tens of qubits at once, an important step towards scalable quantum computing (see section 4.1).

### 3.2.4 Fabrication of SCPB in a CBA resonator

Figure 3.4b, c & d shows an optical image of the completed device. For this particular sample, I fabricated an Al lift-off resonator with a linear regime resonance frequency  $\nu_0 = 9.64$  GHz and a  $Q$  of 160. To fabricate the resonator, photolithography with an LOR5A/S1813 optical resist bilayer is used on a bare Si wafer [83]. The development is optimized to have at least 50 nm of undercut beneath the S1813 to avoid wavy edges and to obtain a sloped edge on the resonator. This sloped edge is obtained by evaporating a 200 nm thick Al layer onto the sample at 0.2 nm/s with an angle of  $5^\circ$  and with a stage rotation of  $10^\circ/\text{s}$ . A more detailed fabrication procedure is described in section 2.4.1.

Next, the quantronium is fabricated using electron beam lithography inside the resonator. A MMA/PMMA resist bilayer and the Dolan bridge double angle evaporation technique are used to fabricate the junctions [55] (see section 1.3.1). This sample actually involves the use of two separate Dolan bridge shadow mask evaporation steps. The split Cooper pair box is fabricated first by itself inside the resonator using the regular lift-off process (Fig. 3.5a). After lift-off, the sample is re-spun with a bilayer of MMA/PMMA resist. However, this time the resist is

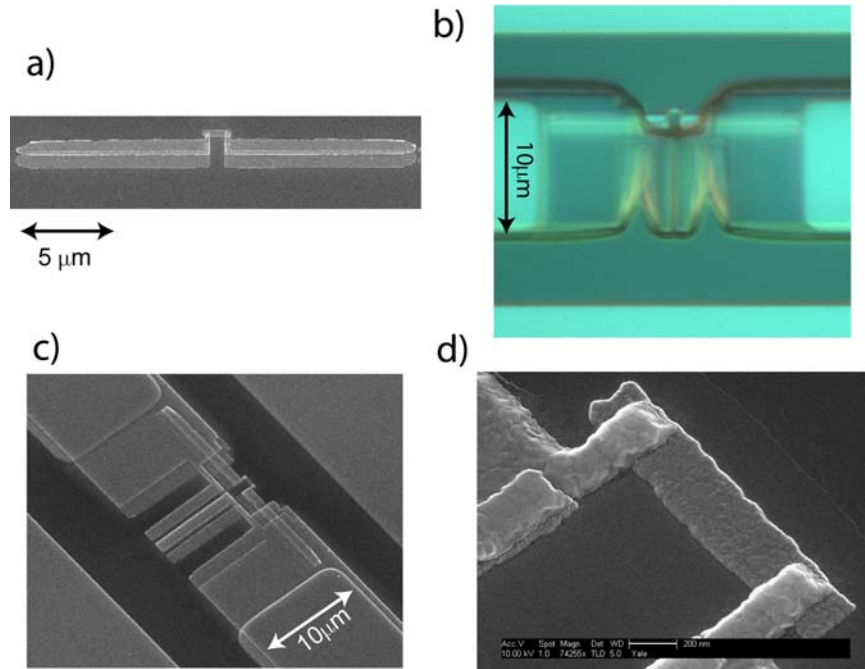


Figure 3.5: **(a)** An SEM image of the SET layer after lift-off. **(b)** An optical image of second layer of resist with the developed pattern for the large readout junction aligned to the SET layer **(c)** An SEM image of the finished qubit sample at the center of the CPW resonator. **(d)** Close up of the SET of the finished qubit sample.

only baked at  $90^\circ$  for 5 min to avoid damaging the SCPB's small junctions. The pattern for the large readout junction is now written in the SEM (Fig. 3.5b). The chip is then placed in the evaporator. Using a hollow cathode Ar ion gun before beginning the evaporation, an ohmic contact is obtained between the two e-beam layers and the resonator.

There are three reasons for separating the fabrication of the SCPB and the readout junction into two steps. Firstly, the resist bilayer can be spun to different thicknesses, depending on the needed size of the lateral shift between the two evaporation angles. The SCPB layer requires a lower resist height compared to the large readout junction layer. The thinner resist layer is better for obtaining

higher resolution and evaporation reproducibility for the SCPB layer. Secondly, different oxidation times and pressures for the SCPB and readout junction could be needed (e.g., 3 – 10 T, 5 – 15 min for readout and 10 – 70 T, 10 – 30 min for qubit). Having two fabrication layers gives more tunability when looking for specific device parameters. Lastly, the resonator’s center pin must be Ar ion cleaned to make a good ohmic contact with the e-beam evaporation layers. However, from previous experience, if Ar ion cleaning is performed before the deposition of the SCPB on a Si substrate, a “leaky” gate line is obtained. This means that when a gate voltage is applied, a small current flows across the gate capacitance  $C_g$ . By making the SCPB in the first layer and Ar ion cleaning in a subsequent layer, when the SCPB is covered with a bilayer of resist (Fig. 3.5b), this problem can be avoided.

In order to get an idea of the SCPB and readout junction resistance, on-chip twins of them are fabricated just off the edge of the resonator’s ground planes. The twin that corresponds to Figs. 3.5c & d had a SCPB normal state resistance of 15 k $\Omega$  with small junction areas of 0.05  $\mu\text{m}^2$ . The typical readout junction resistance is 70  $\Omega$ , corresponding to a critical current of 4  $\mu\text{A}$ .

### 3.2.5 Experimental setup

This experiment was carried out in a Kelvinox 25 dilution refrigerator with a base temperature of 40 mK. The experimental setup shown in Fig. 3.6 is very similar to that used for the CBA readout measurements, with one output RF line and two input RF lines (see section 2.5.1). However, unlike the previous CBA experiments, we have now added a DC gate line onto the output line via a bias tee.

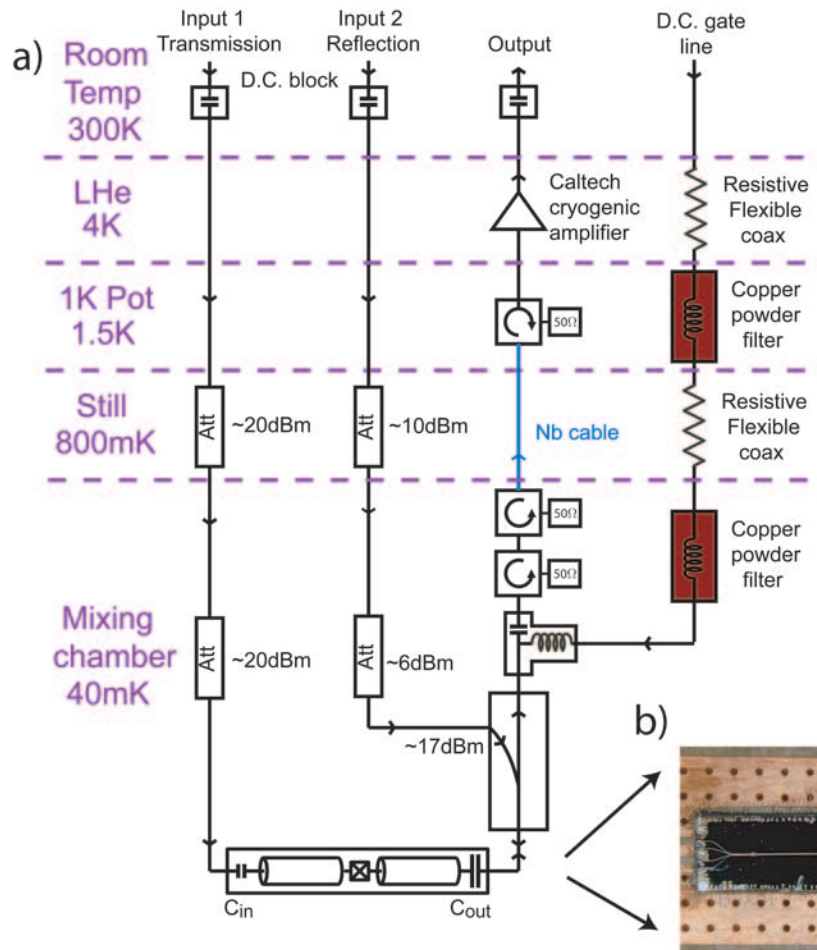


Figure 3.6: (a) A schematic of the kelvinox 25 fridge setup. The sample can be measured either in reflection or transmission measurements. Compared with the CBA readout setup (Fig 2.15) a bias tee is added to input a DC gate line. (b) Picture of the wirebonded mounted sample in a PCB launch.

## RF lines

The input lines are again filtered with attenuators that attenuate noise at all frequencies uniformly. The output lines have three circulators which are thermalized at varying temperatures. These provide excellent filtering in-band. However, for out of band noise, we do not have much filtering on the output RF lines because it proved difficult to fabricate dissipative filters which cutoff at high enough fre-

quencies (see section 2.5.1 and appendix B). This could be a limiting factor for the sensitivity of the CBA readout.

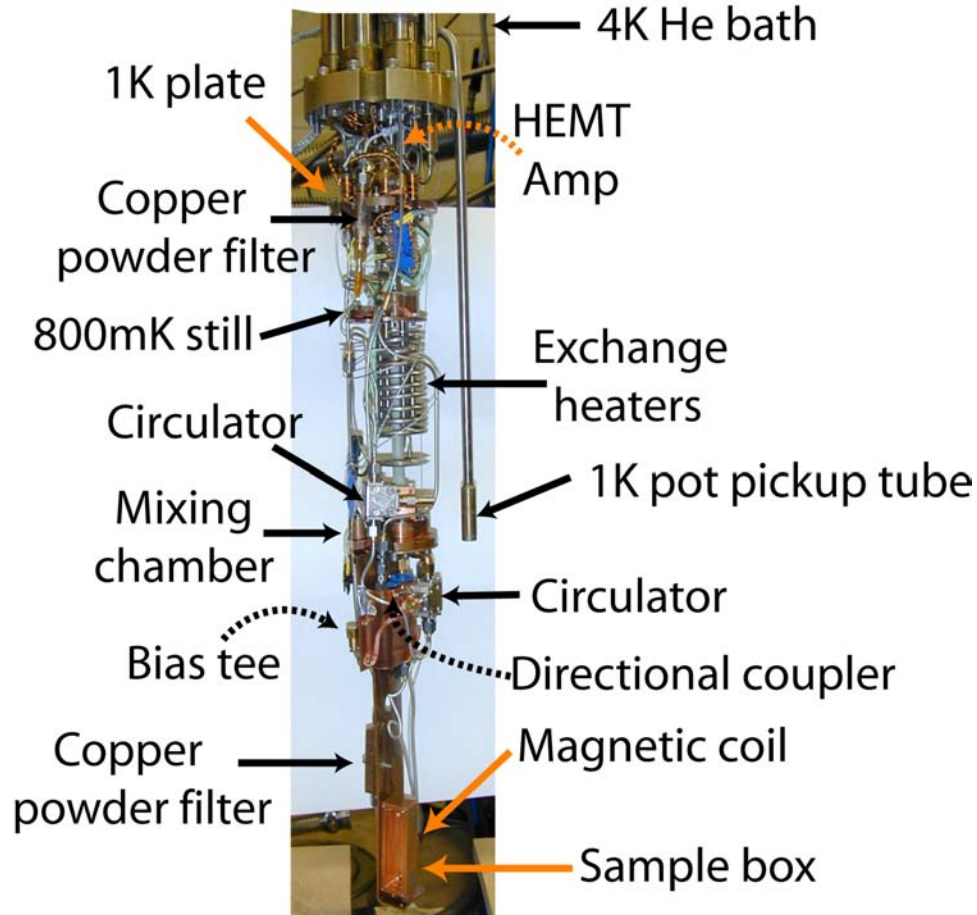


Figure 3.7: A photograph of microwave setup inside the vacuum can of the Oxford Kelvinox 25 refrigerator.

### DC gate lines

Unlike the RF lines, the DC lines do not require a high bandwidth. These lines control the gate charge  $N_g$  of the qubit and is changed on a slow time-scale. Hence, we have used commercial LC low-pass filtering that have megahertz cutoff frequencies. However, as discussed before, at frequencies in the tens of gigahertz

range, these lumped element filters develop resonances and can become transparent near these resonances. Copper powder filters used in the DC lines avoid this problem. These consist of a coil of insulated copper wire immersed in a box of Cu powder which is lossy at high frequencies. Note that low pass filtering is also provided by the large inductance in the bias-tee. This is the device that enables us to combine the RF lines and DC lines together just before launching onto the sample. A capacitor on the RF line isolates it from the DC line.

The DC line is connected onto the large output capacitor  $C_{out}$  of the CBA to maximize the coupling to the island of the SCPB. Considering that typically  $C_{out} \sim 30$  fF and the capacitance of the island to ground is about  $C_g \sim 50$  aF, calculations show that about 1 V is required at room temperature per  $2e$  period of the SCPB.

### Room temperature electronics

Readout and qubit manipulation pulses are constructed by using RF mixers to combine continuous RF signals with fast DC envelope pulses. All these pulses must be synchronized with each other. This was typically achieved using a dual channel arbitrary waveform generator (AWG). This instrument has two outputs that are in-sync and also has two trigger outputs per channel which can be used to trigger many other pulse generators.

In this experiment, leakage of RF power outside the pulse envelope must be minimised. Leakage of the qubit pulse power will lead to uncontrolled qubit state manipulations and can also change the readout biasing point. Similarly leakage in the readout pulse can lead to qubit manipulation errors and also loss of readout signal to noise. An easy method to cancel the leakage outside our qubit pulses at all frequencies is achieved by gating the LO on the mixers shaping our pulses, with

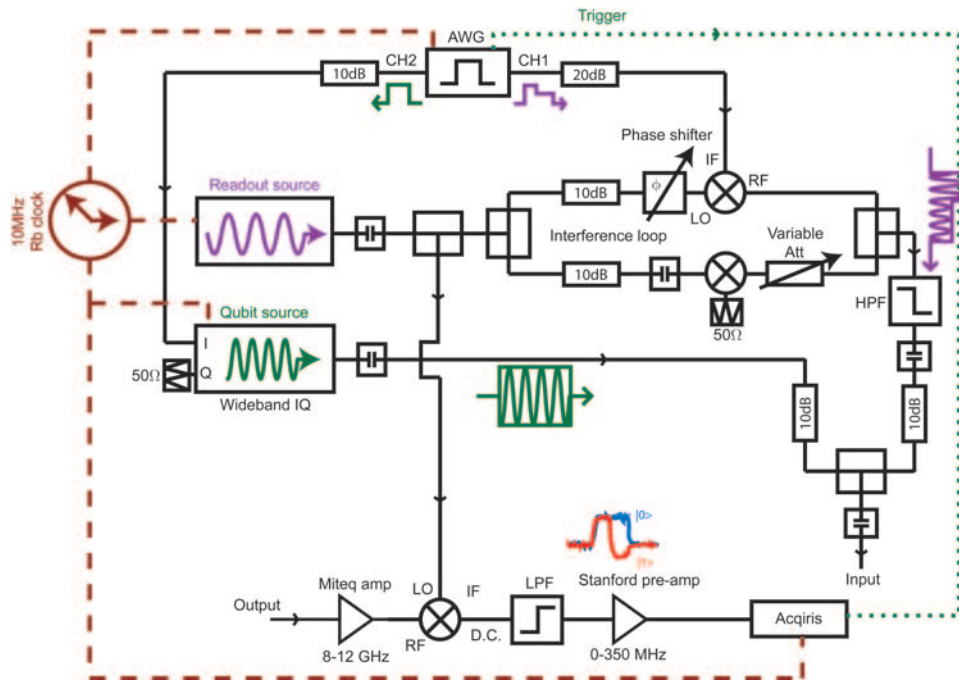


Figure 3.8: A typical schematic for the room temperature setup while performing a qubit manipulation and measurement experiment. Two methods are illustrated for minimizing the pulse leakage. For the readout pulse, the signal is sent through an interferometric loop to cancel the signal outside the pulse. The qubit pulse originates from an IQ built into one of our high frequency sources and can be tuned to have on/off ratios of up to 70dB.

a pulse shape a few nanoseconds longer than the desired pulse. This gating pulse does not require rise times as fast as the desired pulses, so it can be generated using a slow internal pulse generator in our RF sources. However, if this pulse option is not available, the same trick is achieved by placing two mixers in series, with the first mixer pulsing the LO on the second mixer. The disadvantage of this method is a loss in the net output RF power. An expensive method to cancel the leakage is to purchase a high quality IQ mixer which has already been tuned to have low leakage. Such a mixer is built into one of our RF sources and basically consists of a few mixers and amplifiers constructed in a geometry that is designed

to cancel the leakage in a wide frequency band.

If cancelation at only one frequency is needed, such as for our readout pulses, we can use an interferometric method to cancel the leakage (see Fig. 3.8). The RF signal is split into two and sent down two parallel RF lines. On one branch the signal is mixed with a pulse envelope, and on the other branch, the signal is either not mixed at all, or it is mixed with the pulse envelope’s inverse. Then a variable phase shifter on one branch, set to around  $180^\circ$ , and a variable attenuator on the other branch can both be tuned such that when the two signals are recombined, the signal outside the pulse’s shape is canceled.

The output of the CBA is mixed down to DC by an RF signal that is split off the source of the input readout signal. After mixing down, low pass filters remove the high frequency noise, and a 0 – 350 MHz Stanford pre-amp amplifies the signal. Figure 3.8 illustrates a typical signal profile, where a clear voltage step is seen between the output when the qubit is in  $|0\rangle$ , or the output when the qubit is in  $|1\rangle$ . By histogramming this voltage, we can calculate the switching probability of the CBA  $P_{01}$ , which is directly related to the probability of the qubit being in state  $|1\rangle$ .

### 3.3 Qubit characterization

Before performing involved qubit manipulation and measurement experiments, we must first determine the SCPB parameters  $E_J$  and  $E_{CP}$ . We can then predict the entire energy level spectrum of the SCPB and in particular, the qubit transition frequency  $\nu_{01}$  at the “sweet spot” (see section 3.1). The zero of gate charge  $N_g$  is unknown from one experiment to the next (even in the same cool-down) due to random single electron charge jumps and slow charge drifts. Therefore, the usual

method of finding the “sweet spot” is to apply a predetermined pulse sequence at  $\nu_{01}$  and then to vary  $N_g$  until the desired response is measured.

### 3.3.1 Gate modulations

We first performed gate charge and flux modulations while keeping the qubit in its ground state to check that we have flux periodicity and  $2e$  charge periodicity, as shown in Fig. 3.9. Somewhat surprisingly, this measurement also gave us our first estimate of  $E_J$  and  $E_{CP}$ . Initially, the readout was operated in the weakly non-linear mode ( $P_{in} \ll P_b^{(1)}$ ), where we measured changes in the phase of the transmitted signal as the gate charge and flux were varied, keeping the frequency fixed at the maximal phase response point (see Fig. 3.9a). Apart from a slow background modulation due to the changing susceptibility of the ground state, we observe sharp contrast on contours of ellipsoidal shape. These can be interpreted as contours of constant qubit transition frequency coinciding with the readout frequency or its double  $\nu_{01} = \nu, 2\nu$ , an effect similar to that observed by Wallraff et al. [70]. Using the previously derived formula for the energy levels of the quantronium [91] (Eqn. 3.8), we can reproduce the shape of these contours, within the uncertainty due to the low frequency gate charge and flux noises, and extract a Josephson energy of the SCPB  $E_J$  of 15 GHz and charging energy  $E_{CP}$  of 17 GHz. At higher drive powers, close to or in the bifurcation regime, we have observed more complex features involving higher order transitions (see Fig. 3.9b). These can also be fitted and confirm the qubit parameters obtained from the linear readout data.

The pattern that we observe in this gate charge and flux modulation data is highly dependent on  $E_J$  and  $E_{CP}$ , as well as the chosen readout frequency  $\nu$ . Figure 3.10 summarizes the gate and flux modulations from three different qubit

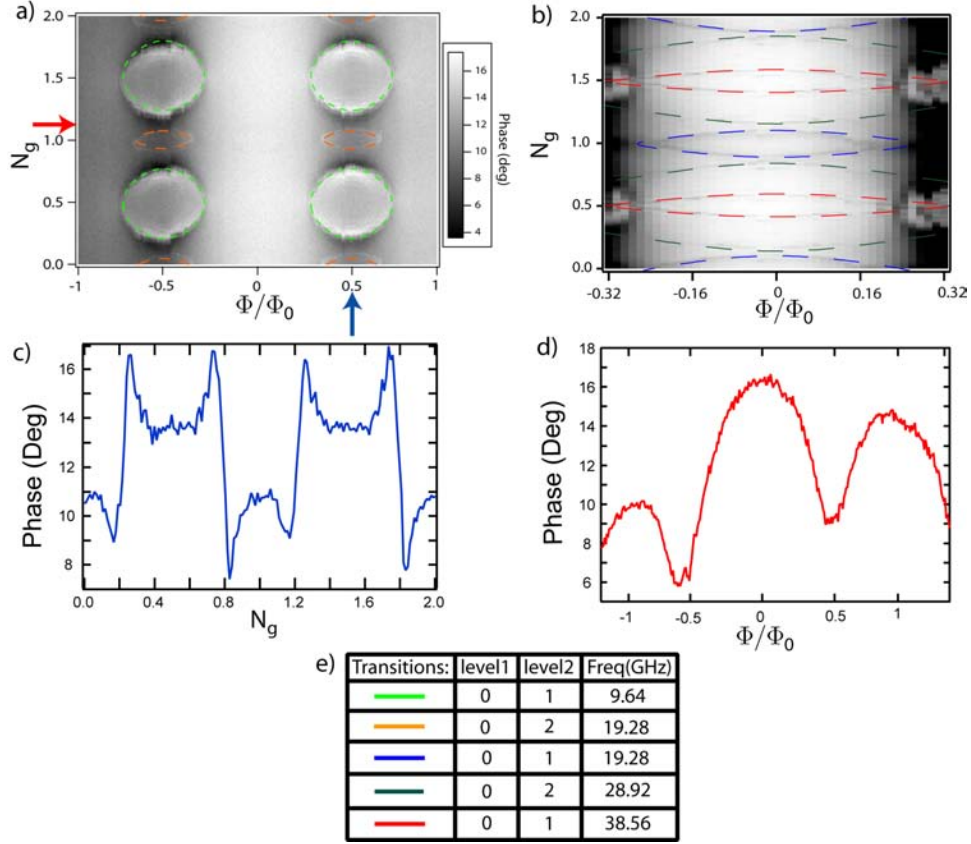


Figure 3.9: (a) Plot of gate charge and flux modulations of our device. We operated in the weakly non-linear mode ( $P_{in} \ll P_b^{(1)}$ ) and monitored the phase of the transmitted signal (gray-scale) as we varied the applied gate charge  $N_g = C_g V_g / 2e$  and flux  $\Phi$  ( $\Phi_0 = \hbar / 2e$ ). The large ellipsoidal contours can be interpreted as induced transitions between the energy levels of the qubit at multiples of the readout frequency. The green fitted lines are transitions between the 0 and 1 energy levels at the readout frequency of 9.64 GHz, while the orange fits are for transitions between the 0 and 2 energy levels at twice the readout frequency, 19.28 GHz. (b) Plot of qubit charge and flux modulations with the readout in the strongly non-linear (but non-bifurcating) mode ( $P_{in} \leq P_b^{(1)}$ ). Higher order transitions are now seen due to the larger input power  $P_{in}$ . (c) Plot of gate charge modulations for the cross section of (a) indicated by the blue arrow. (d) Plot of flux modulation for the cross section of (a) indicated by the red arrow. The qubit ground state modulation has an overall envelope due to the magnetic field changing the critical current  $I_0$  of the large readout junction. (e) Table of fitted transition energies for the fits in (a) and (b).

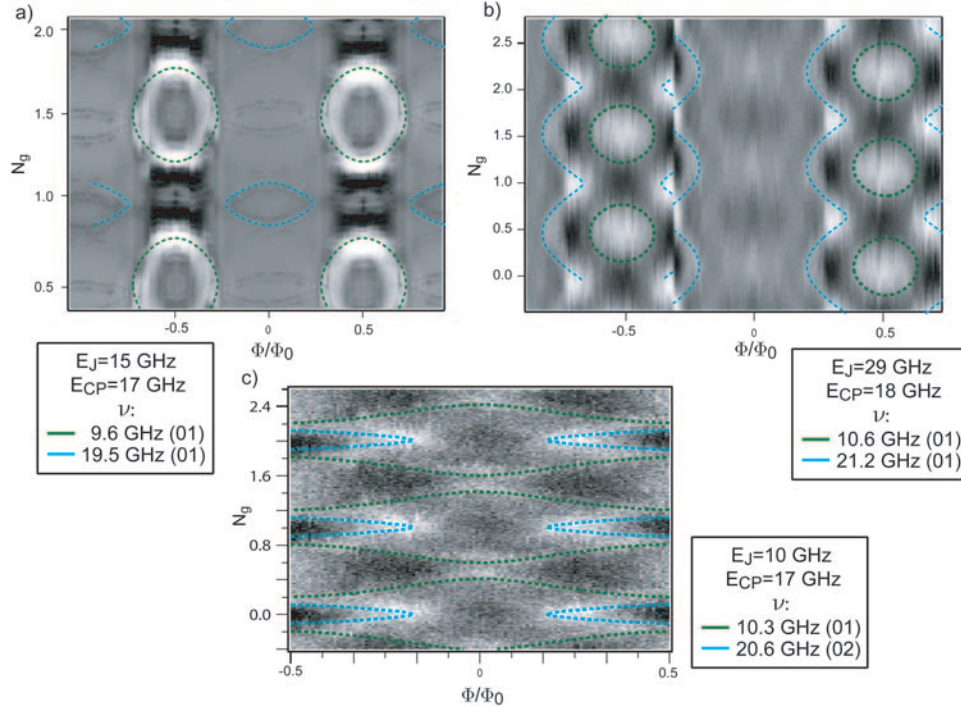


Figure 3.10: The pattern measured while performing gate and flux modulations depends on the  $E_J$  and  $E_{CP}$  of the qubit and the readout frequency  $\nu = \omega/2\pi$ . For (a) and (b) the fits shown are for the transitions between the ground and first excited state at  $\nu$  and  $2\nu$ . (a) Qubit in coplanar waveguide CBA geometry with  $E_J = 15$  GHz and  $E_{CP} = 17$  GHz. (b) Qubit in coplanar stripline CBA geometry with  $E_J = 18$  GHz and  $E_{CP} = 29$  GHz. (c) Qubit in coplanar stripline CBA geometry with  $E_J = 10$  GHz and  $E_{CP} = 17$  GHz. The blue curve is for transitions between the ground and second excited states.

samples that have different values of  $E_J$  and  $E_{CP}$ . Note that the data in Fig. 3.10a is from the same sample as Fig. 3.9, but it is measured using the readout switching probability  $P_{01}$  at high input power  $P_{in}$ . At this high input power, many more qubit transitions are excited and fitting the data is more difficult because the high readout power can Stark shift the qubit transition frequencies downward by up to  $\sim 1$  GHz.

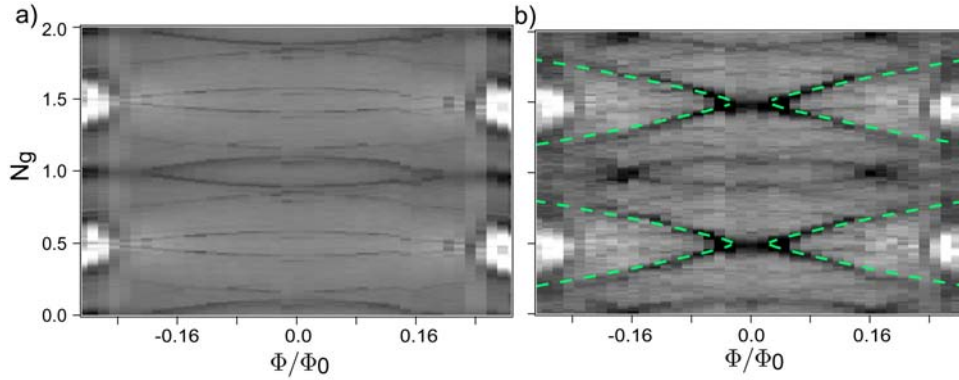


Figure 3.11: **(a)** Plot of gate modulations with the CBA operated in non-linear phase response regime. **(b)** The same gate modulations as in (a) but with an extra tone added in line 1 at 13.75 GHz. The green line is a fit with  $E_J = 14.4$  GHz and  $E_{CP} = 17$  GHz.

### 3.3.2 Spectroscopy of qubit energy levels

The above measurements are, in fact, performing spectroscopy of the qubit energy states at the readout frequency  $\nu$ . To execute spectroscopy in a more controlled manner and to verify the above picture of qubit excitation by the readout frequency, we input an additional continuous RF tone near the qubit transition frequency  $\nu_{01}$ . When this tone is on resonance with the qubit transition, we measure a response in the transmitted phase which moves in a predictable manner with flux and charge. Figure 3.11 displays the additional line when an extra tone is added. This can again be fitted with the expected transition frequency from Eqn. 3.8 to extract the same  $E_J$  and  $E_{CP}$  as above (within error  $\sim \pm 0.5$  GHz).

To get a more precise measurement of  $E_J$  and  $E_{CP}$ , we performed spectroscopy on the qubit at fixed flux by applying a weakly exciting  $1 \mu s$  long spectroscopy pulse, followed by a latching readout pulse. The switching probability  $P_{01}$  between the two metastable states of the CBA is measured as the spectroscopic frequency  $\nu_s$  is swept for each gate charge step at zero flux. Leakage of the spectroscopic

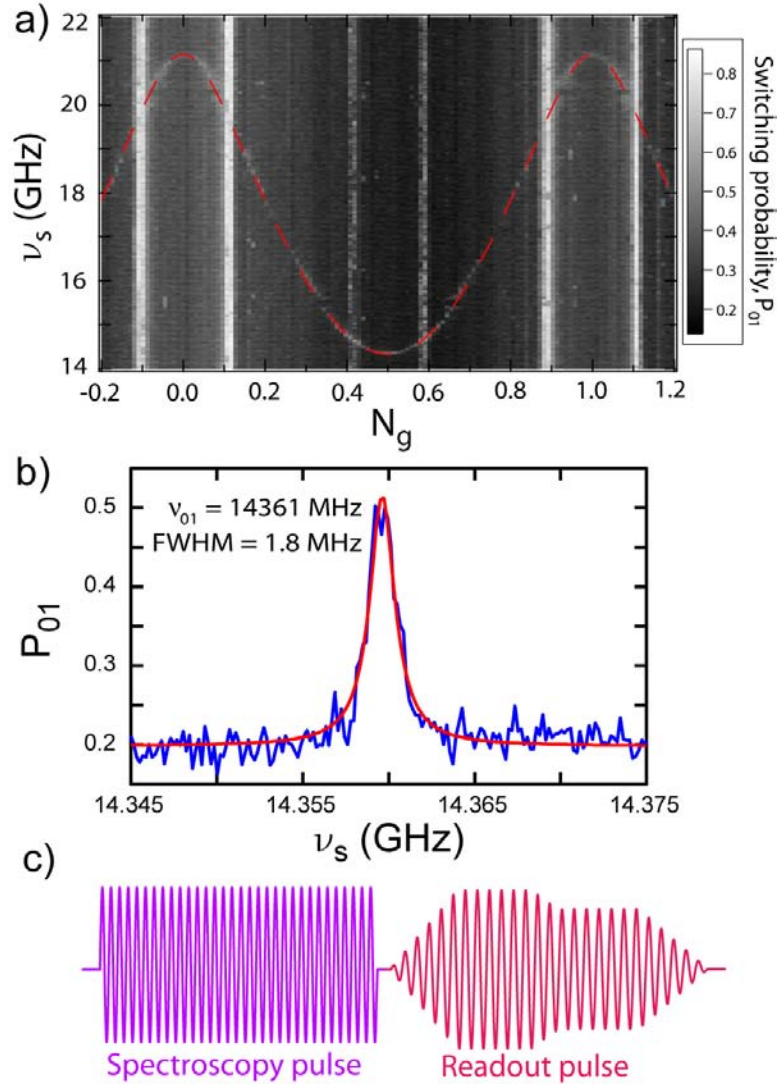


Figure 3.12: **(a)** Plot of spectroscopy peak as a function of gate charge,  $N_g$ . Staying at zero flux, we measure  $P_{01}$  while sweeping  $\nu_s$  and stepping  $N_g$ . The theoretical fit of the resulting sinusoidal like dependance of the peak with  $N_g$  is given by the red dashed line with the fit parameters  $E_J = 15.02$  GHz and  $E_{CP} = 17.00$  GHz. The vertical lines with no  $N_g$  dependance are the excitations between qubit energy levels enduced at multiples of the readout frequency, similar to those seen in Fig. 3.9. **(b)** A cut of  $P_{01}$  vs.  $\nu_s$  with a linewidth of 1.8 MHz. **(c)** The pulse sequence required to perform a spectroscopy experiment.

pulse into the readout pulse changes the readout biasing point in an unpredictable manner with  $\nu_s$ . As a result, we have to ensure that we have zero leakage of

spectroscopic power outside our pulse. This is achieved, as described above in more detail, by gating the LO on the mixers shaping our pulses with a pulse shape a few nanoseconds longer than the spectroscopic pulse. This is the easiest cancellation technique for the spectroscopy measurement because the qubit excitation pulse does not change length.

As a function of frequency, we find a peak in switching probability whose position varies with gate charge with the expected sinusoidal-like shape shown in Fig. 3.12. The theoretical fit, shown in red, refines the previous determination of  $E_J$  and  $E_{CP}$  to the values  $E_J = 15.02$  GHz and  $E_{CP} = 17.00$  GHz. Zooming in to the double “sweet spot”,  $N_g = 0.5$ ,  $\Phi/\Phi_0 = 0$ , where the qubit is immune to charge and flux noise to first order, we measure a Lorentzian spectroscopic peak of width  $\Delta\nu_{01} = 1.8$  MHz and a Larmor frequency  $\nu_{01} = 14.36$  GHz (Fig. 3.12b). This gives a decoherence time of  $T_2 = 1/\pi\Delta\nu_{01}$  of 175 ns. However, large charge jumps move the biasing point off the “sweet spot” causing the linewidth to be widened. More accurate measurements of  $T_2$  will be obtained from Ramsey fringes where  $T_2$  varies with time.

Apart from the ground and first excited state, we can also perform spectroscopy of the transition between the ground and second excited states. The minimum transition frequency between  $|0\rangle$  and  $|2\rangle$  occurs at  $N_g = 0[\text{mod } 1]$ , and if the above fits for  $E_J$  and  $E_{CP}$  are correct, this transition should have a value of  $\nu_{02} = 26.3$  GHz. Since most of our microwave devices do not work at such high frequencies, the best way of seeing this transition is by looking at the 2-photon transition at 13.1 GHz. This data is shown in Fig. 3.13 and agrees with all previous fits.

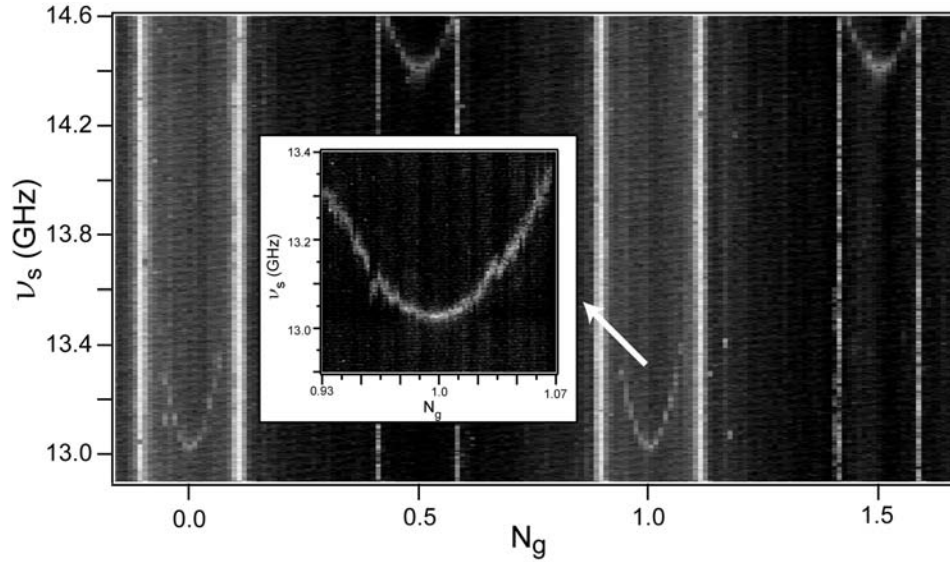


Figure 3.13: These plots are a repeat of spectroscopy experiment but looking lower in frequency. We now can see a spectroscopy peak with a minimum at integer values of  $N_g$ . This corresponds to the transition from the qubit ground state  $|0\rangle$  to the second excited state  $|2\rangle$ . The inset is a zoom of the  $|0\rangle \rightarrow |2\rangle$  transition. The glitches visible in the spectroscopy data are due to gate charge jumps.

### 3.4 Qubit manipulation

Once the qubit parameters are known, we can perform experiments on the qubit to determine the qubit's quality in terms of its energy relaxation time  $T_1$  and decoherence time  $T_2$ . An essential part of these experiments is the need to control the state of the qubit  $|\psi\rangle$  (Eqn. 1.1) precisely. A general qubit state can be built by applying a small resonant or almost resonant microwave pulse  $V$  to the qubit gate line. To describe this effect we begin by describing the qubit two-level system as a fictitious spin  $1/2$  in a magnetic field  $\vec{h}$ . In a basis  $(\vec{x}, \vec{y}, \vec{z})$ , the Hamiltonian of the qubit can be written as

$$H = -\frac{1}{2}\vec{h} \cdot \vec{\sigma}. \quad (3.17)$$

where  $\vec{h} = \hbar\omega_{01}\vec{z}$  and  $\vec{\sigma} = \hat{\sigma}_x\vec{x} + \hat{\sigma}_y\vec{y} + \hat{\sigma}_z\vec{z}$  is the Pauli operator defined by

$$\hat{\sigma}_x = \begin{pmatrix} 0 & 1 \\ 1 & 0 \end{pmatrix}, \quad \hat{\sigma}_y = \begin{pmatrix} 0 & -i \\ i & 0 \end{pmatrix}, \quad \hat{\sigma}_z = \begin{pmatrix} 1 & 0 \\ 0 & -1 \end{pmatrix}. \quad (3.18)$$

This description is called the Bloch sphere representation in which the ground state  $|0\rangle$  corresponds to the spin state pointing along the  $\vec{z}$  direction and the excited state  $|1\rangle$  corresponds to the spin state pointing along the  $-\vec{z}$  direction, i.e.,

$$\hat{\sigma}_z|0\rangle = |0\rangle, \quad \hat{\sigma}_z|1\rangle = -|1\rangle. \quad (3.19)$$

A general state  $|\psi\rangle$  is given by a point on a unit sphere, or Bloch sphere, (Fig. 3.14) and is written as

$$|\psi\rangle = \cos(\theta_u/2)|0\rangle + \sin(\theta_u/2)e^{i\phi_u/2}|1\rangle, \quad (3.20)$$

where  $\theta_u$  and  $\phi_u$  are the zenith and azimuthal angles, respectively, describing the position of the state on the Bloch sphere.

As mentioned above, we can build any state  $|\psi\rangle$  by applying a small resonant or almost resonant microwave pulse  $V(t)$  to the qubit gate line. This method is similar to the techniques developed in atomic physics and in Nuclear Magnetic Resonance. A microwave pulse with a rectangular envelope and frequency  $\nu_s$  [93] can be written as

$$V(t) = \Delta N_g(t) \cos(2\pi\nu_s t + \varphi), \quad (3.21)$$

where  $\Delta N_g(t) = \left(\frac{C_g A}{2e}\right) \Pi\left(\frac{t}{\tau_R} - 0.5\right)$  is the change in gate charge caused by the microwave pulse of amplitude  $A$  and time length  $\tau_R$  ( $\Pi$  is the rectangular function).

The pulse introduces a perturbation into the SCPB's Hamiltonian. Near the qubit transition frequency  $\nu_s \sim \nu_{01}$  and on the charge "sweet spot," the perturbation is given by

$$\vec{h}_{ex} = 4E_{CP}\Delta N_g \cos(2\pi\nu_s t + \varphi)\langle 1|\hat{N}|0\rangle\vec{x}. \quad (3.22)$$

Moving to a  $(\vec{x}', \vec{y}', \vec{z}')$  frame, which rotates at a frequency  $\omega$  around  $\vec{z}$ , and using the “rotating wave approximation,” one obtains

$$\begin{aligned} \vec{h}' &= \hbar(\omega_{01} - \omega_s)\vec{z}', \\ \vec{h}_{ex} &= h\nu_{Rabi}[\vec{x}' \cos(\varphi) + \vec{y}' \sin(\varphi)], \end{aligned} \quad (3.23)$$

where the Rabi frequency  $\nu_{Rabi}$  [94] is given by  $2E_{CP}\Delta N_g \langle 0|N|1 \rangle / h$ . In the

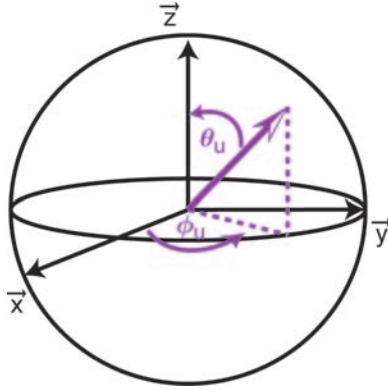


Figure 3.14: A schematic of the Bloch sphere representation in  $(\vec{x}, \vec{y}, \vec{z})$  frame where the qubit state  $|\psi\rangle$  is represented with polar angle coordinates  $\theta_u$  and  $\phi_u$ .

$(\vec{x}', \vec{y}', \vec{z}')$  frame, the qubit state precesses about the direction given by  $\vec{h}' + \vec{h}_{ex}$ , with frequency

$$\nu_p = [(\nu_{Rabi})^2 + (\nu_{01} - \nu_s)^2]^{1/2}. \quad (3.24)$$

When the system is driven on resonance ( $\nu_{01} = \nu_s$ ), we perform a controlled evolution of the qubit state between  $|0\rangle$  and  $|1\rangle$  at frequency  $\nu_{Rabi}$  around an axis in the equatorial plane, and with a direction defined by the microwave pulse phase  $\varphi$ . With no applied microwave pulse ( $A = 0$ ), the qubit state freely evolves at the Ramsey frequency [95]  $\nu_{Ramsey} = |\nu_{01} - \nu_s|$  about  $\vec{z}$ . Any point on the Bloch sphere can therefore be reached using a combination of free evolutions and driven rotations.

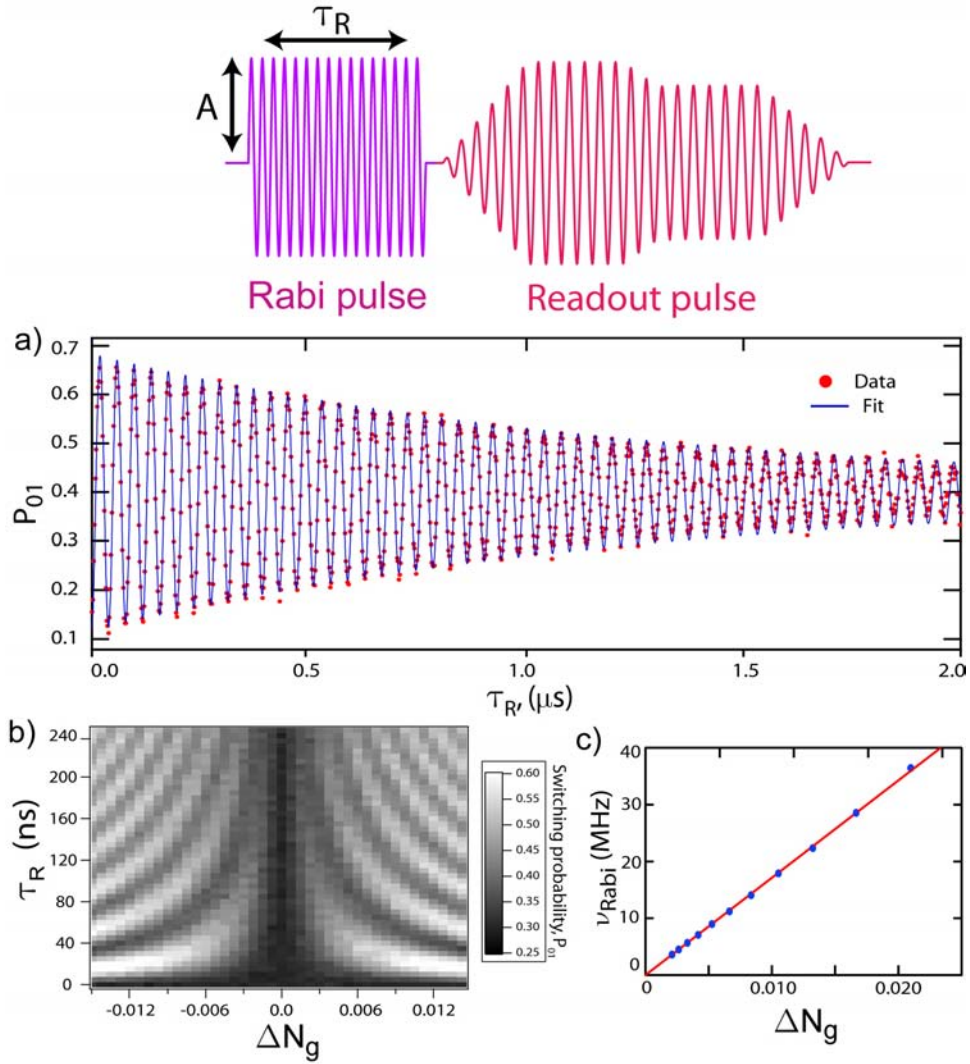


Figure 3.15: **(a)** An example of a Rabi oscillation trace vs. gate pulse length  $\tau_R$ . We can use this data to calibrate our qubit manipulation pulses. The position of the first Rabi oscillation peak gives the length of the Rabi pulse needed to perform a  $\pi$ -pulse on the qubit, i.e., the pulse needed to excite the qubit from the ground state to the first excited state. **(b)** Plot of Rabi oscillations in the switching probability  $P_{01}$ , as a function of gate charge modulation  $\Delta N_g$  and gate pulse time length  $\tau_R$ .  $\Delta N_g$  is calculated from the Rabi pulse envelope voltage  $A$  reaching the sample through the attenuation in the input lines and is plotted in terms of Cooper pairs,  $\Delta N_g = C_g A / 2e$ . Oscillations in the switching probability  $P_{01}$  are seen with both  $\Delta N_g$  and  $\tau_R$ . **(c)** Fitted Rabi frequency  $\nu_{Rabi}$  vs.  $\Delta N_g$ . As expected from a two-level system,  $\nu_{Rabi}$  scales linearly with  $\Delta N_g$ .

### 3.4.1 Rabi oscillations and relaxation time

To measure the Rabi oscillations, the pulse sequence protocol involves a resonant gate pulse at frequency  $\nu_s = \nu_{01}$  with varying amplitude  $A$  and time length  $\tau_R$  (see Fig. 3.15a). A latching readout pulse follows and repeats  $10^4$  times to measure the switching probability  $P_{01}$ . During the Rabi pulse, the azimuthal coordinate  $\theta_u$  increases in proportion to  $A$  and  $\tau_R$ :

$$\theta_u = 2\pi\nu_{Rabi}\tau_R \propto A\tau_R. \quad (3.25)$$

Figure 3.15c displays the oscillations of the switching probability as a function of  $\tau_R$  and  $A$ . The extracted frequency  $\nu_{Rabi}$  scales linearly with  $\Delta N_g$  (Fig. 3.15d), as

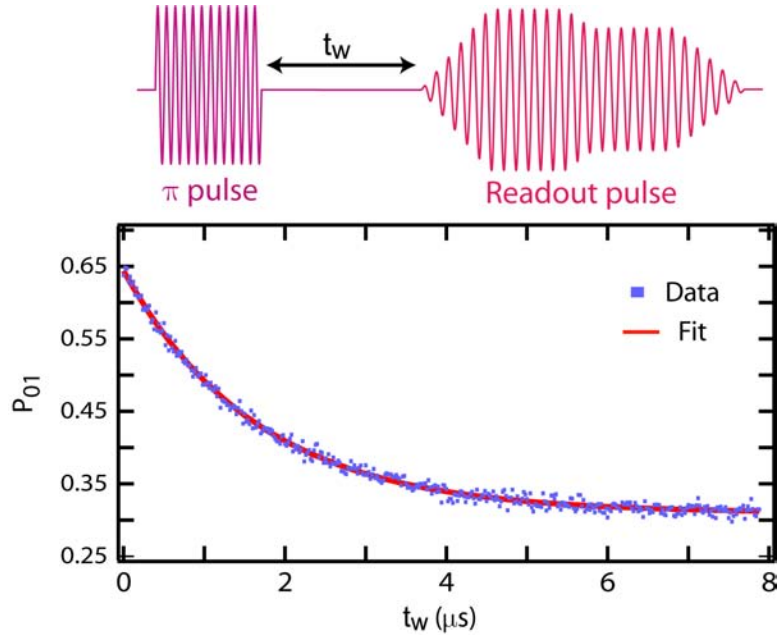


Figure 3.16: **(a)** The pulse sequence used to perform a  $T_1$  measurement. The first pulse excites the qubit in the state  $|1\rangle$ . This is followed by a varying wait time  $t_w$ , during which the qubit can relax to  $|0\rangle$  before being measured. **(b)** Plot of the measured exponential decay of the excited state population, with a decay time of  $T_1 = 1.65$  ns.

expected for a two-level system. From the position of the first maximum of the

Rabi oscillations, we can calibrate the pulse time length necessary for a  $\pi$ -pulse ( $\theta_u = \pi$ ) to drive the qubit from the ground state to the excited state.

Using this  $\pi$ -pulse, one can measure the exponential decay of the population of the excited state (Fig. 3.16) and obtain the relaxation time  $T_1$ . As demonstrated in Fig. 3.16, the pulse sequence protocol involves a resonant gate  $\pi$ -pulse with varying distance  $t_w$  to the following latching readout pulse. On average, we measure a relaxation time of  $T_1 = 1.6 \mu\text{s}$ , which is comparable to the results of Vion et al. [49] and Siddiqi et al. [51].

### 3.4.2 Readout discrimination of qubit states

From the above Rabi and  $T_1$  data, the maximum change in  $P_{01}$  when the qubit changes state is about 60%. This quantity is known as the contrast, and is lower than the theoretical maximum contrast of over 99.9%, calculated for the ideal case of a non-relaxing qubit given the measured parameters of the CBA.

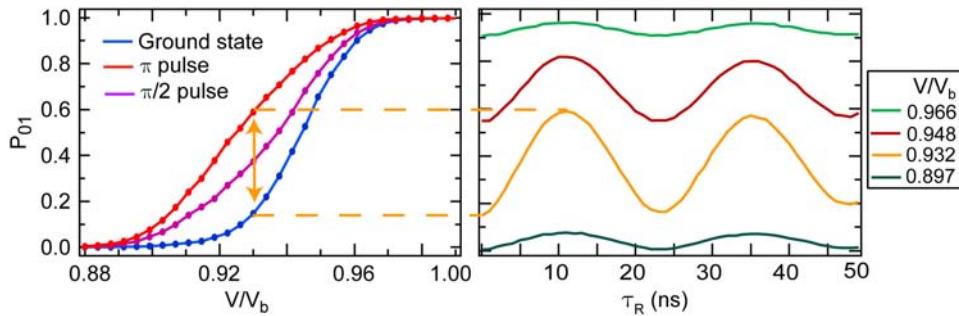


Figure 3.17: Displayed on the left panel we have the measured s-curves of the Quantronium with CBA readout. Preceding the readout pulse we apply a pulse at the qubit transition frequency to manipulate the qubit state. The right panel contains the corresponding Rabi oscillations at four different points along the s-curves. For the Rabi oscillations we apply a pulse of varying length,  $\tau_R$  to the qubit before the readout pulse. This pulse corresponds to a driven coherent evolution of the qubit state. We obtain the expected sinusoidal oscillations with pulse length with a period that depends linearly on pulse power. The contrast of these oscillations depends on the readout biasing point.

To further study the contrast between the qubits states, the s-curves of the CBA are measured again. One s-curve is measured with the qubit in the ground state  $|0\rangle$  and the other with the qubit in the excited state  $|1\rangle$ , obtained by applying a microwave  $\pi$ -pulse to the qubit's gate line before applying the readout pulse. The shift between the two curves again gives the contrast and agrees with the observed contrast in the Rabi oscillations, as shown in the right hand panel of Fig. 3.17. In addition, we see that the observed contrast measured in a Rabi experiment depends on the readout biasing point. The disagreement with the expected contrast is attributed to three main sources. First, the transition between the two oscillating states of the CBA is broadened by more than a factor of 5 from what was expected, probably due to insufficient RF filtering in the output lines. However, this broadening still does not account for all of the discrimination power loss. A 10% loss in contrast is caused by the qubit relaxing before the readout takes place due to its finite relaxation time  $T_1$ . The largest contribution to the loss in contrast comes from the extra qubit relaxation to the ground state as the readout voltage approaches the bifurcation voltage. This loss in contrast could be from Stark shifting the qubit to lower frequencies during readout (even though this Stark shift is much smaller than previous readouts, it oscillates much more frequently), where it can come in resonance with spurious transitions [54] possibly due to defects in the substrate or in the tunnel barrier (note that no avoided crossings were resolved in the spectroscopy data).

## 3.5 Decoherence

### 3.5.1 Highly averaged Ramsey fringe experiment

To measure the coherence time  $T_2$ , we follow a different pulse protocol in which we apply two  $\pi/2$  pulses separated by a free evolution period of length  $\Delta t$ , followed by a readout measurement. The first  $\pi/2$ -pulse creates a state  $(|0\rangle + |1\rangle)/\sqrt{2}$ , and then the qubit freely evolves for a time  $\Delta t$ , during which it can decohere. After time  $\Delta t$ , the azimuthal angle becomes  $\phi_u = 2\pi(\nu_{01} - \nu_s)\Delta t$ . The second  $\pi/2$ -pulse produces a zenith angle  $\theta_u = \pi - \phi_u$  such that the resulting probability of the qubit being in the state  $|1\rangle$  is proportional to

$$P_{01} = \cos^2(\pi\nu_{Ramsey}\Delta t). \quad (3.26)$$

The resulting oscillations are known as Ramsey fringes. In reality, they will exponentially decay, with decay time  $T_2$ , due to decoherence during the free evolution time  $\Delta t$ . As with the Rabi and  $T_1$  experiments, the data is averaged in the same manner as “method A” in [96]. A sequence of 700 Ramsey pulses with varying time  $\Delta t$ , completing a full Ramsey fringe, is applied to the sample and then repeated and averaged to attain the required signal to noise ratio. Figure 3.18 shows an example of the resulting Ramsey fringes, which have been averaged over a 17.5 min period. A readout measurement is taken every 10  $\mu\text{s}$  during the averaging period. By fitting to an exponentially decaying sinusoid, a decay time of  $T_2 = 500$  ns and a Ramsey fringe frequency of  $\nu_{Ramsey} = 30$  MHz are extracted.

The experiment can be repeated while varying excitation frequency  $\nu_s$ , as shown in Fig. 3.19. The average frequency of Ramsey fringes is well fitted by the absolute value of the detuning  $|\nu_s - \nu_{01}|$ , yielding a precise measurement of  $\nu_{01} = 14.361$  GHz.

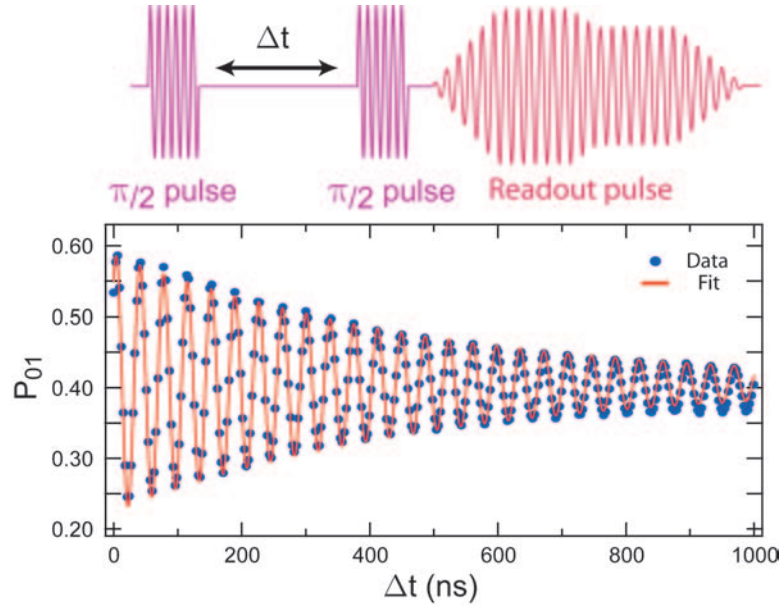


Figure 3.18: **(a)** Pulse sequence used to perform a Ramsey fringe experiment. **(b)** Ramsey fringe obtained after 17.5 min acquisition time. The data is fitted to a sinusoidal exponential decay with a decay time of  $T_2 = 500$  ns.

### 3.5.2 Decoherence noise source

The data described in the last section is highly averaged and it is difficult to determine from this data the mechanisms limiting  $T_2$ . However, we can now take advantage of the CBA's fast repetition rate and large signal to noise ratio to follow the time evolution of  $T_2$  and  $\nu_{01}$  by recording 3000 Ramsey fringes - one every 0.35 s (Fig. 3.20a). We observe stochastic fluctuations of  $T_2$  with an asymmetric bell shaped distribution peaking around 600 ns and a long tail extending down to 150 ns (Fig. 3.20c).

Averaging over all the 3000 above Ramsey traces (17.5 mn period), we get the data shown previously in Fig. 3.18, with an average  $T_2$  that converges to 500 ns. The  $T_2$  is similar to the first Saclay result [49] obtained with a qubit with a similar  $E_J/E_{CP}$ . Note that a Hahn spin echo sequence partly compensates

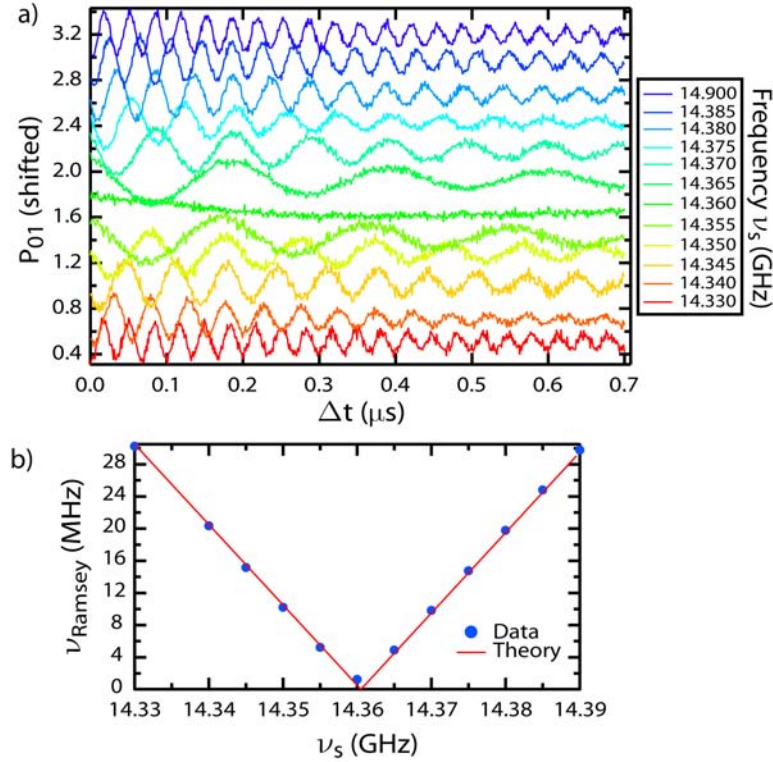


Figure 3.19: **(a)** Ramsey fringes for varying excitation frequency. The curves are offset for clarity. **(b)** Fitted Ramsey frequency from the curves in (a) vs. excitation frequency. The Ramsey frequency goes to zero at the transition frequency  $\omega_{01}/2\pi$ . The fit (red curve) gives a very precise measure of  $\omega_{01}/2\pi = \nu_{01} = 14.361$  GHz.

for decoherence due to low frequency variations of the qubit transition frequency [97]. However, we intentionally perform the standard Ramsey fringe protocol as a manner of studying these low frequency fluctuations and determining their source.

The  $T_2$  fluctuations are correlated with fluctuations in the Ramsey frequency, which only fluctuate towards higher frequencies giving lopsided distributions, as shown on Fig. 3.20d. At the “sweet spot” where we are working, variations in gate charge necessarily increase the transition frequency, whereas variations in flux decrease it. Variations in critical current would supposedly keep the distribution of frequencies more symmetric. We can therefore conclude that charge noise, not

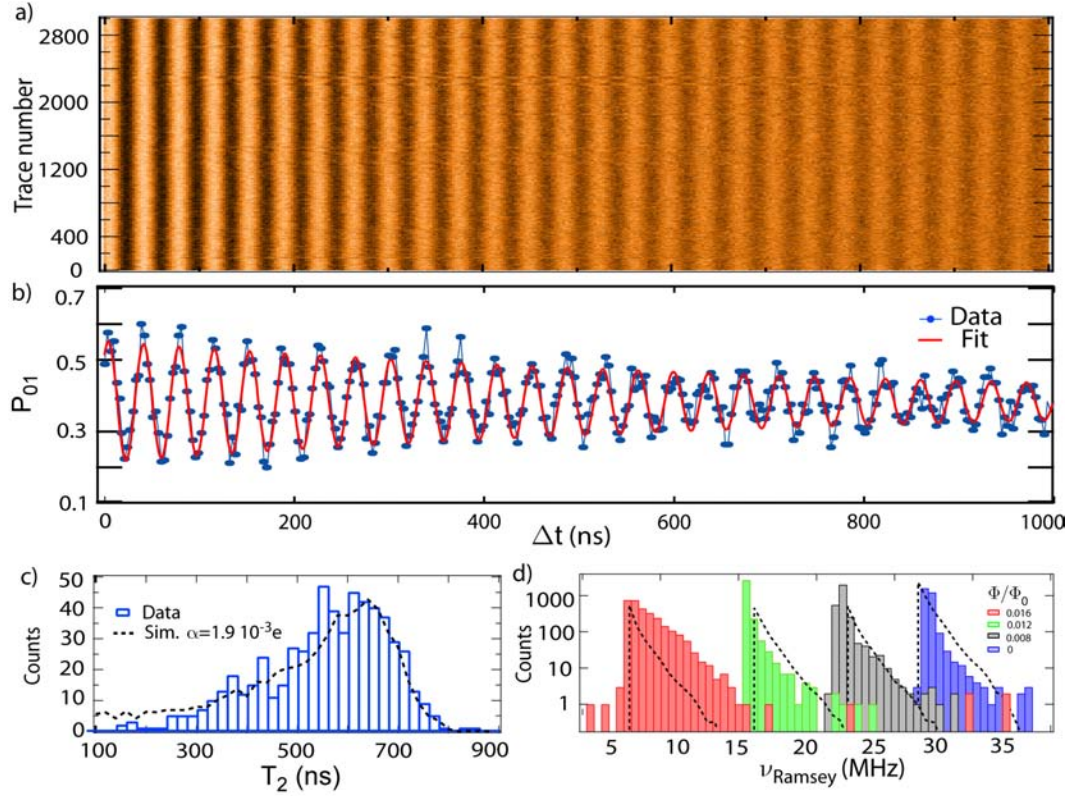


Figure 3.20: **(a)** 3000 Ramsey oscillations as a function of free evolution time  $\Delta t$ . Each trace is  $2.1 \mu\text{s}$  long with 3 ns per step. They each take 0.35 s to acquire. We can see visually the variation of  $T_2$  for the different Ramsey fringes by noticing the variation in contrast in the fringes near  $1 \mu\text{s}$ . **(b)** Sample data fit. We average 5 of the acquired Ramsey traces shown in (a) and fit to a decaying sinusoid to extract the  $T_2$  which is then plotted in (c). For this particular case we have a coherence time of 840 ns and a Ramsey frequency of 26.9 MHz. **(c)** Distribution of  $T_2$  for 3000 of the Ramsey traces (600 fits). The black dashed line is the result of a simulation of the free evolution decay of the Ramsey fringes with  $1/f$  noise fluctuations on the gate,  $S_q(\omega) = \alpha^2/|\omega|$ . In the simulation we used 10 times more points compared to the data to obtain a smoother curve. **(d)** Corresponding distribution of Ramsey frequencies at four different flux biasing points. Each distribution has 3000 Ramsey traces. The blue histogram corresponds to the data in (a), (b) and (c). The Ramsey frequency is extracted from the position of the maximum of the power spectral density of each decaying sinusoid. The distributions are lopsided to higher frequencies as would be expected from fluctuations in the gate charge around our operating point at the “sweet spot”. The dashed line is the expected distribution assuming the same  $1/f$  charge noise as in (c).

flux noise, is the dominant source of decoherence in our sample. Furthermore, if we suppose that the charge noise is Gaussian with a spectral density that has the usually invoked  $1/f$  form [62] given by  $S_q(\omega) = \alpha^2/|\omega|$ , we can check if our data can be explained by this model.

This was carried out by directly numerically simulating the corresponding variations in transition frequency and calculating the Ramsey signal in the conditions of the experiment. At long free evolution times  $\Delta t$ , the variations in  $\nu_{\text{Ramsey}}$  causes the average Ramsey signal to reduce in height. This effect results in the exponential decay of the Ramsey fringes. The simulated distributions of both the extracted  $T_2$  and  $\nu_{\text{Ramsey}}$  values are shown by the dashed lines in Fig. 3.20c and d. We obtain good agreement between the simulation and the data for a noise amplitude of  $\alpha = 1.9 \cdot 10^{-3}e$ , agreeing with the range of previously measured values of this noise intensity parameter [63, 64]. To reduce sensitivity to this charge noise, the energy levels of the qubit can be made almost insensitive to charge by increasing  $E_J/E_{CP}$ . This is achieved by increasing the areas of the junctions in the SCPB or by increasing the capacitance of the island to ground [98], [85] (see section 4.3). An  $E_J/E_{CP}$  of 8 could give a  $T_2$  in the ms range and hence, this device would be  $T_1$  limited.

## 3.6 Tomography

Tomography describes a procedure for mapping out the quantum state of a qubit. In theory this could be done by measuring the qubit state in three different basis sets. However, in our experiment, we can only measure along the  $\vec{z}$  direction. So instead of rotating the measurement basis, we rotate the qubit state in a controlled manner [54] using single qubit rotations prior to measurement. In principle, we

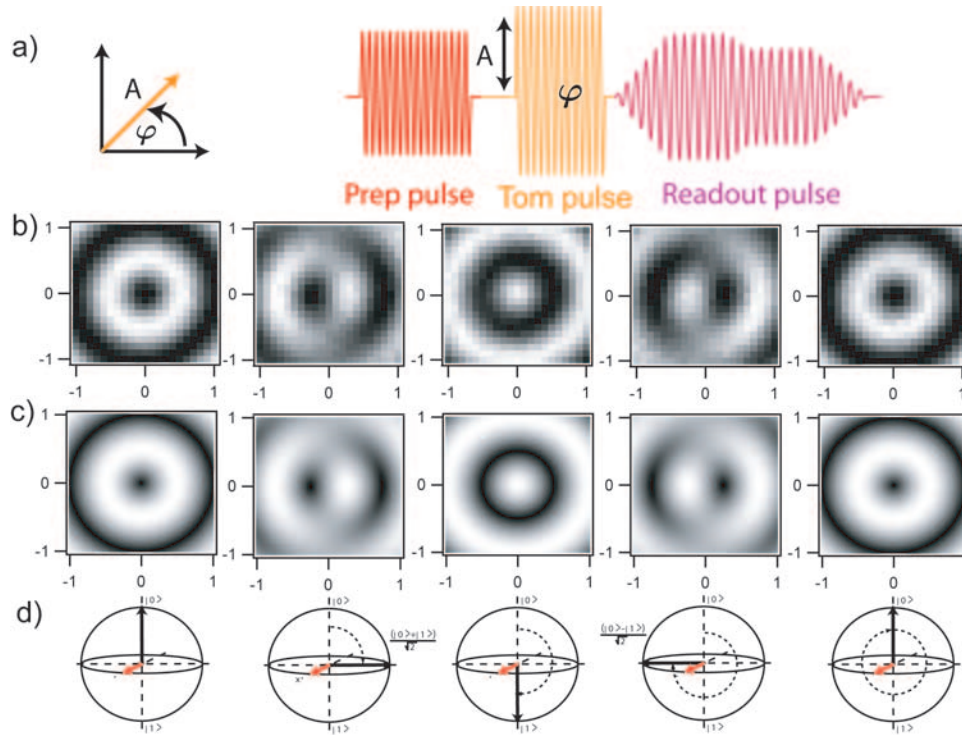


Figure 3.21: **(a)** Pulse sequence used in the tomography experiment. The first pulse prepares the qubit state. This is followed by a sequence of tomography pulses with varying pulse height  $A$  and phase  $\varphi$ . In **(b)** and **(c)**, the length of the vector to each pixel corresponds to  $A$  and the angle corresponds to  $\varphi$ . **(b)** Experimental tomography plots for the initial states shown in **(d)**. **(c)** Theoretical plots for the same states as in **(b)** and **(d)**. The pattern obtained depends on the initial state of the qubit.

only need to make three such rotations and measurements. But in Fig. 3.21, we perform rotations of the qubit state all over the Bloch sphere. This is important to demonstrate our ability in executing well understood and controlled single qubit manipulations.

The experiment begins by preparing the qubit in some initial state using an initial gate pulse at the qubit frequency  $\nu_{01}$ . We then map out this state with a tomography pulse of varying amplitude  $A$  and phase  $\varphi$ . The phase  $\varphi$  determines the axis of rotation in the equatorial plane of the Bloch sphere, while the amplitude

$A$  determines the angle of rotation  $\theta_u$  (see Eqn. 3.23). The resulting switching probability can be plotted in polar coordinates, where  $A$  is the length of the vector to each pixel and  $\varphi$  is the angle this vector makes with the  $x$ -axis. The measurement results are shown in Fig. 3.21 along with a theoretical prediction shown below the experimental data. A single cut of these plots along any single axis of rotation  $\varphi$  is essentially a Rabi oscillation experiment. The measured patterns depend on the initial state of the qubit and can be used to identify it. In future experiments, this will be an important method for demonstrating entanglement between two solid-state qubits [99].

### 3.7 Conclusion

We have successfully implemented the cavity bifurcation amplifier as an improved readout method for the quantronium qubit. Furthermore, in this architecture we have demonstrated precise control of the qubit state by performing tomography on various initially prepared qubit states. Our SCPB qubit has similar relaxation and decoherence times as previously measured samples [51], [49], however, our new readout method has many advantages over previously implemented readouts. This dispersive readout minimally disturbs the qubit state and offers speed, sensitivity and ease of fabrication along with an operating environment which is precisely controlled. Using the CBA's speed and sensitivity we have measured fluctuations in the qubit decoherence time, which were averaged out by previous measurement schemes. With this information, we have demonstrated that the main source of decoherence for low  $E_J/E_{CP}$  samples, is charge noise.

Building on this experiment, we are now designing a new qubit architecture which will be insensitive to charge noise by using a larger  $E_J/E_{CP}$ . Also, we can

reduce flux noise by introducing trapping centers in the superconducting films surrounding the qubit and by placing the sample in a magnetic shield. Furthermore, this CBA geometry is particularly well adapted to the multiplexing of several CBA readouts. Hence, of order ten qubits can be measured at once, offering a path for scaling up of superconducting circuits. In the next chapter, I will describe our efforts along these lines and I will conclude by describing some applications of the CBA, other than as a SCPB readout.

# Chapter 4

## Future directions

In this chapter, I describe the future role that the cavity bifurcation amplifier could play in quantum computing and mesoscopic physics in general. The first section consists of a summary of our first attempts at scaling up to a multi-qubit measurement system by multiplexing up to five CBA resonators on-chip and measuring them simultaneously with the same input and output lines. Next, I emphasize the versatility of the CBA readout system, which has already been adapted for use with the other types of superconducting qubits [71]. At the end of this chapter, I describe some directions our group is currently taking in applying the CBA for mesoscopic measurements outside the field of quantum computing. For example, we are currently developing a Cooper pair counting experiment and we are adapting the CBA for measuring molecular devices.

### 4.1 Multiplexed CBA readout

The initial motivation that fueled research into the application of superconducting quantum circuits in quantum computing, is their inherent scalability. Compared with systems such as NMR and ion traps, it has proven more difficult to develop a single well behaved superconducting qubit due to strong environmental coupling

through, for example, the measurement leads. However, as mentioned in the introduction, once a well behaved single qubit is developed, then superconducting quantum circuits should be relatively easier to scale. This scalability, was one of our main motivations for developing the cavity bifurcation amplifier, because the CPW resonators used to construct the CBA, can be easily multiplexed on-chip. In this multiplexed geometry, each resonator has a different resonance frequency, and are placed in parallel. They are all capacitively coupled to the same input and output lines, but because they have different resonant frequencies, they can be individually addressed and measured (see Fig. 4.1). If a qubit is placed in each resonator, then each qubit can be readout individually at a different frequency. Coupling of the qubits can be achieved through the readout lines or by capacitively coupling each qubit island to a coupling resonator (see Fig. 4.6).

In this section, I begin by describing the initial experiments investigating the behavior of the multiplexed bifurcating readouts. Following this, I present the first implementation of a sample with two coupled qubits using multiplexed readouts.

#### 4.1.1 Design of a sample with five multiplexed resonators

We began by designing and fabricating a chip with five multiplexed resonators in parallel (see Fig. 4.1). 10 GHz resonators are used because, as well as operating at greater speeds, they are short enough so that the center pin is not meandered and hence, can be closely packed, saving chip space. All five resonators can easily fit on a chip with the same dimensions that were used in the single CBA experiments, 10 mm  $\times$  3 mm. Typically, we choose the same input capacitance  $C_{in}$  for each resonator so that each CBA bifurcates at the same input power. The output capacitor  $C_{out}$  for each CBA can be individually chosen to obtain the desired quality factor  $Q$  for each resonator. The ends of the input and output lines can be

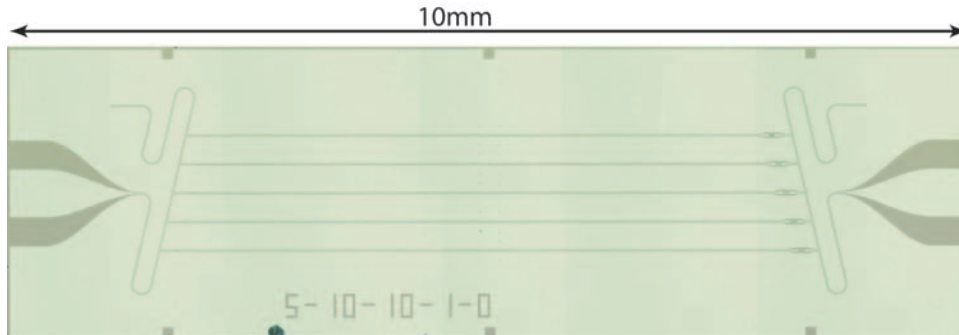


Figure 4.1: An optical image of a chip with five multiplexed resonators. It has one input and one output line, both of which are shorted at the end, resulting in a voltage minimum. These lines are sloped so that each resonator has a different resonance frequency. Also, each resonator is positioned at a voltage maxima of the input line at their respective resonance frequencies.

opens or shorts, giving voltage maxima or minima respectively at these positions. Then, to achieve maximal coupling to each of the capacitively coupled resonators, we position them on the input lines so that a voltage maximum of the input power occurs near their  $C_{in}$ , at their respective resonance frequencies. More specifically, if the ends of the input/output lines are open, then the length of the CPW between  $C_{in}$  and the ends, should be the same length as the resonator itself,  $\lambda/2$ . If the ends are short, then the length between these ends and  $C_{in}$  should be  $\lambda/4$ .

These resonators are fabricated using the same optical mask process as before (see section 2.4), with the Josephson junctions fabricated in a subsequent e-beam process. Also, in the same way as before, we can measure these samples using the transmitted amplitude and phase of a microwave signal near each resonator's resonance frequency.

### 4.1.2 Measurement setup

One of the big advantages of scaling the CBA system using multiplexed resonators, is that the measurement setup is the exact same as that used for a single resonator

measurement (see section 2.5.1). No extra microwave lines or devices are needed. Wirebonding the sample, however, is more complicated for the multiplexed devices. As before, we use as many wirebonds as possible on the center electrode to reduce any series stray inductance, and we wirebond all around the ground planes to eliminate any spurious resonances. In addition, however, we now have

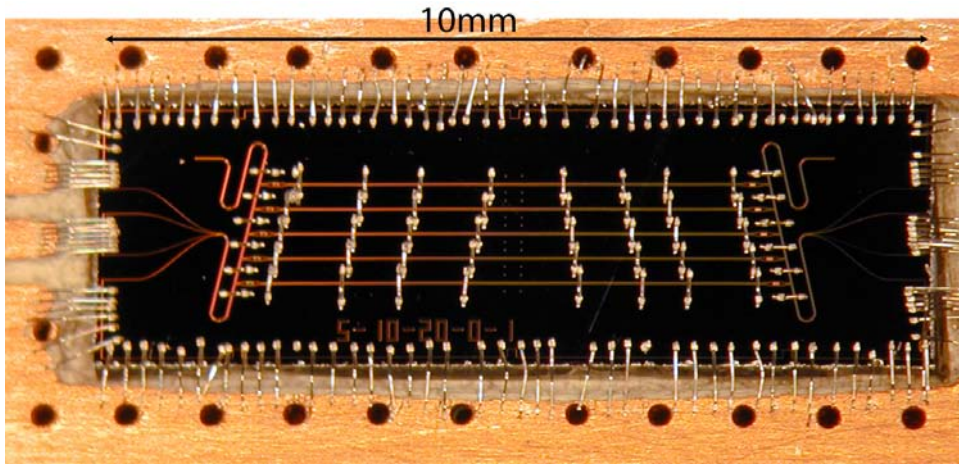


Figure 4.2: An optical image of sample mounted in sample holder. On-chip wirebonds are needed to ensure that the isolated CPW ground planes, enclosed between the multiplexed resonators, are properly grounded.

ground electrodes on-chip which are enclosed between the multiplexed resonators and are therefore not connected to the global ground. Ideally, we would like to build vias into these ground planes, in a similar manner to the PCB, to make contact to the global ground at the back of the chip. Nonetheless, we can avoid this complication by simply using wirebonds which arch over the center electrodes of the CPW resonators, and connect all of the ground planes together (see Fig. 4.2). These bonds have sufficiently low inductance to form low impedance contacts at microwave frequencies.

### 4.1.3 Phase Diagram

To determine whether each resonator in this device bifurcates, and to find their resonance frequencies and quality factors, we begin by measuring the steady state behavior [76] (see section 2.5.2). As before with the single resonator, we input a continuous microwave signal and measure the transmitted amplitude  $P_{out}$  and phase difference  $\phi$  as a function of input frequency  $\nu$  and input power  $P_{in}$ , using a vector network analyzer. As expected, the resonance of each of the five resonances

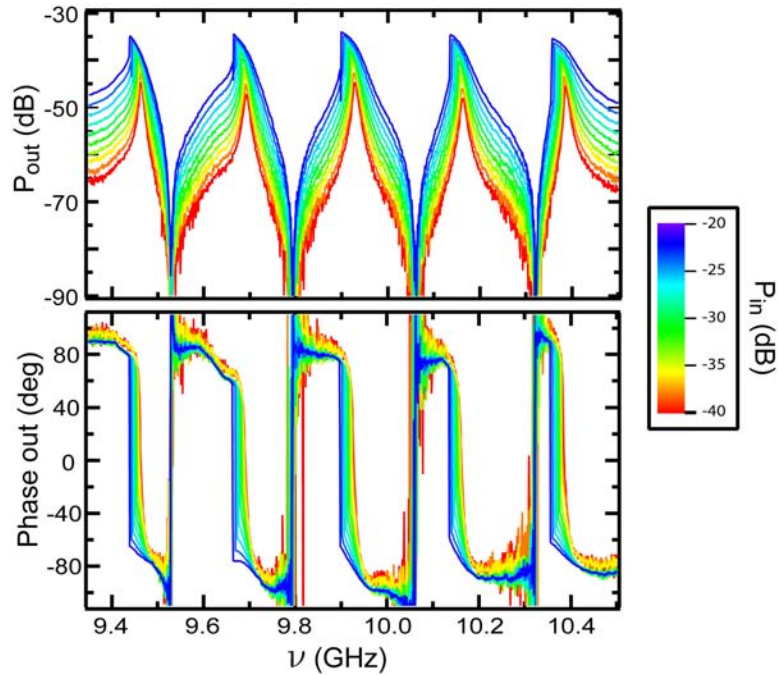


Figure 4.3: Plots of the transmitted amplitude and phase as a function of input frequency  $\nu$ , and input power  $P_{in}$ , for a device with five-multiplexed resonators (sample 4). We can see that each resonator bifurcates as the  $P_{in}$  is increased and each resonance is separated from its neighbor by a few linewidths to prevent crosstalk. We get the expected  $180^\circ$  phase shift for each of the five resonators as we sweep through their resonance frequencies.

bends backwards as the input power  $P_{in}$  is increased (see Fig. 4.3). Then, at a critical power  $P_C$ , which is determined by  $C_{in}$  (see Eqn. 2.35), each resonator

bifurcates and switches from a low oscillating state to a high oscillation state as  $\nu$ , or  $P_{in}$  is ramped up.

An essential part of this design, is that each resonator is separated from its neighbor by a few linewidths, so that each resonator is an ideal Duffing oscillator obeying Eqn. 2.4. To test this hypothesis, we can plot the universal phase diagram for each CBA. This involves extracting the bifurcation points for each resonator in the data of Fig. 4.3, and plotting them against their respective reduced detuning  $\Omega$ .

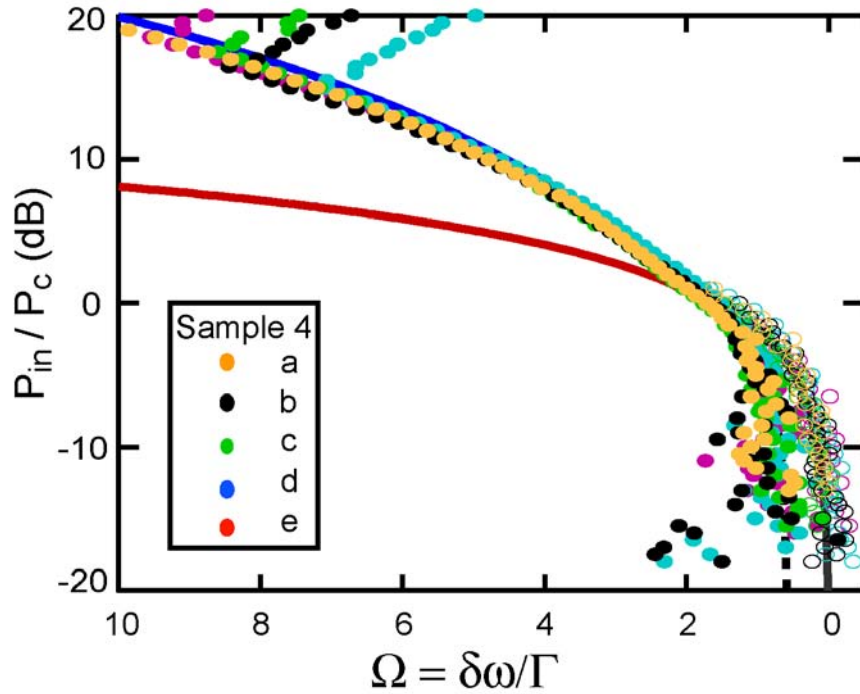


Figure 4.4: Universal plots for all five multiplexed resonators on sample 4. The upturn at high detuning is due to the CBA entering the chaotic region for large  $P_{in}$ . All the data was taken while sweeping the frequency up, and therefore we only see the upper bifurcation points. The solid blue line is the theoretical upper bifurcation point and the solid red line is the lower bifurcation point. The dotted line is the highest derivative of  $P_{out}$  below the critical point  $P_c$ , and the solid grey line is the maximum of  $P_{out}$  below  $P_c$  corresponding to the hollow circle data.

The results are plotted in Fig. 4.4 along with the theoretical prediction given by Eqns. 2.47, 2.46. The solid blue line is the theoretical upper bifurcation point and the solid red line is the lower bifurcation point. The dotted line is the highest derivative of output power below the critical point  $P_c$  and the solid grey line is the maximum of  $P_{out}$  below  $P_c$  which is given by  $P_{max}/P_c = \frac{9}{8\sqrt{3}}$ . Excellent agreement is attained for all five resonators, illustrating that each individual resonator can be used as a bifurcation amplifier near its resonance frequency. The data deviates from the theoretical prediction at higher powers where the system becomes chaotic.

The two samples we have measured with five multiplexed CBA resonators had SQUID junction geometries. By applying an external magnetic field we can modulate the SQUID's critical current  $I_0$ , and hence we can modulate the resonance frequency of the CBA. We chose SQUIDs instead of single junctions because by fitting this modulation, we can extract  $I_0$  (see section 2.5.5). However, these SQUID samples are very sensitive to variations in the local magnetic field near the superconducting SQUID loops. Depending on the magnetic field sweep direction and speed, we can obtain very different modulation patterns for each of the resonators. Fig. 4.5 shows two examples of field sweeps taken from sample 4. The top panel illustrates a typical response where all the resonators have a different field offset. This could be due to different local fields around the SQUID loop because of vortices in the superconducting films. Another example of a magnetic field sweep is shown in the bottom panel, where all the resonators see the same local field. This is the optimum behavior because their maximum linear resonance frequency occurs at the same point in flux. Single junction multiplexed CBAs would not have this problem. If a vortex is trapped in the film sometime during the experiment, the fridge needs to be cycled above the resonator's transition

temperature to remove it.

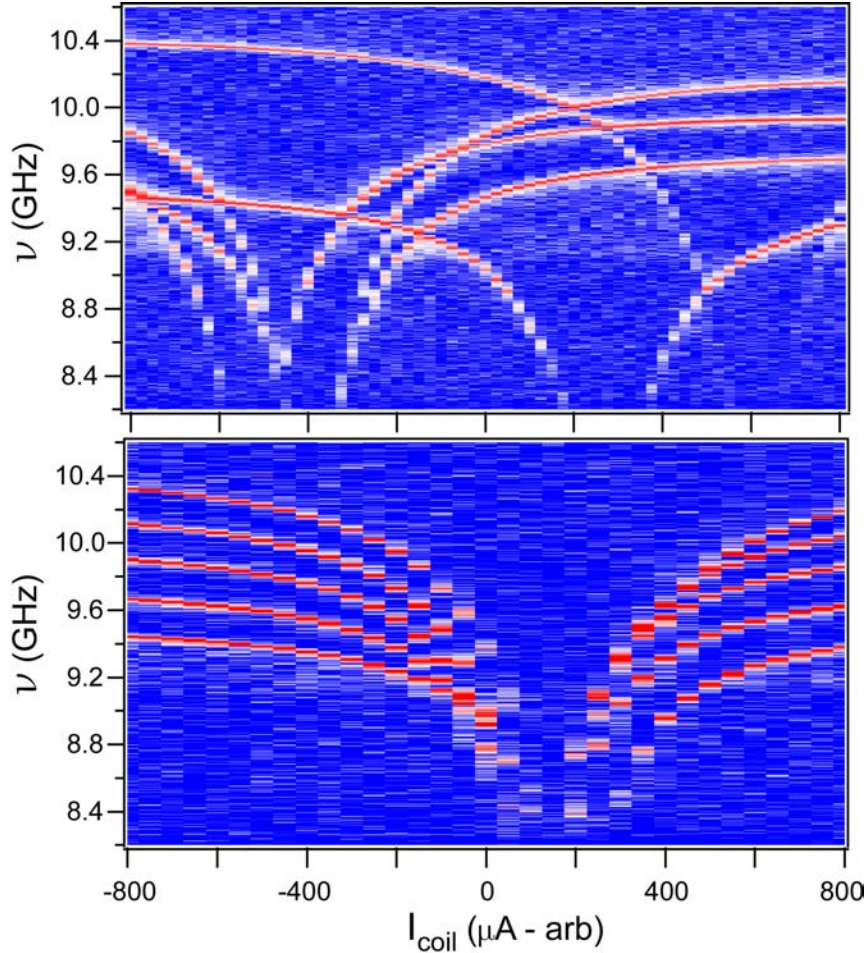


Figure 4.5: Plots of the magnetic field dependence of the linear resonance frequency of sample 4 with five multiplexed resonators. In the top panel we see the typical response with all resonators having different field offsets. Each SQUID has a different local field, probably due to vortices in the superconducting films. However, the modulation pattern is not fixed. For different sweep directions and speeds we can see different patterns. For example, the bottom panel has data where all the resonators see the same local field and have the same periods.

Time domain measurements of these samples were also taken and have been discussed previously in section 2.6.

## 4.2 Multiplexed Qubits

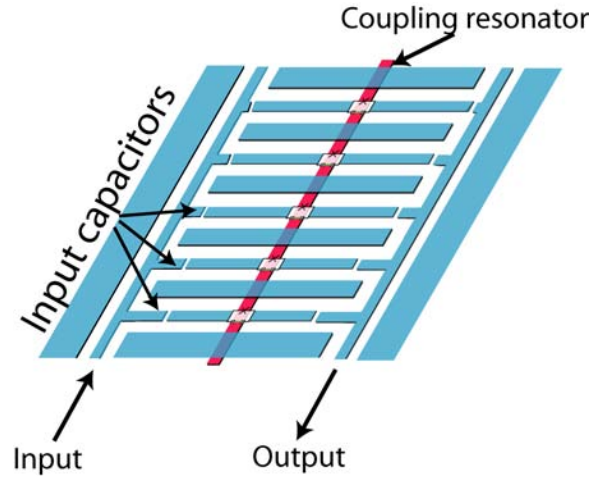


Figure 4.6: Cartoon of a multiplexed CBA sample with coupled qubits. Each resonator has a different length because of the differing distances between the input and output coupling capacitors. The coupling resonator can be fabricated in a different layer from the rest of the circuit, with capacitive coupling to each qubit island.

After establishing that multiplexed CBAs can behave like individual bifurcation readouts near their resonance frequencies, we can place a qubit into each resonator. Each qubit can be readout simultaneously, using the same readout lines (see Fig. 4.6). This could be used to measure many independent (ideally identical) qubits in parallel, in order to build up statistics on qubit behavior. Furthermore, a single qubit parameter (such as SCPB junction area, SCPB junction asymmetry, readout junction's critical current etc.) can be varied systematically over each CBA to find the optimal value of this parameter.

To build a quantum computer we must introduce a coupling mechanism between each qubit placed in a multiplexed device. This can be achieved by building another resonator which is capacitively coupled to each qubit island. This resonator would necessarily be built in a separate fabrication layer in order to couple

to all qubits at the same time. Alternatively, if only nearest neighbor coupling is required, then the coupling resonator can be fabricated at the same time, using the same photomask as the multiplexed CBA (see next section).

An alternative coupling scheme could be implemented through the readout lines, by constructing a resonator on the input (or output) readout lines. The quality factor of this new resonator would be small enough in order to enclose all of the multiplexed resonators within its bandwidth. Then, a potential change on the island of one of the qubits would cause a corresponding potential change on all the other qubit islands whose readout is located within the bandwidth of the coupling resonator.

### 4.2.1 Design of 2 multiplexed qubits

For simplicity, we begin with a two qubit sample with a nearest neighbor coupling resonator. The multiplexed readouts are well separated by about 10-20 linewidths (about 500 MHz) to avoid any spurious coupling. Each resonator has a different  $C_{out}$  in order to give each qubit a different gate voltage period. Hence, we should be able to find a biasing point where both qubits are tuned onto their “sweet spots.” Note that the ends of the input and output lines in this case must be open, not short. This is because the qubit gate is voltage biased through  $C_{out}$  and cannot have a path to ground. Furthermore, with only two multiplexed resonators we do not even need to fabricate extended input and output lines. We can just connect directly to the highest frequency resonator (see Fig. 4.7a), and place the second resonator sufficiently close by so that it is still sufficiently well coupled to the input signal at its resonance frequency.

The qubit coupling in this device is achieved by fabricating a CPW resonator on-chip, in between the two multiplexed CBAs. Each end of the coupling resonator

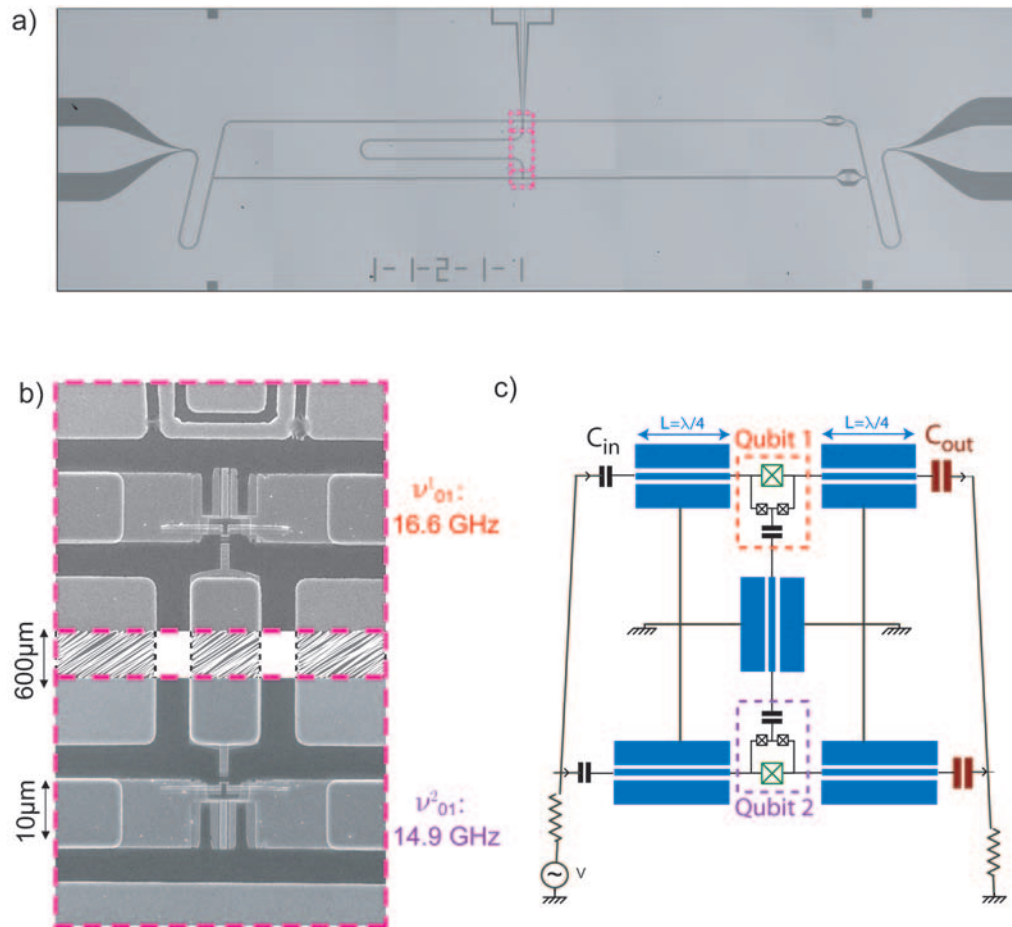


Figure 4.7: **(a)** An optical image of resonator used in the 2 multiplexed qubit measurements. The dashed line indicates the positions of the qubits shown in **(b)**. The coupling resonator meanders in-between the two readout resonators. **(b)** SEM images of the two qubits, which are placed in the two CBA readouts, and whose islands are coupled with a coupling resonator. These qubits are separated by  $600 \mu\text{m}$  on-chip (the coupling resonator is cut out of this picture in order to zoom into the qubits). **(c)** Circuit schematic of the multiplexed qubit device.

is capacitively coupled to the qubit's islands, as shown in Fig. 4.7b. By tuning one qubit in resonance with the coupling resonator we can transfer qubit state information to the resonator. Then, tuning the other qubit into resonance with the coupling resonator, we can transfer this information to the second qubit. The coupling resonator should have a very high quality factor and hence a long

lifetime compared to the qubit relaxation time  $T_1$ . The main difficulty of this approach is in tuning the qubit's transition frequency  $\omega_{01}$  into resonance with the coupling resonator. We can predict  $E_J$  from fabrication with only a certainty of a few gigahertz and if the coupling resonator has a high  $Q$ , we will need to be very accurate in choosing  $\omega_{01}$ . We cannot use flux to tune this frequency because we need to operate on the flux sweet spot to remain insensitive to flux noise (see section 4.3 for a possible solution to this problem). Hence our initial plan is to use the Stark-shift of the readout on the qubit, to pull  $\omega_{01}$  down in frequency. We have learned from previous (JBA) samples that a Stark-shift of a few hundred megahertz can be obtained by inputting a signal which is far detuned from the readout frequency. If we can fabricate  $\omega_{01}$  slightly higher than the coupling resonator's resonance frequency, then we can use this Stark-shift to couple the qubits with the coupling resonator.

### 4.2.2 Fabrication of two coupled qubits with multiplexed readouts

The resonators were fabricated out of Al using the photolithography lift-off process described in section 2.4.1. The chief complication in fabricating this device, is to oppositely orientate the qubits, so that both their islands can be capacitively coupled to the coupling resonator (see Fig. 4.7b). The bottom qubit is fabricated in the same manner as before (section 3.2.4), with the island deposited first, followed by the top electrodes of the CPB junctions. On the other hand, the top qubit's island is deposited in the second angle of evaporation, resulting in a thicker than usual island, and therefore will have a smaller superconducting gap  $\Delta$ , increasing the chance of quasiparticle poisoning.

### 4.2.3 Preliminary measurements on 2 multiplexed qubits

#### Gate modulations and spectroscopy

Fig. 4.8 shows some gate charge and flux modulation data for the qubit in the high frequency readout. This data is taken using a network analyzer by monitoring the reflected phase of the CBA at a fixed frequency, while sweeping the gate charge over a few periods and stepping the flux in the vicinity of  $\delta = 0$ . The ellipsoidal

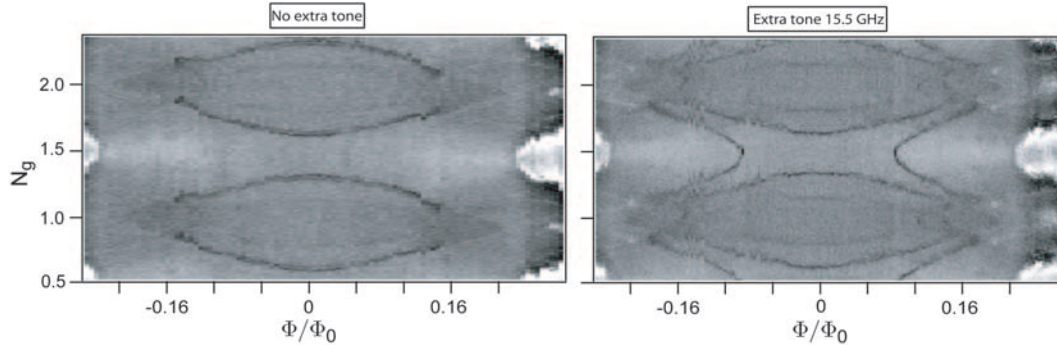


Figure 4.8: Plots of the gate charge and flux modulations of the two multiplexed qubit sample with the readouts operated in the non-linear regime. Data is shown for the qubit in the higher frequency resonator. The left panel is the regular gate charge and flux modulations of the qubit measured with the network analyzer. All the ellipsoidal features present in this figure are due readout induced qubit transitions. The right panel has an extra tone added in through  $C_{in}$  at 15.5 GHz. This results in an extra feature appearing in the modulations (see Fig. 3.11).

features present in the left panel of this figure are the usual readout induced qubit transitions. As before, when an extra tone is added, new features appear when this tone matches the qubit's transition frequency.

In addition, we can also perform intentional spectroscopy on this sample, where we sweep the frequency of the spectroscopic pulse  $\nu_s$  and step the gate charge  $N_g$ . In this experiment we measure the switching probability of the CBA,  $P_{01}$ , at a fixed readout frequency  $\nu$ . We perform spectroscopy on both qubits and find transition frequencies 16.6 GHz and 14.9 GHz at their sweet-spots. Note however, the qubit

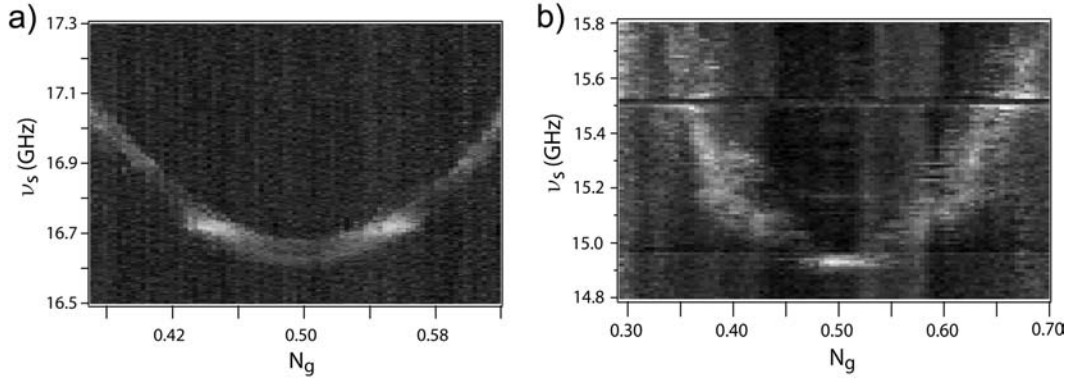


Figure 4.9: Spectroscopic peak vs. gate charge  $N_g$  for both multiplexed qubits. (a) Qubit in higher frequency readout resonator. Note the presence of a double peak near flux degeneracy. (b) The qubit in the low frequency resonator has a lot of local flux noise present, probably due to vortices in the superconducting film.

in the low frequency readout has much more noise compared to the other qubit. This could be due to vortices moving around randomly in the superconducting films near this qubit, causing a lot of flux noise. This problem can be seen while also trying to measure flux modulations of this qubit, because it jumps randomly between different points of the modulation. To cure this problem, the most recent generation of samples have holes fabricated in the superconducting films to pin these vortices (see section 4.3).

### Relaxation and coherence measurements - evidence of coupling

In the spectroscopy data, we see a double peak structure near the charge sweet spot. This could be evidence of coupling and can be investigated further by performing  $T_1$  measurements vs.  $\omega_{01}$ . An example of this data is shown in Fig. 4.10, where  $\omega_{01}$  is changed by varying the gate charge  $N_g$ . On top of the regular  $T_1$  exponential decay, we see oscillations whose position depends on  $\omega_{01}$ . This indicates that the qubit comes into resonance with some other two-level system on chip and exchanges energy with it. The qubit could be exchanging energy

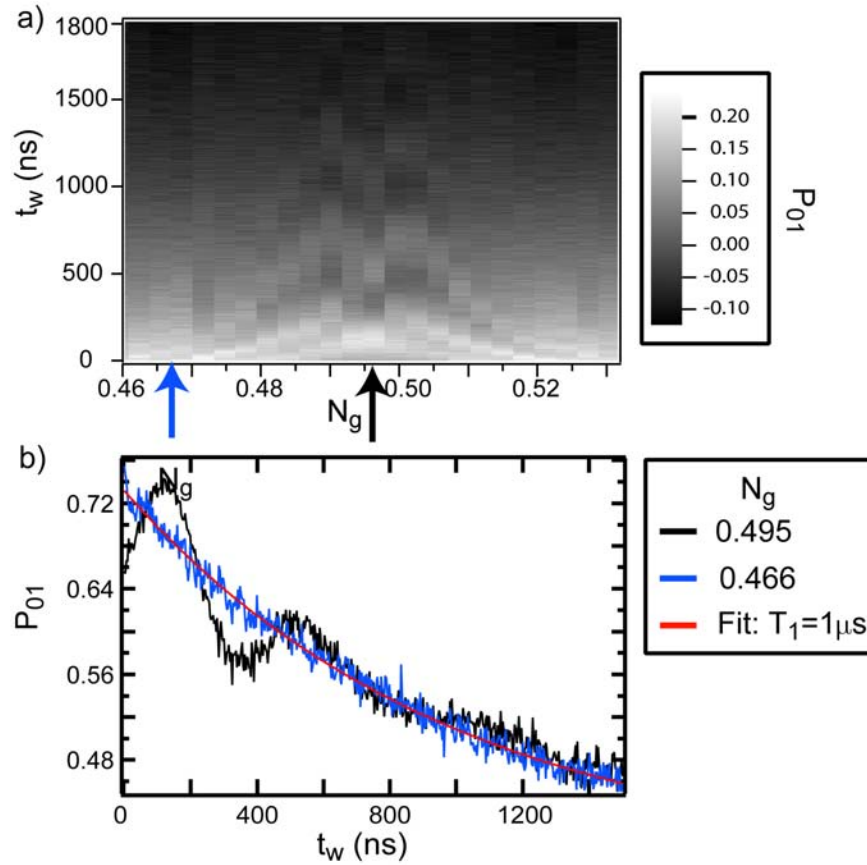


Figure 4.10: (a) Plot of the switching probability vs. gate charge  $N_g$  and wait time  $t_w$  between a  $\pi$ -pulse and the readout pulse. Modulations appear on the regular exponential decay for certain gate charges. (b) Cuts of the  $T_1$  decay for the gate charges indicated by the arrows in (a).

with the coupling resonator, although it would be a big coincidence for  $\omega_{01}$  to coincide exactly with the coupling resonator's frequency. The expected coupling strength between the qubit and the resonator is on the order of 10 MHz, which is compatible with the observed  $T_1$  oscillations.

Further evidence for this coupling can be seen in the Ramsey data. Again we can measure Ramsey fringes vs.  $N_g$  and we see that the fringes have an overall modulation, whose position again depends on  $N_g$ . On the “sweet spot” (black curve), we have measured an average  $T_2$  of  $1.15 \mu\text{s}$  by fitting the tail of the

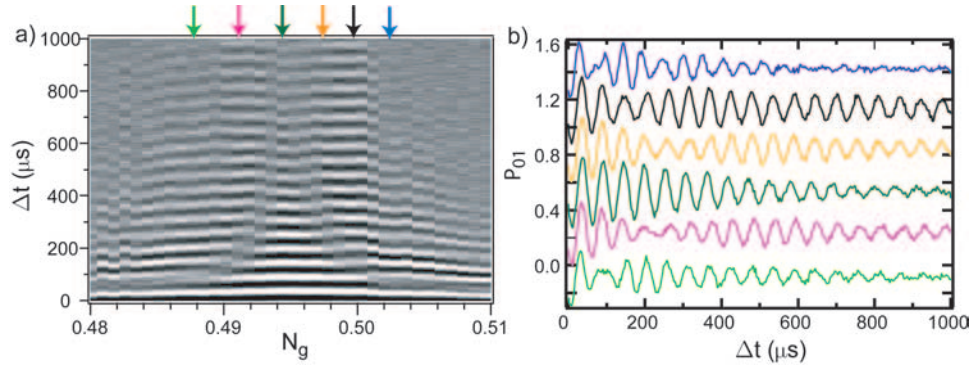


Figure 4.11: **(a)** Plot of the Ramsey fringes as a function gate charge  $N_g$ . We see a modulation pattern which depends on  $N_g$ . On degeneracy, the tail of the Ramsey fringes has a decay time of  $T_2 = 1150$  ns. **(b)** Cuts of the two-dimensional plot in (a) for the gate charges shown by the colored arrows.

Ramsey fringes with an exponentially decaying sine.

Apart from this extra modulation, these Ramsey fringes behave as would be expected from a regular qubit. If we tune  $N_g$  such that the modulation is moved out of the Ramsey fringes (off the “sweet spot”), we can measure the Ramsey frequency  $\nu_{Ramsey}$  vs.  $\nu_s$ . The Ramsey fringe frequency fits  $|\nu_{01} - \nu_s|$  as expected, giving us a precise measurement of  $\omega_{01} = 16.80$  GHz (Fig. 4.12) at this  $N_g$ .

## Conclusion

The above preliminary experiments demonstrate that a multiplexed CBA readout scheme is a feasible scheme for constructing a scalable qubit system. However, before continuing with the multi-qubit experiments, there are some aspects of the individual SCPB qubits that need improving, such as noise properties and tunability. Firstly, we would like an  $E_J$  which is tunable over a large frequency range by using, for example, an applied magnetic flux. This would have to be achieved without causing excessive decoherence of the qubit. A variable  $E_J$  would be useful for bringing each qubit into resonance with the coupling resonator. Also,

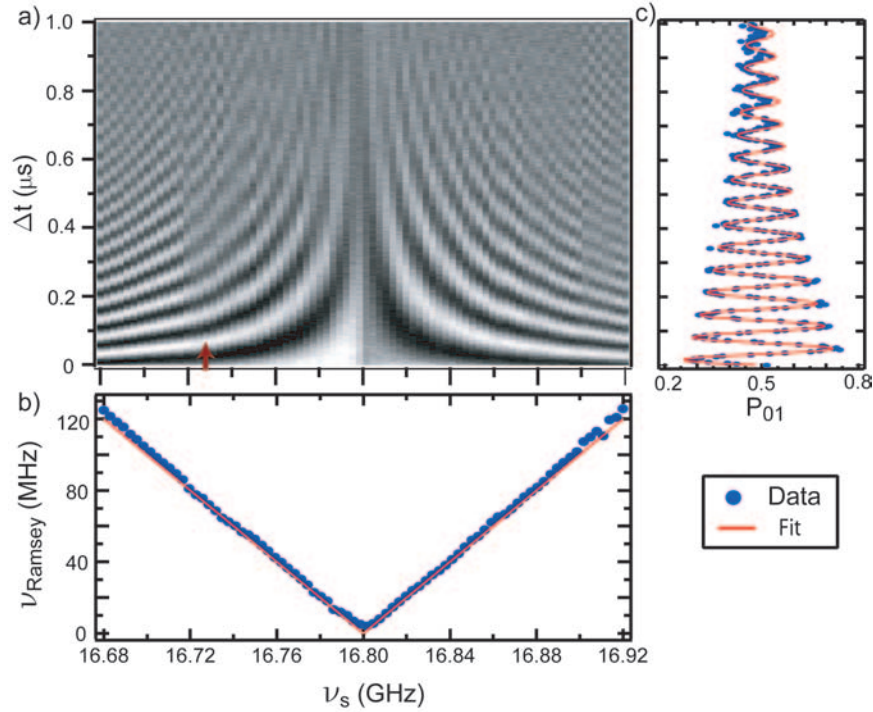


Figure 4.12: **(a)** Plot of the Ramsey fringes as a function of excitation frequency  $\nu_s$ . We see that the Ramsey frequency  $\nu_{Ramsey}$  increases as we move away from the qubit transition frequency  $\omega_{01}/2\pi$  as expected. **(b)** A fit of  $\nu_{Ramsey}$  vs.  $\nu_s$  which gives  $\omega_{01}/2\pi = 16.8$  GHz. **(c)** An example of a Ramsey fringe with excitation frequency  $\nu_s = 16.707$  GHz, whose position in (a) is shown by the brown arrow.

flux noise needs to be reduced to ensure that none of the multiplexed qubits are adversely affected by randomly moving vortices in the superconducting films. Finally, we would like to reduce charge noise, which is the current limiting factor on our coherence times. The next section will deal with all these issues, with a proposal dubbed the “in-line transmon”.

## 4.3 Reduced noise geometry - the “in-line Transmon”

### 4.3.1 Charge noise reduction

The current limitation on the coherence time of the SCPB is gate charge noise. Although we do not know the source of this noise, we can make the SCPB immune to it by increasing  $E_J/E_{CP}$ , so that the energy levels of the qubit become almost insensitive to charge. This can be realized by increasing the areas of the junctions in the SCPB because

$$E_J/E_{CP} \propto C_J/R_N \propto \text{area}^2, \quad (4.1)$$

where  $C_J$  is the junction self capacitance and  $R_N$  is the normal state resistance. However, making the junctions larger may expose the qubit to further sources of decoherence from two-level fluctuators (defects) in the oxide barrier of the junction. Attempts at measuring qubits in the limit of larger  $E_J/E_{CP}$  have proven difficult thus far.

An alternative method, inspired from the Transmon experiments of Schoelkopf and collaborators [85], [98], is to increase  $E_J/E_{CP}$  by enlarging the capacitance of the island to ground  $C_g$  (see Fig. 4.13). The SCPB is fabricated in-line with the center pin of the CPW near  $C_{in}$ , with the two small junctions in parallel. In this geometry, the island is made up of the length,  $x$ , of the center electrode of the CPW from  $C_{in}$  to the SCPB, and therefore the capacitance of the island to ground dominates  $C_g$ . For a 10 GHz resonator, we can increase  $E_J/E_{CP}$  by about a factor of ten by making  $x$  about 10% of  $\lambda/2$ . Thus,  $E_J/E_{CP}$  can be increased by simply increasing  $x$ , however, this increase has to be balanced with the desired amount of coupling between the SCPB and the readout, with the maximum coupling obtained when the SCPB is placed in the center of the resonator ( $x = \lambda/4$ ).

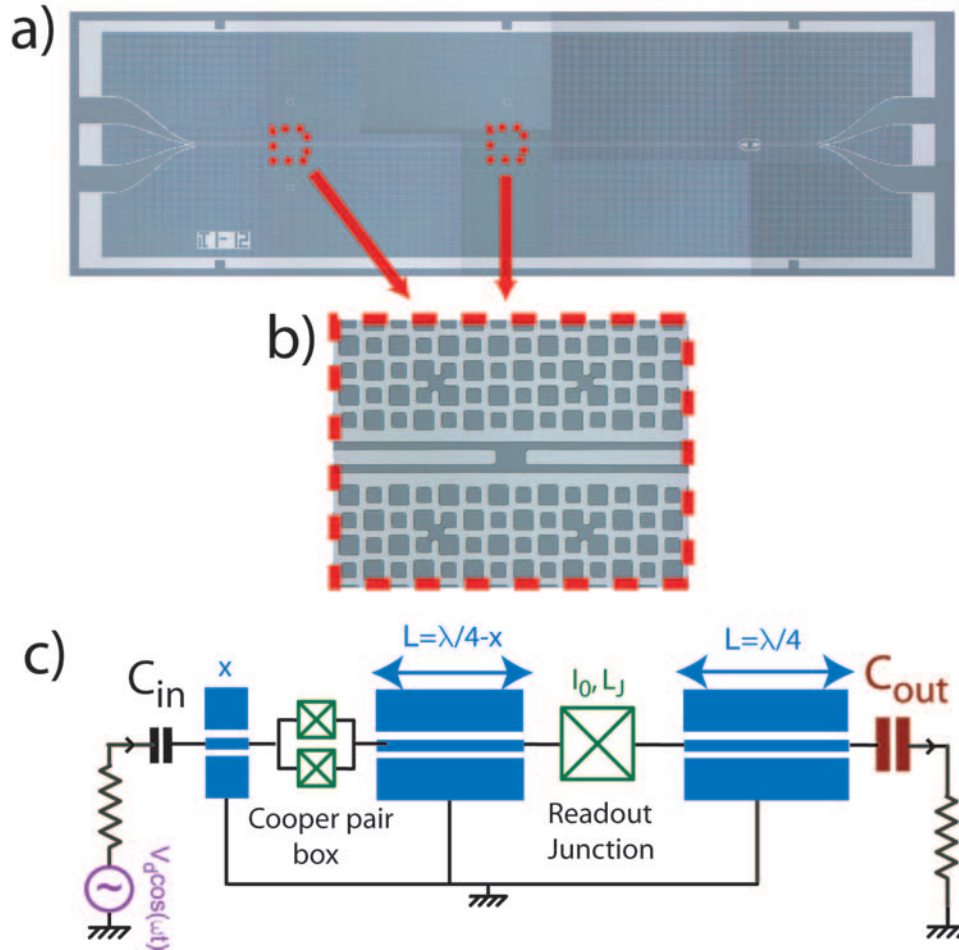


Figure 4.13: (a) Overall optical image of in-line transmon CPW resonator. (b) Zoom in of a gap in the center pin of the resonator, where either the SCPB (left gap) or readout junction (center gap) is placed. (c) Circuit schematic of an in-line Transmon device.

This geometry also has the advantage that the large readout junction is no longer placed in the superconducting loop of the SCPB. This should reduce the amount of phase noise and allow us bias the qubit off the flux “sweet spot”. An external magnetic field can tune the qubit transition energy  $\omega_{01}$  over a large frequency range of a few gigahertz. Asymmetric junctions in the SCPB, lifts the degeneracy of  $|0\rangle$  and  $|1\rangle$  at  $\delta = \pi$ , giving a second “sweet spot” at this flux point.

### 4.3.2 Flux noise reduction

The second main source of noise in superconducting qubit systems is flux noise. Most SCPB qubits are dominated by charge noise and do not have to worry about flux noise, as was the case for our qubit described in chapter two. However, as we saw in section 4.2.3, we need to be careful to minimize this noise source in multiplexed qubit samples. Local vortices trapped in the superconducting films can drastically change the local fields seen by each qubit. If these vortices move around they randomly change  $\omega_{01}$  and hence can reduce  $T_2$ . To combat this source of noise, we fabricate holes inside our superconducting ground planes (see Fig. 4.13b) to pin any vortices present in these films. Furthermore, we wish to cool the sample down to base temperature in zero field and we would like to avoid any randomly changing external magnetic fields when measuring the sample. To achieve this, we can wrap the sample holder in alternative layers of cryoperm and superconducting Al or Pb. The vacuum can of the refrigerator can also be surrounded with superconducting Pb and cryoperm to provide further protection.

## 4.4 Alternative CBA geometry - coupled stripline

There are many methods that could be implemented in building the resonator for the CBA, by using various combinations of lumped or distributed circuit elements. A  $\lambda/2$  CPW resonator was initially chosen because it provides a well understood and controlled environment. However, because of the large size of the CPW resonator, where more than 99% of a 10 mm  $\times$  3 mm chip is covered with metal, it must be fabricated using photolithography. Hence, the process of making a CBA device with CPW's is inherently a two (or more) step process, with alignment and ion cleaning in between the steps. If the CBA is being used to measure a device

that is fabricated first, e.g., carbon nanotube (see section 4.5.3), photolithography is not an option as precise alignment with the nanotube is needed before making the resonator.

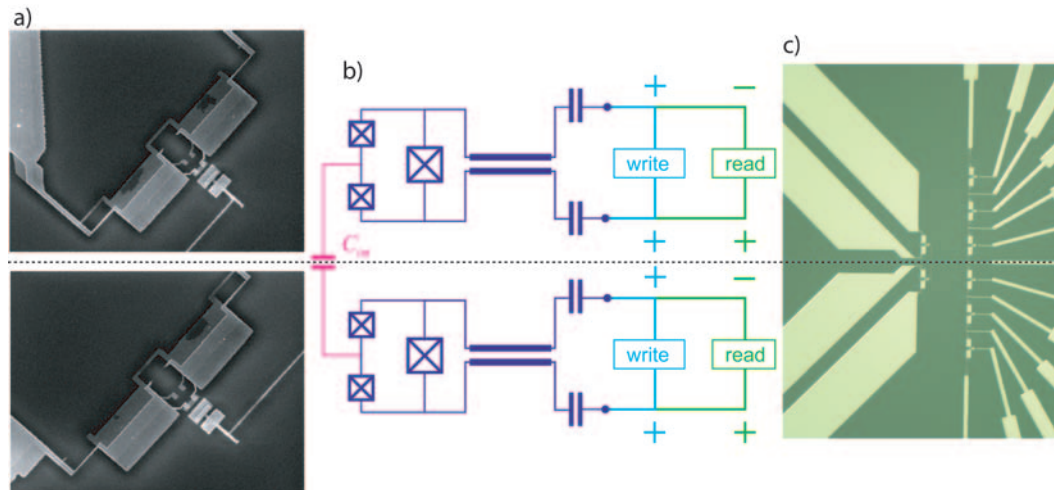


Figure 4.14: Images and a schematic of capacitively coupled qubit device with coplanar stripline CBA readouts (thanks to Chad Rigetti). **(a)** SEM images of each capacitively coupled qubit. **(b)** Circuit schematic of the whole device. **(c)** Optical image showing the ends of both coplanar striplines along with a vertical array of test qubit devices.

An alternative geometry that can be used to construct a distributed element resonator is a coplanar stripline (CPS). Compared with a CPW, which consists of a narrow center electrode and big ground planes covering most of the chip, a CPS only consists of two narrow strips of metal. Therefore, the CPS can be written with a scanning electron microscope by meandering the two striplines to fit in the SEM's field of view. Each line of the CPS is capacitively coupled to the input RF lines and it is these capacitors which limit the  $Q$  of the CBA. A qubit can be placed at the end of a  $\lambda/4$  CPS where there is a voltage minimum. This qubit and its CPS CBA readout can be fabricated in the same e-beam fabrication step, so that a full device can be completed in just a few hours. An example of

such a device is shown in Fig. 4.14, where there are two qubits whose islands are capacitively coupled, and have readouts with two separate CPS CBA's.

The main difficulty encountered when implementing this method is in launching the correct mode in the CPS. The readout is addressed with the differential mode of the resonator with voltages of opposite parity on each strip, while the qubit can be addressed with the common mode, with equal voltages on each strip. To launch these modes we can use a hybrid, which is a microwave device that outputs the sum and difference of its two RF inputs.

The device pictured in Fig. 4.14 is currently being measured in our lab (c.f. Chad Rigetti). To date, we have demonstrated that the CPS bifurcates and we have used it to measure the Rabi oscillations in a coupled qubit device.

## 4.5 Other applications of CBA

### 4.5.1 Readout for other superconducting qubits

One can view the experiments detailed in this thesis, as a test bed for the performance of cavity bifurcation amplification in quantum measurements of mesoscopic systems. Indeed, this method of amplification has since been adapted for use in reading out the state of the other superconducting qubits. A bifurcating readout scheme is currently being developed for flux qubits by the groups of Mooij et al. (Delft) [71], Orlando et al. (MIT) [100] and Nakamura et al. (NEC) (see Fig. 4.15). Also the quantum computing group at Maryland University are currently exploring methods of incorporating this amplification scheme for reading out a phase qubit (private communication).

Two examples of the experiments for reading out a flux qubit with a bifurcating SQUID are shown in Fig. 4.15. In both these cases, a non-linear oscillator is

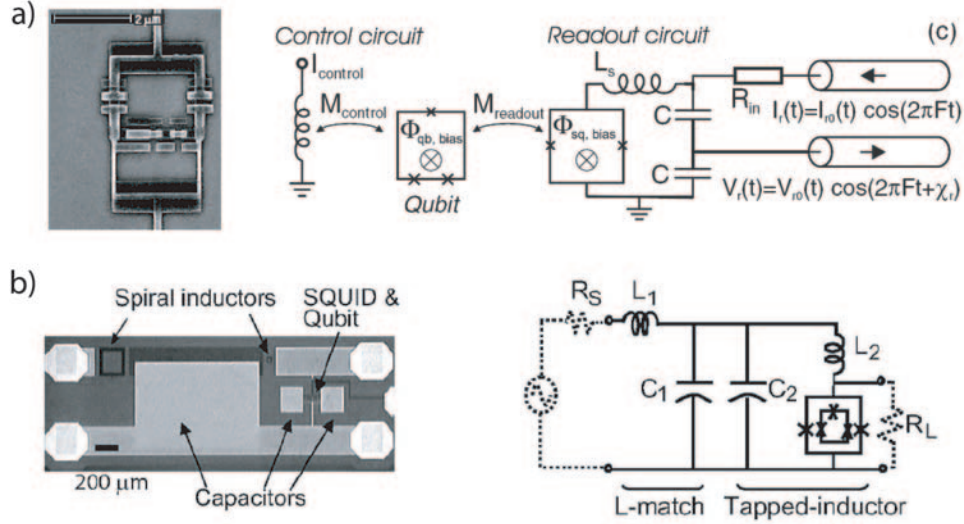


Figure 4.15: **(a)** SEM image and schematic of the experiment of Mooij et. al (Delft) [71]. This experiment uses a bifurcating SQUID to measure the state of a superconducting flux qubit. **(b)** Optical image and schematic of the experiments of Orlando et al. (MIT) [100]. This experiment is similar to that of Mooij et al. but with Nb based devices.

formed by constructing a lumped element LC oscillator, or JBA, from a parallel combination of a capacitor and Josephson junctions in a SQUID geometry. This SQUID JBA is inductively coupled to a 3-junction flux qubit. The main difference between these two experiments, is essentially that one is an Al based device (Mooij), while the other uses Nb technology (Orlando). Just as in our experiments, the state of the qubit will change the effective inductance of the SQUID and hence the switching probability of the JBA,  $P_{01}$ . While the experiments of Orlando et al. are still in the initial stages, the experiments of Mooij et al. have recently demonstrated the quantum non-demolition nature of this readout method [71], by measuring the large correlation between two successive measurements on the same qubit state.

### 4.5.2 Cooper pair counting

Other than measuring superconducting qubits, the CBA can measure any phenomenon which couples to the CBA's effective inductance,  $L_T$ . Without changing the qubit device layout significantly, we can adapt the CBA to count the coherent tunneling of Cooper pairs through a small Josephson junction, in a process called Bloch oscillations [101], [102]. This can be used to create a precise current standard. Due to the CBA's sensitivity and speed, this device could measure currents in the nanoamp range, much better than the present current standards, which operate efficiently in the picoamp range.

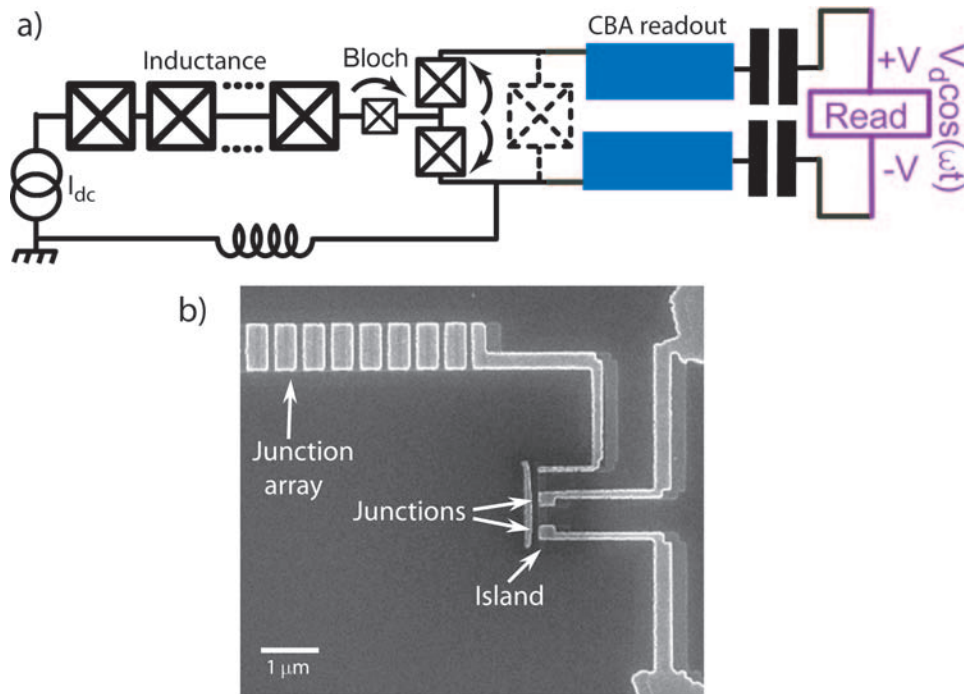


Figure 4.16: **(a)** Schematic of proposed device for counting Cooper pairs. Using the CBA, either in linear or bifurcation mode, we could measure the Bloch oscillations of the Cooper pairs as they tunnel through the junctions leading to the island. **(b)** SEM image of one of the first fabricated devices (c.f. Vladimir Manucharyan, Dec 2007) for use in a device as shown in (a).

In order to obtain Bloch oscillations through a small junction, the junction

capacitance must be small enough so that the charging energy  $E_C = \frac{e^2}{C_J}$  can prevent thermal fluctuations washing out the Bloch oscillations, i.e.,

$$\begin{aligned} E_C &\gg k_B T, \\ \text{or, } C &\ll \frac{e^2}{k_B T}. \end{aligned} \quad (4.2)$$

Furthermore, the junction needs to be isolated from its environment with a large enough impedance  $Z_J$  such that

$$Z_J \gg R_k = \frac{h}{4e^2}, \quad (4.3)$$

where  $R_k = 6.47 \text{ k}\Omega$  is the quantum of resistance. This impedance must be placed sufficiently close to the junction because, if not, the junction's biasing leads have picofarad capacitances to ground, resulting in a low shunting impedance. Previously, this biasing condition has been achieved using on-chip thin film resistors. However, these resistors still limit the linewidth of the Bloch oscillations [103]. Note that Bloch oscillations have been demonstrated in the regular quantum dot with the usual gate capacitor by microwave reflectometry [104]. We propose to bias the junction with an on-chip inductance large enough to have an impedance larger than  $R_k$ . This inductance can be fabricated compactly with an array of Josephson junctions (see Fig. 4.16) and can behave like a pure inductance up to all relevant frequencies,  $E_C/\hbar$ .

In our proposed setup, the array will take the place of the gate capacitor  $C_g$ , which biased the island in the previous qubit samples. At the end of the array, a small junction is connected to the island, through which the oscillations will occur. The tunneling Cooper pairs will change the effective inductance of the two intermediate sized junctions at the end of the resonator, which is then readout by the CBA. The CBA can be operated in the linear regime with a  $\lambda/2$  resonator and hence, no need for a big Josephson junction. Alternatively, it could be operated in

the usual mode, with a  $\lambda/4$  resonator and by measuring the switching probability  $P_{01}$  of the CBA between the two metastable states.

### 4.5.3 Coupling with molecular systems

All the applications that I have described above involve various types of superconducting circuits with Josephson junctions. However, the concept of a bifurcation amplifier is general, and can be applied to the measurement of various mesoscopic systems. For example, our group is currently attempting to apply the cavity bifurcation amplifier to the measurement of molecular systems.

A schematic of the proposed device is shown in Fig. 4.17. The idea is to replace the SCPB with a carbon nanotube, which is placed in parallel with the readout junction. Due to the proximity effect of the superconducting electrodes of the CBA's resonator, this nanotube can carry a supercurrent, up to a critical current of  $\sim 5$  nA [105] (similar in magnitude to the loop currents of the SCPB). The nanotube will act as an effective inductance in parallel with the readout junction and will modify the CBA's switching probability  $P_{01}$ . A gate electrode placed nearby can be used to modulate the nanotube's inductance and hence  $P_{01}$ .

In order to make this device, we first have to locate a prefabricated nanotube on chip. Then we can fabricate the CBA around it using e-beam lithography. Consequently, we must use the coplanar stripline implementation of the CBA (see section 4.4). We also require good contact between the nanotube and the superconducting electrodes. To achieve this, we evaporate a layer of Palladium in between the nanotube and the superconductor. The CBA parameters needed for this measurement are the exact same as that used for the qubit experiment. However, if we wanted to use the nanotube itself as the non-linear inductance, we would necessarily use a higher  $Q$  of up to 5000, in order to avoid reaching the

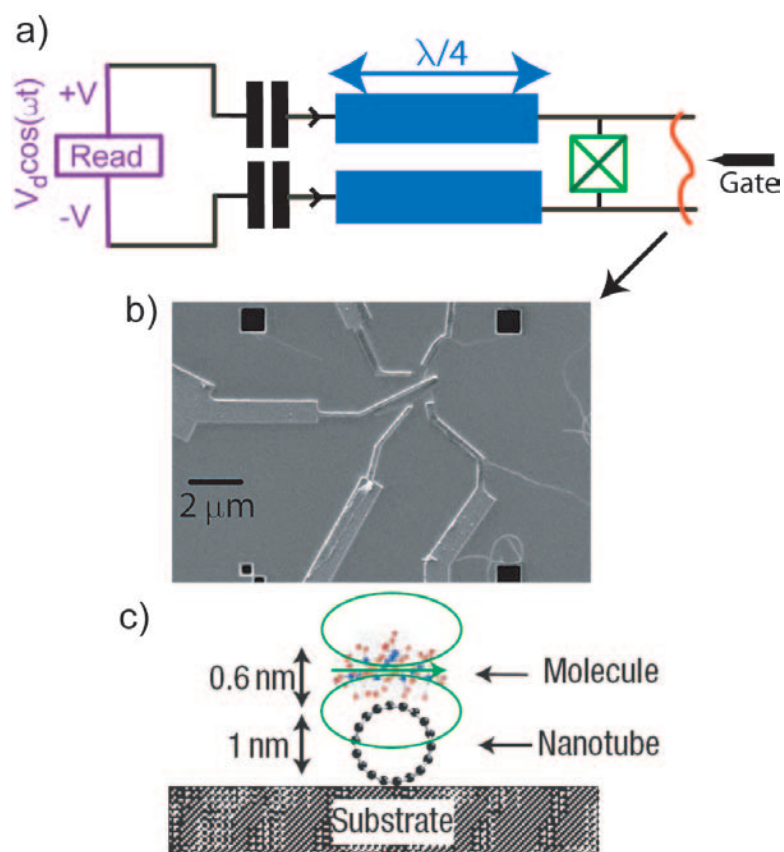


Figure 4.17: (a) Schematic of proposed device for measuring the inductance of a carbon nanotube. (b) SEM image of carbon nanotube fabricated in our lab (c.f. Markus Brink) for use in a device as shown in (a). (c) Cartoon of a potential application of this device for measuring the magnetic moment of a single molecule [105].

chaotic region before the system bifurcates. This device could have an application in measuring the magnetization switching of the magnetic moment of a molecule that is coupled to the carbon nanotube (see Fig. 4.17).

# Chapter 5

## Conclusions of thesis

In this thesis I have described the successful implementation of the bifurcation amplifier and its application as a readout for the Quantronium qubit. Compared with previous readout schemes, the CPW-CBA geometry offers precise control over the environment of the qubit with no stray capacitive or inductive elements; with a resonance frequency which depends on the length of the resonator and a  $Q$  which is determined by the large output capacitor. It is shown in this thesis, that this CBA geometry can easily be multiplexed on-chip so that ten CBA readouts, or more, could be measured simultaneously, each with a different readout frequency. Each multiplexed CBA would readout its own qubit and all would share the same readout lines. This is an important step towards scalable quantum computing.

During measurement the readout junction always remains in the superconducting state and therefore, the repetition rate is only limited by the relaxation time of the qubit and the  $Q$  of the resonator. Since the CBA is hysteretic we can latch its state and we therefore have excellent signal to noise ratio. With the latter two properties of the CBA, we can measure the fluctuations of the qubit's coherence time,  $T_2$ , on time scales as short as a second. We used this information to compensate for the fluctuations in real time and we have determined that the

fluctuations are dominated by  $1/f$  charge noise, agreeing with previous studies and illustrating the dependence of  $T_2$  on the measurement protocol. The CBA measures the susceptibility of the qubit (the qubit's impedance) and therefore the qubit remains on the 'sweet spot' during readout (and manipulation), minimizing loss to spurious environmental resonances.

However, the measured discrimination power of the CBA between the two qubit states is lower than expected, based on the known parameters of the CBA and the qubit. This could be due to the qubit coming into resonance with environmental resonances during readout. Future experiments could compensate for this effect by applying a gate pulse during readout to keep the qubit's transition frequency constant. The sensitivity of the CBA itself can be increased by improving the RF filtering on the measurement lines. Furthermore, we can explore new coupling schemes between the SCPB and the bifurcation amplifier - such as the in-line Transmon geometry, in which the readout junction is removed from the SCPB superconducting loop. This geometry also has reduced sensitivity to charge noise because of an increased  $E_J/E_{CP}$  ratio, and has reduced flux noise due to flux pinning centers in the superconducting ground planes.

Note that the amplifier described in our paper has further applications outside of the realm of superconducting qubit measurements, such as in measuring molecular devices and Cooper pair counting experiments. One can view the qubit in our experiment as a test bed for the performance of cavity bifurcation amplification in quantum measurements of mesoscopic systems. The measurement of any phenomenon that can be coupled to the Josephson energy can in principle benefit from this new type of amplification. Future theses from our group (and others) will, no doubt, demonstrate the CBA's versatility in mesoscopic physics in general.

# Appendix A

## Alternative fabrication methods and supplemental procedures

### A.1 Limitations of traditional Dolan bridge technique - Quantronium with JBA readout case study

The Dolan bridge double angle evaporation technique, outlined in the introduction of this thesis (see section 1.3.1), is the standard method we use to fabricate Josephson junctions in our lab. This technique is very reliable and repeatable once the resist thickness, SEM exposure doses and evaporation angles are determined. However, the Dolan bridge technique comes with some limitations and complications. To describe these limitations, and our techniques for overcoming them, I will concentrate on the fabrication of a Quantronium qubit with JBA readout.

#### A.1.1 Geometry limitations

The Quantronium qubit circuit consists of a large readout junction  $1 - 10 \mu\text{m}^2$  in size, and small Cooper pair box junctions  $0.03 - 0.1 \mu\text{m}^2$  in size. To maximise resolution for the smaller junctions, lower resist height is preferable, whereas to obtain a large enough lateral shift for the readout junctions, a higher resist height

is preferable. In reality we have to settle for a compromise, somewhere in between. Furthermore, fabricating both of these junctions simultaneously and placing both of them in the same superconducting loop, places restrictions on the possible geometries that we can fabricate. Fig. A.1a shows an SEM image of the resist used for this device. The superconducting loop is highlighted by the dashed white circle. In order to ensure that the loop doesn't collapse, it must be large enough to retain a pillar of MMA resist underneath. This also places a restriction on the SEM exposure doses for all the features surrounding the loop. If the pillar isn't large enough it may tilt to one side (or collapse all together) and cause the Cooper pair box junctions to become asymmetric.

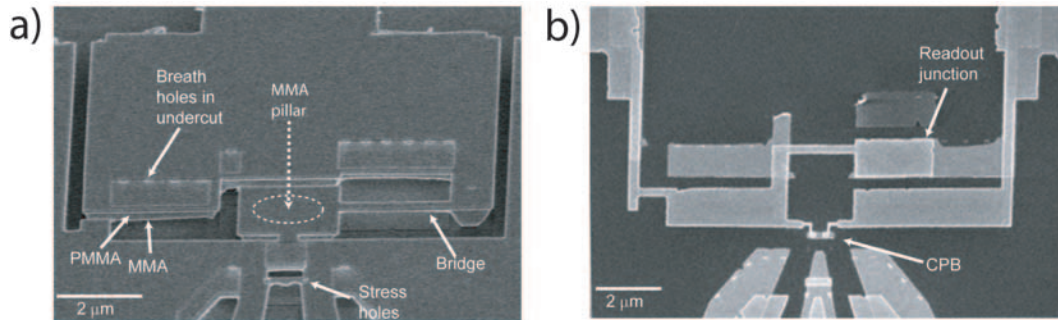


Figure A.1: **(a)** SEM image of resist for a Quantronium with JBA readout. The resist has  $\sim 10$  nm of Cu deposited on top to reduce the damage caused by viewing the sample. We are viewing the resist with the same angle that would be used in the Al deposition ( $\sim 30^\circ$ ). **(b)** SEM image of finished Quantronium with JBA readout.

### A.1.2 Undercut

Undercut is an essential feature of resist used in a Dolan bridge double angle evaporation process. Undercut is the term used to describe an area of a MMA/PMMA resist bilayer which has all the MMA removed from underneath the PMMA layer. For example, when making the large readout junction we need to construct a

PMMA bridge - or, in other words, a long narrow piece of suspended PMMA, as seen in Fig. A.1a. In addition to this suspended bridge, the rest of the circuit has undercut along the evaporation direction. This is present to ensure that the evaporated Al sticks cleanly onto the substrate without hitting the resist wall and tearing off during lift-off. Around 100 – 300 nm of unavoidable undercut is obtained around fully exposed areas of PMMA, with the larger exposed features obtaining more undercut. However, we can increase this undercut and pattern it as desired, by gently exposing the resist in predetermined areas. Because the MMA is more sensitive to exposure than PMMA, this gentle exposure is enough to get rid of the MMA, while leaving the PMMA behind. These areas of undercut can be clearly seen in Fig. A.1a as brighter rectangular features on the surface of the resist. In the larger areas of undercut we have placed “breath holes”, which are fully exposed holes through the PMMA layer, located on the edge of the undercut regions. These holes guarantee that the MIBK developer completely dissolves the undercut regions within the development time.

Another trick at our disposal is to intentionally avoid undercut in certain areas, so that the evaporated Al falls completely on the resist wall and is hence removed during lift-off. In Fig. A.1a we are viewing along the evaporation direction and, therefore, evaporated Al will hit resist in the areas where MMA is visible. For example, the small wire at the back of the resist pillar for the superconducting loop does not get deposited at this angle. We can use this technique to disconnect any spurious electrodes which do not form part of the designed circuit.

Large areas of undercut places strain on the PMMA layer, causing it to tear along lines of weakness. An example of such an area in our circuit is the gate capacitor of the SCPB, as shown in Fig. A.2a. In this region, the large gate electrodes must be fabricated within a few hundred nanometers of the SCPB’s

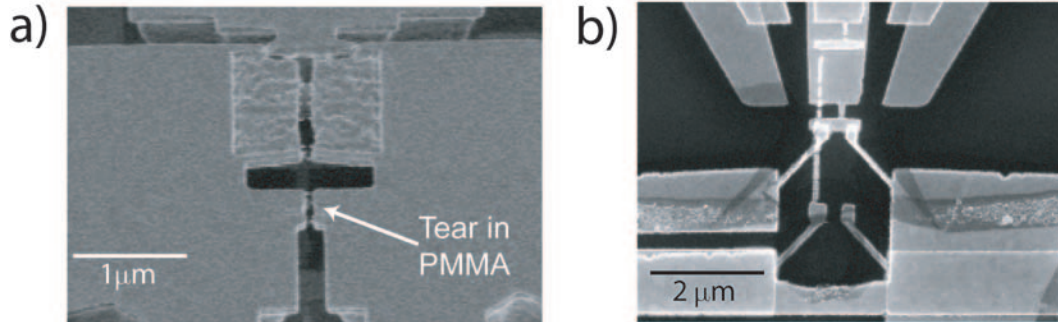


Figure A.2: **(a)** SEM image of resist with a tear due to stress in the PMMA layer. Again we are viewing at an angle of  $\sim 30^\circ$ . **(b)** SEM image of a deposited sample which had a tear in the resist.

island in order to have a sufficiently large gate capacitance. These large gate electrodes have unavoidable large areas of undercut around them. Furthermore, an undercut box is placed on the opposite side of the island to form the PMMA bridge for the SCPB's junctions. Hence, there is a lot of suspended PMMA in this area and tears frequently occur in the resist which short circuit the junctions and/or the gate capacitor (see Fig. A.2b). We can reduce the probability of obtaining these cracks by intentionally punching holes through the resist in predetermined areas to relieve the stress in the PMMA. Two such holes can be seen in Fig. A.1a, located on either side of the gate capacitor.

## A.2 Multi-layer Al junctions

Due to the many complications involved in fabricating a Quantronium circuit with the Dolan bridge technique, we have developed an alternative multi-layer fabrication technique (although these samples have yet to be measured). This method has none of the geometry limitations inherent with the Dolan bridge method and the resist height is only limited by the thickness of metal deposited. Furthermore, only a minimal amount of undercut is needed to prevent rough edges on the

deposited metal and no spurious electrodes or junctions are deposited with this method. The fabrication procedure begins with depositing Au alignment marks

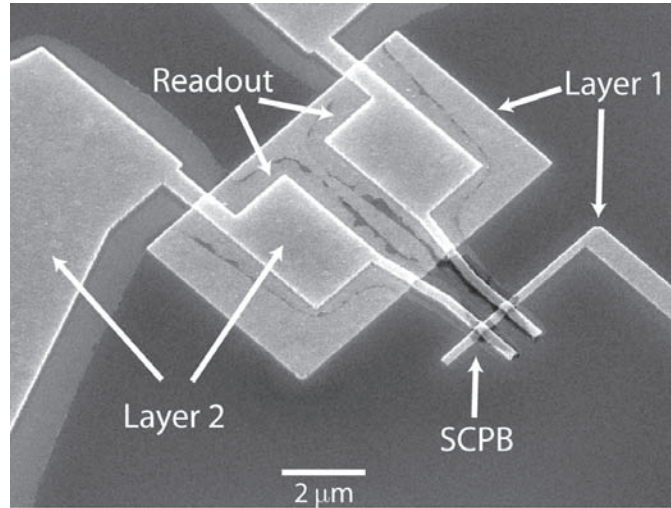


Figure A.3: SEM image of a Quantronium fabricated with multilayer junctions.

on a full two inch wafer. These marks are used to align the various fabrication layers with each other in the SEM. After the Au is deposited, we spin a bilayer of MMA/PMMA on the full wafer and then dice it up into individual chips. Next, we expose and deposit the bottom electrode of the junction using a simple  $0^\circ$  evaporation of 20 – 30 nm. Following lift-off, we again re-spin a bilayer of resist on the chip and expose the second electrode of the junction. Before depositing the top electrode in the evaporator, we Ar ion clean the first layer in order to remove any native oxide on the surface of the metal. We then controllably oxidise the Al and deposit the top electrode. The second layer is made about twice as thick as the first layer to ensure that it is continuous.

An example of the Quantronium fabricated with this method is shown in Fig. A.3. In layer one we deposit the island of the SCPB and the bottom electrode of the readout junction. Layer two consists of the top electrodes of the readout and

SCPB junctions, along with the measurement leads and the gate electrodes. Note, with this fabrication method we have full control over the area of the superconducting loop and size of the junctions. Furthermore, the large spurious junctions inherently present in the measurement leads as a result of using the Dolan bridge technique, are now absent.

### A.3 Aluminium oxide capacitors

The complicated structure of the capacitor used in making the JBA readout (see section 2.3.1) for the Quantronium was one of the main motivations for moving away from this lumped element device, to the simpler structure of a CPW distributed element resonator, used in the CBA. However, we can simplify the construction of the capacitor using a multilayer technique, in a similar manner to the previous section. We begin by fabricating the Quantronium along with the bottom electrodes of the shunting capacitor. We then re-spin a bilayer of resist on the chip. However, this resist must be baked at only 90°C for 5 min to avoid damaging the previously deposited junctions. We then expose the top electrode of the capacitor and evaporate  $\text{Al}_2\text{O}_3$  to form the capacitors insulator. This layer is deposited with a rotating stage and with a sharp evaporation angle to use all the available undercut. Next, the top electrode of the capacitor is deposited at 0° (see Fig. A.4) to avoid shorts through the insulator.

### A.4 Sapphire substrate

Sapphire is the ideal substrate for our devices because it has a very low loss tangent. However, it is a perfect insulator and, hence, it is difficult to write a device in the scanning electron microscope due to charging effects. Because of

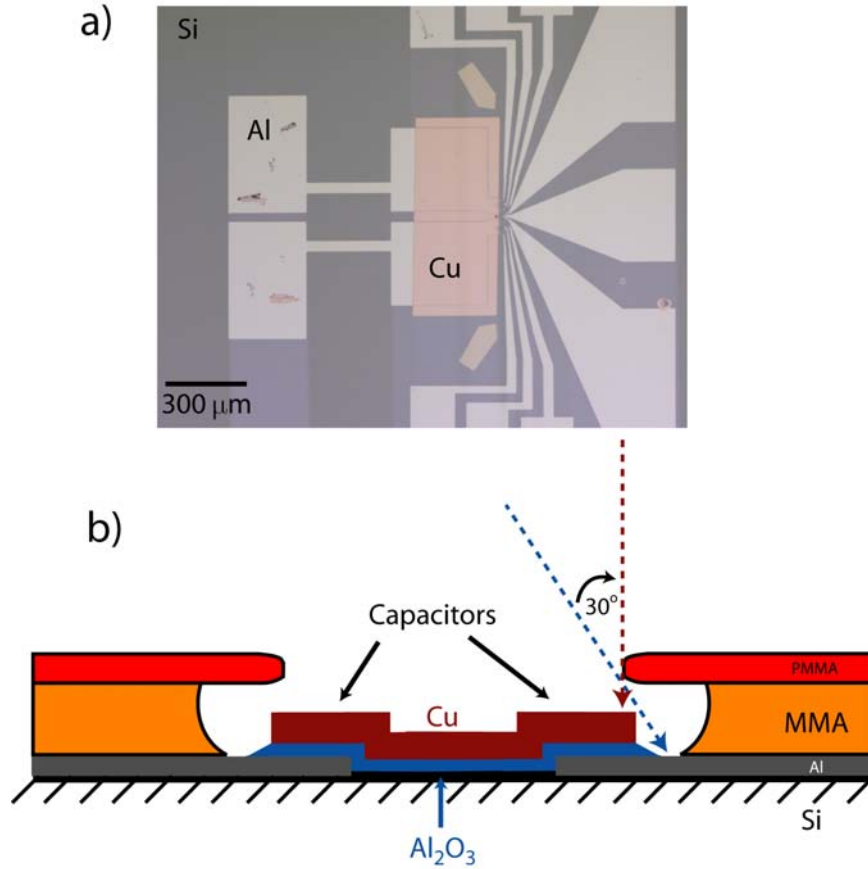


Figure A.4: **(a)** Optical image of  $\text{Al}_2\text{O}_3$  capacitors for a Quantonium sample with JBA readout. See section 1.3.3 for further details of the fabrication of this multilayer qubit device. **(b)** Schematic of the evaporation process used to fabricate the  $\text{Al}_2\text{O}_3$  capacitors. 30 nm of oxide is deposited at a sharp angle ( $\sim 30^\circ$ ) and with the sample rotating at approximately  $10^\circ\text{sec}^{-1}$ . Following this, Cu is deposited at  $0^\circ$  to avoid any shorts through the capacitor.

this, we have used a low resistivity Boron doped Si wafer for the majority of the devices described in this thesis.

In order to avoid these charging effects, we can deposit a thin layer ( $\sim 10$  nm) of Al on the surface of the MMA/PMMA resist bilayer. This Al provides a path to ground during the SEM writing step. Before developing the exposed sample, this thin Al layer is removed with a TMAH solution (typically MF312). The usual

development and evaporation procedure follows.

## A.5 Quasiparticle traps and gap engineering

Non-equilibrium quasiparticles tunneling onto the SCPB island can reduce the qubit's coherence time and can limit the measurement repetition rate. Fortunately, there are three main methods presently known which can reduce this quasiparticle poisoning. The original Quantronium experiments in Sacaly used a normal metal quasiparticle trap, placed close to the SCPB's island [106]. This type of trap can easily be incorporated into our qubit design, without significantly changing the design, as shown in Fig. A.5. We write two extra lines on either side of the SCPB. Following the double angle junction fabrication, we rotate the stage by  $90^\circ$  to evaporate along the long axis of the the extra wires and then we tilt the stage to about  $80^\circ$ . At this sharp angle, Au metal is deposited only in the large

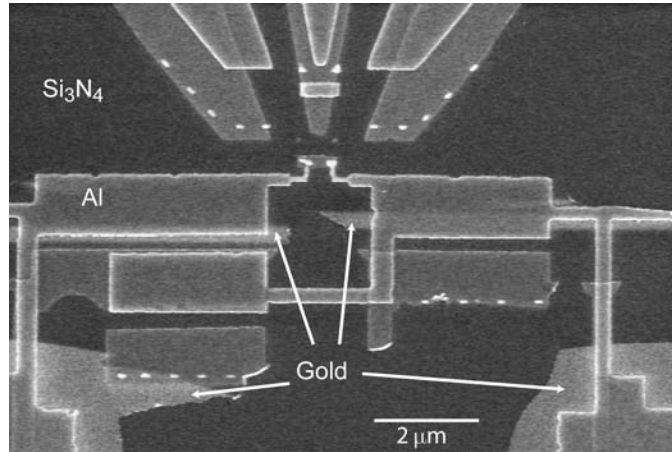


Figure A.5: SEM image of a Quantronium fabricated with Au quasiparticle traps. The traps are deposited last, after the Al layers. The stage is rotated by  $90^\circ$  and tilted to around  $80^\circ$  for the Au deposition.

measurement leads and along the long extra wires that we have written. Alternatively, at the expense of increasing the fabrication time, we can easily make the

Au traps in an extra fabrication layer.

An alternative method known to prevent quasiparticle poisoning, is to increase the superconducting gap of the island relative to the leads. This prevents quasiparticles from entering the island and speeds up their exit. The gap can be increased by evaporating the island in an atmosphere of oxygen [107] and/or making the island thinner [108] (e.g., 10 nm).

# Appendix B

## Dissipative RF filters

It is essential in a CBA experiment to filter external noise at all frequencies which could reach the sample through the input and output RF lines. Without sufficient filtering, the CBA's transition between its two metastable states is broadened, reducing the sensitivity. This broadening can be described in the experiment as an elevated effective escape temperature,  $T_{\text{esc}}$ , larger than the fridge bath temperature,  $T_{\text{esc}} > T$ .

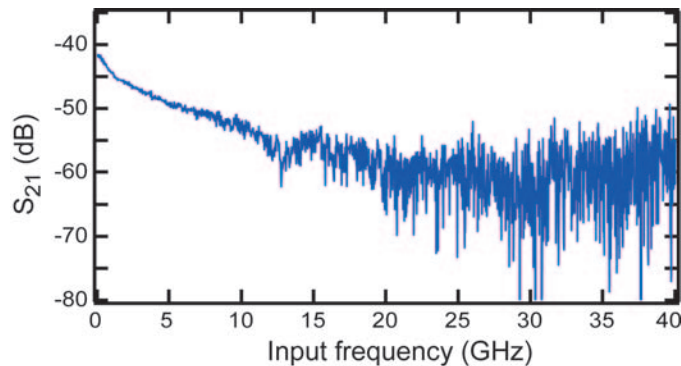


Figure B.1: Plot of the transmission of an input RF line used in a typical CBA experiment. We get about 60 dB of attenuation for 20 – 40 GHz.

Different filtering strategies are used for the input and output lines. The input lines are simply heavily attenuated to reduce any noise propagating down the line. The amount of attenuation increases with frequency and typically flattens out

around 20 GHz at approximately  $-55$  to  $-65$  dB, depending on the experiment (see example in Fig. B.1). This strategy is possible on the input lines because we have the freedom to input an arbitrarily large amount of power to the sample when performing our experiments. However, we cannot repeat this on the output

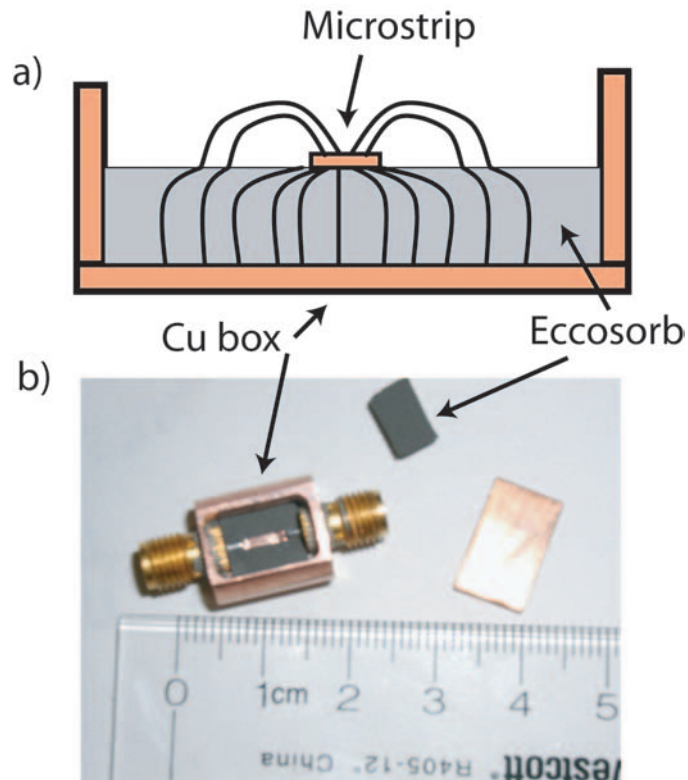


Figure B.2: **(a)** Schematic of a dissipative RF filter, designed to attenuate high frequency signals. It consists of a  $50\ \Omega$  microwave line on a dissipative substrate called Eccosorb. **(b)** Optical image of a completed RF dissipative filter.

lines because we would reduce our output signal, which is fixed to a certain range of powers. In our measurement band, we have filtering provided by the circulators. However, outside the band we need to attenuate all frequencies. We begin by using some commercial lumped element low pass and high pass filters (e.g. minicircuits). These filters can give a sharp cutoff around our measurement band. However, for frequencies larger than  $10 - 20$  GHz, they develop parasitics and hence begin to

fail.

To filter out these higher frequencies, we need to develop a dissipative RF filter. A reflective filter (e.g. DC block) is not as good due to the possibility of setting up standing waves. Ideally, our dissipative RF filter would be a good  $50 \Omega$

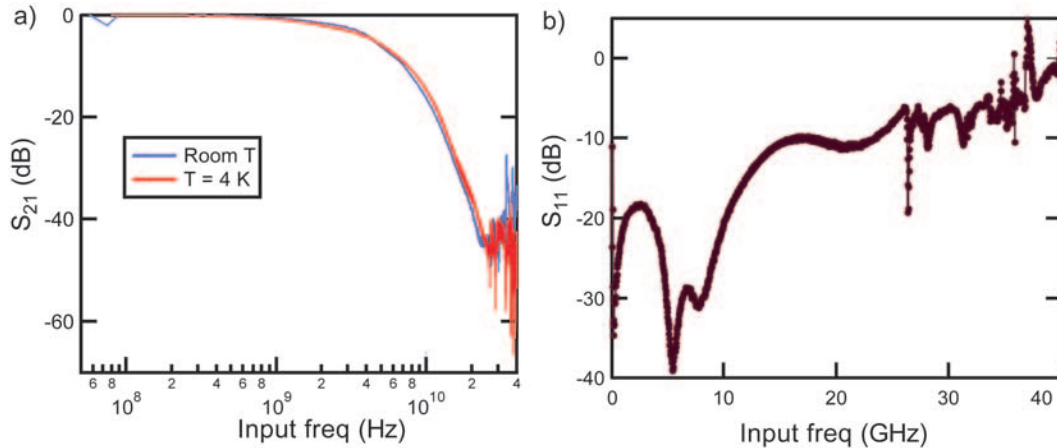


Figure B.3: **(a)** Plot of the transmission through the Eccosorb dissipative RF filter at room temperature and at 4 K. The  $-3$  dB point is around 2 GHz. **(b)** Plot of the reflection from the Eccosorb filter. The device has an impedance close to  $50 \Omega$  up to 30 GHz.

line to prevent any reflections and would preferentially damp high ( $> 10$  GHz) frequencies. Our design (shown in Fig. B.2) consists of a microstrip line on top of a dissipative substrate. For a substrate we began with Eccosorb - a commercially available magnetic material which is dissipative at microwave frequencies. For example, the material we used has 3 dB/cm at 1 GHz and 118 dB/cm at 18 GHz.

The performance of this device is shown in Fig. B.3. It only has 1 – 2 dB of loss in the band of 1 – 2 GHz and up to 40 dB of loss at 40 GHz. Furthermore, its impedance remains close to  $50 \Omega$  up to 30 GHz. When combined with some commercial lumped element filters, this provides sufficient filtering on the output lines for the CBA experiments in the 1 – 2 GHz range. Subsequent designs replaced

the Eccosorb with copper powder in epoxy. This has the advantage of being easy to thermalize; however, its transmission changed from cooldown to cooldown.

We were unable to extend the cutoff of this device above 10 GHz. This would require us to reduce the size of the device by a factor of 5 - which proved impossible with the current design. With more lossy Eccosorb we can potentially push the 3 dB point of the filter to 10 GHz. Then, however, only approximately 6 dB of loss would be present at 20 GHz, because this material generally has a linear falloff with frequency. Hence, we need a lumped element LC filter, or, a distributed element reflective filter which have a sharp cutoff above 10 GHz and which are effective until at least 30 GHz, at which point an Eccosorb filter can take over. Such filters are difficult to purchase or construct because precise microwave engineering is required. Alternatively, copper powder filters can have a sharper cutoff compared to Eccosorb filters and if the correct combination of size of copper grains and length of filter is found, we can potentially fabricate a copper powder filter which cuts sharply just above 10 GHz. These avenues of investigation are currently being pursued and should be implemented in the next generation of CBA experiments (for more recent work on Eccosorb filters see [109]).

# Appendix C

## Simulation procedure

### C.1 Equations of motion

The Duffing oscillator model is excellent for understanding the weak non-linear steady state behavior of the CBA. The Duffing oscillator equation, Eqn. 2.29, describes the behavior of the CBA in a rotating frame at the drive frequency and in the approximation  $\dot{q}/I_0 \ll 1$ . This rotating frame approximation greatly speeds up simulations. However, these approximations are poor for low Q samples and difficulties arise when trying to understand switching from the high amplitude to the low amplitude metastable state at the lower bifurcation point,  $\beta_b^-$  and the highly non-linear chaotic behavior at large input powers. Instead I run simulations based on the full series LRC single mode model, with the equation of motion

$$\left( L_{\text{eff}} + \frac{L_J}{\sqrt{1 - \dot{q}^2/I_0^2}} \right) \ddot{q} + R_{\text{eff}}\dot{q} + \frac{q}{C_{\text{eff}}} = V_d \cos(\omega t) + V_N(t), \quad (\text{C.1})$$

using a fourth order Runge-Kutta method, a numerical algorithm that I will describe later in this appendix.

In order to numerically solve this equation we must first break it down into two dimensionless first order differential equations. When numerically solving differential equations, it is good practice to make them dimensionless to avoid any scaling errors and to understand the important free parameters in the system. We

begin by dividing across by the total inductance  $L_T = L_{\text{eff}} + L_J$ , to get:

$$\left(1 - p^s + \frac{p^s}{\sqrt{1 - \dot{q}^2/I_0^2}}\right) \ddot{q} + 2\Gamma\dot{q} + \omega_0^2 q = \frac{V_d}{L_T} \cos(\omega t) + \frac{V_N(t)}{L_T}, \quad (\text{C.2})$$

where  $p^s = \frac{L_J}{L_T}$  is the participation ratio,  $\Gamma = \frac{R_{\text{eff}}}{2L_T}$  is the half width at half maximum of the linear resonance peak,  $\omega_0 = \frac{1}{\sqrt{L_T C_{\text{eff}}}}$  is the linear resonance angular frequency and the noise  $V_N$  satisfies  $\langle V_N(t)V_N(0) \rangle = 2k_B T R_{\text{eff}} \delta(t)$ . Next, we translate to dimensionless time  $\tau = \omega_0 t$  to get:

$$\left(1 - p^s + \frac{p^s}{\sqrt{1 - (\frac{\dot{q}\omega_0}{I_0})^2}}\right) \ddot{q} + \frac{\dot{q}}{Q} + q = \frac{V_d}{\omega_0^2 L_T} \cos\left(\left(1 - \frac{\Omega}{2Q}\right)\tau\right) + \frac{V_N(t)}{\omega_0^2 L_T}, \quad (\text{C.3})$$

where  $Q = \frac{\omega_0}{2\Gamma}$  is the linear resonance quality factor and  $\Omega = \frac{\omega_0 - \omega}{\Gamma}$  is the reduced detuning. Finally, we translate to dimensionless charge  $q \mapsto q \frac{\omega_0}{I_0}$  and multiply both sides by  $\frac{\omega_0}{I_0}$  to get

$$\left(1 - p^s + \frac{p^s}{\sqrt{1 - \dot{q}^2}}\right) \ddot{q} + \frac{\dot{q}}{Q} + q = \frac{V_d}{I_0 \omega_0 L_T} \cos\left(\left(1 - \frac{\Omega}{2Q}\right)\tau\right) + \frac{V_N(t)}{I_0 \omega_0 L_T}. \quad (\text{C.4})$$

Hence, we get the two first order dimensionless differential equations:

$$\begin{aligned} \dot{q} &= I, \\ \dot{I} &= \frac{-I/Q - q + \tilde{V}_d \cos\left(\left(1 - \frac{\Omega}{2Q}\right)\tau\right) + \tilde{V}_N}{1 - p^s + \frac{p^s}{\sqrt{1 - \dot{q}^2}}}. \end{aligned} \quad (\text{C.5})$$

The dimensionless drive  $\tilde{V}_d$  is given by:

$$\tilde{V}_d = \frac{V_d}{V_b} p^s \sqrt{8\beta_b(\Omega)\Omega^3 \epsilon^3}, \quad (\text{C.6})$$

where  $\beta_b(\Omega)$  is the reduced drive power at the bifurcation point (see Eqn. 2.8) and  $\epsilon = \sqrt{\frac{1}{p^s Q}}$ . The dimensionless noise  $\tilde{V}_N$  satisfies:

$$\langle \tilde{V}_N(0)\tilde{V}_N(\tau) \rangle = \frac{2k_B T}{\omega_0 Q E_J} \delta\left(\frac{\tau}{\omega_0}\right). \quad (\text{C.7})$$

These are the equations I solve using the Runge-Kutta algorithm described in the next section.

## C.2 Runge Kutta algorithm

To numerically solve ordinary differential equations (ODEs), we reduce them to a set of  $N$  coupled first-order differential equations for the functions  $y_i$ ,  $i = 1, 2, \dots, N$ , having the general form:

$$\frac{dy_i}{dx}(x) = f_i(x, y_1, \dots, y_N), i = 1, \dots, N. \quad (\text{C.8})$$

These equations are not sufficient to find a solution numerically; boundary conditions are also required. In our case, we have an initial value problem, where all the  $y_i$  are given at some starting value  $x_s$ , and we wish to find the  $y_i$ 's at some final point  $x_f$ .

The most basic numerical method for solving differential equations is known as Euler's method. It involves adding small increments to the functions  $y_i$  corresponding to derivatives (right-hand sides of the equations) multiplied by stepsizes  $h = \Delta x$ . In other words

$$y_{n+1} = y_n + hf(x_n, y_n) + O(h^2), \quad (\text{C.9})$$

which advances a solution from  $x_n$  to  $x_{n+1} = x_n + h$ . However, this method is not very accurate compared with other methods with the same stepsize,  $h$ , and it is also not very stable.

In this thesis, I use Runge-Kutta methods (see [110]), which generalizes Euler's method by propagating a solution over an interval by combining the information from several Euler-style steps (each involving one evaluation of the right-hand  $f$ 's). For the fourth order Runge-Kutta algorithm, the derivative in Euler's method is replaced by an effective derivative, which is a weighted average of the derivatives  $k_1, k_2, k_3, k_4$ ; where,  $k_1$  is the slope at the beginning of the interval;  $k_2$  is the slope at the midpoint of the interval, using slope  $k_1$  to determine the value of  $y$  at the

point  $x_n + h/2$  using Euler's method;  $k_3$  is again the slope at the midpoint, but now using the slope  $k_2$  to determine the  $y$ -value; and finally,  $k_4$  is the slope at the end of the interval, with its  $y$ -value determined using  $k_3$ . In summary, the fourth order Runge-Kutta algorithm is given by:

$$\begin{aligned}
 k_1 &= hf(x_n, y_n), \\
 k_2 &= hf(x_n + h/2, y_n + k_1/2), \\
 k_3 &= hf(x_n + h/2, y_n + k_2/2), \\
 k_4 &= hf(x_n + h, y_n + k_3), \\
 y_{n+1} &= y_n + \frac{k_1}{6} + \frac{k_2}{3} + \frac{k_3}{3} + \frac{k_4}{6} + O(h^5).
 \end{aligned} \tag{C.10}$$

This is the standard method used by most scientists - however, more complicated algorithms exist, with for example, adaptive step sizes.

### C.3 Noise generation

In order to simulate thermal noise, we need to generate Gaussian pseudo-random numbers given a source of uniform pseudo-random numbers. A Gaussian distribution with mean  $\mu$  and variance  $\Sigma^2$  is given by:

$$P(x) = \frac{1}{\Sigma\sqrt{2\pi}} e^{\left(-\frac{(x-\mu)^2}{2\Sigma^2}\right)}, \tag{C.11}$$

where  $P(a \leq x \leq b) = \int_a^b P(x)dx$  is the probability of finding  $x$  in the interval  $(a, b)$ .

I use a transformation known as the Box-Muller [111] transformation, which takes two independent random numbers from a uniform distribution in the interval  $(0, 1)$ ,  $x_1$  and  $x_2$ , and transforms them into two independent random numbers from a Gaussian distribution,  $y_1$  and  $y_2$ , with  $\mu = 0$  and  $\Sigma = 1$ . The most basic form of this transformation looks like:

$$\begin{aligned}
 y_1 &= \sqrt{-2\ln(x_1)} \cos(2\pi x_2), \\
 y_2 &= \sqrt{-2\ln(x_1)} \sin(2\pi x_2),
 \end{aligned} \tag{C.12}$$

However, this formulation may be slow due to many calls to the math library and, also, it may may not be stable when  $x_1$  is very close to 1. Hence, I use the polar form of the Box-Muller transformation, which is both faster and more robust numerically:

$$\begin{aligned}
 &\text{do}\{ \\
 &\quad x_1 = 2 * \text{rand}() - 1; \\
 &\quad x_2 = 2 * \text{rand}() - 1; \\
 &\quad w = x_1^2 + x_2^2; \\
 &\quad \}\text{while}(w \geq 1); \\
 &w = \sqrt{\frac{-2 \ln(w)}{w}}; \\
 &y_1 = x_1 * w; \\
 &y_2 = x_2 * w;
 \end{aligned} \tag{C.13}$$

After these random numbers are generated, I multiply them by the standard deviation given by Eqn. C.7.  $\delta(\tau)$  is approximated by the inverse of the stepsize,  $h$ , used in the simulation:

$$\delta(t) = \delta\left(\frac{\tau}{\omega_0}\right) \approx \frac{\omega_0}{h}. \tag{C.14}$$

Hence, the variance of the noise is given by

$$\langle V_N(0)V_N(\tau) \rangle = \frac{2k_B T}{hQE_J}. \tag{C.15}$$

## C.4 Schematic simulation procedure

The simulation follows the same procedure as in a real experiment. It begins with inputting a function representing the latching voltage pulse,  $V_d$ , in reduced time units  $\tau$ , as shown in the top panel of Fig. C.1. The Runge-Kutta algorithm then solves for  $q(\tau)$  and  $\dot{q}(\tau)$ . The output is multiplied by a signal at the drive frequency  $\omega$  and filtered to keep only the d.c. component. An example result is shown in the bottom panel of Fig. C.1. The output signal is averaged over time  $t_{meas}$  and if the result is larger than an assigned ‘‘threshold’’ value, it is counted

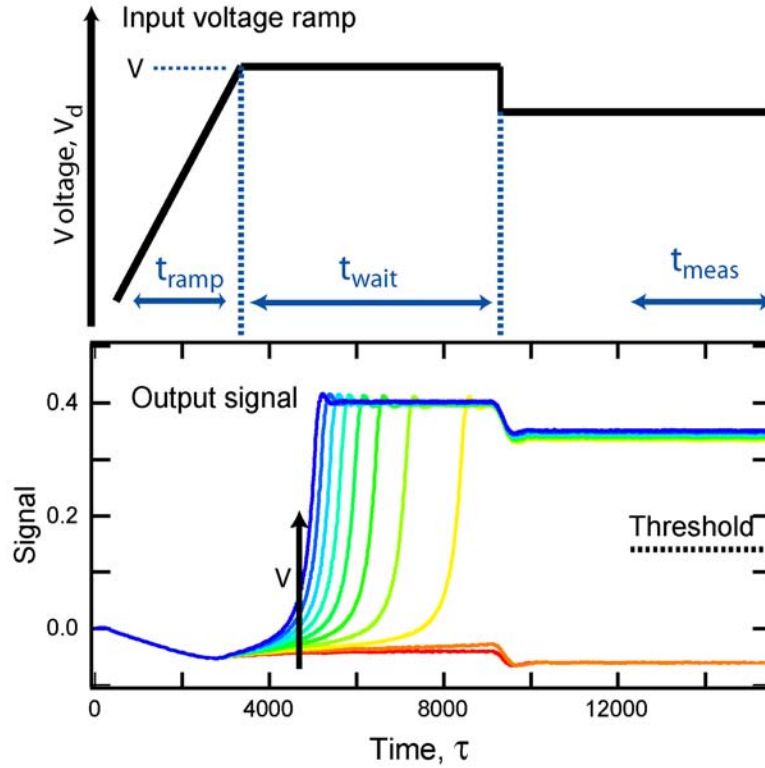


Figure C.1: The input voltage to the simulation is the latching pulse shape shown in the top panel. The bottom panel illustrates an example output from the simulation. Measurement is done during time  $t_{meas}$  and if the result is above the “threshold,” it is counted as a switching event. This is an example with no noise and in which the voltage is stepped up through the bifurcation point,  $V_b$ , with the orange and red curve being below  $V_b$  and the rest above.

as a switching event. In this manner, I repeat the simulation a few hundred times to calculate the switching probability  $P_{01}(V)$  for each input voltage ramp,  $V$ .

# Appendix D

## Table of variables, acronyms and fundamental constants

(Alphabetical order)

Symbol	Meaning
$ 0\rangle$	Ground state of a qubit
$ 1\rangle$	First excited state of a qubit
$\alpha$	Amplitude of 1/f charge noise
$a_k$	probability amplitude for the state $ k\rangle$
$A(t)$	Slowly moving complex amplitude of the charge variable of the CBA in the rotating frame (Units: Coulombs)
$\beta = \frac{V_d^2}{\phi_0^2 \omega^2} \left( \frac{1}{2\Omega\epsilon^2} \right)^2$	Dimensionless drive power
$\beta_b^\pm$	Dimensionless drive power at the upper and lower bifurcation points
$\beta_c$	Dimensionless drive power at the critical point
$\beta_{ms}$	Dimensionless drive power at the points of maximum susceptibility below the critical point
$b(\Omega)$	coefficient of $\frac{x^3}{3}$ term in the cubic meta-potential of the CBA
$B(t) = \frac{A(t)\omega}{I_0} \sqrt{\frac{1}{2\Omega\epsilon^2}}$	Dimensionless rescaling of $A(t)$
$B_c$	Slow re-scaled oscillation amplitude at the critical point
CBA	Cavity bifurcation amplifier
$C_{\text{eff}}$	Effective capacitance of the equivalent circuit model for the CBA
$C_g$	Gate capacitance of CPB $\sim 100$ aF
$C_{in}$	Input finger capacitor for the CPW CBA resonator
$C_J$	Capacitance between the two electrodes of a Josephson junction $\sim 50$ fF/ $\mu\text{m}^2$

$C_k$	Effective capacitance of the $k_{th}$ qubit energy eigenstate
$C_{out}$	Output capacitor for the CPW CBA resonator. This capacitor typically determines the Q of the resonator
$C_s$	Parallel plate capacitor shunting the large junction in a JBA device
$C_\Sigma$	Total capacitance of superconducting island of CPB to ground
CPB	Cooper pair box
$\Delta$	Superconducting gap. Al has a gap of $\Delta/2e \sim 200 \mu\text{V}$ or $2\Delta/h \sim 100 \text{ GHz}$
$\delta = \Phi/\phi_0$	Superconducting phase difference across a Josephson junction
$\Delta I$	Period of the SQUID modulation in the CBA
$\Delta I_0$	Smallest critical current change detectable by the CBA
$\Delta t$	Free evolution time between qubit manipulation pulses (Used in $T_2$ measurements)
$\delta\omega = \omega_0 - \omega$	Detuning frequency when driving CBA
$\delta V$	Width of s-curve of CBA
$\epsilon = \sqrt{\frac{L_T}{L_J} \frac{1}{Q}}$	Need $\epsilon \ll 1$ to have bistability without chaos
$\epsilon$	Coefficient of $x$ term in the cubic potential of the CBA meta-potential
$E_{01} = \hbar\omega_{01}$	Transition energy of a qubit between the ground and first excited state
$E_{CP} = \frac{(2e)^2}{2C_\Sigma}$	Cooper pair charging energy of the Cooper pair box with a total island capacitance of $C_\Sigma$
$E_J = \frac{\hbar}{2e} I_0 = \phi_0 I_0$	Josephson energy of a single Josephson junction with $I_0$ critical current or the total Josephson energy of a Cooper pair box
$E_J^0$	Josephson energy of the large readout junction in the Quantronium circuit
$E_J^* = E_J \cos(\delta/2)$	Effective Josephson energy of a SCPB for zero asymmetry $\sigma = 0$
$E_k$	$k^{th}$ energy level of SCPB
$F$	Amplitude of an external force applied to a non-linear pendulum at frequency $\omega$
$F_N$	External noise source connected to a non-linear pendulum
$ \psi\rangle = a 0\rangle + b 1\rangle$	General quantum state of a two level system with ground state $ 0\rangle$ and excited state $ 1\rangle$
$ \Psi\rangle$	Quantum state of an n-qubit system
$g$	Acceleration due to gravity

$\gamma = \frac{\omega_a}{2\pi} e^{U/k_B T}$	Arrhenius law for escape rate of the CBA out of the lower oscillating metastable state
$\Gamma = \frac{R_{\text{eff}}}{2L_T}$	Half width at half maximum of linear resonance peak
$\hat{H} = \hat{H}_{el} + \hat{H}_J$	Total hamiltonian of CPB
$\hbar = \frac{h}{2\pi}$ $1.054 \cdot 10^{-34} \text{ J}\cdot\text{s}^{-1}$	Reduced Planck constant
$\hat{H}_{el}$	Electrostatic hamiltonian of CPB
$\hat{H}_J$	Josephson hamiltonian of Josephson junction
$\iota_k$	Superconducting current in the loop of a SCPB for the energy level $E_k$
$\hat{I}$	Operator for the loop current in a SCPB
$I_0$ $\frac{\pi\Delta}{2R_n e} \tanh\left(\frac{\Delta}{2k_B T}\right)$	Critical current of a Josephson junction made from a superconductor with gap $\Delta$ and normal state resistance $R_n$ at temperature T
$I_{coil}$	Current through the magnetic field coil
$I_{off}$	Offset current needed to move to the max of a CBA SQUID modulation
JBA	Josephson bifurcation amplifier
$ k\rangle$	$k^{th}$ energy eigenstate of CPB
$k_B$	Boltzmann's constant= $1.38 \cdot 10^{-23} \text{ J/K}$
$\lambda = \frac{L_J}{L_{loop}} - 1$	Non-linearity parameter for flux qubit
$L$	Half the length of the CPW resonator or $L = \lambda/4$
$L_{\text{eff}}$	Effective inductance of the equivalent circuit model for the CBA
$L_J = \frac{\phi_0}{I_0}$	Inductance of a Josephson junction with critical current $I_0$
$L_k$	Effective inductance of the $k^{th}$ qubit energy eigenstate
$L_{loop}$	Inductance of a superconducting loop (c.f. Flux qubit)
$L_T = L_{\text{eff}} + L_J$	Total inductance in effective model of CBA
$L_T^p = \frac{L_J L_p}{L_J + L_p}$	Total inductance in the JBA implementation
$\mathcal{M}_A$	Mathieu characteristic function A (used in CPB eigenenergies)
$\mathcal{M}_{C\&S}$	Mathieu functions used in CPB eigenstates
$\nu$	Frequency of microwave drive for CBA readout
$\nu_0$	Linear resonance frequency of CBA
$\nu_{01}$	Qubit transition frequency between the first two energy levels
$\nu_p$	Qubit precession frequency in a frame rotating at the excitation frequency $\nu_s$
$\nu_{Rabi}$	Qubit Rabi frequency
$\nu_{Ramsey}$	Qubit Ramsey fringe frequency
$\nu_s$	Frequency of qubit manipulation pulses

$\nu_N(\tau)$	Noise in rotating frame at reduced time $\tau$
$N$	Number of excess Cooper pairs on the island of a CPB with total charge $-2eN$
$ N\rangle$	$N^{\text{th}}$ charge eigenstate of CPB
$N_g = \frac{C_g V_g}{2e}$	Gate charge of the CPB in terms of Cooper pairs
$n_g = \frac{C_g V_g}{e}$	Gate charge of the CPB in terms of single electrons
$\Phi$	Externally applied magnetic field
$\phi$	Phase change of either the transmitted or reflected microwave signal from the CBA resonator
$\Phi_0 = \frac{h}{2e}$	Superconducting flux quantum
$\phi_0 = \frac{\hbar}{2e}$	Reduced flux quantum
$\Phi_{\text{ext}}$	Externally applied flux (c.f. flux qubit)
$\phi_u$	Polar angle coordinate for Bloch sphere representation of qubit state
$P_{01}$	Switching probability of the CBA out of the lower amplitude oscillation amplitude metastable state
$P_b$	Bifurcation power
$P_b^{ 0,1\rangle}$	Input power at the bifurcation point for qubit states $ 0\rangle$ or $ 1\rangle$
$P_c$	Power at critical point where the upper and lower bifurcation points coincide
$P_{\text{in}}$	Input microwave drive power to the CBA
$P_{\text{out}}$	Transmitted microwave power from the CBA
$p^p = \frac{L_T^p}{L_J}$	Participation ratio in the JBA implementation
$p^s = \frac{L_J}{L_T}$	Participation ratio in the CBA implementation
$P(v)$	Number of switching events at voltage $v$ in a voltage ramp
$Q = \frac{\omega_0}{2\Gamma}$	Quality factor of CBA
QP	Quasi-particles
QND	Quantum non demolition
$\theta$	Superconducting phase of island in SCPB
$\vartheta$	Angle of deflection for a driven, damped, non-linear pendulum
$\theta_u$	Polar coordinate for the Bloch sphere representation of the qubit state
$q(t) = \int_{-\infty}^t I(t') dt'$	Branch charge with current $I(t)$
$R_{\text{eff}}$	Effective resistance of the equivalent circuit model for the CBA
$R_n$	Normal state resistance of a Josephson junction
$\Sigma$	Standard deviation of a Gaussian distribution
$\sigma$	Asymmetry between the two Josephson junctions in the CPB
SCPB	Split Cooper pair box

SQUID	Superconducting quantum interference device
$\tau = \delta\omega t = (\omega_0 - \omega)t$	Dimensionless time used in Duffing oscillator equation
$\tau_R$	Length of Rabi pulse
$T$	Bath temperature of the fridge
$T_1$	Energy relaxation time of a qubit
$T_2$	Decoherence time of a qubit obtained by fitting an exponentially decaying Ramsey fringe.
$T_{\text{esc}}$	Effective escape temperature of the CBA out of its lower oscillation amplitude metastable state
$t_W$	Wait time between qubit manipulation pulse and readout pulse (used in $T_1$ measurements)
$U$	Unitary transformation
$U(V_d)$	Effective barrier for escape of the CBA out of the low oscillating state for R.F. drive $V_d$
$V(t)$	Voltage pulse used to manipulate a qubit state at time $t$ , amplitude $A$ , and time duration $\tau_R$
$\hat{V}$	Potential of the superconducting island of the CPB
$V_b$	Bifurcation voltage of the CBA
$V_d$	Voltage amplitude of microwave drive
$V_g$	Gate voltage of CPB
$V_N(t)$	Voltage noise produced in effective CBA model
$V(x)$	Effective potential seen by the CBA in the rotating frame near the bifurcation point
$\omega$	Microwave drive angular frequency
$\Omega = \frac{\omega_0 - \omega}{\Gamma} = \frac{\delta\omega}{\Gamma}$	Reduced detuning of CBA
$\Omega_c$	Reduced detuning at the critical point
$\omega_a$	Attempt angular frequency of CBA in escape process
$\omega_p$	Plasma frequency of a Josephson junction
$\omega_0 = \frac{1}{\sqrt{C_{\text{eff}} L_T}}$	Linear resonance angular frequency of CBA
$\omega_{01}$	Transition angular frequency between the first two energy levels of the SCPB
$Y(\omega)$	Environmental parallel admittance at frequency $\omega$
$Z(\omega)$	Environmental series impedance at frequency $\omega$
$Z_0$	Impedance of the CPW resonator designed to be 50 $\Omega$
$Z_{\text{res}}$	Impedance seen by the junction when the biasing circuitry consists of a resonator
$Z_{\text{series}}$	Impedance seen by the junction when biased with a series LRC circuit

# Bibliography

- [1] J. Gruska, *Quantum Computing*, McGraw-Hill Publishing Company, 1999.
- [2] M. A. Nielsen and I. L. Chuang, *Quantum Computation and Quantum Information*, Cambridge University Press, Sep 2000.
- [3] G. E. Moore, Cramming more components onto integrated circuits, *Electronics* **38**(8) (Apr 19 1965).
- [4] R. W. Keyes, Physical Limits in Information-Processing, *Advances in Electronics and Electron Physics* **70**, 159–214 (1988).
- [5] R. P. Feynman, Simulating Physics with Computers, *International Journal of Theoretical Physics* **21**(6-7), 467–488 (1982).
- [6] D. Deutsch, Quantum-Theory, the Church-Turing Principle and the Universal Quantum Computer, *Proceedings of the Royal Society of London Series A-Mathematical Physical and Engineering Sciences* **400**(1818), 97–117 (1985).
- [7] D. Deutsch and R. Jozsa, Rapid Solution of Problems by Quantum Computation, *Proceedings of the Royal Society of London Series A-Mathematical Physical and Engineering Sciences* **439**(1907), 553–558 (Dec 8 1992).

- [8] P. W. Shor, Polynomial-time algorithms for prime factorization and discrete logarithms on a quantum computer, *Siam Journal on Computing* **26**(5), 1484–1509 (Oct 1997).
- [9] L. K. Grover, Quantum mechanics helps in searching for a needle in a haystack, *Physical Review Letters* **79**(2), 325–328 (Jul 14 1997).
- [10] L. K. Grover, From Schrodinger’s equation to the quantum search algorithm, *American Journal of Physics* **69**(7), 769–777 (Jul 2001).
- [11] P. W. Shor, Scheme for Reducing Decoherence in Quantum Computer Memory, *Physical Review A* **52**(4), R2493–R2496 (Oct 1995).
- [12] A. M. Steane, Error correcting codes in quantum theory, *Physical Review Letters* **77**(5), 793–797 (Jul 29 1996).
- [13] I. L. Chuang, N. Gershenfeld, and M. Kubinec, Experimental implementation of fast quantum searching, *Physical Review Letters* **80**(15), 3408–3411 (Apr 13 1998).
- [14] J. A. Jones, M. Mosca, and R. H. Hansen, Implementation of a quantum search algorithm on a quantum computer, *Nature* **393**(6683), 344–346 (May 28 1998).
- [15] L. M. K. Vandersypen, M. Steffen, G. Breyta, C. S. Yannoni, M. H. Sherwood, and I. L. Chuang, Experimental realization of Shor’s quantum factoring algorithm using nuclear magnetic resonance, *Nature* **414**(6866), 883–887 (Dec 20 2001).

- [16] D. G. Cory, A. F. Fahmy, and T. F. Havel, Ensemble quantum computing by NMR spectroscopy, *Proceedings of the National Academy of Sciences of the United States of America* **94**(5), 1634–1639 (Mar 4 1997).
- [17] N. A. Gershenfeld and I. L. Chuang, Bulk spin-resonance quantum computation, *Science* **275**(5298), 350–356 (Jan 17 1997).
- [18] J. I. Cirac and P. Zoller, Quantum Computations with Cold Trapped Ions, *Physical Review Letters* **74**(20), 4091–4094 (May 15 1995).
- [19] C. Monroe, D. M. Meekhof, B. E. King, W. M. Itano, and D. J. Wineland, Demonstration of a Fundamental Quantum Logic Gate, *Physical Review Letters* **75**(25), 4714–4717 (Dec 18 1995).
- [20] W. K. Hensinger, S. Olmschenk, D. Stick, D. Hucul, M. Yeo, M. Acton, L. Deslauriers, C. Monroe, and J. Rabchuk, T-junction ion trap array for two-dimensional ion shuttling, storage, and manipulation, *Applied Physics Letters* **88**(3), 034101 (Jan 16 2006).
- [21] C. Henkel, Magnetostatic field noise near metallic surfaces, *European Physical Journal D* **35**(1), 59–67 (Aug 2005).
- [22] J. Chiaverini, D. Leibfried, T. Schaetz, M. D. Barrett, R. B. Blakestad, J. Britton, W. M. Itano, J. D. Jost, E. Knill, C. Langer, R. Ozeri, and D. J. Wineland, Realization of quantum error correction, *Nature* **432**(7017), 602–605 (Dec 2 2004).
- [23] M. Riebe, H. Haffner, C. F. Roos, W. Hansel, J. Benhelm, G. P. T. Lancaster, T. W. Korber, C. Becher, F. Schmidt-Kaler, D. F. V. James,

- and R. Blatt, Deterministic quantum teleportation with atoms, *Nature* **429**(6993), 734–737 (Jun 17 2004).
- [24] K. A. Brickman, P. C. Haljan, P. J. Lee, M. Acton, L. Deslauriers, and C. Monroe, Implementation of Grover’s quantum search algorithm in a scalable system, *Physical Review A* **72**(5), 050306 (Nov 2005).
- [25] R. Folman, P. Kruger, J. Schmiedmayer, J. Denschlag, and C. Henkel, Microscopic atom optics: From wires to an atom chip, *Advances in Atomic, Molecular, and Optical Physics*, Vol 48 **48**, 263–356 (2002).
- [26] D. Loss and D. P. DiVincenzo, Quantum computation with quantum dots, *Physical Review A* **57**(1), 120–126 (Jan 1998).
- [27] L. P. Kouwenhoven, D. G. Austing, and S. Tarucha, Few-electron quantum dots, *Reports on Progress in Physics* **64**(6), 701–736 (Jun 2001).
- [28] J. M. Elzerman, R. Hanson, L. H. W. van Beveren, B. Witkamp, L. M. K. Vandersypen, and L. P. Kouwenhoven, Single-shot read-out of an individual electron spin in a quantum dot, *Nature* **430**(6998), 431–435 (Jul 22 2004).
- [29] A. Imamoglu, D. D. Awschalom, G. Burkard, D. P. DiVincenzo, D. Loss, M. Sherwin, and A. Small, Quantum information processing using quantum dot spins and cavity QED, *Physical Review Letters* **83**(20), 4204–4207 (Nov 15 1999).
- [30] A. Badolato, K. Hennessy, M. Atature, J. Dreiser, E. Hu, P. M. Petroff, and A. Imamoglu, Deterministic coupling of single quantum dots to single nanocavity modes, *Science* **308**(5725), 1158–1161 (May 20 2005).

- [31] A. Imamoglu, S. Falt, J. Dreiser, G. Fernandez, M. Atature, K. Hennessy, A. Badolato, and D. Gerace, Coupling quantum dot spins to a photonic crystal nanocavity, *Journal of Applied Physics* **101**(8), 081602 (Apr 15 2007).
- [32] J. M. Taylor, J. R. Petta, A. C. Johnson, A. Yacoby, C. M. Marcus, and M. D. Lukin, Relaxation, dephasing, and quantum control of electron spins in double quantum dots, *Physical Review B* **76**(3), 035315 (Jul 2007).
- [33] M. H. Devoret, *Quantum Fluctuations: Les Houches Session LXIII*, page 351, Elsevier, Amsterdam, The Netherlands, 1997.
- [34] A. J. Leggett, Testing the limits of quantum mechanics: motivation, state of play, prospects, *Journal of Physics-Condensed Matter* **14**(15), R415–R451 (Apr 22 2002).
- [35] A. O. Caldeira and A. J. Leggett, Quantum Tunnelling in a Dissipative System, *Annals of Physics* **149**(2), 374–456 (1983).
- [36] M. H. Devoret, J. M. Martinis, and J. Clarke, Measurements of Macroscopic Quantum Tunneling Out of the Zero-Voltage State of a Current-Biased Josephson Junction, *Physical Review Letters* **55**(18), 1908–1911 (1985).
- [37] J. Clarke, A. N. Cleland, M. H. Devoret, D. Esteve, and J. M. Martinis, Quantum-Mechanics of a Macroscopic Variable - the Phase Difference of a Josephson Junction, *Science* **239**(4843), 992–997 (Feb 26 1988).
- [38] I. Giaever, Energy Gap in Superconductors Measured by Electron Tunneling, *Physical Review Letters* **5**(147), 464 (1960).

- [39] B. D. Josephson, Possible New Effects in Superconductive Tunnelling, *Physics Letters* **1**(7), 251–253 (1962).
- [40] B. D. Josephson, Coupled Superconductors, *Reviews of Modern Physics* **36** (1964).
- [41] M. H. Devoret, A. Wallraff, and J. M. Martinis, Superconducting Qubits: a Short Review, *cond-mat/0411174* (2004).
- [42] S. Y. Han, R. Rouse, and J. E. Lukens, Observation of cascaded two-photon-induced transitions between fluxoid states of a SQUID, *Physical Review Letters* **84**(6), 1300–1303 (Feb 7 2000).
- [43] J. R. Friedman, V. Patel, W. Chen, S. K. Tolpygo, and J. E. Lukens, Quantum superposition of distinct macroscopic states, *Nature* **406**(6791), 43–46 (Jul 6 2000).
- [44] J. E. Mooij, T. P. Orlando, L. Levitov, L. Tian, C. H. van der Wal, and S. Lloyd, Josephson persistent-current qubit, *Science* **285**(5430), 1036–1039 (Aug 13 1999).
- [45] I. Chiorescu, Y. Nakamura, C. J. P. M. Harmans, and J. E. Mooij, Coherent quantum dynamics of a superconducting flux qubit, *Science* **299**(5614), 1869–1871 (Mar 21 2003).
- [46] F. Yoshihara, K. Harrabi, A. O. Niskanen, Y. Nakamura, and J. S. Tsai, Decoherence of flux qubits due to  $1/f$  noise, *Physical Review Letters* **97**(16), 167001 (Oct 20 2006).

- [47] B. Savo, F. C. Wellstood, and J. Clarke, Low-Frequency Excess Noise in Nb-Al<sub>2</sub>O<sub>3</sub>-Nb Josephson Tunnel-Junctions, *Applied Physics Letters* **50**(24), 1757–1759 (Jun 15 1987).
- [48] M. Buttiker, Zero-Current Persistent Potential Drop Across Small-Capacitance Josephson-Junctions, *Physical Review B* **36**(7), 3548–3555 (Sep 1 1987).
- [49] D. Vion, A. Aassime, A. Cottet, P. Joyez, H. Pothier, C. Urbina, D. Esteve, and M. H. Devoret, Manipulating the quantum state of an electrical circuit, *Science* **296**(5569), 886–889 (May 3 2002).
- [50] A. Wallraff, D. I. Schuster, A. Blais, L. Frunzio, J. Majer, M. H. Devoret, S. M. Girvin, and R. J. Schoelkopf, Approaching unit visibility for control of a superconducting qubit with dispersive readout, *Physical Review Letters* **95**(6), 060501 (Aug 5 2005).
- [51] I. Siddiqi, R. Vijay, M. Metcalfe, E. Boaknin, L. Frunzio, R. J. Schoelkopf, and M. H. Devoret, Dispersive measurements of superconducting qubit coherence with a fast latching readout, *Physical Review B* **73**(5), 054510 (Feb 2006).
- [52] M. Metcalfe, E. Boaknin, V. Manucharyan, R. Vijay, I. Siddiqi, C. Rigetti, L. Frunzio, R. J. Schoelkopf, and M. H. Devoret, Measuring the Decoherence of a Quantronium Qubit with the Cavity Bifurcation Amplifier, arXiv:0706.0765, accepted to *Physical Review B* (Jun 2007).
- [53] J. M. Martinis, S. Nam, J. Aumentado, and C. Urbina, Rabi oscillations in a large Josephson-junction qubit, *Physical Review Letters* **89**(11), 117901 (Sep 9 2002).

- [54] M. Steffen, M. Ansmann, R. McDermott, N. Katz, R. C. Bialczak, E. Lucero, M. Neeley, E. M. Weig, A. N. Cleland, and J. M. Martinis, State tomography of capacitively shunted phase qubits with high fidelity, *Physical Review Letters* **97**(5), 050502 (Aug 4 2006).
- [55] G. J. Dolan, Offset masks for lift-off processing, *Applied Physics Letters* **31**, 337–339 (1977).
- [56] E. Dobisz, S. Brandow, R. Bass, and J. Mitterender, Effects of molecular properties on nanolithography in PMMA, *NRL Journal of Vacuum, Science and Technology* **18**(1), 107–111 (Jan/Feb 2000).
- [57] V. Bouchiat, D. Vion, P. Joyez, D. Esteve, and M. H. Devoret, Quantum coherence with a single Cooper pair, *Physica Scripta* **T76**, 165–170 (1998).
- [58] V. Bouchiat, D. Vion, P. Joyez, D. Esteve, C. Urbina, and M. H. Devoret, Single Cooper pair electronics, *Applied Superconductivity* **6**(10-12), 491–494 (Oct-Dec 1998).
- [59] T. A. Fulton, P. L. Gammel, D. J. Bishop, L. N. Dunkleberger, and G. J. Dolan, Observation of Combined Josephson and Charging Effects in Small Tunnel Junction Circuits, *Physical Review Letters* **63**(12), 1307–1310 (Sep 18 1989).
- [60] Y. Nakamura, Y. A. Pashkin, and J. S. Tsai, Coherent control of macroscopic quantum states in a single-Cooper-pair box, *Nature* **398**(6730), 786–788 (Apr 29 1999).

- [61] Y. Nakamura and J. S. Tsai, A coherent two-level system in a superconducting single-electron transistor observed through photon-assisted Cooper-pair tunneling, *Journal of Superconductivity* **12**(6), 799–806 (Dec 1999).
- [62] A. B. Zorin, F. J. Ahlers, J. Niemeyer, T. Weimann, H. Wolf, V. A. Krupenin, and S. V. Lotkhov, Background charge noise in metallic single-electron tunneling devices, *Physical Review B* **53**(20), 13682–13687 (May 15 1996).
- [63] Y. Nakamura, Y. A. Pashkin, T. Yamamoto, and J. S. Tsai, Charge echo in a Cooper-pair box, *Physical Review Letters* **88**(4), 047901 (Jan 28 2002).
- [64] G. Ithier, E. Collin, P. Joyez, P. J. Meeson, D. Vion, D. Esteve, F. Chiarello, A. Shnirman, Y. Makhlin, J. Schrieffer, and G. Schon, Decoherence in a superconducting quantum bit circuit, *Physical Review B* **72**(13), 134519 (Oct 2005).
- [65] Y. Nakamura, Y. A. Pashkin, T. Yamamoto, and J. S. Tsai, Charge echo in a Cooper-pair box, *Physical Review Letters* **88**(4), 047901 (Jan 28 2002).
- [66] A. Aassime, G. Johansson, G. Wendin, R. J. Schoelkopf, and P. Delsing, Radio-frequency single-electron transistor as readout device for qubits: Charge sensitivity and backaction, *Physical Review Letters* **86**(15), 3376–3379 (Apr 9 2001).
- [67] T. Duty, D. Gunnarsson, K. Bladh, and P. Delsing, Coherent dynamics of a Josephson charge qubit, *Physical Review B* **69**(14), 140503 (Apr 2004).
- [68] K. Bladh, T. Duty, D. Gunnarsson, and P. Delsing, The single Cooper-pair box as a charge qubit, *New Journal of Physics* **7**, 180 (Aug 26 2005).

- [69] A. Cottet, D. Vion, A. Aassime, P. Joyez, D. Esteve, and M. H. Devoret, Implementation of a combined charge-phase quantum bit in a superconducting circuit, *Physica C-Superconductivity and its Applications* **367**(1-4), 197–203 (Feb 15 2002).
- [70] A. Wallraff, D. I. Schuster, A. Blais, L. Frunzio, R. S. Huang, J. Majer, S. Kumar, S. M. Girvin, and R. J. Schoelkopf, Strong coupling of a single photon to a superconducting qubit using circuit quantum electrodynamics, *Nature* **431**(7005), 162–167 (Sep 9 2004).
- [71] A. Lupascu, S. Saito, T. Picot, P. C. D. Groot, C. J. P. M. Harmans, and J. E. Mooij, Quantum non-demolition measurement of a superconducting two-level system, *Nature Physics* **3**(2), 119–123 (Feb 2007).
- [72] E. Il'ichev, N. Oukhanski, A. Izmailkov, T. Wagner, M. Grajcar, H. G. Meyer, A. Y. Smirnov, A. M. van den Brink, M. H. S. Amin, and A. M. Zagoskin, Continuous monitoring of Rabi oscillations in a Josephson flux qubit, *Physical Review Letters* **91**(9), 097906 (Aug 29 2003).
- [73] M. A. Sillanpää, T. Lehtinen, A. Paila, Y. Makhlin, L. Roschier, and P. J. Hakonen, Direct observation of Josephson capacitance, *Physical Review Letters* **95**(20), 206806 (Nov 11 2005).
- [74] I. Siddiqi, R. Vijay, F. Pierre, C. M. Wilson, M. Metcalfe, C. Rigetti, L. Frunzio, and M. H. Devoret, RF-driven Josephson bifurcation amplifier for quantum measurement, *Physical Review Letters* **93**(20), 207002 (Nov 12 2004).
- [75] I. Siddiqi, R. Vijay, F. Pierre, C. M. Wilson, L. Frunzio, M. Metcalfe, C. Rigetti, R. J. Schoelkopf, M. H. Devoret, D. Vion, and D. Esteve, Direct

- observation of dynamical bifurcation between two driven oscillation states of a Josephson junction, *Physical Review Letters* **94**(2), 027005 (Jan 21 2005).
- [76] E. Boaknin, V. E. Manucharyan, S. Fissette, M. Metcalfe, L. Frunzio, R. Vijay, I. Siddiqi, A. Wallraff, R. J. Schoelkopf, and M. Devoret, Dispersive microwave bifurcation of a superconducting resonator cavity incorporating a Josephson junction, *cond-mat/0702445* (Feb 2007).
- [77] R. Vijay, *Thesis: Josephson bifurcation amplifier*, Yale University, 2008.
- [78] M. I. Dykman and M. A. Krivoglaz, Fluctuations in Non-Linear Systems Near Bifurcations Corresponding to the Appearance of New Stable States, *Physica A* **104**(3), 480–494 (1980).
- [79] V. E. Manucharyan, E. Boaknin, M. Metcalfe, R. Vijay, I. Siddiqi, and M. H. Devoret, RF bifurcation of a Josephson junction: microwave embedding circuit requirements, *Physical Review B* **76**, 014524 (26 Jul 2007).
- [80] L. D. Landau and E. M. Lifshitz, *Mechanics*, Pergamon, Oxford, 1969.
- [81] D. M. Pozar, *Microwave engineering*, Wiley, 1997.
- [82] P. K. Day, H. G. LeDuc, B. A. Mazin, A. Vayonakis, and J. Zmuidzinas, A broadband superconducting detector suitable for use in large arrays, *Nature* **425**(6960), 817–821 (Oct 23 2003).
- [83] L. Frunzio, A. Wallraff, D. Schuster, J. Majer, and R. Schoelkopf, Fabrication and characterization of superconducting circuit QED devices for quantum computation, *IEEE Transactions on Applied Superconductivity* **15**(2), 860–863 (Jun 2005).

- [84] F. Pobell, *Matter and methods at low temperatures*, Springer-Verlag, 1992.
- [85] D. Schuster, *Thesis: Circuit quantum electrodynamics*, Yale University, 2007.
- [86] A. Blais, R. S. Huang, A. Wallraff, S. M. Girvin, and R. J. Schoelkopf, Cavity quantum electrodynamics for superconducting electrical circuits: An architecture for quantum computation, *Physical Review A* **69**(6), 062320 (Jun 2004).
- [87] D. I. Schuster, A. Wallraff, A. Blais, L. Frunzio, R. S. Huang, J. Majer, S. M. Girvin, and R. J. Schoelkopf, AC Stark shift and dephasing of a superconducting qubit strongly coupled to a cavity field, *Physical Review Letters* **94**(12), 123602 (Apr 1 2005).
- [88] B. Abdo, E. Segev, O. Shtempler, and E. Buks, Nonlinear dynamics in the resonance line shape of NbN superconducting resonators, *Physical Review B* **73**(13), 134513 (Apr 2006).
- [89] E. A. Tholen, A. Ergul, E. M. Doherty, F. M. Weber, F. Gregis, and D. B. Haviland, Nonlinearities and parametric amplification in superconducting coplanar waveguide resonators, *Applied Physics Letters* **90**(25), 253509 (Jun 18 2007).
- [90] T. A. Fulton and L. N. Dunkleberger, Lifetime of Zero-Voltage State in Josephson Tunnel-Junctions, *Physical Review B* **9**(11), 4760–4768 (1974).
- [91] A. Cottet, *Thesis: Implementation of a quantum bit in a superconducting circuit*, University of P. and M. Curie Paris, 2002.

- [92] A. Erdlyi, W. Magnus, F. Oberhettinger, and F. G. Tricomi, *Higher transcendental functions*, volume 3, McGraw-Hill, 1955.
- [93] D. Vion, Josephson Quantum Bits Based on a Cooper Pair Box, in *Quantum entanglement and information processing*, 2004.
- [94] I. I. Rabi, Space quantization in a gyrating magnetic field, *Physical Review* **51**(8), 0652–0654 (Apr 1937).
- [95] N. F. Ramsey, A Molecular Beam Resonance Method with Separated Oscillating Fields, *Physical Review* **78**(6), 695–699 (1950).
- [96] D. J. V. Harlingen, T. L. Robertson, B. L. T. Plourde, P. A. Reichardt, T. A. Crane, and J. Clarke, Decoherence in Josephson-junction qubits due to critical-current fluctuations, *Physical Review B* **70**(6) (Aug 2004).
- [97] E. Collin, G. Ithier, A. Aassime, P. Joyez, D. Vion, and D. Esteve, (2004).
- [98] J. Koch, T. M. Yu, D. I. Schuster, J. Majer, A. Blais, M. H. Devoret, S. M. Girvin, and R. J. Schoelkopf, Charge Insensitive Qubit Design from Optimizing the Cooper-Pair Box, cond-mat/0703002, accepted to *Physical Review A* (2007).
- [99] M. Steffen, M. Ansmann, R. C. Bialczak, N. Katz, E. Lucero, R. McDermott, M. Neeley, E. M. Weig, A. N. Cleland, and J. M. Martinis, Measurement of the entanglement of two superconducting qubits via state tomography, *Science* **313**(5792), 1423–1425 (Sep 8 2006).
- [100] J. C. Lee, W. D. Oliver, K. K. Berggren, and T. P. Orlando, Nonlinear resonant behavior of a dispersive readout circuit for a superconducting flux qubit, *Physical Review B* **75**(14), 144505 (Apr 2007).

- [101] M. Watanabe and D. B. Haviland, Quantum effects in small-capacitance single Josephson junctions, *Physical Review B* **67**(9), 094505 (Mar 1 2003).
- [102] U. Geigenmuller and G. Schon, Single Electron Effects and Bloch Oscillations in Normal and Superconducting Tunnel-Junctions, *Physica B* **152**(1-2), 186–202 (Aug 1988).
- [103] L. Kuzmin, Y. Pashkin, A. Zorin, and T. Claeson, Linewidth of Bloch oscillations in small Josephson junctions, *Physics B* **203**, 376–380 (1994).
- [104] F. Nguyen, N. Boulant, G. Ithier, P. Bertet, H. Pothier, D. Vion, and D. Esteve, Current to Frequency Conversion in a Josephson Circuit, *Physical Review Letters* **99**, 187005 (2007).
- [105] J. P. Cleuziou, W. Wernsdorfer, V. Bouchiat, T. Ondarcuhu, and M. Monthieux, Carbon nanotube superconducting quantum interference device, *Nature Nanotechnology* **1**, 53 (2006).
- [106] L. Kuzmin, I. Agulo, M. Fominsky, A. Savin, and M. Tarasov, Optimization of electron cooling by SIN tunnel junctions, *Superconductor Science and Technology* **17**(5), 400–405 (May 2004).
- [107] J. Aumentado, M. W. Keller, J. M. Martinis, and M. H. Devoret, Nonequilibrium quasiparticles and  $2e$  periodicity in single-Cooper-pair transistors, *Physical Review Letters* **92**(6), 066802 (Feb 13 2004).
- [108] A. J. Ferguson, N. A. Court, F. E. Hudson, and R. G. Clark, Thin film aluminium for superconducting qubits, *Nanoscience and nanotechnology, ICONN'06* , 574–577 (July 2006).

- [109] D. F. Santavicca and D. E. Prober, Impedance-matched low-pass stripline filters, arXiv:0802.1343v1 (2008).
- [110] W. H. Press, S. A. Teukolsky, W. T. Vetterling, and B. P. Flannery, *Numerical Recipes: The Art of Scientific Computing*, Cambridge University Press, 2007.
- [111] G. E. P. Box and M. E. Muller, A Note on the Generation of Random Normal Deviates, *Annals of Mathematical Statistics* **29**(2), 610–611 (1958).